



**HAL**  
open science

# Architecture of the Early to Late Miocene Upper Cibulakan Formation, North West Java Basin, Indonesia : Insights from sequence stratigraphy and Stratigraphic Modeling

Nanda Natasia

► **To cite this version:**

Nanda Natasia. Architecture of the Early to Late Miocene Upper Cibulakan Formation, North West Java Basin, Indonesia : Insights from sequence stratigraphy and Stratigraphic Modeling. Applied geology. Sorbonne Université, 2024. English. NNT : 2024SORUS040 . tel-04950609

**HAL Id: tel-04950609**

**<https://theses.hal.science/tel-04950609v1>**

Submitted on 17 Feb 2025

**HAL** is a multi-disciplinary open access archive for the deposit and dissemination of scientific research documents, whether they are published or not. The documents may come from teaching and research institutions in France or abroad, or from public or private research centers.

L'archive ouverte pluridisciplinaire **HAL**, est destinée au dépôt et à la diffusion de documents scientifiques de niveau recherche, publiés ou non, émanant des établissements d'enseignement et de recherche français ou étrangers, des laboratoires publics ou privés.

# Sorbonne Université

Ecole doctorale 398 << Géosciences, Ressources Naturelles, Environnement >>

*Institut des Sciences de la Terre de Paris*

## **Architecture of the Early to Late Miocene Upper Cibulakan Formation, North West Java Basin, Indonesia:**

*Insights from sequence stratigraphy and Stratigraphic  
Modeling*

By Nanda Natasia

Thèse de doctorat de Science de la Terre

Dirigée par Fadi Henri NADER et Damien DO COUTO

Présentée et soutenue publiquement le 16 février 2024

Devant un jury composé de :

Mme. Sylvie Leroy	Directrice de recherche, Sorbonne Université	Président du jury
M. Manuel Pubellier	Directeur de recherche, CNRS	Rapporteur
Mme. Sophie Leleu	Maitre de conférences, Université de Bordeaux	Rapporteuse
M. Remy Deschamps	Ingénieur de recherche, IFPEN	Examineur
Mme. Estelle Leroux	Chercheuse, IFREMER	Examineur
M. Ildrem Syafri	Professeur, Padjadjaran University	Examineur
M. Fadi H. Nader	Chef de projet, IFPEN; Professeur, Utrecht	Directeur de thèse
M. Damien Do Couto	Maitre de conférences, Sorbonne Université	Co-encadrant



*Dedicated to Papa and Mama, whose unwavering support and love have been my guiding light throughout this journey. To my beloved wife, Sabine, whose patience, encouragement, and understanding made this endeavor possible. And to my cherished children, Naufal and Keenan, whose presence brings joy and purpose to every achievement. This dissertation is a tribute to the love and strength of my family*





# Acknowledgement

I extend my deepest appreciation to my supervisors, Damien Do Couto and Fadi Nader, for their exceptional guidance and support throughout the entire dissertation process at IStEP ED398 Sorbonne Université. Damien not only served as a dedicated supervisor but also proved to be a supportive and helpful friend during my time at the university. His mentorship went beyond academic guidance, and his friendship added a valuable layer of understanding and support to my journey. Fadi's expertise and insightful feedback greatly contributed to the refinement of this research, and I am thankful for his unwavering support. I would also like to express my gratitude to the members of my committee, Remy Deschamps, who has been a regular presence in my annual reports, providing valuable insights and encouragement. Special thanks to Christian Gorini for his role as the representative of the doctoral school. His consistent monitoring and assistance have been valuable in ensuring the progress of my thesis and Jean Loup Rubino for his time in guiding me in the interpretation of the data, I learn a lot from his experience.

I want to acknowledge IStEP for providing the necessary resources and fostering an atmosphere of academic excellence, especially those on the 5th-floor corridor of towers 56-66, for their unwavering support and warm welcome during my four years in the lab. To my fellow doctoral and researcher, Ikena, Dea, Eva, Thomas, Camille, Goulwen, Sylvain, and Guillaume, I appreciate your camaraderie, discussions, and assistance in every aspect of my academic journey. Whether it was helping with my less-than-beginner level of French, or sharing moments of laughter and insightful conversations, your contributions have made a lasting impact.

I extend my heartfelt thanks to Ildrem Syafri who directed me to pursue my academic journey. Without his encouragement, this thesis would not have been realized. My friends and colleagues at the Faculty of Geological Engineering, UNPAD, for their support and discussions. Special thanks to Pak Abdurrokhim, Pak Iyan Haryanto, Pak Febriwan, and Ibu Lia Jurnaliah for their discussions on stratigraphy, structural geology, and biostratigraphy in the West Java region. I also want to acknowledge Kang Rahmat at Pertamina Hulu Energi for his valuable insights and discussions.

I am deeply grateful to *LPDP* (Indonesia Endowment Fund for Education Agency) Ministry of Finance, Republic of Indonesia for funding my pursuit of this degree through scholarship No. 201912220215811; and to *Pusdatin ESDM* (National Data Repository management on energy and mineral sector) Ministry of Energy and Mineral Resources of Republic of Indonesia for granting permission to utilize data through permit No. 9Pj/KS.01/SJD.2/2021. Without the support of these two institutions, I would not have been able to continue my doctoral studies.

Lastly, my deepest thanks go to my family for their constant encouragement and understanding. Their support has been my pillar of strength. I want to express my profound gratitude to my wife, Sabine, and my children, Naufal and Keenan, for their unwavering support and understanding throughout this challenging journey. Their love has been my source of inspiration, and this achievement is as much theirs as it is mine.

Paris, 2024

Nanda



# Abstract

This study explores the sequence stratigraphic evolution of the Early to late Miocene Upper Cibulakan Formation in the North West Java Basin, Indonesia. The primary objectives are to reconstruct depositional environments, understand regional stratigraphic evolution, and forecast the physical and dynamic parameters controlling the distribution of potential reservoir stratigraphic forward modeling. The study employs a model-independent sequence stratigraphic approach, integrating sedimentological, biostratigraphic, well log, and seismic data.

The methodology involves two main phases: the development of a sequence stratigraphic framework and stratigraphic forward modeling. The sequence stratigraphic framework is built by identifying sequence boundaries, maximum flooding surfaces, and transgressive surfaces. Biostratigraphic data, electrofacies determination, well-to-well correlation, and seismic interpretation contribute to this framework. Seismic facies identification further enhances understanding, linking seismic reflector geometries to depositional processes. The second phase employs stratigraphic forward modeling using the Dionisoflow. This numerical technique simulates basin infill over geological time scales, considering factors like tectonic deformation, subsidence, sea level fluctuations, and sediment flux. Calibration involves structural evolution, sediment input settings, and transport parameters. The models are classified based on depositional facies, and uncertainty and sensitivity analyses assess the impact of various parameters.

Results showcase the integration of biostratigraphic, well, and seismic data, providing insights into the geological evolution of the North West Java Basin. Twelve third-order sequences, organized into three second-order sequences, were interpreted within the Upper Cibulakan Formation. Four facies association has been revealed, based on gamma-ray log values; and nine seismic facies were identified, characterized by unique geometry and reflector configuration as well as stratal termination. The Aquitanian – early Burdigalian marked the dominance of northern and northeastern deltas, while the Burdigalian – early Langhian saw further deltaic progradation southward. The Langhian – Serravallian was characterized by a transgression, leading to the abandonment of the delta and the emergence of marine tidal bars. The Tortonian witnessed basin subsidence, reduced sediment supply, and the formation of isolated carbonate reefs.

The Stratigraphic Forward Modeling simulation, involving a timeframe from 22.2 to 8.4 Ma, was constructed. The accommodation of sediment is governed first by tectonics, then by eustasy; the sediment transport parameters, are carefully selected through systematic analysis and sensitivity testing, ensuring accuracy of the models in replicating observed thickness and lithological variations. The analysis of potential reservoir distribution shows that the prospective sandy reservoir zones tend to

follow a north-south orientation, influenced by rift direction that led to different sediment compaction and delta geometry, which influence accommodation space. Based on uncertainty and sensitivity analysis, sediment supply appears to be the most influential parameter compared to other parameters in the modeling.

# Résumé

Cette étude explore l'évolution stratigraphique séquentielle de la Formation Cibulakan supérieure, du Miocène inférieur au Miocène supérieur, dans le bassin Nord-Ouest Java, en Indonésie. Les objectifs principaux de ce travail sont de reconstruire les environnements de dépôt, de comprendre l'évolution stratigraphique régionale et de comprendre quels sont les paramètres contrôlant l'architecture des dépôts et des formations réservoirs par une étude de sensibilité du modèle stratigraphique. L'étude utilise une approche stratigraphique séquentielle indépendante du modèle, intégrant des données sédimentologiques, biostratigraphiques, de diagraphie et sismiques.

La méthodologie comprend deux phases principales: le développement d'un cadre stratigraphique séquentiel et la modélisation stratigraphique. Le cadre stratigraphique séquentiel est construit en identifiant les limites de séquence, les surfaces d'inondation maximale et les surfaces de transgression. Les données biostratigraphiques, la détermination des électrofaciès, la corrélation puits à puits et l'interprétation sismique contribuent à définir ce cadre stratigraphique. L'identification des faciès sismiques renforce davantage la compréhension, en reliant les géométries des réflecteurs sismiques aux processus de dépôt. La deuxième phase utilise la modélisation stratigraphique par l'utilisation du logiciel Dionisosflow. Cette technique numérique simule le remplissage du bassin sur des échelles de temps géologiques, en tenant compte de facteurs tels que la déformation tectonique, la subsidence, les fluctuations du niveau de la mer et le flux sédimentaire. L'étalonnage implique l'évolution structurelle du bassin, les paramètres d'entrée des sédiments (source, taille de grain, flux d'eau) et les paramètres de transport particuliers. Les modèles sont classés en fonction des faciès de dépôt, et des analyses d'incertitude et de sensibilité évaluant l'impact de divers paramètres.

Les résultats montrent l'intégration des données biostratigraphiques, des données de puits et des données sismiques, ce qui permet de mieux comprendre l'évolution géologique du bassin du nord-ouest de Java. Douze séquences stratigraphiques de troisième ordre, imbriquées en trois séquences du deuxième ordre, ont été interprétées au sein de la Formation Cibulakan supérieure. Quatre associations de faciès ont été révélées, basées sur l'évolution des diagraphies (gamma-ray) ; et neuf faciès sismiques ont été identifiés, tous caractérisés par une géométrie et une configuration de réflecteurs (incluant les terminaisons tritales) uniques. L'Aquitainien - le Burdigalien précoce a marqué la dominance des deltas nordiques et nord-est, tandis que le Burdigalien - le Langhien précoce a vu une progradation deltaïque ultérieure vers le sud. Le Langhien - le Serravallien a été caractérisé par une transgression, entraînant l'abandon du delta et l'émergence de bancs marins de marée. Le Tortonien a été marqué par une subsidence du bassin, une diminution de l'approvisionnement en sédiments et la formation de récifs carbonatés isolés.

La simulation de la modélisation stratigraphique a été réalisée sur une période de 22,2 à 8,4 millions d'années. L'accommodation des sédiments est d'abord régie par la tectonique puis l'eustatisme; les paramètres de transport des sédiments sont soigneusement sélectionnés par une analyse systématique et des tests de sensibilité sont effectués afin de garantir l'exactitude des modèles dans la reproduction des variations observées d'épaisseur et de lithologie. L'analyse de la distribution potentielle des réservoirs montre que les zones de réservoir sableux prospectives ont tendance à suivre une orientation nord-sud, influencée par la direction du rift qui a conduit à une compaction différentielle des sédiments et à une géométrie deltaïque, influençant l'espace d'accommodation.

# Table of Content

Acknowledgement.....	iii
Abstract .....	v
Résumé.....	vii
Table of Content.....	ix
Table of Figures .....	xiii
CHAPTER 1:GENERAL INTRODUCTION.....	1
1.1. Introduction .....	3
1.2. Rationale.....	5
1.3. Location of the study.....	7
1.4. Objective of the study .....	7
CHAPTER 2:REGIONAL GEOLOGY.....	9
2.1. Geodynamic of North West Java Basin .....	11
2.1.1. Jurassic to Cretaceous .....	14
2.1.2. Paleocene-Eocene.....	15
2.1.3. Miocene-Pliocene.....	16
2.2. Stratigraphy of North West Java Basin .....	17
2.2.1. Basement .....	17
2.2.2. Pre-Talangakar Group (Pre TAF) .....	19
2.2.3. Talangakar Formation (TAF) .....	22
2.2.4. Baturaja Formation (BRF) .....	24
2.2.5. Upper Cibulakan Formation (UCF) .....	26
2.2.6. Parigi and Cisubuh Formations .....	33
2.3. Petroleum system .....	34
2.3.1. Source Rocks.....	34
2.3.2. Maturation .....	35
2.3.3. Migration.....	35
2.3.4. Reservoir .....	36
2.3.5. Trap type .....	36
2.3.6. Seals .....	36
CHAPTER 3:DATASET AND METHODOLOGY.....	39
3.1. Dataset.....	41
3.2. Methodology .....	45
3.2.1. Sequence Stratigraphic Framework Development.....	46
3.2.2. Stratigraphic Forward Modeling .....	51
CHAPTER 4:GEOLOGY OF ARDJUNA SUB-BASIN .....	57
4.1. Biostratigraphic data review and reinterpretation .....	59
4.1.1. Available biostratigraphic data review.....	59
4.1.2. Biostratigraphic age reinterpretation .....	65
4.2. Well to Well Correlation .....	69
4.3. Seismic interpretation.....	79
4.3.1. Well to Seismic Ties .....	79
4.3.2. Fault interpretation .....	82
4.3.3. Horizon Interpretation .....	84



4.4. Discussion .....	96
4.4.1. Paleogeographic reconstruction .....	96
4.4.2. Impact of the fault on the architecture of the sedimentary filling and thickness distributions .....	102
4.4.3. Mid-Main, Pre-Parigi, and Parigi Carbonate distribution .....	108

**CHAPTER 5:SEQUENCE STRATIGRAPHY OF THE UPPER CIBULAKAN FORMATION .....**

5.1. Introduction .....	111
5.2. Electrofacies Determination .....	111
5.2.1. Facies Association 1: Distributary channel and point bar facies deposited in delta plain .....	113
5.2.2. Facies Association 2: Delta front to prodelta environment with tidal influenced mouth bar or shelf ridge.....	115
5.2.3. Facies Association 3: Reworked or clastic carbonate in a storm dominated marine environment.....	119
5.2.4. Facies Association 4: Reefal carbonate.....	119
5.3. Sequence Stratigraphy Interpretation .....	123
5.3.1. Sequence 1.....	123
5.3.2. Sequence 2.....	127
5.3.3. Sequence 3.....	128
5.3.4. Sequence 4.....	130
5.3.5. Sequence 5.....	130
5.3.6. Sequence 6.....	131
5.3.7. Sequence 7.....	131
5.3.8. Sequence 8.....	132
5.3.9. Sequence 9.....	132
5.3.10. Sequence 10.....	133
5.3.11. Sequence 11.....	133
5.3.12. Sequence 12.....	134
5.3.13. Sequence 13.....	134
5.4. Seismic Stratigraphy Interpretation.....	135
5.4.1. Seismic Facies .....	135
5.4.2. Third Order Sequence Seismic horizon interpretation .....	140
5.4.3. Second order sequences .....	152
5.5. Depositional environment .....	158
5.6. Conclusions .....	161

**CHAPTER 6:STRATIGRAPHIC FORWARD MODELING.....**

6.1. Introduction .....	165
6.2. Base Model Simulation .....	171
6.2.1. Accomodation .....	171
6.2.2. Transport Parameters.....	172
6.2.3. Sediment Input .....	174
6.2.4. Model Calibration .....	176
6.3. Model result.....	180
6.4. Multi simulation uncertainty and sensitivity .....	185
6.5. Reservoir prediction .....	189
6.6. Discussion .....	191
6.6.1. Sediment supply, bathymetry and subsidence curve.....	191

6.6.2. Reservoir distribution.....	194
6.7. Conclusion.....	195
CHAPTER 7:CONCLUSIONS AND OUTLOOKS .....	197
7.1. Conclusion.....	199
7.2. Outlook.....	201
References .....	203



# Table of Figures

Figure 1.1 Study location area.....	4
Figure 1.2 Location map of North West Java Basin. ....	11
Figure 2.1 Digital Elevation Model showing principal surface features of the Sundaland region. ....	12
Figure 2.2 Regional cross-section through the West Java margin. ....	12
Figure 2.3 Tectonic map of South East Asia.....	13
Figure 2.4 Sundaland and surrounding area plate tectonic reconstruction at 90 Ma.....	14
Figure 2.5 Series of plate reconstructions highlighting the timing of basin evolution.....	16
Figure 2.6 Correlation chart of the basins of Sundaland. ....	18
Figure 2.7 Seismic derived basement times structure map of North West Java Basin .....	19
Figure 2.8 Tectonostratigraphic chart of the North West Java Basin.....	21
Figure 2.9 West – East cross section line in Northern Ardjuna Sub Basin based on seismic data .....	22
Figure 2.10 A generalized paleotopography and drainage pattern during the Talangakar Formation ...	23
Figure 2.11 Paleogeography of the NW Java during the Early Miocene Baturaja Formation.....	24
Figure 2.12 Schematic diagram of the Early Miocene Baturaja Formation ramp.....	25
Figure 2.13 Lithofacies map of Upper Cibulakan Formation. ....	28
Figure 2.14 Facies association of Upper Cibulakan Formation depositional facies.....	28
Figure 2.15 Paleodepositional reconstruction of Upper Cibulakan Formation .....	30
Figure 2.16 Map view of all the shelf ridges observed at FXE and E field areas. ....	31
Figure 2.17 Paleogeography reconstruction of West Java area during Middle Miocene.....	32
Figure 2.18 Mid Main Carbonate depositional model.....	34
Figure 3.1 Base map of study area .....	43
Figure 3.2 W-E 2D seismic section showing the quality of the seismic data visually .....	44
Figure 3.3 Workflow of the study .....	45
Figure 3.4 Nomenclature of systems tracts .....	49
Figure 4.1 3D view of the Baturaja Formation in the Ardjuna sub-basin .....	59
Figure 4.2 Calcareous nannofossils and planktonic foraminifera age chart.....	65
Figure 4.3 Arbitrary well correlation cross-section A.....	68
Figure 4.4 Well to well correlation line and selected seismic base map used in this report. ....	72
Figure 4.5 North South correlation (NS 1 line).....	73
Figure 4.6 North South correlation (NS 2 line).....	74
Figure 4.7 North South correlation (NS 3 line).....	75

Figure 4.8 West East correlation (WE 1 line) .....	76
Figure 4.9 West East correlation (WE 2 line) .....	77
Figure 4.10 West East correlation (WE 3 line) .....	78
Figure 4.11 Available check shot data used for well to seismic ties .....	79
Figure 4.12 SH-1 well to seismic ties analysis .....	81
Figure 4.13 GGG-1 well to seismic ties analysis .....	81
Figure 4.14 Horizon and fault interpretation on NW – SE Seismic line .....	83
Figure 4.15 3D view of the top basement grid .....	83
Figure 4.16 Top Basement time structure map .....	86
Figure 4.17 Top Talangakar Formation time structure map.....	86
Figure 4.18 Top Baturaja Formation time structure map .....	87
Figure 4.19 Top Massive unit time structure map.....	87
Figure 4.20 Top Upper Cibulakan Formation time structure map .....	88
Figure 4.21 Top Parigi Formation time structure map .....	88
Figure 4.22 Seismic line S1.....	89
Figure 4.23 2D seismic line S7 and S6 .....	90
Figure 4.24 N – S seismic line S8 .....	91
Figure 4.25 N – S seismic line S9 .....	92
Figure 4.26 Talangakar Formation thickness map derived from seismic interpretation. ....	93
Figure 4.27 Baturaja Formation thickness map derived from seismic interpretation.....	93
Figure 4.28 Lower part of Upper Cibulakan Formation thickness map.....	94
Figure 4.29 Upper part of Upper Cibulakan Formation thickness map .....	94
Figure 4.30 Parigi Formation thickness map derived from seismic interpretation.....	95
Figure 4.31 typical gamma ray log response in Talangakar Formation. ....	98
Figure 4.32 General paleogeography reconstruction of Talangakar Formation.....	99
Figure 4.33 GR log response and paleogeography reconstruction during the Baturaja Formation....	100
Figure 4.34 Arbitrary line correlation in the Upper Cibulakan Formation.....	103
Figure 4.35 N – S seismic line S10 section.....	104
Figure 4.36 Paleogeography reconstruction of Upper Cibulakan Formation.....	105
Figure 5.1 Generalized location map of North West Java sea showing the study area.....	112
Figure 5.2 SZN-1 composite log showing example of blocky and bell gamma ray facies .....	114
Figure 5.3 Zoom in of SZN-1 composite 3280 – 3365 ft.....	115
Figure 5.4 Composite log showing example of funnel gamma ray facies (GRF3).....	116
Figure 5.5 Composite log showing example of blocky serrated gamma ray facies (GRF4).....	117
Figure 5.6 Composite log showing example GRF5, 6, and 7 at GGG-1 well.....	118

Figure 5.7. The general sequence stratigraphic chart of the Ardjuna sub basin NWJB based on the analysis of the SD-1.....	120
Figure 5.8. SD-1 well sequence stratigraphic interpretation with biostratigraphic report.....	124
Figure 5.9. North – South sequence stratigraphic. ....	125
Figure 5.10. West – East sequence stratigraphic.....	126
Figure 5.11. Correlation on SH-1; SD-1; and SZ-1 well.....	128
Figure 5.12. Dip meter and frequency plot of the dip direction in SH-1.....	129
Figure 5.13. Sequence boundary interpretation on seismic line NS1a.....	141
Figure 5.14. Sequence boundary interpretation on seismic line NS1b and NS1c.....	142
Figure 5.15. Sequence boundary interpretation on seismic line NS2.....	143
Figure 5.16. Sequence boundary interpretation on seismic line NS3.....	144
Figure 5.17. Sequence boundary interpretation on seismic line NS4.....	145
Figure 5.18. Sequence boundary interpretation on seismic line WE1.....	146
Figure 5.19. Sequence boundary interpretation on seismic line WE2.....	147
Figure 5.20. Sequence boundary interpretation on seismic line WE3.....	148
Figure 5.21. Sequence boundary interpretation in composite line NS1abc.....	150
Figure 5.22. Zoom on the interpreted seismic line NS2.....	151
Figure 5.23. Zoom into the interpreted seismic line NS4 showing the location of SF3.....	152
Figure 5.24. Sequence stratigraphic interpretation of the NS1b line.....	153
Figure 5.25 Line drawing interpretation and sequence stratigraphic interpretation in Upper Cibulakan formation. ....	154
Figure 5.26 thickness maps in time domain at three deposition time intervals.....	155
Figure 5.27 Schematic gross depositional environment of the Upper Cibulakan Formation in the Ardjuna sub-basin of the North West Java Basin. ....	159
Figure 6.1 Proposed paleogeography of North West Java basin at Langhian.....	166
Figure 6.2 Schematic diagram illustrating the paleobathymetric reconstruction.....	167
Figure 6.3 North-south cross section of base model depth at the beginning of deposition.....	168
Figure 6.4 Example of the adjustment applied to subsidence at 19 Ma. ....	169
Figure 6.5 Paleobathymetry map at the base of the model (22.2 Ma).....	170
Figure 6.6 North-south cross section of the bathymetric model for different Kg and Kw in continental environment.....	173
Figure 6.7 North-south cross section of the bathymetric model for different Kg and Kw in marine environment.....	173
Figure 6.8 Sediment supply, fluvial discharge and lithological variation curve used in the model. ...	174
Figure 6.9 In-situ carbonate production rate vs depth curve.....	175
Figure 6.10 thickness error percentage map and thickness calibration rate.....	177

Figure 6.11 Well correlation plane showing the comparison simulated grid with well log .....	179
Figure 6.12 Stratigraphic forward modeling simulation result.....	181
Figure 6.13 3D fence diagrams. ....	182
Figure 6.14 Simulated facies and seismic section in North – South direction .....	184
Figure 6.15 Simulated facies and seismic section in West – East direction.....	184
Figure 6.16. Matrix scatter plot of designed parameters .....	187
Figure 6.17. The multi parameters simulation sensitivity results.....	188
Figure 6.18. Reservoir distribution probability map .....	190
Figure 6.19 Final input curve that were used in the stratigraphic modeling. ....	192

## **CHAPTER 1: GENERAL INTRODUCTION**





## 1.1. Introduction

Global oil and gas discoveries have experienced a significant downturn in recent years. In Indonesia, exploration activities are primarily directed toward frontier areas, deep water regions, and high-temperature environments, which come with greater uncertainty. These factors have deterred decision-makers from investing in such risky exploration ventures. Many fields that have entered the production decline phase may still hold significant potential through the application of Enhanced Oil Recovery (EOR) or by re-evaluating reservoir layers. Numerous oil and gas fields, categorized as brownfields (reaching a production plateau in mature fields), may still offer substantial opportunities in Indonesia. Therefore, advancements in technology, reservoir characterization and numerical modeling are needed to further unlock the exploration and production potential of Indonesia.

Facing the challenge of bringing energy to Indonesia's growing population in a responsible way, oil and natural gas still are and will remain the primary sources to fulfill Indonesia energy needs, despite the obligation to continue developing and transitioning to new and renewable energy. In 2017, the Indonesian government, through Special task force for upstream oil and gas business activities of the Republic of Indonesia (SKKMIGAS), issued the national general energy plan, abbreviated as RUEN. This plan represents the government's policy for managing national-level energy, including Indonesia's ambition to achieve energy self-sufficiency and national energy resilience in sustainable development. This is articulated in the vision, mission, objectives, and targets of the national energy that are aligned with the National Energy Commission (KEN).

Through the modeling of oil and natural gas energy supply in RUEN, it is predicted that Indonesia will require a supply of 1.76 million barrels of oil equivalent per day (MBOPD) in 2025 and 3.72 MBOPD in 2050 (SKKMIGAS, 2021). To achieve energy self-sufficiency, these needs are still far from being met, especially when compared to the national oil production, which averaged around 745 MBOPD at the end of 2022 (SKKMIGAS, 2023).

SKKMIGAS, tasked with overseeing upstream oil and gas activities in Indonesia, has formulated medium and long-term targets of 1 million barrels per day (1,000 MBOPD) by 2030. This target is envisioned to be achieved through the optimization (O) of existing fields, increased production from enhanced oil recovery (EOR), and the transformation (T) of measured reserves into production reserves, as well as new exploration (E). The last two

planning sources mentioned (T and E), are the responsibilities of the national earth scientists to discover new reserves and confirm newly discovered fields through emerging technologies.

The North West Java Basin (NWJB) is a sedimentary basin of great importance in term of oil and gas resources in Indonesia. This basin has proven oil reserves (PR) of 204.8 million barrels (MMstb) and gas reserves of 1,415 billion standard cubic feet (Bscf). Additionally, it has possible recoverable resources (RR) of 1,669 MMstb of oil and 2,470 Bscf of gas (Indonesia oil and gas reserve map, 2020). This means that only 12% of the proven PR for oil has been converted to RR.

This thesis evaluates the development of sedimentary sequences in the Miocene age (22.2-8.4 Ma) in NWJB (figure 1.1), which is one of the primary targets for future responsible hydrocarbon exploration in Indonesia. An integrated sequence stratigraphy analysis based on 2D seismic data, wireline log, and biostratigraphic data was conducted on the upper Cibulakan Formation (Miocene), within the Ardjuna sub-basin of the North West Java Basin. This research provides insights into the geological processes governing sediment supply, bathymetry, subsidence rates, and the development of potential reservoir zones by using stratigraphic forward modeling techniques. It offers valuable geological insights into the Ardjuna sub-basin, serving as a foundation for future exploration and resource development endeavors, by understanding the complexities of sedimentary processes and reservoir distribution.

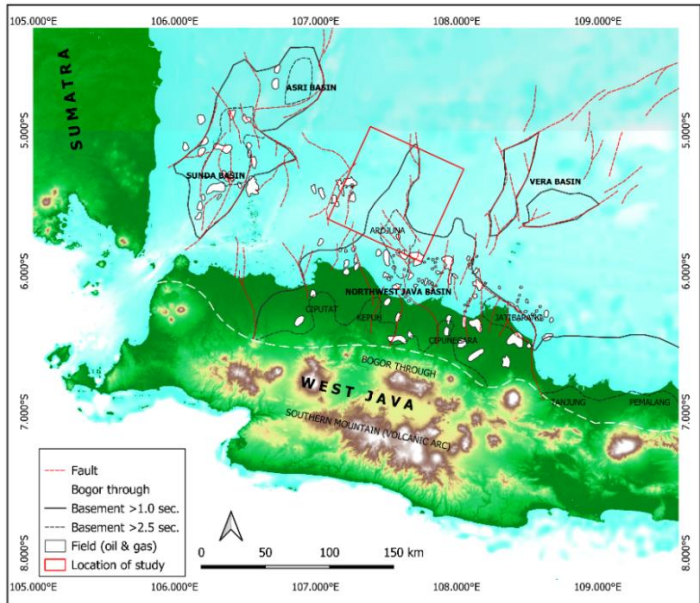


Figure 1.1 Location map of North West Java Basin (modified from Noble, 1993). The red rectangle represents the study area.

## 1.2. Rationale

One of the greatest challenges in hydrocarbon exploration within a basin is predicting the presence of reservoirs (Jahn *et al.*, 2008; Smyth *et al.*, 2014; Tobin and Schwarzer, 2014), including their spatial distribution patterns, as well as understanding the architecture and quality of these reservoirs (McBride, 1984; Mode *et al.*, 2017). This challenge is not unique to hydrocarbons, as predicting reservoir distribution for any kind of subsurface resources or utilization poses a similar difficulty. Integrating all available data, such as seismic data, wireline logs, lithological information (Chaki *et al.*, 2018; Stright *et al.*, 2009), along with regional geological concepts like tectonics and stratigraphy, as well as an understanding of sedimentation processes like erosion, transport, and deposition (Allen and Allen, 2013; Allen, 2008), is critically important to achieve reliable results and to enhance the likelihood of success in the exploration or development stages of a hydrocarbon field (Rose, 1987; Smalley *et al.*, 2008). Over the past three decades, the development of a generic sequence stratigraphic model for rift basins has garnered significant attention. In this model, particular emphasis has been placed on the role of accommodation space primarily governed by tectonic subsidence (Gawthorpe *et al.*, 1994; Martins-Neto and Catuneanu, 2010; Wescott *et al.*, 1996). The interplay between tectonic subsidence, sediment supply and global sea level variations collectively shape the sequence development within rift basins (Miller *et al.*, 2018; Mitchum *et al.*, 1977; Mitchum and Van Wagoner, 1991; Posamentier *et al.*, 1988). Among these driving factors, basin subsidence and sediment supply act as external forces. Consequently, when the accommodation space created by the subsidence is balanced by the sediment supply, the external force is neutralized, and changes in the stacking pattern are primarily driven by sea level fluctuations (Xu and Pang, 2021). The post-rift phase is characterized by accommodation space predominantly influenced by long-term thermal subsidence, which can be periodically or spatially perturbed in fault-controlled basins (Gawthorpe *et al.*, 1994; Reuter *et al.*, 2017; Royden and Keen, 1980; Yu *et al.*, 2013). The complex interplay of subsiding and uplifting areas due to tectonic forces, shapes both erosional and depositional domains, as well as pathways for sediment transport (Gawthorpe *et al.*, 1994). Consequently, the stratigraphic architecture and heterogeneity of depositional facies in rift basins, which dictate the distribution of varying reservoir properties, are intimately linked to these fundamental driving factors

Recent advancements in seismic geomorphology technology have significantly improved the ability to identify reservoir facies through seismic resolution (Alves *et al.*, 2014; Davies,

2007; Posamentier *et al.*, 2007). Nevertheless, not all regions have access to detailed 3D seismic data, necessitating the exploration of alternative, cost-effective analysis techniques. Evaluating such areas requires a comprehensive approach to gain a deeper understanding of the sedimentation processes at both regional and local levels during deposition. The techniques used to analyze and depict these interactions can generally be grouped into the following categories:

- first, the deterministic approach, which involves geologists in depicting depositional environments based on concrete data, their regional knowledge, and conceptual understanding. This analysis is often used in combination with direct seismic to outcrop comparison. While effective over the years, this method has significant drawbacks due to its high level of subjectivity, relying on individual interpretations (Bond *et al.*, 2012; Curtis, 2012; Polson and Curtis, 2010).
- second, the widely used mathematical method leverages geostatistical approaches to combine all available data and existing knowledge (Deutsch and Journel, 1995; Falade *et al.*, 2022; Tinker, 1996). This method allows for the calculation of uncertainties in all parameters involved in the depositional environment processes, providing more measurable and reliable results (Ortiz C. and Deutsch, 2002; Todini, 2001).
- lastly, there is a relatively new and less commonly utilized method known as geologic process modeling, or stratigraphic forward modeling (SFM) (Bosscher and Schlager, 1992; Granjeon, 2019, 2014; Hawie *et al.*, 2019; Tetzlaff *et al.*, 2014). SFM embraces more advanced numerical approaches, utilizing diffusion equations to depict sediment transport and accumulation processes. SFM enables the modeling of sediment erosion, transportation, and deposition across extensive regions over specific geological timeframes, while accounting for uncertainties and sensitivity to the modeled parameters (Burgess *et al.*, 2006; Granjeon, 2014; Tetzlaff *et al.*, 2014). A profound understanding of these methods assists scientists and geologists in developing a better comprehension of geological history and the potential resources within depositional environments.

Geodynamic, sedimentology and the petroleum system analyses of the North West Java Basin (NWJB) have been investigated by many researchers since the early 20th century. Many of them discussed the regional-scale tectonic and/or stratigraphic evolution (Abdurrokhim, 2014; Burbury, 1977; Clements and Hall, 2011; Hall, 2012; Pubellier and Morley, 2014), and

also the practical implications of the datasets to the exploration of hydrocarbons (Arpandi and Patmosukismo, 1975; Atkinson, 1993; Aveliansyah *et al.*, 2016; Reksalegora *et al.*, 1996). In contrast, no recent comprehensive study on depositional environment and reservoir characterization, including new dataset concerning the North West Java Basin, have been conducted yet.

The primary focus of our study is to reveal the sequences of sediment formation and distribution in the North West Java Basin. In the upcoming sections, we thoroughly address each question that arises, offering important insights to enhance our understanding of the geological history and the remaining potential in the NWJB.

### **1.3. Location of the study**

The selected study area is located approximately 50 km north of Jakarta City, covering an area of 125 km by 74 km. Geographically, the area is located in the western part of the Java Sea, with an investigated area of 9,250 square kilometers, situated at latitude coordinates between 5°51' S and 5°11' S, and longitude coordinates between 106°44.5' E and 107°52.5' E. The North West Java Basin is bordered by the Seribu Islands Platform to the west, the Sunda Basin and Asri Basin to the northwest, and to the north, it is adjacent to the Sunda Platform. To the east, it shares its boundaries with the Vera Basin, Karimun Jawa Arc, and North Central Java Basin. To the south, it is bordered by the Bogor Trough. (figure 1.1).

### **1.4. Objective of the study**

This study focused on the sequence stratigraphic evolution of the Early – late Miocene Upper Cibulakan Formation in order to elucidate and predict- the reservoir distribution and quality in a shallow – marginal marine succession documented in the area, which covers the northern part of North West Java Basin. We integrate sedimentological and biostratigraphic data throughout the entire rock sequence of the Upper Cibulakan Formation (UCF) in the North West Java Basin (NWJB), Indonesia. The objectives of the study are:

1) to reconstruct the depositional environments within the Miocene series of the Upper Cibulakan Formation by conducting a comprehensive sequence stratigraphic analysis using well log and seismic data. Furthermore, it offers a broader perspective on the regional stratigraphic evolution, taking into account major sea level events and local geodynamics,

which, in turn, enhances our understanding of the extent of sedimentary facies within the basin; and

2) to forecast the distribution and quality of reservoirs by using stratigraphic forward modeling. This effort represents a significant step in improving our understanding of the geological history and resource potential in the NWJB.

The main expected outcome of this study is a better understanding of the sedimentary facies and the distribution of the reservoir facies in the NWJB. In addition, this study is also expected to contribute to the refinement of a regional geological frameworks of the NWJB area. To be able to achieve the objective, several scientific questions need to be answered:

- how the faults are formed and how the faults pattern evolution affects the sedimentation in the North West Java Basin?
- What is the lithofacies organization of the mixed siliciclastic and carbonate succession of the Early-Middle Miocene Upper Cibulakan Formation?
- where was the sedimentation taking place? Which depositional environment pictured the Upper Cibulakan Formation, and how this depositional environment setting influences the facies distribution? This step will be crucial to achieve a paleogeographic reconstruction of the Upper Cibulakan Formation;
- How to predict the reservoir facies in the area?

## **CHAPTER 2: REGIONAL GEOLOGY**





## 2.1. Geodynamic of North West Java Basin

The North West Java Basin is located within the Indonesian archipelago, along the southern margin of Sundaland and the Eurasian Plate. Sundaland is a continental promontory in Southeast Asia (figure 2.1). The North West Java Basin (NWJB) is a back-arc basin formed over time through the accretion of blocks along the Eurasian margin (Adnan *et al.*, 1991; Clements *et al.*, 2009) (figure 2.2). Its formation dates back to the Late Cretaceous period (Adnan *et al.*, 1991; Advokaat *et al.*, 2018; Hall, 2011; Pubellier and Morley, 2014).

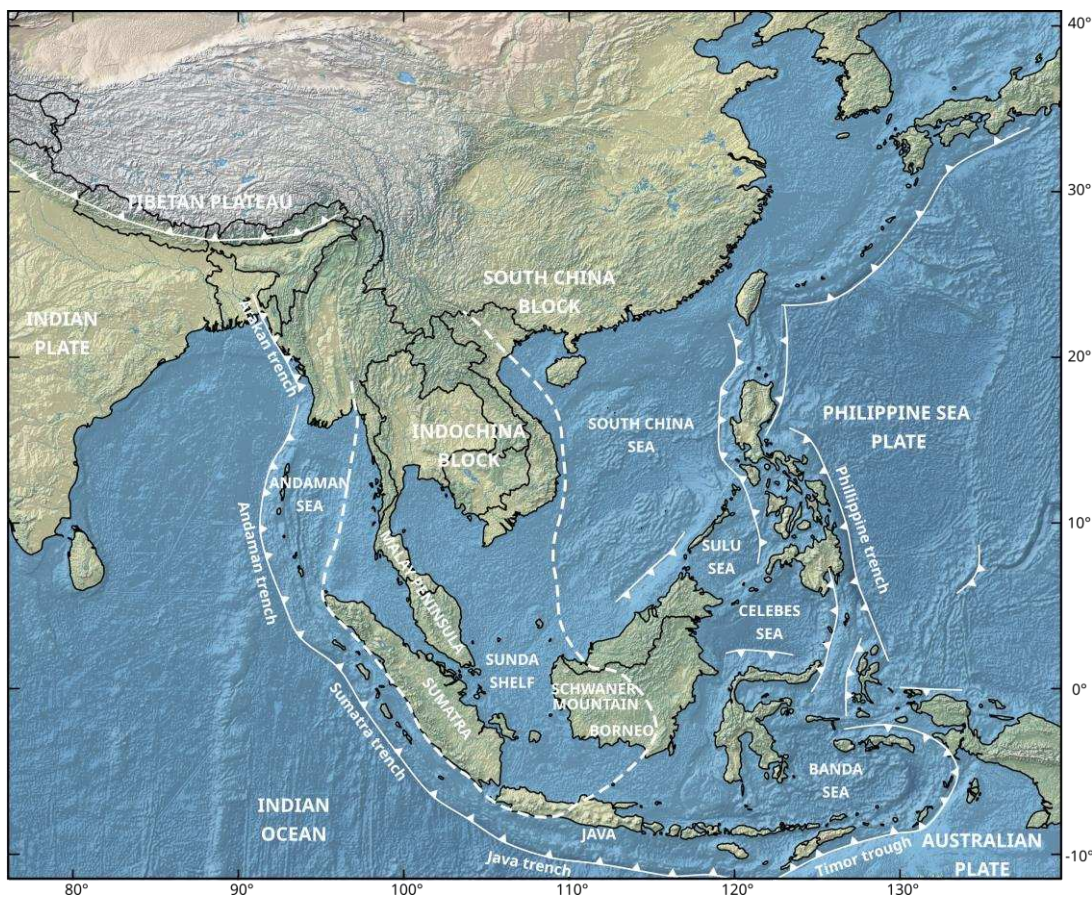


Figure 2.1 Digital Elevation Model illustrating the principal surface features of the Sundaland region (outlined by a dashed white line). The seafloor bathymetry and topography data are sourced from the General Bathymetric Chart of the Oceans Grid (2023), while the main active tectonic boundary is based on Metcalfe (2012). The boundary of Sundaland is defined according to Hall and Morley (2004).

Traditionally, Sundaland has been regarded as part of the Eurasian Plate, located in Southeast Asia, covering regions such as Sumatra Island, Western Java, southwest Borneo, the Sunda Shelf, the Malay Peninsula, and the Indochina Block. The boundary between Eurasian Plate with the Indian ocean and Australian Plate is found in the continental areas of Southeast Asia, particularly along the Sumatra – Java trench and Timor trough (figure 2.1).

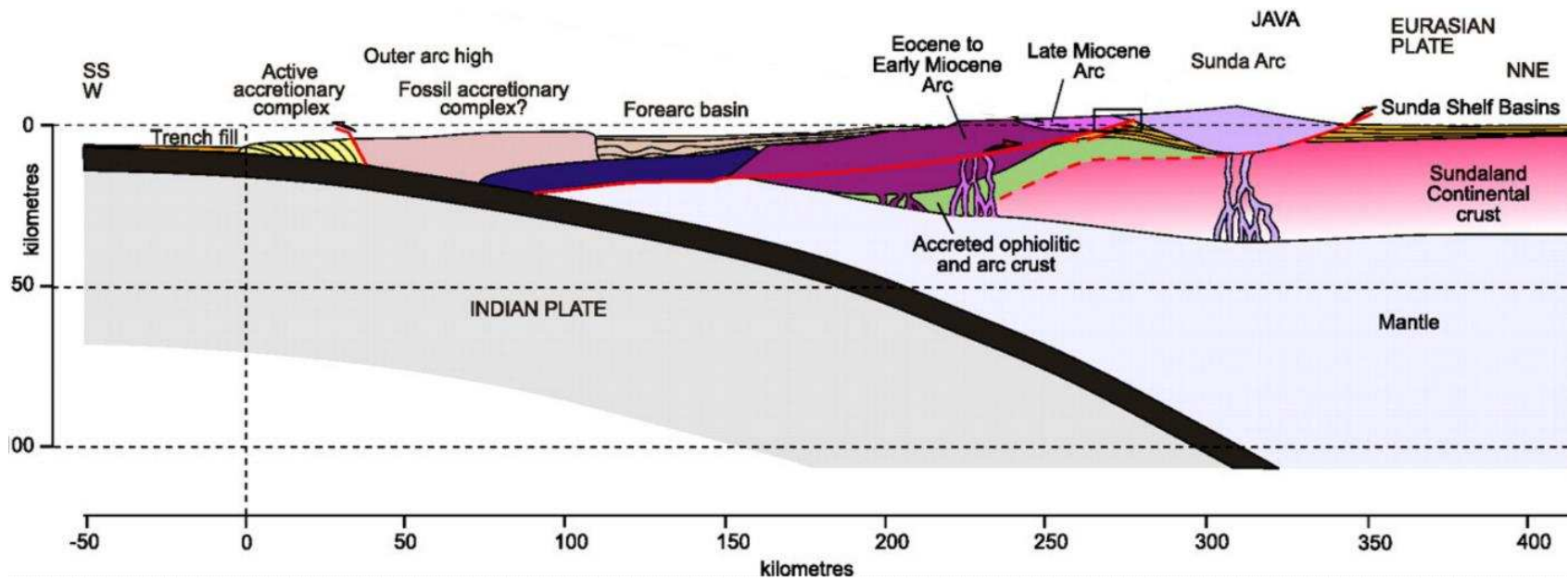


Figure 2.2 Regional cross-section through the West Java margin, (Clements et al., 2009). The North West Java Basin, cited as Sunda Shelf Basin in the figure, is a back arc basin with a relative flat dipping basin to the north of Sunda arc.

Sundaland is composed of microcontinent from Gondwana, specifically East Malaya, Sibumasu, and West Sumatra. These landmasses are separated by the Bentong-Billiton Accretionary Complex and the Medial Sumatran Tectonic Zone (Advokaat *et al.*, 2018; Barber and Crow, 2009; Metcalfe, 2013) (figure 2.3). Sundaland came into existence during the Permian and Triassic periods through the amalgamation of these fragments (Barber *et al.*, 2005; Barber and Crow, 2009; Metcalfe, 2013). Extensive magmatic activity in the Late Triassic is believed to have resulted from the collision between Sibumasu and East Malaya (Metcalf, 2013). Two other blocks, with Gondwana origins, were subsequently added to the core of Sundaland; the SW Borneo Block (Hall, 2011) followed by the East Java–West Sulawesi Block (Hall, 2012; Smyth *et al.*, 2007) (figure 2.3).

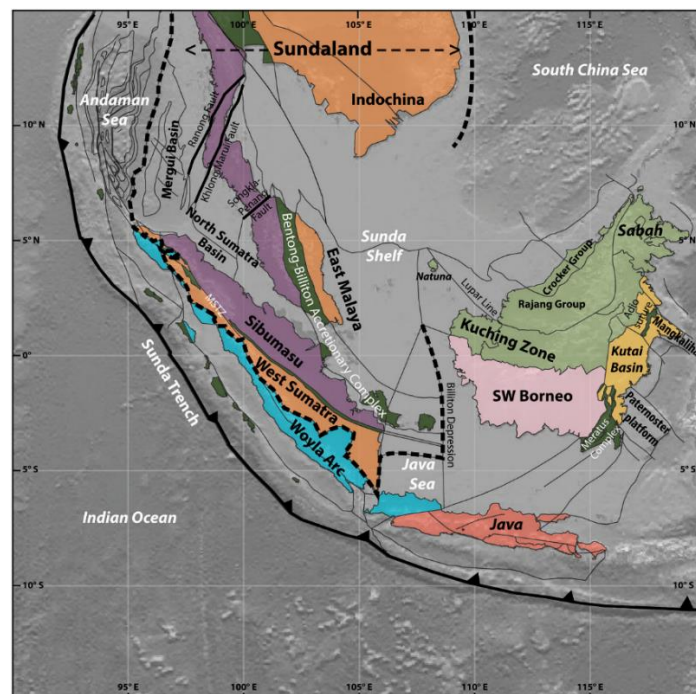


Figure 2.3 Tectonic map of South East Asia (Advokaat *et al.*, 2018) showing the microcontinent element of sundaland.

During the Late Palaeozoic period, subduction and, later, Triassic collision events in Thailand and the Malay Peninsula were accompanied by multiple occurrences of granite intrusion (Clements and Hall, 2011). These granites were linked to the subduction process preceding the collision and, subsequently, with the thickening of the continental crust after the collision (Hutchinson, 1989; Sevastjanova *et al.*, 2011). As a result, the region is home to numerous Permian and Triassic granite. The majority of these granites are part of the Southeast



Asian tin belt, which extends from Myanmar through the Thai-Malay Peninsula into the Indonesian Tin Islands (Clements and Hall, 2011).

2.1.1. Jurassic to Cretaceous

In the Jurassic and Cretaceous periods, the region underwent several phases of uplift and erosion, often accompanied by additional episodes of granite intrusion (Clements and Hall, 2011). Cretaceous granites have been identified in various locations, including the currently submerged Sunda Shelf (Hamilton, 1991), the Schwaner Mountains of SW Borneo (Williams *et al.*, 1988) as well as smaller occurrences in Sumatra (Barber and Crow, 2009), and in the Central Belt of the Malay Peninsula (Cobbing *et al.*, 1986). The basement rocks in the North West Java Basin area consist of Cretaceous granites and metamorphic rocks currently exposed in Borneo, Sumatra, and the Malay Peninsula (Hamilton, 1991; Metcalfe, 1996). By the end of the Cretaceous, much of Sundaland emerged as a continental region (Hall and Morley, 2004; Pubellier and Morley, 2014). It likely had a passive margin south of Java and a subduction margin to the south of Sumatra, facilitating the northward movement of India (Advokaat *et al.*, 2018; Hall, 2012) (figure 2.4).

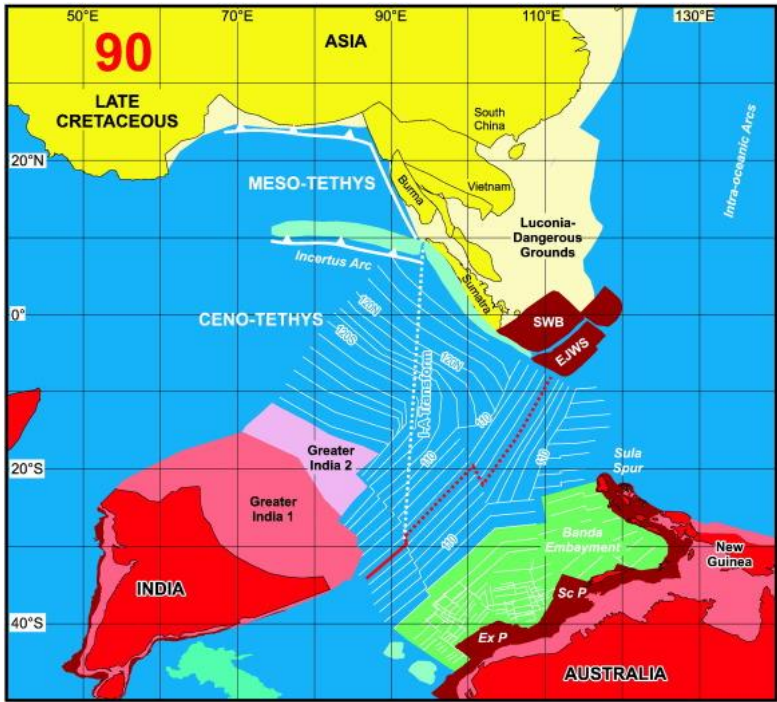


Figure 2.4 Sundaland and surrounding area plate tectonic reconstruction at 90 Ma (Hall, 2012) showing the important age where the subduction in Sumatra and Java was ceased. The boundary between SW Borneo (SWB) and E Java – W Sulawesi (EJWS) was the Meratus suture.

The most significant geological change occurred around 90 Ma (figure 2.4), when subduction beneath Sundaland ceased (Hall, 2012). This marked the point at which Sundaland transformed into an almost entirely elevated and emerged continental region, with its surrounding margins becoming inactive. As highlighted by Clements *et al.* (2011), the cessation of subduction not only triggered a dynamic shift in the landscape but also induced profound alterations in the topography and geological characteristics of the region.

### 2.1.2. Paleogene

For the majority of the period from 90 Ma to 45 Ma, there was no subduction occurring around most of Sundaland, except for the region north of Sumatra (Hall, 2012). During this time, there was an inactive margin to the south of Sumatra and Java until approximately 70 Ma, coinciding with the slowing-down of Australia northward movement. As a result, the significantly low igneous activity during this interval can be attributed to the absence of subduction (Hall, 2012). There is evidence of minor Paleocene volcanic activity in north Sumatra, to the west of the India-Australia transform boundary (Crow, 2005). This suggests that geological activity and subduction were not uniform across the entire Sundaland region during this time frame, and localized geological phenomena were present in certain areas (Hall, 2012).

Rapid northward movement of Australia began in the Eocene, establishing the present-day active subduction zone south of Java (Advokaat *et al.*, 2018; Clements *et al.*, 2009; Clements and Hall, 2007; Hall, 2012). The collision between these two plates resulted in a counterclockwise rotation in Sundaland (Advokaat *et al.*, 2018; Pubellier and Morley, 2014) (figure 2.5). This counterclockwise rotation played a key role in the significant extensional tectonics that occurred in Sumatra and Java (Advokaat *et al.*, 2018; Pubellier and Morley, 2014). Pubellier and Morley (2014) provide a correlation chart focusing on the major basins in the Sundaland region (figure 2.6). The charts highlight the periods of different rifting initiation and the subsequent postrift phases across the basin that varies from Paleocene to Late Miocene. In the regions of west Java, Sumatra, Malaysia, the Gulf of Thailand, and the Andaman Sea, the evidence indicates that the rifting activity in those areas occurred slightly later than the Early Eocene, ranging from the Middle Eocene to the Late Eocene (Pubellier and Morley, 2014).

The late Eocene to early Oligocene period marked the initiation of compressional tectonics resulting from the north-directed subduction of the Australian Plate (figure 2.5). This shift towards compressional tectonics brought an end to the extensional activity in the region, resulting in relative stability (Hall and Morley, 2004; Pubellier and Morley, 2014).

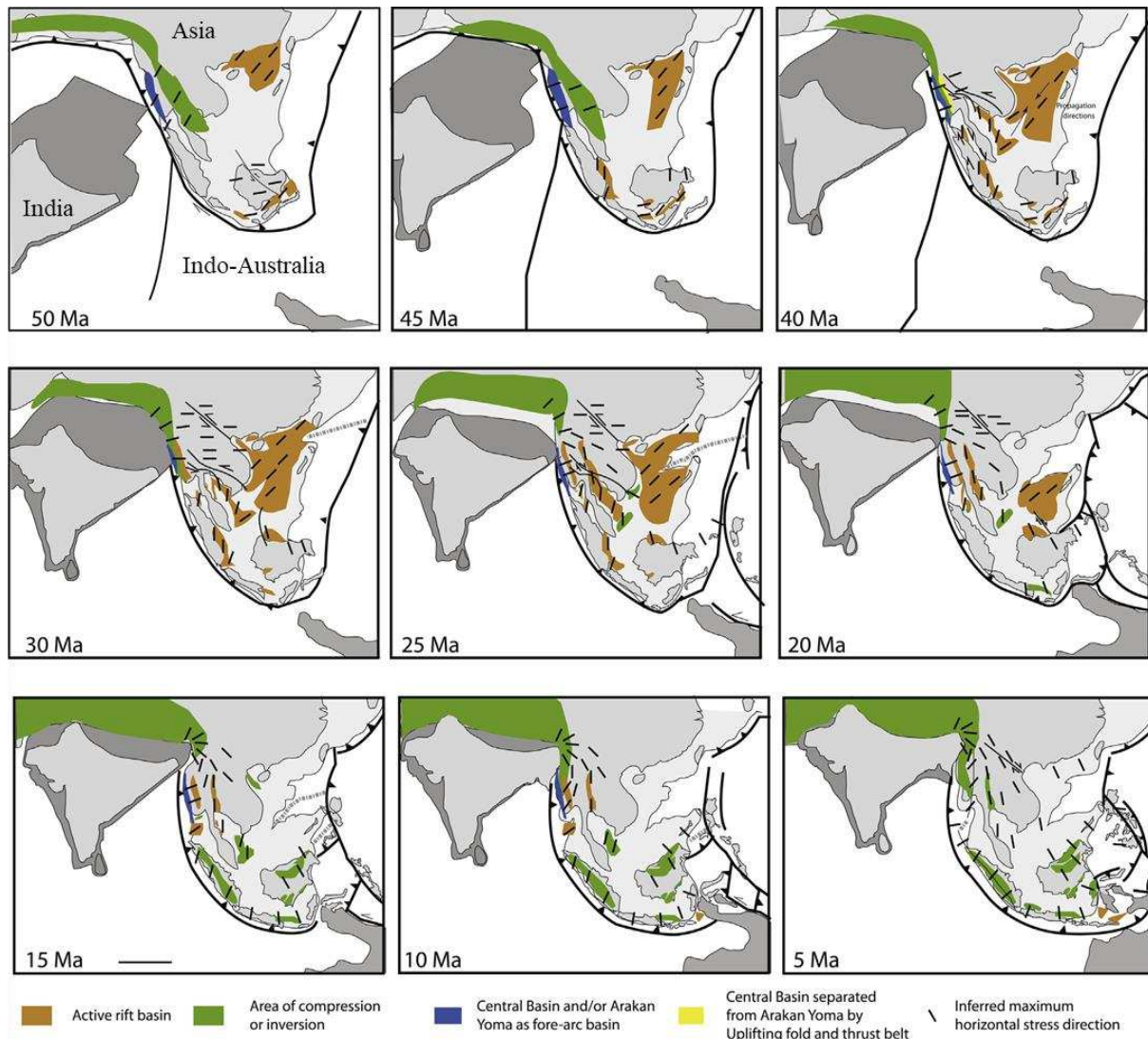


Figure 2.5 Series of plate reconstructions highlighting the timing of basin evolution with the respective locations of India, Asia, and the Indo-Australia Plate during the Tertiary (Pubellier and Morley, 2014).

### 2.1.3. Neogene

From 25 Ma to 15 Ma, convergence of the Australian plate and its interaction with Eurasia were accommodated through various processes. These included the subduction of the Indian Ocean at the Java Trench, the subduction of the Proto-South China Sea, a wide and flexible counterclockwise rotation of the Sundaland landmass (figure 2.5) (encompassing areas like

Borneo, West Sulawesi, and Java), internal deformation within Sundaland, and the compression, elevation, and weathering of land in East and Southeast Sulawesi (Hall, 2011).

Regionally, Java island continued its extended period of inversion tectonics into the Pliocene (Matthews and Bransden, 1995), as evidenced by the formation of thrust faults onshore of Java (Martodjojo, 1984). During this period, the southern part of the basin experienced uplift, known as the Southern Mountain, which led to significant tectonic inversion in the North West Java Basin (NWJB) (figure 2.6).

Currently, the West Java region marks the transition between frontal subduction to the south of Java Island and oblique subduction to the west of Sumatra Island (Malod *et al.*, 1995).

## **2.2. Stratigraphy of North West Java Basin**

The formation of the North West Java Basin is the result of continuous subsidence and a southward tilt of the Sundaland that began during the Eocene (Hamilton, 1991). Rapid northward movement of Australia in the Eocene initiated a series of north-south to northwest-southeast normal fault, influencing the development of horsts and grabens, multiple sub-basins and basement highs emerged (Patmosukismo and Yahya, 1974). While there are some disagreements about the precise timing of rifting activation, with some suggesting it occurred in the Paleocene (Patmosukismo and Yahya, 1974), early to middle Eocene (Adnan *et al.*, 1991; Gresko *et al.*, 1995), or the late Eocene (Hall, 2002; Suyono *et al.*, 2005), it is widely accepted to be related to the collision between India and Asia. This collision led to a significant influx of coarse clastic sediments in newly formed basins (Advokaat *et al.*, 2018; Pubellier and Meresse, 2013).

### **2.2.1. Basement**

Patmosukismo and Yahya (1974) provided a definition for the basement in this area, characterizing it as a composition of igneous and metamorphic rocks dating from pre-Tertiary to the Paleocene. This definition was crucial to differentiate the basement from the Jatibarang Formation (onlapping the basement), primarily composed of volcanic rocks, and to clarify that the basement unlikely hosts hydrocarbon. The oldest metamorphic basement rocks in the region dates back to around 213 $\pm$ 11 Ma (Triassic), while the youngest originates from igneous rocks at approximately 57.8 $\pm$ 3.5 Ma (Paleocene).



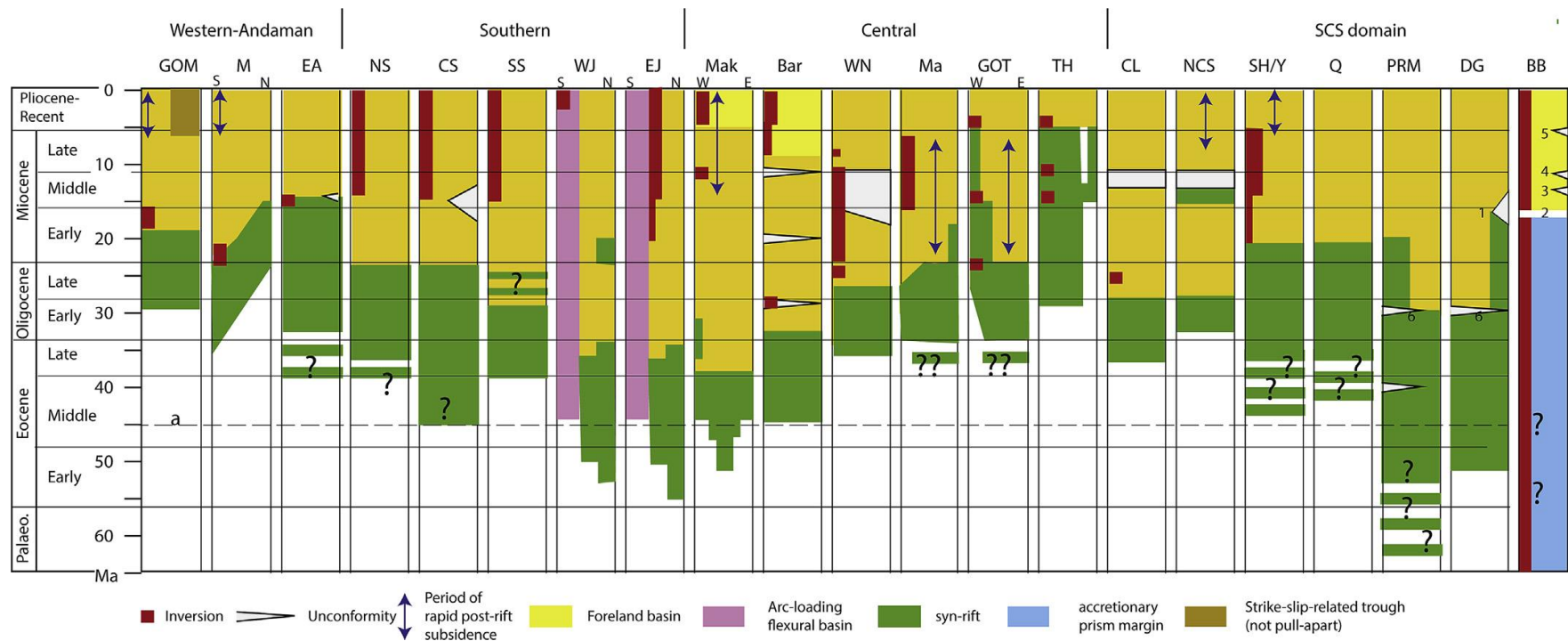


Figure 2.6 Correlation chart of the basins of Sundaland with emphasis on the rifting period (green) and the postrift (orange). GOM = Gulf of Martaban, M = Mergui Basin, EA = East Andaman Basin, NS = North Sumatra Basin, CS = Central Sumatra Basin, SS = South Sumatra Basin, WJ = Western Java, EJ = East Java, Mak = Makassar Straits, Bar = Barito Basin, WN = West Natuna Basin, M = Malay Basin, GOT = Gulf of Thailand, TH = Onshore basins of central and northern Thailand, CL = Cuu Long Basin, NCS = Nam Con Son Basin (Pubellier and Morley, 2014).

The basement, as observed from drilling ditch cuttings from 319 exploration wells which penetrated the basement across the North West Java Basin, is composed of Mesozoic igneous and low-grade metamorphic rocks (Arpandi and Patmosukismo, 1975; Aveliansyah et al., 2016). The basement structure is primarily affected by NW-SE trending faults, the majority of which are normal faults (figure 2.7).

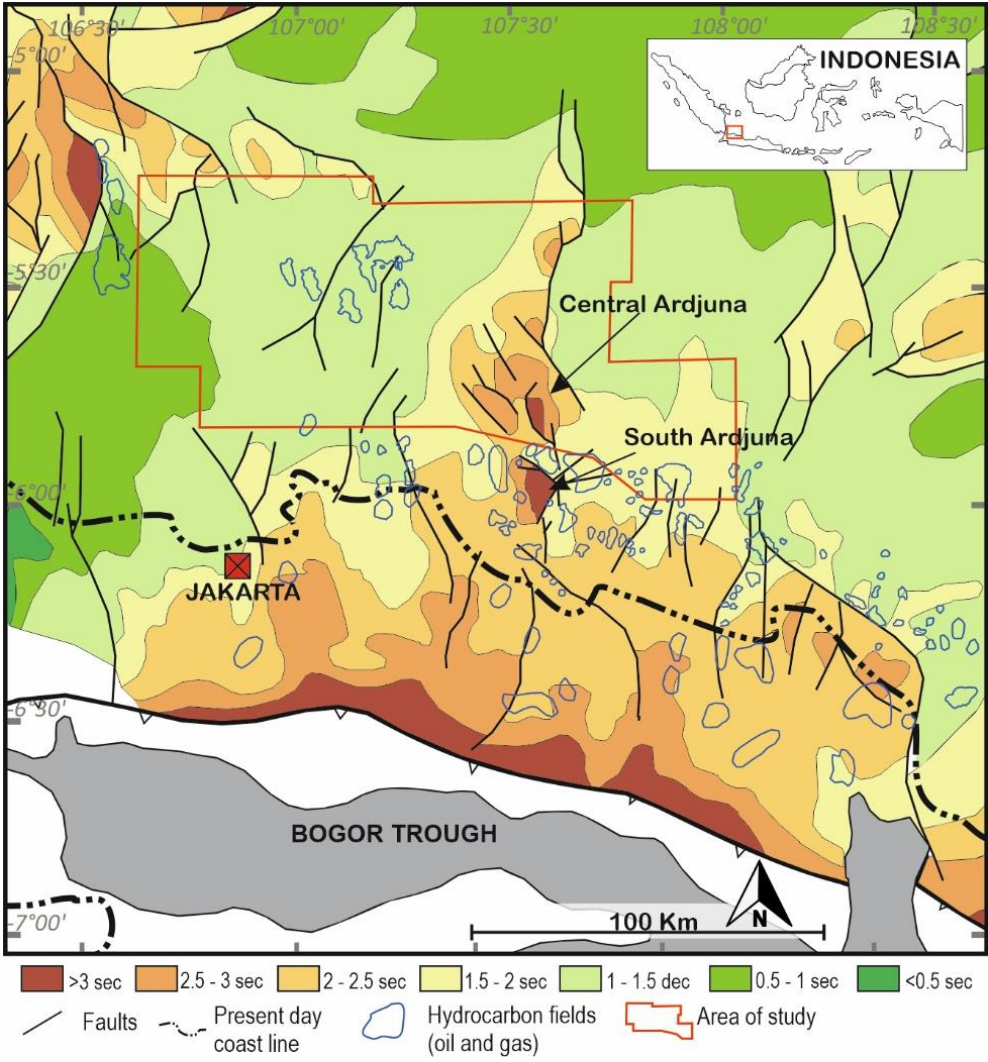


Figure 2.7 Seismic derived basement times structure map of North West Java Basin (Noble et al., 1997)

2.2.2. Pre-Talangakar Group (Pre TAF)

The oldest deposition contrast to basement in the North West Java Basin was previously identified by a drilling as the Late Eocene to Early Oligocene Jatibarang Formation (Martodjojo, 1984; Noble et al., 1991; Patmosukismo and Yahya, 1974). This formation is consisting of tuff, porphyry andesite, basalt, and red claystones (Adnan et al., 1991), indicative

of the pre- to syn-rift phase. However, recent drilling in the KL field (see fig 2.11 for the KL field location) penetrated the carbonate rocks dating from 33-37 Ma, corresponding to the Late Eocene (Aveliаныyah *et al.*, 2016). This discovery has updated the stratigraphic arrangement of the NWJB region, particularly in the interval previously defined as the Jatibarang Formation and Basement. Recent studies have defined these stratigraphic intervals as a Pre-Talangakar Formation, which includes the previously defined Jatibarang Formation; Late Eocene carbonate rocks, calcareous sandstone, and shale; Early Eocene and Late Paleocene volcanic rocks (Aveliаныyah *et al.*, 2016; Permana *et al.*, 2019; Wibowo *et al.*, 2018). Here, we refer to this stratigraphic interval as the Pre-Talangakar Group, comprising of volcanoclastic deposits of the Jatibarang Formation, sedimentary rock formations from the Late Eocene, and volcanic rocks formation from the Early Eocene and Late Paleocene. However, aside from the Jatibarang Formation, there is currently no comprehensive study providing detailed information about these deposits.

The Jatibarang Formation (Late Eocene – Early Oligocene), is typically characterized by alternating layers of lacustrine clastic sediments and volcanoclastic materials deposited within isolated half-grabens during a syn-rift setting above the underlying basement rock and beneath an angular unconformity that likely formed around 34 Ma (Gresko *et al.*, 1995) (figure 2.8, 2.9). A similar but probably non-synchronous angular unconformity is observed not only in all of the Ardjuna sub-basins but also in other nearby basins like the Vera grabens, as well as the Jatibarang, Sunda, and Palembang basins. The Jatibarang deposits are typically found overlying the basement within most half-grabens but are absent on most structural highs. It is still unclear whether these elevated areas were areas of no sedimentation or if they underwent erosion after the deposition of the Jatibarang Formation.

The top of the Jatibarang Formation shows an erosional unconformity (figure 2.9), most prominently visible along the hanging wall margin, particularly the western margin of the northern Ardjuna sub-basin. Toward the center of the basin, this unconformity is less apparent and may even be conformable. In areas adjacent to the Ardjuna basin, the Jatibarang Formation serves as both a source rock for hydrocarbons and a reservoir, (*i.e.* the onshore Jatibarang Field) where production is derived from fractured volcanic tuffs (Noble *et al.*, 1997).

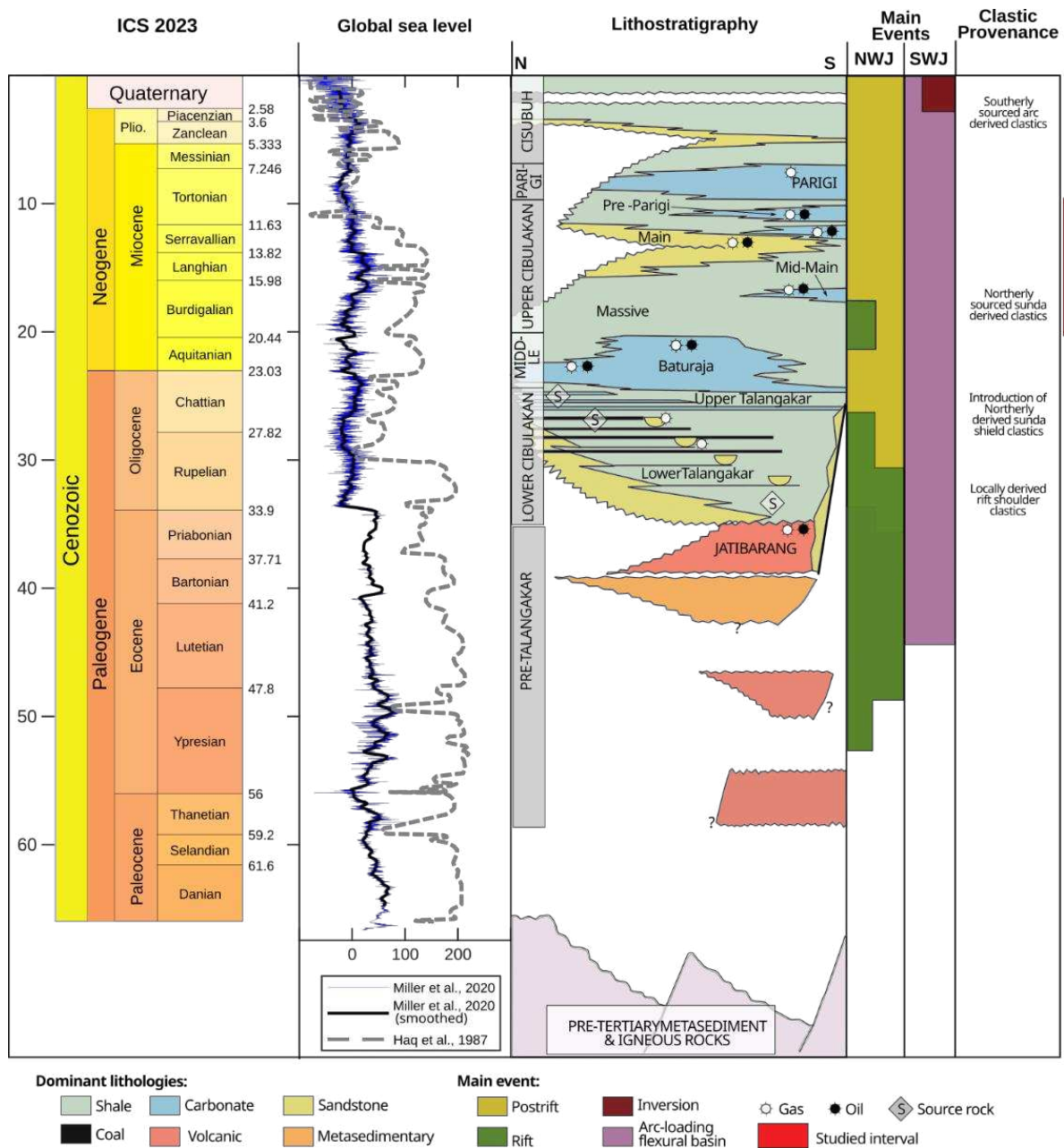


Figure 2.8 Tectonostratigraphic chart of the North West Java Basin. the lithostratigraphy scheme and clastic provenance are modified from Nobel et. al. 1997, Suyono et. al. 2005, and Aveliansyah et. al. 2016; Main tectonic events are from Adnan et al. 1991, and Pubellier and Morley 2013.

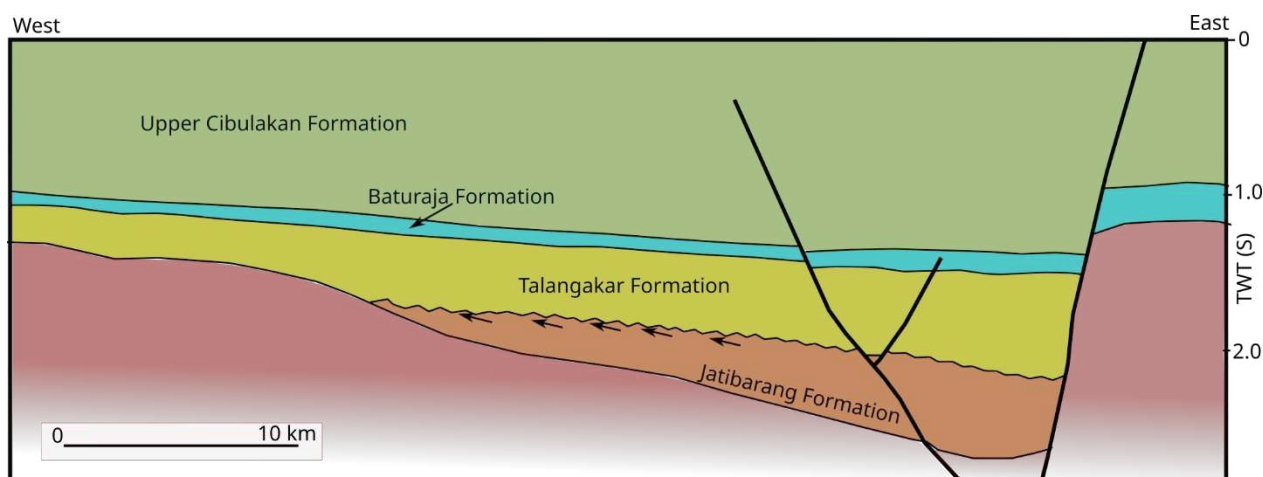


Figure 2.9 West – East cross section line in Northern Ardjuna Sub Basin based on seismic data (modified after Gresko et al., 1995) showing the asymmetric half graben and angular unconformity on top of Jatibarang Formation.

### 2.2.3. Talangakar Formation (TAF)

Above the Jatibarang Formation or the basement rock in cases where the Jatibarang is absent, the Talangakar Formation (TAF), also known as the Lower Cibulakan Formation, (figure 2.8) was deposited from Oligocene to Early Miocene. The TAF is marked by a transgressive sequence primarily composed of carbonaceous shale, accompanied by minor occurrences of sandstone, siltstone, and coal (Clements and Hall, 2007; Martodjojo, 1984; Noble et al., 1991). These sedimentary deposits are divided into lacustrine to paralic setting within the lower Talangakar, and carbonate-rich sediment within a shallow marine environment, known as upper Talangakar (Noble et al., 1991; Patmosukismo and Yahya, 1974).

The Lower Talangakar is primarily characterized by non-marine very coarse-grained, massive, pebbly conglomerates, as well as medium to coarse-grained litharenite sandstones, fine-grained lacustrine mudstones, paleosoils, and tuffs. These sediments were previously categorized as the continental member of the Talangakar (Ponto et al., 1988). The exact age of this sedimentary interval is challenging to determine precisely because it primarily represents continental deposits and contains relatively few datable taxa. However, sparse nannofossils suggest that the upper portion of the lower Talangakar were deposited during the Early Oligocene (Gresko et al., 1995). The source of the coarse-grained clastic materials within the lower Talangakar Formation is the nearby uplifted igneous and metasedimentary rocks of the basement. Generally, the reservoir quality within the clastic rocks of the lower Talangakar is poor (Gresko et al., 1995).



The most significant lithostratigraphic transition is associated with the occurrence of a coal interval, up to 15 m thick. This transition presents consistent evidence of brackish and marine influence, as well as the occasional occurrence of thin marine limestone (Young and Atkinson, 1993). This particular lithological boundary has been used to divide the Talangakar Formation into the lower Talangakar and the upper Talangakar. The sandstones in the Upper Talangakar display better sorting and finer grain sizes when compared to the sandstones in the Lower Talangakar. Additionally, the Upper Talangakar Formation contains typically black, amorphous coal deposits of varying thicknesses, with well-defined, sharp lower basal contacts (Gresko *et al.*, 1995).

Ponto *et al.* (1988) reconstructed the paleogeography of the Talangakar Formation (figure 2.10). They indicated that by the end of the Oligocene, the Sunda and Asri Basins had become emerged areas, with limited access to the sea. In contrast, the Ardjuna and Jatibarang sub-basins were situated closer to open marine environments, serving as locations for delta front and shelfal sedimentation, respectively. As the Sunda margin continued to subside, the basin expanded during the early Miocene period. The deltaic facies in the Asri Basin during this time are equivalent with the shelf sediments in the Sunda and Ardjuna areas, and with the formation of shallow marine build-up carbonates in the Jatibarang region.

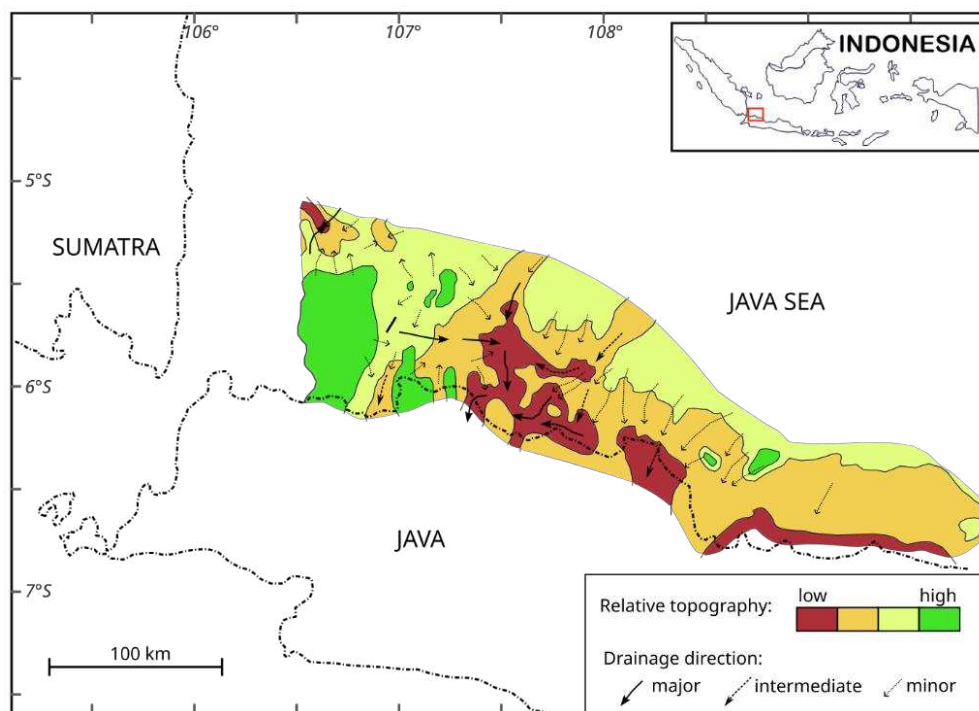


Figure 2.10 A generalized paleotopography and drainage pattern during the deposition of the Talangakar Formation (after Ponto *et al.*, 1988)

#### 2.2.4. Baturaja Formation (BRF)

The Middle Cibulakan, now known as the Baturaja Formation (BRF) (Burbury, 1977) (figure 2.8), is primarily composed of large carbonate build-ups deposited in a shallow marine environment. During the early Miocene, carbonate production dominated, with minimal clastic supply. At this time, major structural elements were well-established, and tectonic activity had become stable (the first tectonic quiescence phase in the study area) (Burbury, 1977). Major carbonate build-ups were identified near bounding faults or basement highs (figure 2.11), while reworked carbonates or shaly facies were found in structurally lower areas (Burbury, 1977).

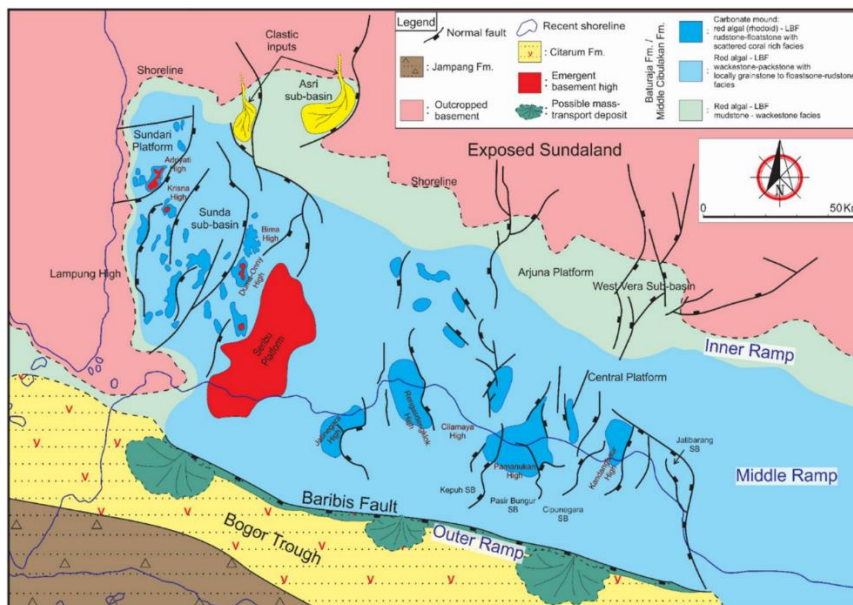


Figure 2.11 Paleogeography of the NW Java during the Early Miocene Baturaja Formation deposition (Widodo, 2018).

The Baturaja Formation represents a sequence of carbonate deposits formed during the Early Miocene marine transgression (Bishop, 2000; Koesoemadinata and Pulunggono, 1974; Sudarmono *et al.*, 1997). The pre-existing landscape consisted of relatively flat with occasional low and gently incised valleys inherited from the Talangakar Formation. These features provided a shallow marine environment conducive to the development of transgressive carbonate facies (Park *et al.*, 2010).

During the Late Oligocene and Early Miocene, the volcanic arc located at the southern tip of the present-day Java Island emerged, while the shelf edge experienced rapid subsidence. The formation of the Bogor Trough (figure 2.11), situated between this volcanic arc and the shelf margin, was a response to the loading effect caused by the conglomeratic volcanic and

volcaniclastic deposits during the Late Eocene (Clements and Hall, 2007). This loading process likely initiated the development of the West – East trended Baribis Fault (Satyana *et al.*, 2002) (figure 2.11). The Baribis Fault acts as the boundary that separates the NW Java Basin from the steeply southward dipping Bogor Trough (Bishop, 2000; Ponto *et al.*, 1988; Wu, 1991) (figure 2.11). This resulted in the creation of a gently southward dipping carbonate ramp for the sedimentary succession of the Baturaja Formation, which gradually steepens towards the distal end (figure 2.12).

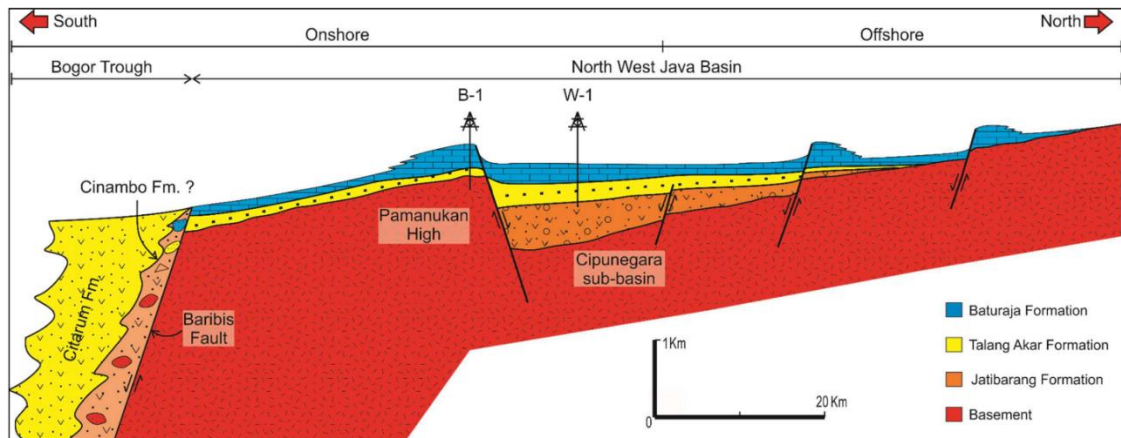


Figure 2.12 Schematic diagram of the Early Miocene Baturaja Formation ramp. The distally-steepened portion of the ramp was likely controlled by the Baribis Fault. Carbonate mounds were developed on the paleotopographic highs and uplifted fault blocks (Widodo, 2018).

Widodo (2018) performed a thorough analysis to the Baturaja Formation, and developed a depositional model that divided the Baturaja Formation morphologically into two areas, the topographically higher carbonate mound and the inter-mound areas (figure 2.11). The facies associated with carbonate mounds primarily comprise floatstone-rudstone and packstone-grainstone, characterized by the presence of red algae and larger benthic foraminifera. These mounds were likely situated within the euphotic zone, where light penetration is most abundant. Furthermore, Widodo, 2018, implies that while small and scattered corals are present, they were unable to construct a structural barrier extending to sea level. Within the inter-mound areas, the facies correspond to the varying depths of the meso-oligophotic zone and are characteristic of a relatively low-energy environment. Furthermore, Widodo, 2018, also identified a localized presence of glauconitic quartz sandstone as thin submarine sand sheets (less than 2 m) originated from the exposed Sundaland to the north. This facies likely formed through the reworking and re-transportation of clastic deposits during periods of high marine flooding.



Based on isopach analysis, [Burbury \(1977\)](#) revealed that the Baturaja limestone exhibits thin layers over the Seribu platform, with certain areas showing signs of non-deposition on the higher platform. A modest thickening of the limestone is observed to the east, extending over the gently sloping eastern flank of the Seribu Platform. The limestone buildups are relatively small in terms of both area and vertical extent, and they are exclusively developed over ancient structural features. On the western side of the Ardjuna trough and in the eastern portion of the Ardjuna sub-basin, a more substantial subsidence rate extended the growth of limestone buildups. As a result, larger buildups have been formed in these areas, all of which overlay the old basement and Talangakar. The limestone layers thin towards the central axis of the Ardjuna trough.

#### 2.2.5. Upper Cibulakan Formation (UCF)

On top of the BRF, the Upper Cibulakan Formation (UCF) represents an overall regressive sea level phase that occurred during the latest early Miocene-Middle Miocene ([figure 2.8](#)) and followed by a major transgressive sequence. It includes isolated carbonate build-ups known as the Middle Main Carbonate and Pre Parigi Carbonate, which grade laterally into deeper marine muds. Several researchers divide the Upper Cibulakan Formation into four units: Massive, Main, Mid-Main Carbonate, and Pre-Parigi Carbonate. However, this division heavily relies on lithostratigraphy, which can be quite useful for stratigraphic distinctions on a local – field scale correlation. Yet, for a broader regional context, we opt to categorize the Upper Cibulakan Formation into two stratigraphic units: Massive unit at the lower part and the Main unit at the top. Meanwhile, the Mid-Main Carbonate and Pre-Parigi Carbonate are considered parts of the Main unit.

In the Early Miocene, the South Sumatra and West Java basins experienced a significant event with the cessation of rifting, and most of the Sundaland basins entered a phase of post-rift subsidence ([Pubellier and Morley, 2014](#)). Detailed seismic surveys and onshore fieldwork conducted across Java revealed that basin inversion occurred during the Mid Miocene, leading to the formation of a fold and thrust belt near the volcanic arc. Consequently, the structural orientation of the formations north of Java shifted from NE-SW to E-W ([Matthews and Bransden, 1995](#); [Waltham \*et al.\*, 2008](#)). In Late Miocene period, there is a clear indication of overall compression occurring in the eastern and southeastern parts of Sundaland ([Pubellier and Morley, 2014](#)). Although it has been commonly believed that the North West Java Basin

(NWJB) remained relatively stable during the Miocene, often considered a post-rift period (Arpandi and Patmosukismo, 1975; Burbury, 1977; Gresko *et al.*, 1995), Hall and Morley (2004) proposed that there was a renewed period of Miocene subsidence in southern Sundaland, including the NWJB. Their hypothesis suggests that three significant events occurring at approximately 25 Ma, 15-17 Ma, and 5 Ma were primarily driven by tectonic forces.

The UCF lithology comprises sandstones, shales, and limestone deposited in a marine shelf/littoral environment (Purantoro *et al.*, 1994). The sandstones in the lower and middle sections are typically fine to medium-grained and poorly to moderately sorted. Laterally restricted carbonates and associated carbonate build-ups developed at two stratigraphic levels in structurally controlled areas. These carbonates are referred to by the informal names of Mid-Main Carbonate and Pre-Parigi Carbonate (figure 2.8). One of the earliest study describing the Upper Cibulakan Formation by using extensive well log data might be the one published by Arpandi and Patmosukismo (1975). By using simple sand to shale ratio calculated on several wells, they developed a sand to shale ratio map within UCF on North West Java Basin (figure 2.13). From this map, it can be seen that the source of clastics were predominantly coming from the northern area that was subaerially exposed (emerged) at the time of deposition.

Detailed studies using core and seismic data suggest that the upper part of UCF can be subdivided into ten depositional facies (table 2.1) (figure 2.14), reflecting deposition in deltaic to nearshore sub-environments (Atkinson, 1993) (figure 2.15). Sandstones in this formation are believed to have originated from a reworked shelf that was part of a fluvial deltaic shoreline during a relative sea-level lowstand (Purantoro *et al.*, 1994). Posamentier (2002), using 3D seismic data in E and FXE fields (see figure 2.15 for location of FXE fields), identifies widespread ancient shelf sand bodies of the late Miocene Main member of the UCF. By using seismic horizon slices, he observed linear features with consistent and parallel distribution (N20 – 30° oriented) and commonly ranging in dimensions from 0.3 – 2 km wide, 312+ km long, and 2-17 m thick (figure 2.16). The orientation of these linear features are perpendicular or oblique to the regional paleo shoreline (Atkinson, 1993). Each of this individual linear feature commonly has a thicker sharp edge (leading edge) in the one side (usually at the West sides). Based on 3D seismic and core description, Posamentier (2002) concluded that those shelf ridges formed predominantly due to tidal process associated with the transgression of a broad river valley, analog with the Yangtze river where each successive landward step of embayment

mouth, results in a new cluster of ridge formed: the oldest located at the outer shelf and the youngest located on the inner shelf.

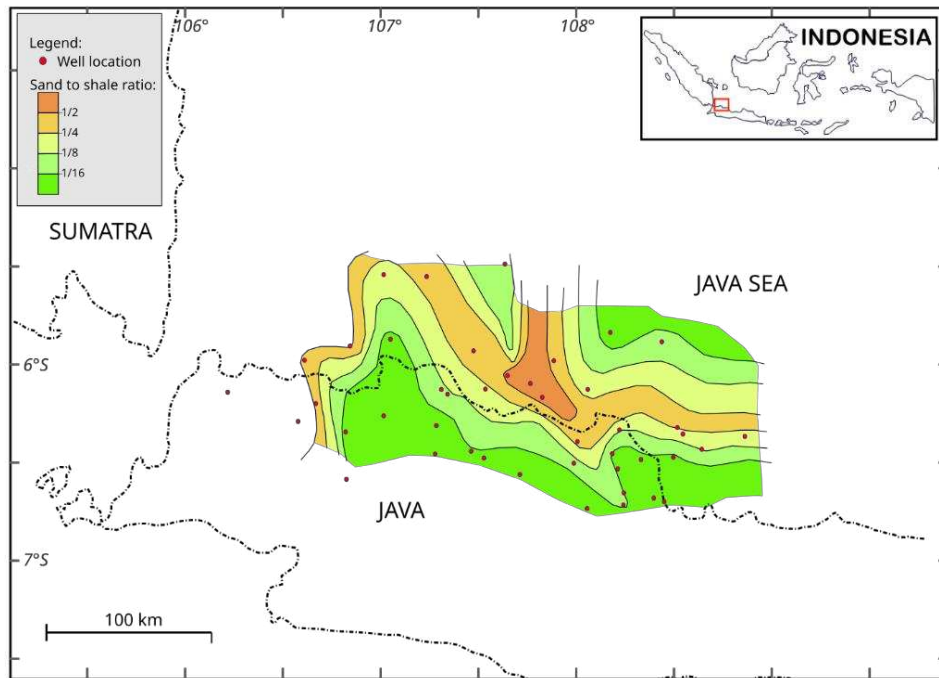


Figure 2.13 Lithofacies map of Upper Cibulakan Formation (Arpandi and Patmosukismo, 1975).

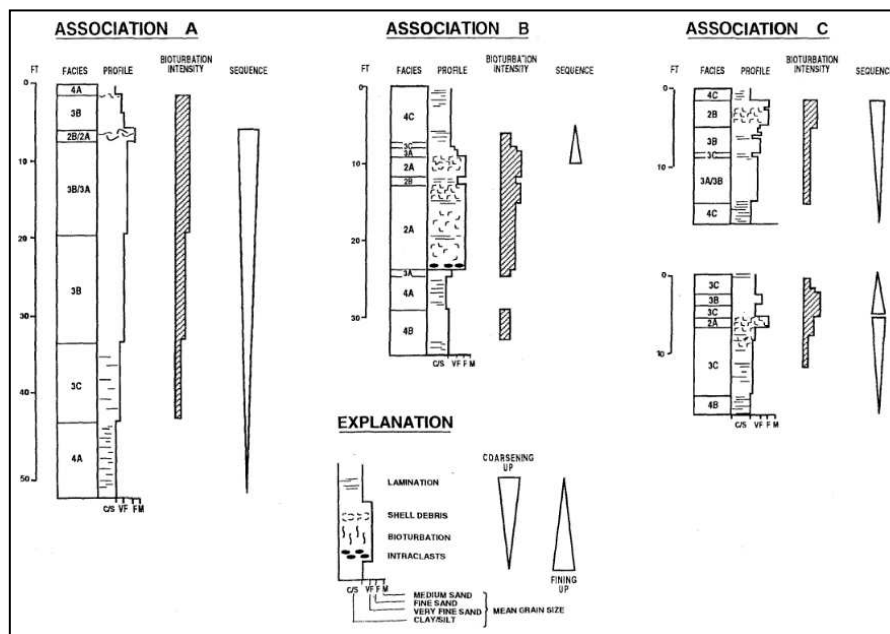


Figure 2.14 Facies association of Upper Cibulakan Formation depositional facies based on four conventional core in B field (see location in fig. 2.15), North West Java Basin (Atkinson, 1993)

Table 2.1 summaries of Upper Cibulakan Formation depositional facies based on four conventional core in B field, North West Java Basin (Atkinson, 1993)

No	Facies	characteristics	description
1	Limestone		comprise fragments of bivalves, coral, echinoderms and foraminifera tests set within a fine grained sandy, dolomitic matrix. Dissolution moldic macropores, mainly remnants of former bivalve shells, are commonly observed.
2a	calcareneous sandstone	>95% sand	moderate to poorly sorted mixture of very fine to medium grained sands, fine to coarse silts, clay and calcareous shell fragments. Bioturbation highlighted by the silt/clay distribution is ubiquitous and no physical sedimentary structures are evident.
2b	bioturbated silty sandstone	95 - 75% sand	higher silt/clay content (up to 25%) and a lower percentage of shell debris. Bioturbation is intense although some isolated silt/clay laminae are evident. Patchy calcite cement is present, with lower percentage of shell material.
3a	bioturbated silty sandstone	75 - 50% sand	grey-brown color, bioturbated, poorly sorted mixture of very fine to fine-grained sand. silt/clay contents can be up to 50%. Sand material tends to occur as isolated to tortuously interconnected burrow fill, and small distorted lenses set within the silt/clay matrix. Some lamination is visible with higher silt-clay content. burrow types include Planolites, Teichichnus, Terebelina, Chondrites and Rhizocorallium. isolated laminae of carbonaceous debris are common but no shell fragments are evident.
3b	bioturbated sandy siltstone	10 - 50% sand	poorly sorted and strongly bioturbated, silt/clay contents > 50%, up to 90%. Identified burrow types include Planolites and Terebelina. isolated to tortuously interconnected burrow fill within the silt-clay matrix. higher carbonaceous content. No shell debris is evident.
3c	bioturbated sandy siltstone	<10% sand	poorly sorted silt/clay dominated facies. the sand is predominantly very fine-grained and occurs as isolated, thin, lenticular encased completely within the silt/clay matrix. Carbonaceous material is present in larger amounts as laminatio. The bioturbation is less common. Siderite nodules are seen occasionally.
4a	grey shale	<5 carbonaceous material, calcareous forams,	pale grey in color and characterized by the presence of calcareous foraminifera tests and by less than 5% carbonaceous debris. No obvious bioturbation is seen. The clays possess obvious swelling properties with the result that this facies has a distinctive "weathered" appearance in core.
4b	dark grey shale	>5% carbonaceous material, no forams or siderite	much darker colored, contains abundant carbonaceous material, lacks calcareous foraminifera and contains a significant amount of coarser-grained silt. thin lignitic or coaly laminae are present. Small burrow traces, possibly Terebelina and Teichichnus, are sometimes observed especially near to the transition into siltstones. Occasional siderite nodules are sometimes present.
4c	shale laminated with siderite	> 5% carbonaceous material	slightly lower percentage of carbonaceous material and by the presence of siderite banding.

No	Facies	characteristics	description
5	sideritized shell hash		< 0.3 m (1 ft) isolated horizons at various levels. It comprises concentrations of shelly debris set within a siderite cemented, moderate to poorly sorted, bioturbated, silty-sandy matrix. occasional moldic macropores. The base of each horizon varies from sharp to irregular and in most cases is clearly erosional into the underlying sediments, usually overlain by facies 4a calcareous shales.

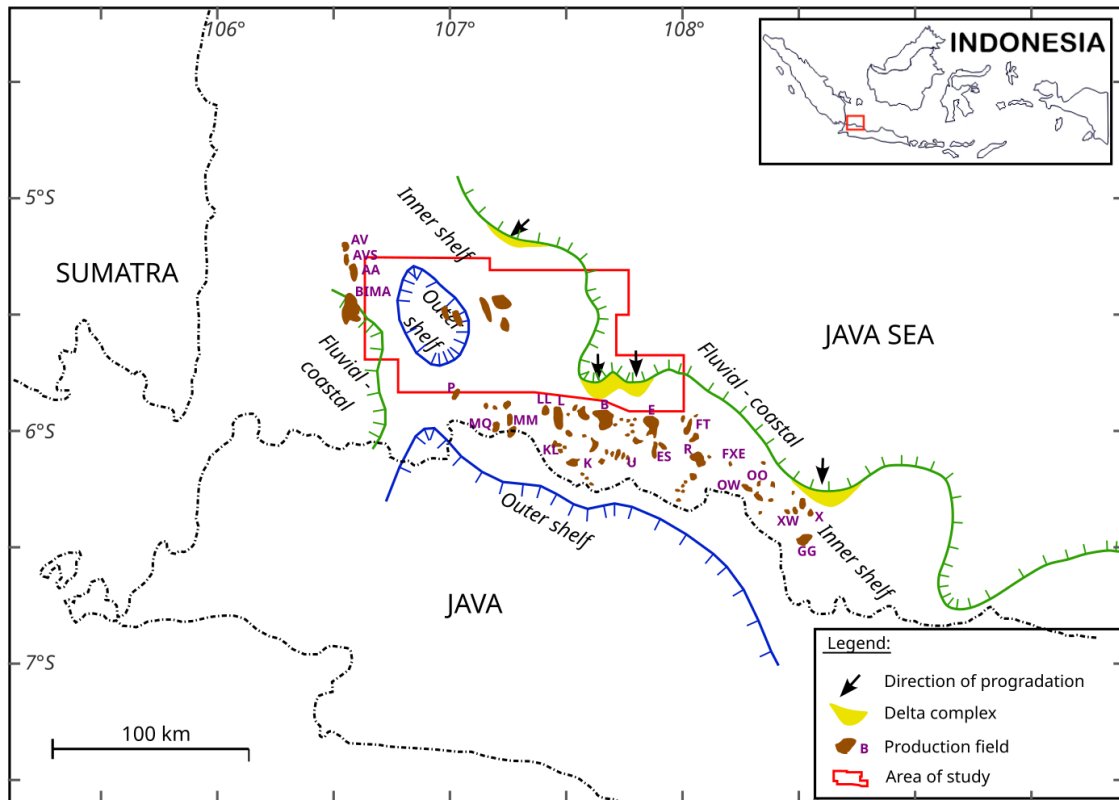


Figure 2.15 Paleodepositional reconstruction of Upper Cibulakan Formation, North West Java Basin (Purantoro et al., 1994).

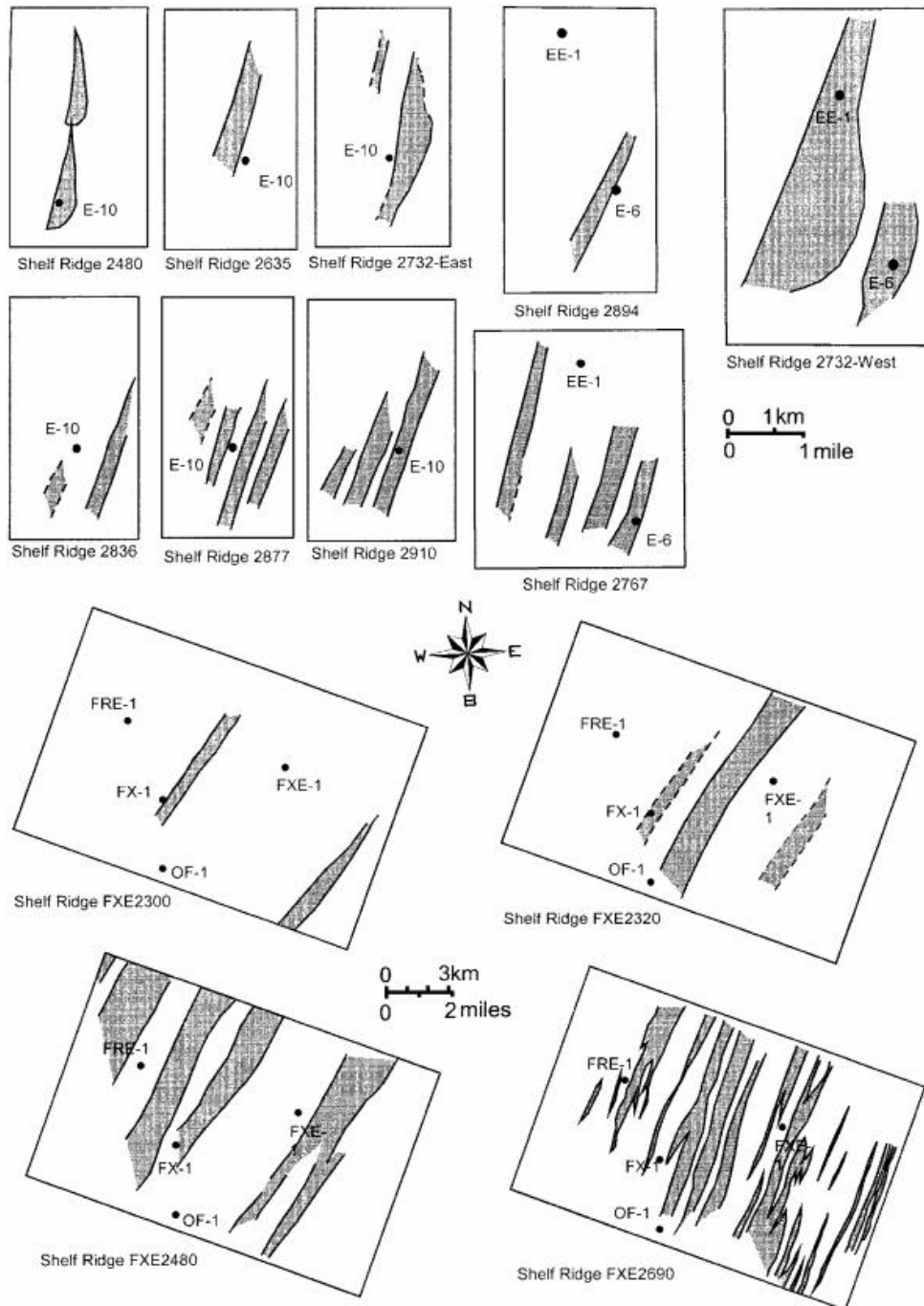


Figure 2.16 Map view of all the shelf ridges observed at FxE and E field areas (Posamentier, 2002).

Clements and Hall (2007), based on field work in the West Java, concluded that in SW and Central Java, the Middle Miocene limestone (equivalent to UCF) lies unconformably above the Oligocene Miocene volcanic rocks formation, suggesting that the volcanic activity had diminished. To the north of Java island, the lithology consists of limestones, terrigenous and shallow marine conglomerates, sandstones and marls assigned to the Cimandiri Formation



(Sukamto, 1975). Shallow marine and terrestrial deposits of the Cimandiri Formation represent the final stages of basin fill within a flexural basin behind the arc in the west (Molasse). Further to the east subsidence continued as calciturbidites of the Cinambo Formation were deposited. To the north, deposition of the Upper Cibulakan Formation initiated and included the Massive and Main clastic units as well as Mid Main and Pre Parigi carbonates (figure 2.17). A decline in volcanic activity during the Middle Miocene is evident in Java and extends further eastward. This decrease has been explained as a consequence of the advancing subduction hinge linked to the counterclockwise rotation of Borneo and Java, which started after the initiation of Australian collision in East Indonesia (Hall, 2002).

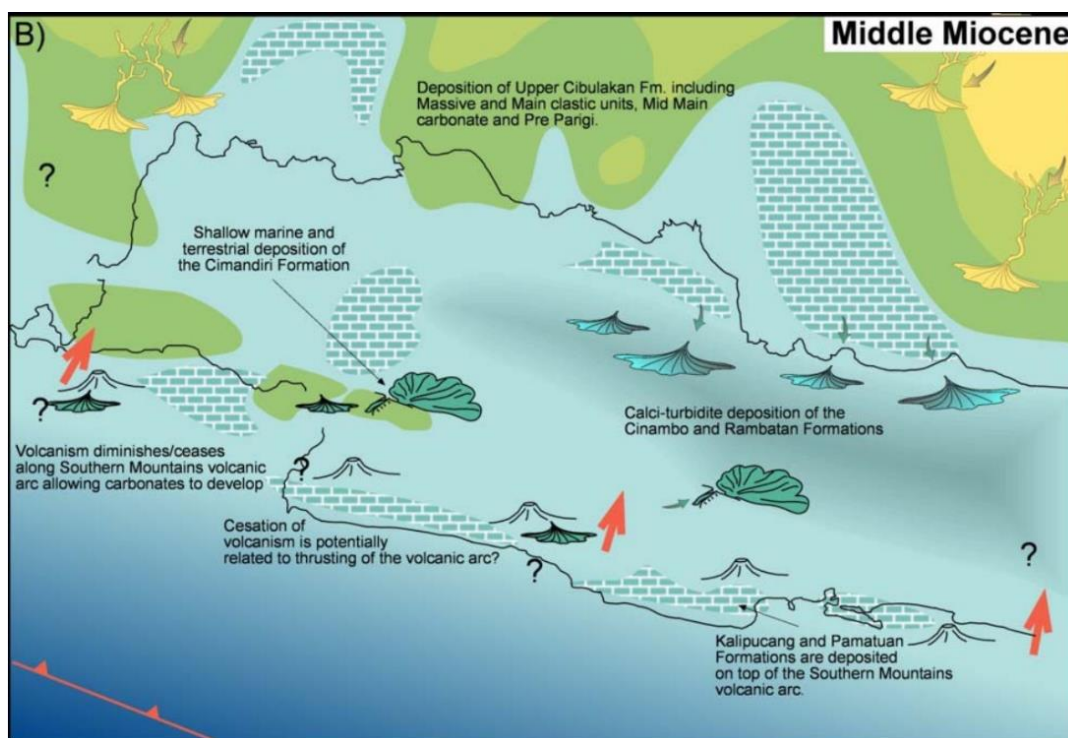


Figure 2.17 Paleogeography reconstruction of West Java area during Middle Miocene (Clements and Hall, 2007).

During the clastic deposition phase that succeeded the Baturaja limestone in the upper Cibulakan period, certain carbonate buildups formed in specific structural areas at two distinct stratigraphic levels (Burbury, 1977). These carbonate formations are not widespread but exist as isolated buildups that transition laterally into deeper marine silts and muds containing occasional limestone lenses. The "Mid-Main Carbonates" are confined exclusively to the southeastern shelf and the shelf edge of the Seribu platform and in the Rengasdengklok high (see figure 2.11 for location), whereas the Pre Parigi limestone are found within the same region

and additionally extend over some paleo-highs on the western flank of the Ardjuna sub-basin (Burbury, 1977).

Thorough petrographic analysis by Ratkolo (1994), revealed that the Mid Main Carbonate is primarily characterized by the reef build-ups that demonstrate a relatively rapid intercalation of various, often mixed, coral, foraminiferal and algal facies. These limestone facies consist of bioclastic wackestone-packstone or floatstone, and bioclastic packstone-grainstone or rudstone textures. Typically, the allochems (grains and clasts) are coarse in size and show moderate to poor sorting. They mainly consist of fragments of coral, benthic foraminifera, red algae, bivalves, echinoderms, and bryozoans, with minor amounts of quartz and occasional authigenic clay minerals. The matrix is composed of carbonate mud and micrite, and both ferroan and non-ferroan calcite cements are commonly present within the limestone.

Based on lithological and palaeontological characteristics, Ratkolo (1994) interpreted that the Mid Main Carbonate represents a shelf margin reef that deposited in an inner shelf marine environment with a low energy tidal zones (water depths of less than 30 m). This includes restricted marine, back-reef and reef subenvironments. The environments that are characterized by prolific growth of scleractinian corals, larger foraminifers and red algae, are well known as coralgal reefs. Isworo *et al.*, (1999) further interpreted the Mid Main Carbonate as a retrograding carbonate buildup developed near the shoreline on a well-oxygenated shelf. This carbonate buildup is composed of multiple hydrocarbon compartments, separated by layers of shale. The presence of these various compartments results from different stages in the development of the buildup, corresponding to changes in relative sea level positions over time (figure 2.18).

#### 2.2.6. Parigi and Cisubuh Formations

The Late Miocene Parigi Formation marks the second transgressive phase of the Neogene cycle of sedimentation (figure 2.3). It consists mainly of light grey limestone. The thickness of this formation increases southward regionally, showing no direct correlation with older structural trends, indicating that the carbonates were deposited during the second tectonic quiescence phase (Burbury, 1977).

The Late Miocene to Pleistocene Cisubuh Formation was deposited during a regressive phase in the Neogene (figure 2.3). It is characterized by carbonaceous shales and thin sandstones. Common features include glauconite and thin coal seams (Suyono *et al.*, 2005).



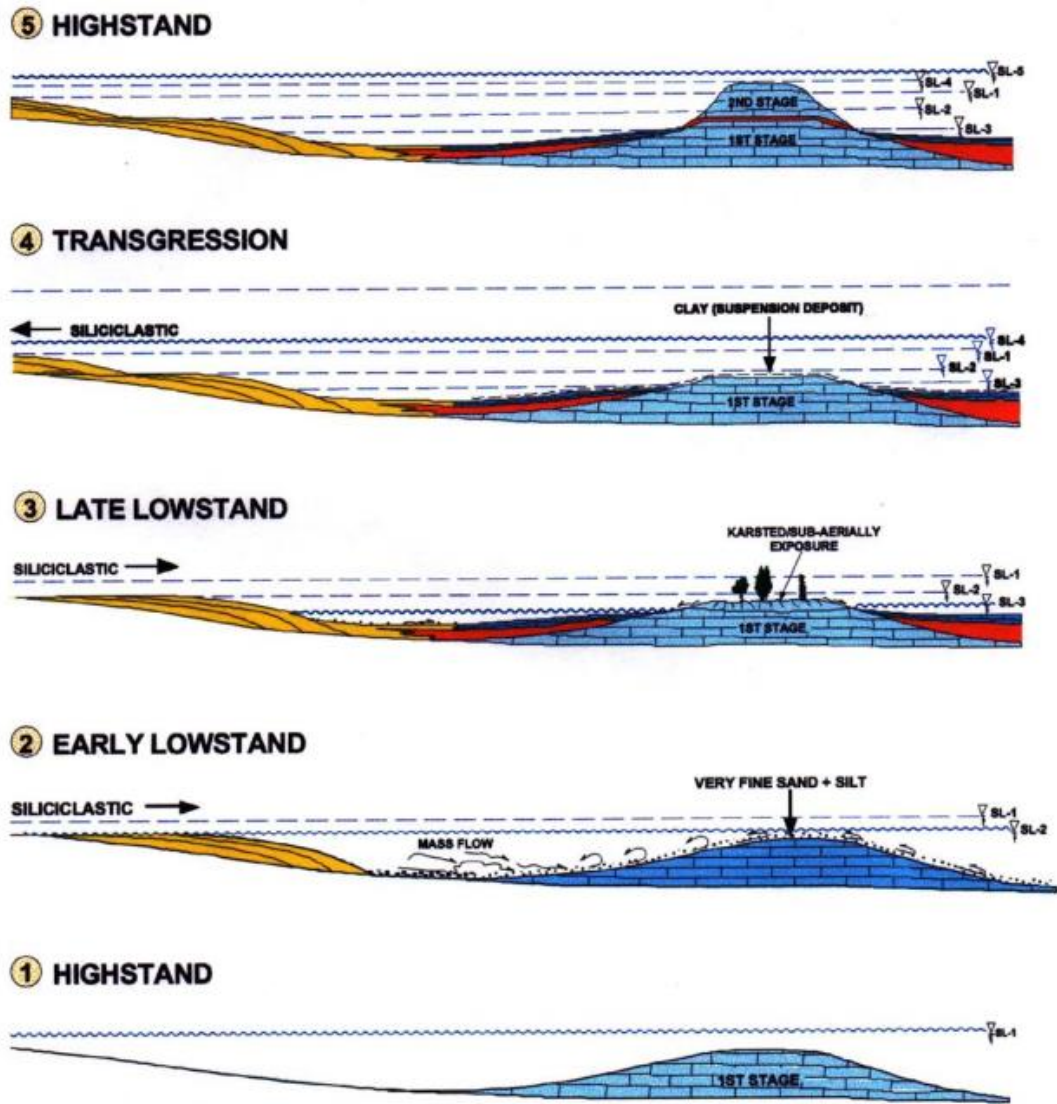


Figure 2.18 Mid Main Carbonate depositional model (Isworo et al., 1999).

## 2.3. Petroleum system

### 2.3.1. Source Rocks

The primary source rocks in the NWJB consist of deltaic carbonaceous shales and coals that belong to the late Oligocene upper Talangakar Formation (figure 2.3). They were formed during late synrift to post-rift tectonics (Gresko et al., 1995; Noble et al., 1997; Ponto et al., 1988), and they are classified as type II and III, capable of generating both oil and gas. They exhibit a total organic carbon (TOC) content ranging from 40% to 70% in the coals and 0.5%

to 9% in the shales, with a hydrogen index (HI) within the range of 200 to 400 (Ponto *et al.*, 1988). Less prominent source rocks are indicated by lacustrine strata located in the lower Talangakar Formation (Noble *et al.*, 1997), and potentially within the Jatibarang Formation in the Jatibarang sub-basin. Thirdly, some source rocks are found within the Parigi and Cisubuh Formations, and are believed to have been deposited in a marine environment, displaying unique features linked to methanogenic bacterial processes. These processes are responsible for the breakdown of organic material within a marine setting (Noble *et al.*, 1997).

### 2.3.2. Maturation

The timeline for hydrocarbon generation in the North West Java Basin spans a wide range, from as early as 25 Ma for the lower units of the Talangakar to as recently as 1 Ma for the later units. Several sub-basins formed as half grabens with thick section of TAF are recognized to contain mature source rocks (Noble *et al.*, 1997). Oil in fields to the west and northern part of NWJB are attributed to TAF source rock (Noble *et al.*, 1997). The Kepuh and Pasir Bungur areas (see fig. 2.11 for location), rich in mature source rocks, contain substantial coal deposits within the Talangakar Formation (Noble *et al.*, 1997). Hydrocarbons originating from these mature areas are believed to charge clastic reservoirs within the Talangakar Formation and carbonate reservoirs of the Mid-Main carbonate, both in onshore and offshore fields to the north (Noble *et al.*, 1997). The migration of oil from the Cipunegara area (see figure 2.11 for location), is predominantly directed to the north, influencing both onshore and offshore fields.

Offshore, areas with mature source rocks include the South and Central Ardjuna sub-basins (see figure 2.7 for location), where over 30 meters of coal source rocks are found. They contribute to the Main and Massive clastic reservoirs, along with some Talangakar clastic reservoirs in nearby fields. Hydrocarbons generated in the Central Ardjuna sub-basin are believed to migrate towards fields in the south, while northward migration is not been proven yet (Noble *et al.*, 1997).

### 2.3.3. Migration

Clastic channels found in the Talangakar Formation, running from north to south, are considered essential pathways for the migration of hydrocarbons in the region (Noble *et al.*, 1997). They enable the movement of these resources up-dip to the north, contributing to the filling of various stacked reservoirs (Bishop, 2000). This region relies on a combination of both vertical and lateral migration mechanisms to support this process.

The gas present in the shallow carbonate fields of the Pre-Parigi and Parigi Formations is likely sourced from the Talangakar source rocks (Bishop, 2000). This connection is especially evident when these carbonate buildups are situated along fault lines, which controlled the subsidence of certain mature sub-basins. Conversely, carbonate buildups without a fault system tend to have little to no gas. Buildups located away from these sub-basins and fault systems may contain gas of biogenic origin (Bishop, 2000).

#### 2.3.4. Reservoir

In the North West Java Basin (NWJB), all the stratigraphic sequences boast excellent reservoir characteristics (Arpandi and Patmosukismo, 1975; Atkinson, 1993; Posamentier, 2002; Reksalegora *et al.*, 1996), leading to the presence of numerous fields with substantial reserves. The largest reserves are primarily associated with sandstones in both the Upper Cibulakan and the Talangakar Formation (Posamentier, 2002; Suyono *et al.*, 2005) (figure 2.3). Furthermore, oil production has been successfully achieved from fractured volcanoclastic rocks within the Jatibarang Formation (Adnan *et al.*, 1991) and produce 7,924 bopd of oil and 41.9 mmscfd of gas in 2020 in the Jatibarang Field NWJB (SKKMIGAS, 2021). In areas where the Baturaja limestone exhibits good porosity, there's potential for significant accumulations (Burbury, 1977; Carter and Hutabarat, 1994; Satyana, 2005).

#### 2.3.5. Trap type

Trap types within all the petroleum systems of the North West Java Basin exhibit a similarity which is predominantly comprises broad dome anticlines and tilted fault block traps (Bishop, 2000; Noble *et al.*, 1997). This uniformity arises from the tectonic history of all sedimentary basins along the southern boundary of Sundaland, shared geological structural features, and nearly identical trapping mechanisms (Bishop, 2000). In areas where there are reef build-up reservoirs, stratigraphic traps also come into play. These stratigraphic traps are typically a result of the restricted distribution of limestone and variations in facies (Satyana, 2005).

#### 2.3.6. Seals

Seals exhibit a close correlation with basin stage and manifest as either intra-formational or more broadly developed. In the context of interbedded deltaic seals, intra-formational shale seals are commonly observed in deltaic sequences, where they serve as top seals for sands

arranged in layers or, in conjunction with faults, act as side seals for fault closures, often involving clay smearing (Noble *et al.*, 1997). The late synrift seals were analyzed by Kaldi and Atkinson (1997) in the Talang Akar Formation of Northwest Java, focusing on seal capacity, geometry, and integrity of shale interbeds. The primary lithofacies responsible for sealing, ordered by increasing seal capacity, include delta plain, channel, prodelta, and delta front shales. These findings are likely applicable to late postrift deltaic sequences as well.

In terms of thicker seal formations and regional seals, the marine shales from the early postrift emerge as the sole authentic regional seals in the NMJB. They may serve as ultimate seals for the late synrift deltaic sediments or envelop the carbonate build-ups from the early postrift (Bishop, 2000; Noble *et al.*, 1997).



**CHAPTER 3: DATASET AND METHODOLOGY**



### 3.1. Dataset

The dataset comprises complete wireline log data in LAS format of 28 wells (Table 3.1) and 650 2D seismic lines (figure 3.1). Among these wells, 11 have undergone coring, with two featuring conventional cores and the remaining utilizing side-wall cores. Two wells (GSX-1 and SSY-1) only contain data from the Pre Parigi and Parigi Formations. Biostratigraphic analysis was carried out on five wells between 1989 and 1994 (GGG-1, SZN-1, SD-1, SZ-1, and BEN-1). The well information comprises check shots, wireline logs (e.g., gamma-ray, resistivity, sonic, neutron, and density), lithologic data from ditch cutting description, core reports, biostratigraphy reports, and interpreted dip-meter log. These data were integrated with the seismic data to enhance and validate the seismic interpretations. Well-log data are used to interpret the sequence stratigraphic framework and depositional systems based on gamma-ray (gr) curves. Unpublished biostratigraphic data (Noon *et al.*, 1993; Romein *et al.*, 1987) are employed to calibrate the biostratigraphic ages of strata and sequence boundaries.

The 650 2D seismic lines have a total length of 18,489 km (figure 3.1). 15 lines were acquired in between 1971 to 1973 by Western Geophysical Company with poor data quality, 30 lines from 1979 to 1981 by Western Geophysical Company with moderate quality, and 196 lines acquired between 1982 to 1992 by Western Geophysical Company and Delta Exploration Company, characterized by moderate to good quality. Additional 97 lines were acquired in 2013 and 12 lines in 2016 by PT. Elnusa Tbk, these have good quality (figure 3.2) (Table 3.2). Most of the seismic have a time domain depth reaching up to 4000 ms two-way travel-time (twt). The seismic lines were previously reprocessed and compiled into a unified dataset for this study. The resolution of the seismic is estimated to range between 20 and 33 m calculated from a seismic dataset with a dominant frequency of 15-25 Hz and an average velocity of 1980 m/s. This resolution provides detailed subsurface geological information. To convert the interpreted results into the depth domain, the interval transit time velocity obtained from 26 check shot measurements was utilized.

These datasets have undergone quality checks, including processing, importation, and filtering, to prepare them for analysis within the interpretation software.



Table 3.1 Well data used in this study

No.	Wells	FWR	mud log	Wireline log	SWC	Conv. C	RCAL report	Remarks
1	NI-4	v	v	v	v		v	
2	AAA-1	v	v	v		v	v	
3	Z-1	v	v	v				
4	O-1	v	v	v				
5	PZ-1	v	v	v				
6	MGN-1	v	v	v				
7	MG-1	v	v	v		v	v	
8	CF-1	v	v	v				
9	PM-1	v	v	v	v			
10	MEE-1	v	v	v				
11	APN-6	v	v	v	v	v		
12	GSX-1	v	v	v				No GR in UCF
13	GS-1	v	v	v			v	
14	GGG-1	v	v	v		v	v	
15	W-1	v	v	v				
16	SZN-1	v	v	v			v	
17	SSZ-1	v	v	v				
18	SK-1	v	v	v				
19	SSY-1	v	v	v				No GR in UCF
20	SH-1	v	v	v				
21	SD-1	v	v	v	v	v	v	
22	SZ-1	v	v	v		v	v	
23	BEN-1	v	v	v	v	v	v	
24	BQN-1	v	v	v				
25	EVS-1	v	v	v				
26	EU-1	v	v	v				
27	DN-1	v	v	v				
28	HZU-1	v	v	v				

SWC: side wall core

RCAL: Rutin core analysis

Conv. C: Conventional core

FWR: Final well report

Table 3.2 Seismic data used in this study

Year	Line	Total Length (m)	Quality	Year	Line	Total Length (m)	Quality
1971	3	27724	Poor	1984	28	369300	good
1972	10	451578	Poor	1987	9	147458	good
1973	2	63616	Poor	1988	30	284567	good
1979	1	6940	moderate	1990	17	211044	good
1980	24	363410	moderate	1991	74	3360749	good
1981	5	37853	moderate	1992	110	3641604	good
1982	98	1680204	good	2013	12	979096	good
1983	130	4320233	good	2016	97	2543714	good

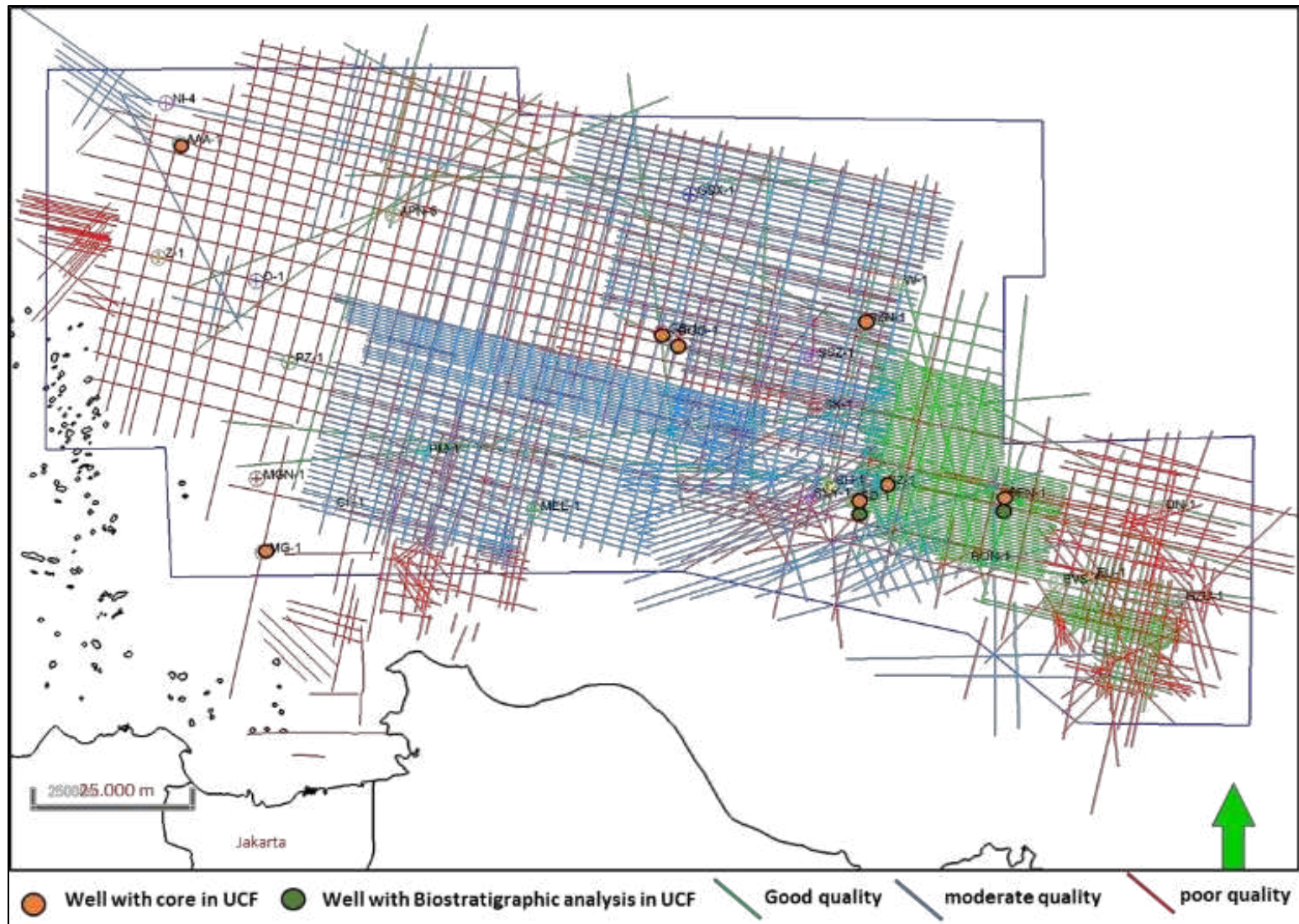


Figure 3.1 Base map of study area

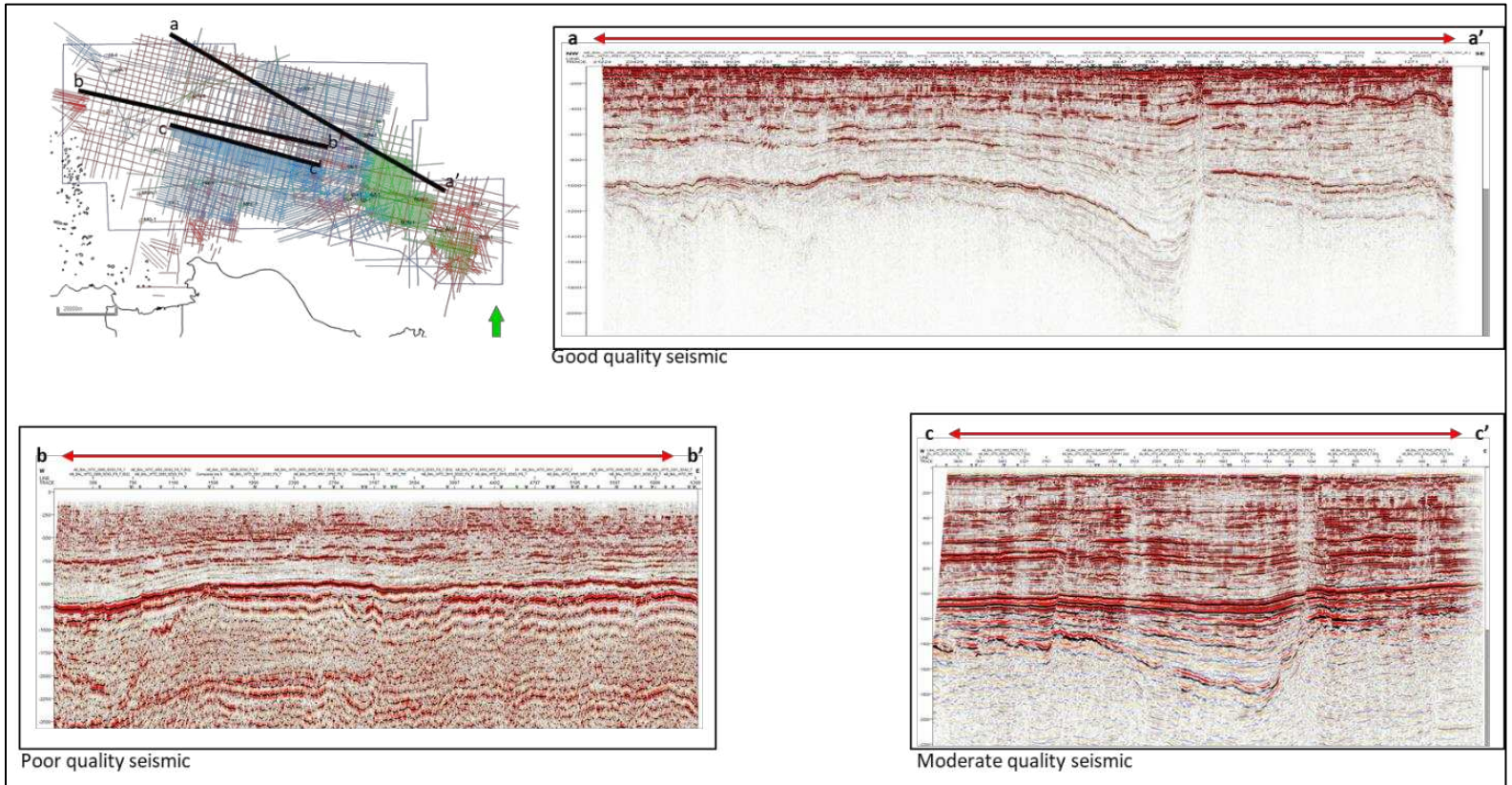


Figure 3.2 W-E 2D seismic section showing the quality of the seismic data visually

### 3.2. Methodology

This study has 2 main objectives that can be summarized as: 1) to reconstruct the depositional environments within the Miocene series of the Upper Cibulakan Formation; and 2) to forecast the distribution and quality of reservoirs.

To address the questions raised in this study, a structured research approach was employed, which can be divided into two primary phases. The first step involves the development of a detailed sequence stratigraphic framework, which integrates all available data to analyze the sedimentology and stratigraphy within the study area. This initial phase addressed the first objective of the study (figure 3.3). Subsequently, the second step involves a stratigraphic forward modeling, designed to test the interpreted sequence stratigraphy using numerical techniques, predict the reservoir quality and distribution and unravel the controlling factors of the sedimentary architecture. This latter stage served to address the second objective of the study.

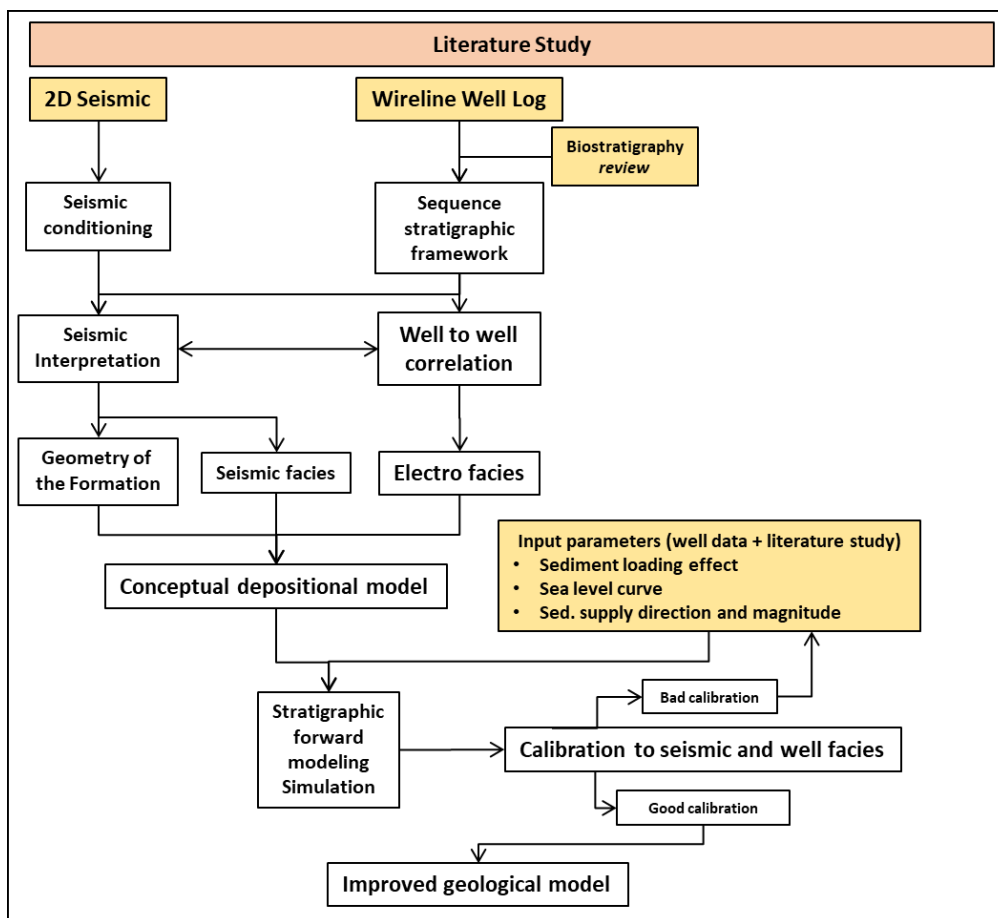


Figure 3.3 Workflow of the study



### 3.2.1. Sequence Stratigraphic Framework Development

Numerous sequence stratigraphic models have emerged in recent decades, primarily distinguished by variations in the selection of the surface designated as a sequence boundary, the approach to sequence subdivision, the structure of sequence hierarchy, and the factors influencing sequence evolution (Catuneanu, 2019, 2017; Catuneanu et al., 2009; Embry, 1995). Each methodology has its advantages and drawbacks, and the decision on which approach to adopt was largely driven by individual preferences. Nevertheless, the various models resulted in a complex and different terminology. Furthermore, once a specific sequence stratigraphic method was chosen, geologists were constrained to use the defined nomenclature and assumptions of the model chosen, regardless of the characteristics of the particular basin being analyzed.

Efforts have been undertaken over the past decade to formulate a methodology that independent of the specific models, focuses on the fundamental principles of sequence stratigraphy (Catuneanu, 2019, 2017; Catuneanu et al., 2009). This approach aims to be consistently applicable across geological settings, observation scales, and varying types and resolutions of available data. The model-independent approach prioritizes observable physical criteria, such as patterns in stratal stacking, terminations of strata, as well as facies and well-log patterns. This methodology aims to establish a framework for systems tracts and sequence stratigraphic surfaces. Model-dependent decisions can be introduced concerning the selection of the sequence stratigraphic surface to be designated as the sequence boundary. This choice is guided by factors such as mappability and ease of identification within the target succession and the available data. The selection of the sequence boundary subsequently determines the particular type of sequence that is employed (Catuneanu, 2019, 2017; Catuneanu et al., 2009). Following this workflow, a revised definition of a stratigraphic sequence emerges as a sedimentary succession deposited during a cycle of change in stratal stacking patterns, as delineated by the repetitive occurrence of a specific type of sequence stratigraphic surface, namely the sequence boundary (Catuneanu, 2019, 2017; Catuneanu et al., 2009). This definition remains independent of model, scale, and data considerations. It underscores the insignificance of the internal composition, specifically the number of developed systems tracts, and advocates that the selection of the sequence boundary should prioritize practicality rather than being model-driven.

During a single cycle of relative sea-level rise and fall, four conformable sequence stratigraphic surfaces could develop, denoting different events on the relative sea-level curve and corresponding change in stratal stacking patterns (figure 3.4):

1. the onset of relative sea-level fall, called the basal surface of forced regression (BSFR) (Hunt and Tucker, 1992) or the correlative conformity (CC) in the sense of depositional sequence I and II (Posamentier et al., 1988; Posamentier and Vail, 1988), represents the lower boundaries of forced regressive deposits (Hunt and Tucker, 1992; Plint and Nummedal, 2000; Posamentier et al., 1992; Posamentier and Morris, 2000).
2. the end of relative sea-level fall, also called the correlative conformity (CC) but in the sense of depositional sequence III and IV (Hunt and Tucker, 1992; Wagoner et al., 1988), represent the lower boundaries of lowstand normal regressive deposits.
3. the end of regression, called the maximum regressive surface (MRS) (Helland-Hansen and Hampson, 2009), represents the lower boundaries of transgressive deposits (Cattaneo and Steel, 2003).
4. and the end of transgression or the maximum flooding surface (MFS) (Galloway, 1989; Wagoner et al., 1988), represents the lower boundaries of highstand normal regressive deposits.

Unconformities may develop during two stages:

1. during stages of forced regression, called the subaerial unconformity (SU) and the regressive surface of marine erosion (RSME) (Plint, 1988; Sloss, 1949),
2. during stages of transgression, called the transgressive surface of erosion (TSE) (Allen and Posamentier, 1993; Posamentier and Vail, 1988; Zecchin et al., 2019).

The identification of sequence stratigraphic surfaces may not be universally feasible in every case study, dependent on factors such as tectonic and depositional settings, as well as the available data. We followed an iterative process in interpreting sequence stratigraphy with the available data quality. In the first stage, we interpreted sequence stratigraphy based on well data. At this point, sequence boundaries (SB) and maximum flooding surfaces (MFS) are identified. In the second stage, each defined SB and MFS from the wireline logs were tied to 2D reflection seismic data. Thus, horizon interpretation was conducted following well marker data. Simultaneously, we interpreted seismic facies based on the configuration of reflectors and

their stratal terminations geometries following [Mitchum \*et al.\*, \(1977\)](#). During this stage, we successfully identified transgressive surfaces (TS).

Using our model-independent observations (well logs, and seismic interpretation), we were able to identify the end of relative sea-level fall, here we refer as sequence boundary (SB) as the lower boundaries of lowstand system tract (LST), the end of regression, here we refer as transgressive surface (TS) as the lower boundary of transgressive system tract (TST), and maximum flooding surface (MFS), represent the lower boundaries of highstands system tract (HST). The discussion of the applied methodology is further elaborated below.

Initially, a thorough data conditioning and verification process was carried out to ensure the accuracy and readiness of the provided data for interpretation. All seismic and log data were imported into Petrel E&P<sup>TM</sup> package and conditioned by Pertamina. This included seismic miss tie analysis, amplitude balancing, and well-to-seismic tie procedures. As a result, all data used in this study are prepared and ready for interpretation.

#### **3.2.1.1. Biostratigraphic Review**

The existing biostratigraphic data, which consists of planktonic foraminifera and calcareous nannofossils, were thoroughly examined and updated to incorporate the most recent knowledge regarding species ranges. The Global Stratigraphic Section and Point (GSSP) Time Scale of 2020 ([Gradstein \*et al.\*, 2020](#)) was utilized as a reference for correlating the bio events observed in the study with global bio events. This process facilitated the determination of the age of Neogene stratigraphic intervals with improved accuracy and precision.

#### **3.2.1.1. Electro Facies Determination**

Standard wireline logs and checkshot data were used for the interpretation of lithology and for the seismic well-tie process. Lithology descriptions from the mud log and core also provided additional information for lithological interpretation. The electrofacies classification follows the log profile pattern by [Serra and Serra \(2004\)](#) ([figure 3.5](#)), and the geological interpretation of gamma ray logs follows the methodology defined by [Rider and Kennedy \(2011\)](#).

#### **3.2.1.2. Well-to-Well Correlation**

A visual examination of the gamma-ray stacking pattern, combined with mud log lithological data from a key well (containing the most comprehensive data set), was conducted

to analyze the sequence stratigraphic framework using Petrel E&P™ package (licensed to Sorbonne University). This approach provided an optimal visualization of well-log stacking patterns and their related lithology. Sequence boundaries and maximum flooding surfaces were defined based on changes in the stacking pattern, lithology, or grain size, following the methodologies of Mitchum and Van Wagoner, 1991; Posamentier *et al.*, 1988; Wagoner *et al.*, 1990, 1988. Third-order sequence boundaries and maximum flooding surfaces were identified in accordance with the hierarchy of stratal units. These interpretations were then linked to the global sea-level curve (Miller *et al.*, 2020) to understand the interplay of subsidence and sea-level variations in the area.

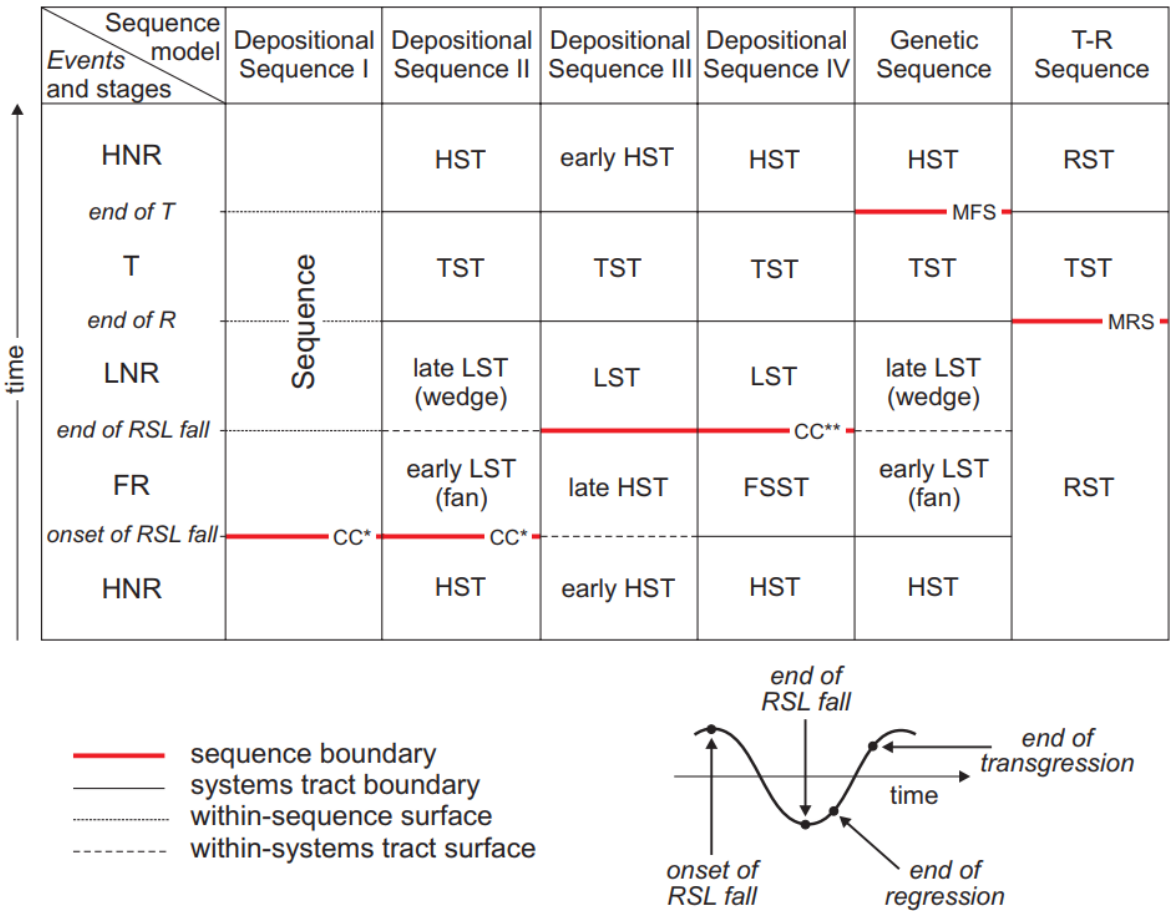


Figure 3.4 Nomenclature of systems tracts, and timing of sequence boundaries for the various sequence stratigraphic approaches (Catuneanu *et al.* 2011). Abbreviations: RSL – relative sea level; T – transgression; R – regression; FR – forced regression; LNR – lowstand normal regression; HNR – highstand normal regression; LST – lowstand systems tract; TST – transgressive systems tract; HST – highstand systems tract; FSST – falling-stage systems tract; RST – regressive systems tract; T-R – transgressive-regressive; CC\* – correlative conformity in the sense of Posamentier and Allen (1999); CC\*\* – correlative conformity in the sense of Hunt and Tucker (1992); MFS – maximum flooding surface; MRS – maximum regressive surface.



Correlation between wells was performed to establish the stratigraphic framework of the research area. The available biostratigraphic data were used to determine deposition age and environment. These interpretations served as the foundation for understanding the composite stratigraphy in the region, providing a calibration for seismic interpretation.

**3.2.1.3. Seismic Interpretation**

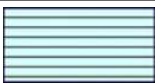

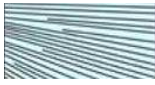
This stage involved the interpretation of eleven seismic horizons, using the industry standard Petrel™ software of Schlumberger (licensed to Sorbonne University), labeled as SB-1, 5, 7, 9, 10, 12, and 13 (as per their identification on key well), as well as the top Basement, top BRF, top Parigi, and a continuous reflector above interpreted Parigi carbonate. The lithological differences between the BRF and Parigi formations, primarily consisting of thick carbonate with overlying shale intervals, made it easier to track the top limits of these formations thanks to their strong amplitude characteristics in the seismic data.


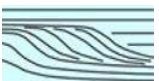





All the boreholes used in this study have been tied to seismic data using check shot data from each well. Out of the 28 available wells, only 2 wells (SK-1 and SSY-1) lack check shot data. To help convert these well logs to the time domain, synthetic check shot data from the nearest wells were used. Subsequently, well logs can be plotted in terms of equivalent two-way travel time.

**3.2.1.4. Seismic Facies Identification**

Once a regionally consistent seismic interpretation was completed, seismic facies in three selected key seismic lines were performed to reveal the depositional environment evolution through time. Identification of the seismic reflector geometries following (Mitchum *et al.*, 1977) is the first step towards facies classification and provides information about the depositional processes (table 3.3).

Tabel 3.3 Seismic reflector geometries

Reflection geometry		Interpretation
<b>Parallel</b>		Uniform deposition of continuous reflectors.
<b>Subparallel</b>		Mostly parallel with a small degree of reflector thickening and thinning.
<b>Divergent</b>		Reflectors disappear internally.

<b>Sigmoidal</b>		downlapping character building outward and upward (aggrading) into a basin. Sigmoidal patterns are indicative of fine-grained low energy deposition.
<b>Oblique</b>		Reflectors toplapping and outward building into a basin. Oblique patterns are indicative of sedimentation rates and commonly contains clean sand in the upper portion of the bedform. Oblique bedform types typically require water depths of 500 meters or more.
<b>Shingled</b>		Thin interval of toplapping and downlapping reflector geometries outbuilding onto a shelf. This is similar to the oblique bedform process of deposition but with a shallower water depth.
<b>Mounded</b>		Bi-directional downlapping reflectors with an increasing number of reflectors towards the center on the structure. Adjacent units onlap the mound. This geometry can be indicative of a carbonate mound or deep-water marine fan.
<b>Hummocky</b>		Random thickening and thinning of reflectors and can be indicative of shallow marine sands.
<b>Deformed</b>		Sliding or slumping of reflectors typically found on a continental slope where once continuous reflectors become discontinuous as they move downward.
<b>Chaotic</b>		Refers to reflections that that have no continuity with other reflectors in a unit.
<b>Reflection Free</b>		Having no reflections from internal structures.

### 3.2.2. Stratigraphic Forward Modeling

Stratigraphic forward modeling (SFM) has proven to be a powerful method for reconstruct the stratigraphic architecture of sedimentary basin at a regional scale (Granjeon, 2014), to improve the understanding of reservoir presence, distribution, quality, and architecture in the petroleum exploration (Granjeon, 2019; Hawie *et al.*, 2019; Otoo and Hodgetts, 2021; Yong *et al.*, 2019), to assess the regional controls on organic matter accumulation (Crombez *et al.*, 2017), as well as predicting other sedimentation-related aspects within depositional basins (Ayranci, 2022; Crombez *et al.*, 2017). By integrating the physical processes and geological constraints, such as sediment source to sink systems, base level cycles, and sediment transport in a 3-D framework, SFM provides comprehensive analysis into the complex dynamics of sedimentary systems (Gervais *et al.*, 2018; Granjeon, 2019). Moreover, SFM has been applied in sensitivity analysis and probability mapping of reservoir presence, enhancing the assessment of geological scenarios and the identification of potential reservoir facies (Falivene *et al.*, 2020; Gervais *et al.*, 2018).

The use of stratigraphic forward modeling is not limited to predicting sediment distribution in regional scale only, it has also been applied in the context of reservoir prediction

in field scale analysis as well, where it serves as a numerical, process-based algorithm simulating sedimentary and tectonic processes controlling depositional architecture (Falivene *et al.*, 2020). Additionally, it has been utilized to increase the predictive power of geostatistical reservoir models by integrating geological constraints and guiding the reconstruction of internal reservoir geometry, thereby reducing uncertainty (Burgess *et al.*, 2006; Sacchi *et al.*, 2016).

Stratigraphic forward modeling emerges as a valuable tool for predicting sediment distribution across diverse depositional environment, including continental margins and incised valleys (Granjeon, 2014), deltas (Ayranci, 2022), and shallow marine environments (Otoo and Hodgetts, 2021). This modeling technique extends its utility to investigate specific geological parameters within the depositional environment, as for instance: the impacts of morphological parameters on sediment budget partitioning and channel networks in delta-canyon-fan systems (Wan *et al.*, 2022; Falivene *et al.*, 2020), the analysis of forced regressions, offering insights into the genesis of attached and detached lowstand systems in deltaic environments (Ainsworth *et al.*, 2000), as well as predicting the evolution and internal structure of different reef morphotypes (Montaggioni *et al.*, 2015).

In conducting Stratigraphic Forward Modeling (SFM), we utilize the DionisosFlow package (IFPEN, licensed to Paris Sorbonne University). DionisosFlow is a deterministic 3D multi-lithology forward stratigraphic model designed to replicate basin infill processes occurring over extended geological timeframes. It replicates the cumulative outcome of sediment supply, transportation, and accommodation dynamics, accounting for factors such as uplift, subsidence, and sea level fluctuations in the modeled grid (Granjeon, 2019, 2014; Hawie *et al.*, 2019). Several essential input data are required to establish the base model in SFM. These include information regarding: 1) the structural evolution of the basin, encompassing initial topography, sediment thickness, and eustasy which is then translated into subsidence maps; 2) data related to sediment input settings, including sediment supply and carbonate production; and finally 3) the determination of transport parameters, such as diffusivity, plays a crucial role in the modeling process.

#### 3.2.2.1. Structural evolution

Three thickness maps generated from seismic interpretation were utilized for defining the structural evolution of Ardjuna sub-basin, each representing distinct geological periods. These maps correspond to the Early Miocene transgression during the Aquitanian to Early Burdigalian

period, the Early Miocene regression in the Burdigalian to Early Langhian period, and the Middle to Late Miocene transgression in the Langhian to Tortonian period. The global eustatic curve (Miller *et al.*, 2020) was used. The thickness data for these maps were derived from the interpretation of 2D seismic data. Fourteen time markers obtained from the stratigraphic sequence analysis were used to calibrate the thickness of each deposition sequence in the model.

The initial bathymetry map is a highly significant input as it defines the accommodation space and deposition geometry of stratigraphic units. To obtain this map, we used a combination of the Baturaja carbonate thickness map, derived from the interpretation of a substantial dataset of 2D seismic analyses, along with the results from seismic stratigraphy analysis, gross-depositional environment (GDE) mapping, and unpublished biostratigraphy analysis. Eight reference wells were employed to constrain the bathymetry map. Subsidence maps were generated by utilizing isopach maps that were divided into fourteen sequence stratigraphic markers and subsequently refined manually in areas with inconsistencies.

#### 3.2.2.2. Sediment input setting

The lithological description, obtained from both drilling ditch cuttings and core samples collected from eight boreholes, illustrates a prevailing lithology consisting mainly of very fine to fine-grained sand, silt, and shale. To model this lithology information, two distinct sediment classes were introduced in the model, each characterizing the transportation of fine (clay) and coarser (sand) particles. Subsequently, an examination was conducted to identify the optimal continuous sediment supply (Qs), and sand-to-shale ratio, variation that replicates the observed thickness and lithological variations in the reference well. This involves a systematic iteration through various sediment values until we identify the best fit combination for our model. These iterations continued until we achieved calibration values (thickness and lithology percentage) exceeding 90% (with a 10% error threshold) when compared to the well bore interpretation. After obtaining the appropriate values, direct comparison with the sediment mass flux from East Asia (Clift and Plumb, 2008; Clift and Webb, 2019) were conducted to analyze the deriving factor controlling the sediment input in this area.

We simulate the in-place generation of sediments in carbonate rocks by taking into consideration the carbonate production rate in various water depths, with additional contributions from wave energy, slope angle, and siliciclastic input affecting the ultimate deposition rate. The rates of carbonate production are established by taking into account

published carbonate production principles, such as those outlined by [Bosscher and Schlager \(1992\)](#). These principles indicate that the highest carbonate production occurs in shallow waters (up to 15 meters), and as water depth increases, carbonate production gradually decreases, reaching a limit at around 45 meters depth.

The simulated models were then classified according to a depositional facies scheme based on bathymetry of deposition, sand percentage, carbonate percentage, and the volume of fluvial discharge. In this facies scheme, the distinction between a delta and submerged delta lobe is based on the bathymetry of deposition. Please note that the use of water discharge is not intended to represent the actual channelization process but rather to signify high-discharge transport conditions where distributary channels might be expected to develop. Areas with lower discharge may experience more dispersed sediment.

### 3.2.2.3. Transport parameter

We employed non-linear equations that account for both water and slope-driven processes ([Granjeon, 2014](#)) to model the transport of sediment within our model.

$$Q_{sw,k} = K_{w,k} C_k \bar{Q}_w^n S^{m_w} \text{ with } \bar{Q}_w = \left( \frac{Q_w}{Q_{wo}} \right) \quad (1)$$

Equation 1: definition of the non-linear water-driven and slope-driven flux ([Granjeon, 2014](#)),  $Q_{sw,k}$  [ $\text{m}^2\text{s}^{-1}$ ], of the grain-size fraction  $k$ , where  $C_k$  is the surface concentration,  $Q_w$  the local water discharge ( $\text{m}^3\text{s}^{-1}$ ),  $\bar{Q}_w$ , is the local dimensionless water discharge,  $Q_{wo}=1 \text{ m}^3\text{s}^{-1}$  is the reference water discharge;  $S$  is the basin slope ( $-$ ),  $K_{w,k}$  is the water-driven diffusion coefficient of the grain-size fraction  $k$ , defined as a function of water depth;  $n$  and  $m_w$  are two constants, usually between 1 and 2 ([Tucker & Slingerland, 1994](#)).

To obtain suitable and optimal sediment transport parameters for this model, we began with hypothetical values based on the work of [Burgess et al. \(2006\)](#). These values were then fine-tuned through sensitivity analysis to determine the best parameters, ensuring that the diffusivity values could transfer sediments across the entire model block and produce a geometry that closely approximates the observed seismic facies.

### 3.2.2.4. Model calibration

Multiple basin infill scenarios were tested by varying the locations of sedimentary sources and their lithological content (sand and shale ratios), the sediment supply ( $Q_s$ ), water discharge

(Qw), and by preserving the empirical ratios (marine versus continental for the different grain sizes) of the diffusion coefficients. The overall model calibration is based on the comparison of (1) the simulation thickness results and the isopach maps of the UCF, (2) the simulated depositional facies with gross depositional environment (GDE) maps, and (3) overall expected sand volume with well data.

#### 3.2.2.5. **Uncertainty and sensitivity**

To assess the impact of each parameter on the calibration data, we employed a multi-simulation analysis varying parameters that affect accommodation, sediment supply, as well as sediment transport. The CougarFlow package (IFPEN licensed to Paris Sorbonne University) was used to perform this analysis, utilizing a Latin hypercube experimental design to distribute the values of each parameter in each simulation, optimizing the total simulations required (Deutsch and Deutsch, 2012; Helton and Davis, 2003; Mckay *et al.*, 1979). We set the distribution to follow the triangular law. In this case, the most frequently chosen parameters were selected to be close to our reference model values. This approach allows for comprehensive sampling across the entire uncertain domain. Furthermore, equal weight to each parameters was assigned to ensure that there is no interrelationship between design variables. Sensitivity maps and risk analysis maps of reservoir distribution and standard deviation of the thickness were calculated to approximate the best reservoir distribution location.



## **CHAPTER 4: GEOLOGY OF ARDJUNA SUB-BASIN**





## 4.1. Biostratigraphic data review and reinterpretation

### 4.1.1. Available biostratigraphic data review

#### Well SD-1

The SD-1 exploratory well was drilled in 1992 to test a three-way dip closure on the downthrown side of a N-S trending normal fault in the deeper part of Ardjuna sub-basin (figure 4.1). The borehole reached a total depth of 3101 m (10174 ft) and drilled, following the original stratigraphic interpretations, from top to bottom the Cisubuh Formation (base at 574 m (1883 ft)), the Parigi Formation (base at 620 m (2034 ft)), the Upper Cibulakan Formation (base at 1844 m 6050 ft), and Baturaja Formation (base at 1926 m (6319 ft)) before ending in the Talangakar Formation. Noon *et al.*, (1993) carried out biostratigraphy analyses at the entire borehole interval.

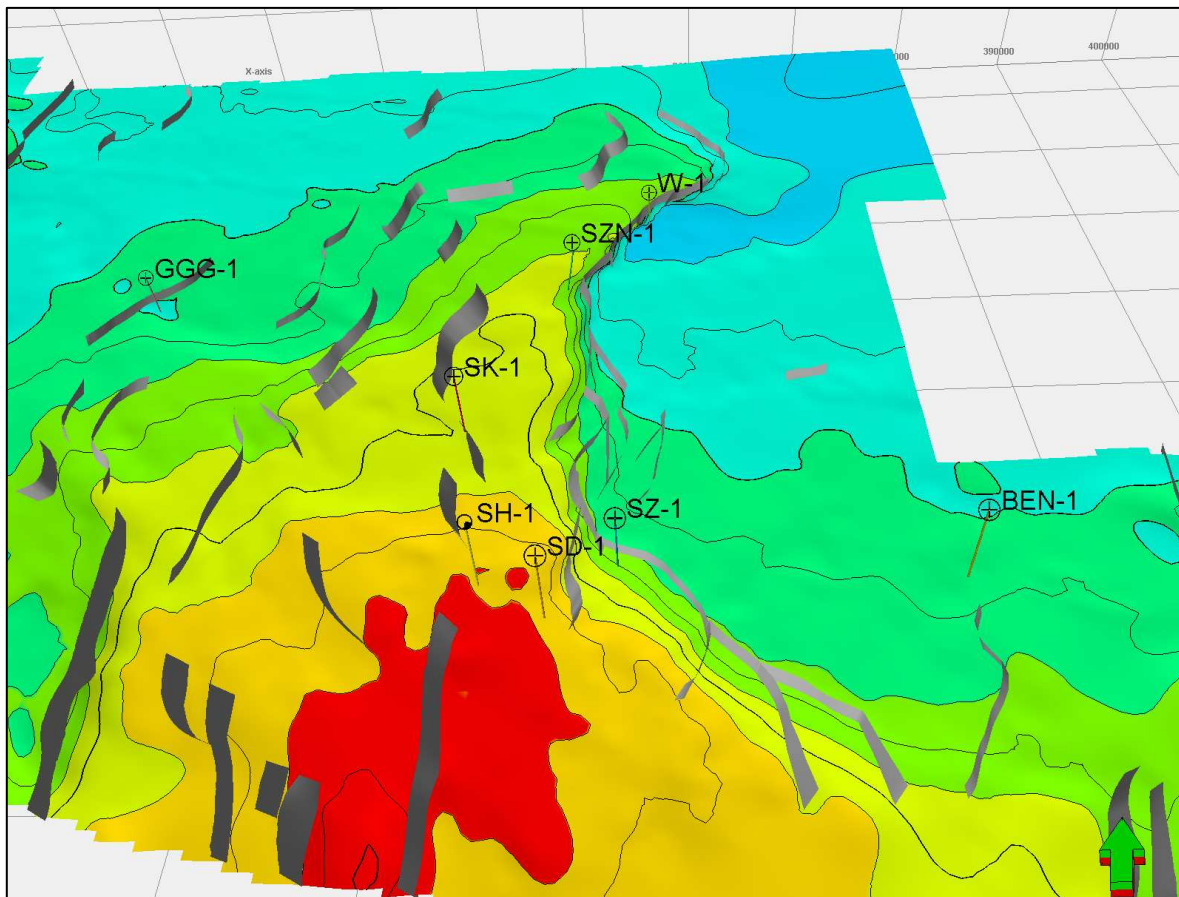


Figure 4.1 3D view of the Baturaja Formation in the Ardjuna sub-basin, illustrating the position of wellbore data in relation to the fault (white polygon).

The stratigraphical interpretation from a total of 141 ditch cutting and 32 sidewall core samples indicated deposition of the Upper Cibulakan Formation at this location was initiated during the end of NN1 Nano zonation (Martini, 1971). This boundary is recognized by the last appearance datum (Los) of *Cyclicargolithus abisectus* (NN1) at 1874 m (6148 ft), following with Los of *Triquetrorhabdulus carinatus* (NN2) and *Sphenolithus dissimilis* (NN2 and older) at 1783 m (5850 ft) depth. Important nannofossils and planktonic foraminifera that serve as key maker used in age determination is shown in table 4.1.

Major shallowing was detected at the base of UCF by the absence of the deep-water benthic faunas and dominated by *Ammonia*, *Cibicides*, *Bolivina* and *Eponides* as well as the decrease in diversity and abundance that reflect shallow environment. Shallowing and deepening event based on the faunal diversity and abundance was recognized. In general, based on biostratigraphic analysis, the UCF was deposited in the transitional to shallow marine environment.

### **Well GGG-1**

GGG-1 is an exploratory well drilled on 1974 to test a faulted anticline on the northwest edge of Ardjuna sub-basin (figure 4.1). The borehole reached a total depth of 1332.28 m (4371 ft) and drilled, following the original stratigraphic interpretations, from top to bottom the Cisubuh Formation (base at 542.5 m (1780 ft)), the Parigi Formation (base at 622 m (2040.5 ft)), the Upper Cibulakan Formation (base at 917.75 m (3011 ft)), the Baturaja Formation (base at 998.82 m (3277 ft)), and the Talangakar Formation (base at 1315.82 m (4317 ft)) before ending in the granitic basement. Biostratigraphy analyses was performed on 1993 using 92 ditch cutting samples from entire drilled interval.

The stratigraphical interpretation indicated the deposition of UCF at this location is marked by a sharp increase in planktonic foraminifera including *Globigerinoides altiapertura* (N5 – N6), suggesting younger age compared to SD-1 well. This time gap could indicate that a non-deposition unconformity took placed at the location of GGG-1 well. Important nannofossils and planktonic foraminifera that serve as key maker used in age determination is shown in table 4.1.

### **Well SZN-1**

SZN-1 is an exploratory well drilled on 1983 to test a downthrown fault closure on the major basin margin fault of Ardjuna sub-basin ([figure 3.1](#)). The borehole reached a total depth of 2101.6 m (6893.7 ft) and drilled, following the original stratigraphic interpretations, from top to bottom the Cisubuh Formation (base at 592.8 m (1943.6 ft)), the Parigi Formation (base at 652.8 m (2139.8 ft)), the Upper Cibulakan Formation (base at 917.75 m (3010.1 ft)), the Baturaja Formation (base at 1411.8 m (4628.3 ft)), and the Talangakar Formation (base at 1832.5 m (6007.9 ft)) before ending in the granitic basement. Biostratigraphy analyses were performed in 1987 using 81 ditch cutting and 21 sidewall core samples from the entire drilled interval.

Due to the infrequent sample intervals and the limited number of species found in the samples, which are not sufficiently representative within this well, the determination of age or biozone cannot be accurately established in this location. Important nannofossils and planktonic foraminifera useful for correlation can be seen in [table 4.1](#).

### **Well BEN-1**

BEN-1, an exploratory well drilled in 1993, aimed to test a 4-way dip closure on the upthrown block in the western part of the Ardjuna sub-basin ([figure 4.1](#)). The well reached a total depth of 1261.26 m (4139.56 ft), following the original stratigraphic interpretations, and encountered the following formations from top to bottom: Cisubuh Formation (base at 342.9 m (1125.5 ft)), Parigi Formation (base at 429.46 m (1408.5 ft)), Upper Cibulakan Formation (base at 1004 m (3293.5 ft)), Baturaja Formation (base at 1155.19 m (3788 ft)), and Talangakar Formation (base at 1205.78 m (3957.65 ft)), before reaching the granitic basement. In 1994, biostratigraphy analysis was conducted using 11 sidewall core samples collected from the entire drilled interval. However, due to the sparse sample intervals and the limited diversity of species found, which are not adequately representative in this well, it is challenging to accurately establish the age or biozone in this particular location. [Table 4.1](#) provides information on important nannofossils and planktonic foraminifera that can be used for correlation purposes.

### **Well SZ-1**

The SZ-1 exploratory well was drilled in 1979 on the downthrown side of a N-S trending normal fault in the deeper part of Ardjuna sub-basin ([figure 4.1](#)). The borehole reached a total

depth of 1948 m (6390.73 ft) and drilled, following the original stratigraphic interpretations, from top to bottom the Cisubuh Formation (base at 463.9 m (1522.64 ft)), the Parigi Formation (base at 490.73 m (1608.46 ft)), the Upper Cibulakan Formation (base at 1301.5 m (4266.14 ft)), the Baturaja Formation (base at 1490.47 m (4888.24 ft)), and the Talangakar Formation (base at 1888.5 m (6194.23 ft)) before ending in the Talangakar Formation.

The stratigraphical interpretation from a total of 63 ditch cutting samples indicated that the deposition of the Upper Cibulakan Formation at this location was initiated during the end of NN1 Nano zonation (Martini, 1971). This boundary is recognized by the last appearance datum (Los) of *Cyclicargolithus abisectus* (NN1) at 1301.5 m (4266 ft), following with Los of *Triquetrorhabdulus carinatus* (NN2) at 1402 m (4598.5 ft) depth, and Los of *Sphenolithus belemnos* (NN3) at 1200.9 m (3937 ft). Useful foraminifera taxa were identified in the UCF interval, including Los of *Catapsydrax stainforthi* that indicates penetration of N7 and confirms the early Miocene age. The presence of N7 marker *Globigerinoides altiapertura* from 1255.7 m (4117 ft) confirms the planktonic zonal age. Zone N6 is recognized at 1280.16 m (4203 ft) on the Los of *Catapsydrax dissimilis*. Important nannofossils and planktonic foraminifera that serve as key maker used in age determination is shown in [table 4.1](#).

The depositional environment at the SZ-1 well location in the Upper Cibulakan Formation (UCF) is marked by the presence of shallow-water benthic foraminifera, which includes species such as *Operculina*, *Amphistegina*, *Pseudorotalia*, *Ammonia*, *Quinqueloculina*, as well as larger foraminifera like *Lepidocyclina*, *Miogypsina*, and *Cycloclypeus*. The scarce deeper-water species suggest that the prevailing conditions in this area were generally in the outer to inner sublittoral range. In between these layers, there are sandy horizons that exhibit a less diverse benthic fauna. These horizons may indicate transitions from shallower inner sublittoral to inner sublittoral environments.

Table 4.1 Calcareous nannofossils and planktonic foraminifera species list used to determine depositional age of Upper Cibulakan Formation

Calcareous nannofossil	Well name										Biozone
	SD-1		GGG-1		SZN-1		BEN-1		SZ-1		
Planktonik foraminifera	Los (m)	Fos (m)	Los (m)	Fos (m)	Los (m)	Fos (m)	Los (m)	Fos (m)	Los (m)	Fos (m)	
<i>Globoquadrina baroemouensis</i>	585.2	-	-	-	-	-	-	-	-	1517.8	N18
<i>Discoaster quinquerramus</i>	603.5	640.0	-	-	-	-	-	-	-	-	NN11
<i>Discoaster bollii</i>	694.9	-	-	-	603.5	865.6	-	-	548.6	-	NN10
<i>Discoaster calcaris</i>	713.2	-	-	-	-	-	-	-	457.2	-	NN10
<i>Discoaster hamatus</i>	749.8	804.6	448.0	466.3	-	-	-	-	548.6	676.6	NN9
<i>Neogloboquadrina continua</i>	749.8	-	-	-	-	-	-	-	652.2	1584.9	N16
<i>Globorotalia siakensis/mayeri</i>	822.9	-	649.2	1060.7	792.4	975.3	-	-	853.4	1536.1	N14
<i>Cassigerinella chipolensis</i>	871.1	-	-	-	603.5	1377.6	-	-	670.5	1286.2	N13
<i>Globigerinoides subquadratus</i>	871.1	-	649.2	1106.4	612.6	877.8	-	-	725.4	1517.8	N13
<i>Discoaster exilis</i>	896.1	-	-	-	621.8	780.2	-	-	652.2	-	NN8
<i>Cyclicargolithus floridanus</i>	969.2	-	493.8	-	780.2	1450.8	-	-	688.8	-	NN6
<i>Sphenolithus heteromorphus</i>	1060.7	-	594.3	-	987.5	1249.6	623.9	854.0	780.2	-	NN5
<i>Globorotalia peripheroronda</i>	1078.9	1298.4	-	-	-	-	-	-	-	-	N10
<i>Globigerinoides diminuta</i>	1133.8	1261.8	-	-	-	-	-	-	999.7	1408.1	N9-N7
<i>Praeorbulina glomerosa</i>	1133.8	-	-	-	-	-	-	-	-	-	N9-N8
<i>Globigerinoides cf. sicanus</i>	1152.1	1298.4	-	-	902.16*	-	-	-	-	-	N9-N8
<i>Praeorbulina circularis</i>	1188.7	-	-	-	-	-	-	-	-	-	N9-N8

<i>Globorotalia cf. binargeae</i>	1261.8	-	-	-	-	-	-	-	-	-	N8-N7
<i>Helicosphaera ampliapertura</i>	1280.1	-	859.5	950.9	841.2	960.1	623.9	1006.4	871.7	-	NN4
<i>Helicosphaera obliquua</i>	1419.1	-	996.6	1042.4	-	-	795.8	1006.4	908.3	-	NN4
<i>Sphenolithus belemnos</i>	1636.7	1778.7	758.9	-	-	-	-	-	1200.9	-	NN3
<i>Discoaster adamanteus</i>	1636.7	-	-	-	-	-	-	-	1164.3	-	NN3
<i>Globigerinoides cf. primordius</i>	1749.5	-	1106.4	1142.9	-	-	-	-	-	-	N5
<i>Triquetrorhabdulus carinatus</i>	1783.0	-	923.5	1078.9	-	-	-	-	1402.0	1463.0	NN2
<i>Sphenolithus dissimilis</i>	1783.0	-	859.5	1088.1	-	-	-	-	-	-	NN2
<i>Globigerinoides altiapertura</i>			917.5								N5-N6
<i>Cyclicargolithus abisectus</i>	1874.4	-	996.6	1014.9	-	-	-	-	1438.6	-	NN1
<i>Globigerina binaiensis</i>	1874.4	-	-	-	-	-	-	-	-	-	N5
<i>Globigerina cf. ciperoensis</i>	1911*	-	1106.37*	-	-	-	-	-	-	-	N4
<i>Globigerinoides</i>	-	1966.5	-	-	-	-	-	-	-	-	N4
<i>Globorotalia opima nana</i>	1984.2	-	-	-	-	-	-	-	-	-	N4
* Single occurrence		los = last occurrences			Fos = first occurrences						

#### 4.1.2. Biostratigraphic age reinterpretation

Upon reviewing the biostratigraphic data, we have opted to use well SD-1 as the primary key well for age interpretation in this study. This choice is reinforced by the fact that well SD-1 contains the most complete dataset and was drilled in a location notably distant from the major fault and is situated in the deepest region of this basin. While well SZ-1 offers a significant biostratigraphic information, it was drilled in close proximity to the major fault, which raises the possibility that the recorded stratigraphy might have been influenced by fault movements, potentially resulting in missing or repeated sections (fig 4.1).

We established the ages for the first occurrences (Fos) and last occurrences (Los) of significant Cenozoic planktonic foraminifera (pf) and calcareous nannofossils (cn) using equivalent ages referenced from GSSP 2020 (Gradstein *et al.*, 2020) (Table 4.2, 4.3 , figure 4.2).

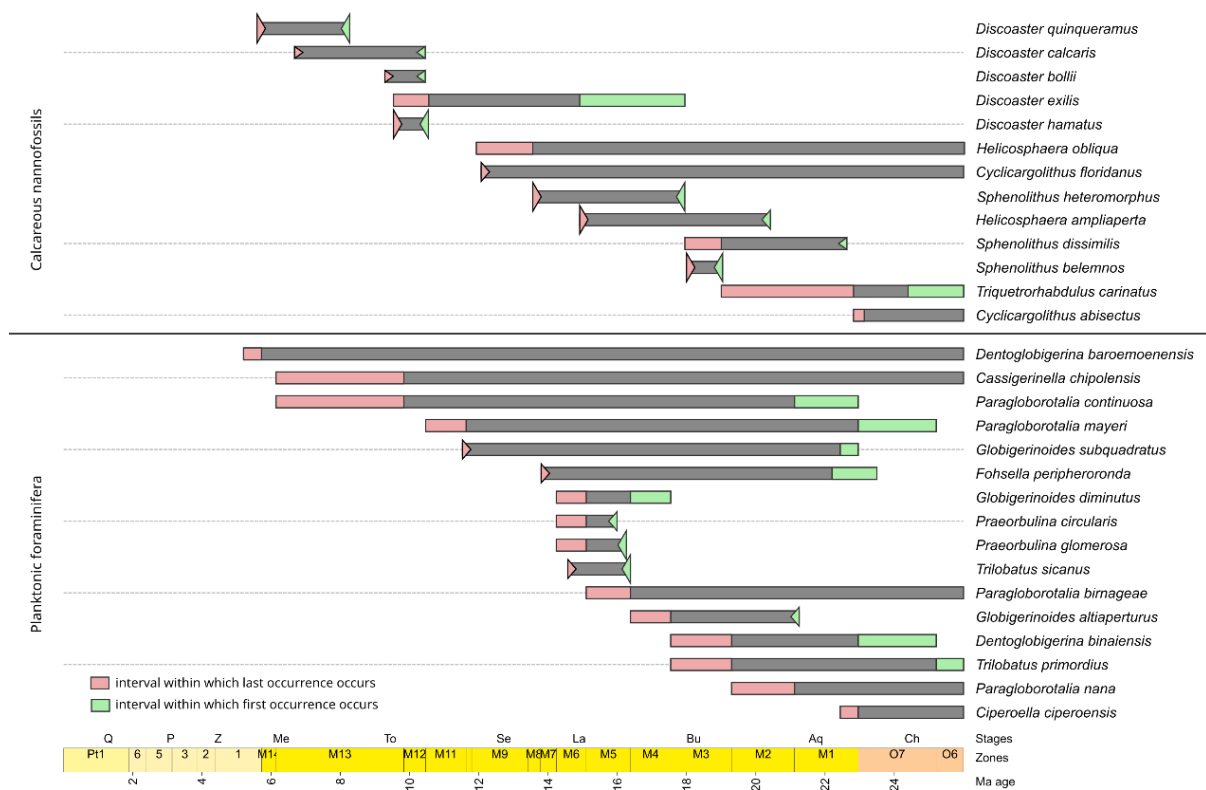


Figure 4.2 Calcareous nannofossils and planktonic foraminifera age chart used to determine depositional age of Upper Cibulakan Formation



Table 4.2 Calcareous nannofossils age range used to determine depositional age of Upper Cibulakan Formation

<b>Calcareous nannofossil</b>	<b>Last occurrence (top) (Ma)</b>	<b>First occurrence (base) (Ma)</b>	<b>Citation</b>
Discoaster quinquerramus	5.6	8.3	Discoaster quinquerramus Gartner 1969
Discoaster bollii	9.3	10.4	Discoaster bollii Martini and Bramlette, 1963
Discoaster calcaris	6.7	10.4	Discoaster calcaris Gartner 1967
Discoaster hamatus	9.5	10.6	Discoaster hamatus Martini and Bramlette, 1963
Discoaster exilis	9.53 - 10.55	14.90 - 17.95	Discoaster exilis Martini and Bramlette, 1963
Cyclicargolithus floridanus	12.1	42.87 - 46.29	Cyclicargolithus floridanus Bukry, 1971
Sphenolithus heteromorphus	13.5	18	Sphenolithus heteromorphus Deflandre 1953
Helicosphaera ampliapertura	14.9	20.4	Helicosphaera ampliapertura Bramlette and Wilcoxon, 1967
Helicosphaera obliqua	11.9 - 13.53	26.84 - 29.62	Helicosphaera obliqua Bramlette & Wilcoxon, 1967
Sphenolithus belemnos	18	19	Sphenolithus belemnos Bramlette and Wilcoxon, 1967
Triquetrorhabdulus carinatus	19 - 22.82	24.4 - 26.84	Triquetrorhabdulus carinatus Martini, 1965
Sphenolithus dissimilis	17.95 - 19	22.6	Sphenolithus dissimilis Bukry and Percival, 1971
Cyclicargolithus abisectus	22.82 - 23.13	29.62 - 32.02	Cyclicargolithus abisectus (Muller, 1970) Wise, 1973

Table 4.3 Planktonic foraminifera age range used to determine depositional age of Upper Cibulakan Formation

<b>Planktonic foraminifera</b>	<b>Last occurrence (top) (Ma)</b>	<b>First occurrence (base) (Ma)</b>	<b>Citation</b>
Globoquadrina baroemoenensis	5.2 - 5.72	30.28 - 32.1	Dentoglobigerina baroemoenensis (LeRoy, 1939)
Neogloboquadrina continuosa	6.14 - 9.83	21.12 - 22.96	Paragloborotalia continuosa (Blow, 1959)
Globorotalia mayeri	10.46 - 11.63	22.96 - 25.21	Paragloborotalia mayeri (Cushman and Ellisor, 1939)
Cassigerinella chipolensis	6.14 - 9.83	33.9 - 34.68	Cassigerinella chipolensis (Cushman & Ponton 1932)
Globigerinoides subquadratus	11.5	22.44 - 22.96	Globigerinoides subquadratus Brönnimann, in Todd et al. 1954
Globorotalia peripheroronda	13.8	22.2 - 23.5	Fohsella peripheroronda (Blow & Banner, 1966)
Globigerinoides diminuta	14.24 - 15.1	16.38 - 17.54	Globigerinoides diminutus Bolli, 1957
Praeorbulina glomerosa	14.24 - 15.1	16.3	Praeorbulina glomerosa (Blow 1956)
Globigerinoides sicanus	14.6	16.4	Trilobatus sicanus (de Stefani 1952)
Praeorbulina circularis	14.24 - 15.1	16	Praeorbulina circularis (Blow, 1956)
Globorotalia birnageae	15.1 - 16.38	26.93 - 28.09	Paragloborotalia birnageae (Blow, 1959)
Globigerinoides primordius	17.54 - 19.3	25.21 - 26.93	Trilobatus primordius (Blow and Banner, 1962)
Globigerinoides altiapertura	16.38 - 17.54	21.3	Globigerinoides altiapertura Bolli, 1957

Planktonic foraminifera	Last occurrence (top) (Ma)	First occurrence (base) (Ma)	Citation
<i>Globigerina binaiensis</i>	17.54 - 19.3	22.96 - 25.21	<i>Dentoglobigerina binaiensis</i> (Koch, 1935)
<i>Globigerina ciperoensis</i>	22.44 - 22.96	29.18 - 30.28	<i>Ciperoella ciperoensis</i> (Bolli, 1954)
<i>Globorotalia opima nana</i>	19.3 - 21.12	37.99 - 39.97	<i>Paragloborotalia nana</i> (Bolli 1957)

The lower boundary of the Baturaja Formation (Base BRF) or Top Talangakar Formation (Top TAF) can be identified lithologically in the well log by the appearance of the initial extensive carbonate series in the Chattian-Aquitainian period. In SD-1, this transition can be pinpointed at a depth of 1920 meters (6299 ft), characterized by a marked contrast in gamma ray values, shifting from high to low values. This identified boundary is positioned approximately 20 m (65 ft) below the presence of *G. ciperoensis*. The gamma-ray shift indicates a period characterized by decreased clastic sediment input and the commencement of tectonic stability in most of the foreland basin in Indonesia. These conditions facilitated the widespread development of carbonate production (Burbury, 1977).

Although *G. ciperoensis* is encountered only once at a depth of 1900 m (6233 ft), it holds significant value as a marker due to its presence in the sidewall core sample. Consequently, the base of the BRF is inferred to be older than the lowest occurrence of *G. ciperoensis* Los (approximately ~22.9 Ma). Furthermore, the detailed analysis conducted on the BRF suggests that the lower part of the formation was deposited during a transgressive phase, and the lower boundary may represent the end of regressive phase (Widodo, 2018). Additionally, it may be linked to a brief sea-level drop during the Chattian-Aquitainian transition (23.04 Ma) (Miller *et al.*, 2020). This interpretation aligns with the sedimentological details provided by Widodo (2018), reinforcing our preliminary age assignment of around 23.04 Ma for the base of the BRF (figure 4.3).

In well SD-1, the top of the Baturaja Formation is situated at a depth of 1823 meters (5981.63 ft). There, the Baturaja Formation consists of thin limestone layers changing gradually to claystones in its upper part. This horizon occurs 40 meters (131.23 ft) above the occurrence of *G. ciperoensis* (Los at 22.9 Ma), further analysis of the stratigraphic sequence indicates that this horizon can be correlated with a short-term sea level fall during Aquitainian (22.2 Ma) (further discussion in chapter 5). Thus, we assigned the age of top BRF to ~22.2 Ma (figure 4.3).

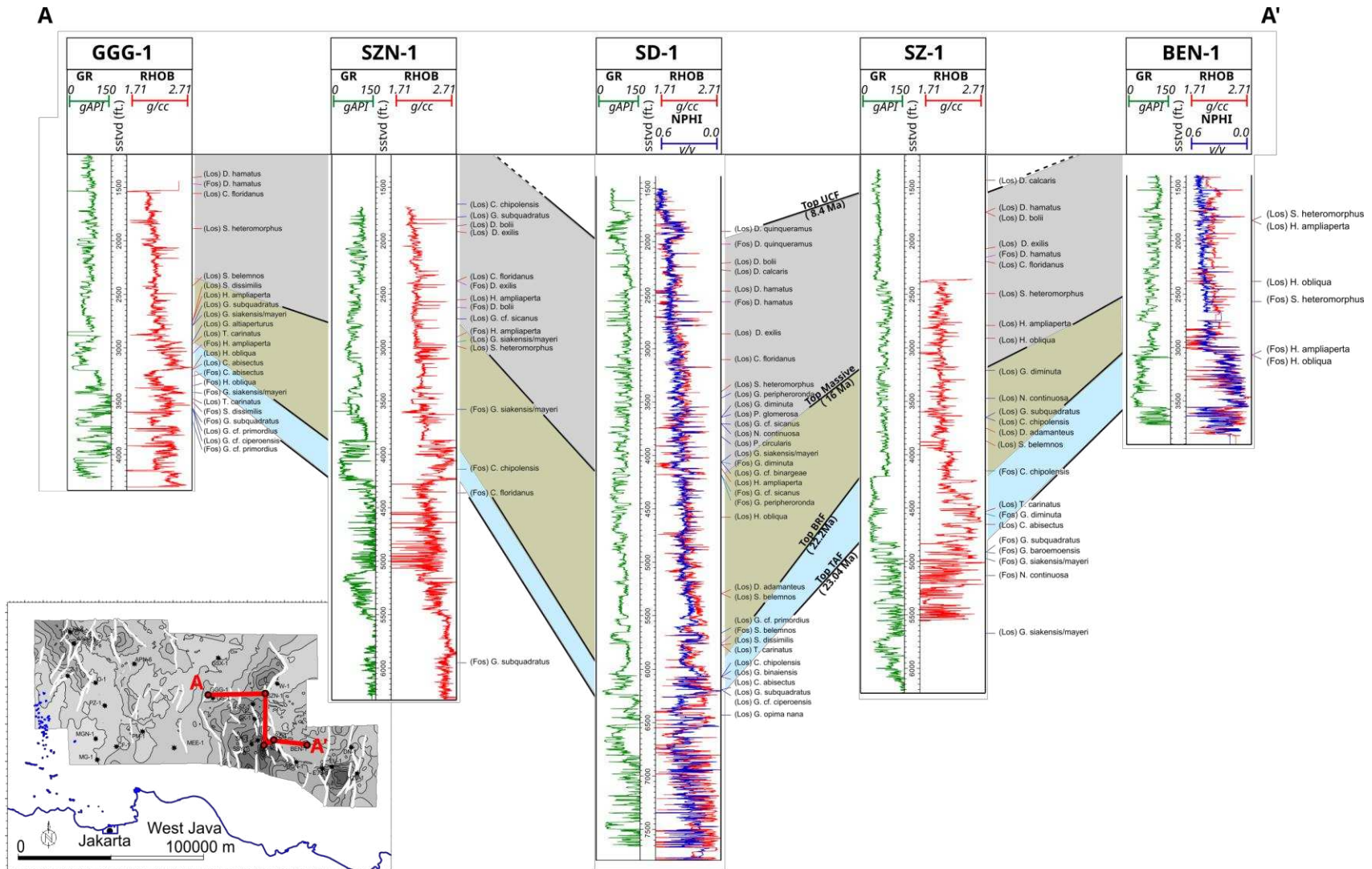


Figure 4.3 Arbitrary well correlation cross-section A showing the available biostratigraphy data. The inset map is basement structure map (see fig 4.4 for the detailed map)

The Massive unit is characterized by the thick progradational sandstone deposition in well SD-1. It is identified by the presence of *H. ampliaperta* (cn), *P. glomerosa* (pf), *G. sicanus* (pf), and *G. diminuta* (pf). Based on these characteristic species, we correlated it with a short-term sea level drop that occurred at the beginning of the Langhian stage (Miller *et al.*, 2020) and tentatively assigned an age of approximately 16 Ma.

The upper boundary of the analyzed interval, which corresponds to the top of Upper Cibulakan Formation (Top UCF), is defined by the emergence of the second carbonate series during the late Tortonian period. In SD-1, this transition occurred at a depth of 612 meters (2007.55 ft), where a shift from an alternation of carbonate and shale to a substantial layer of massive carbonate is evident. This transition is clearly visible in the gamma ray curve, featuring a low gamma ray values. The identified boundary falls between the first occurrence (Fos) and last occurrence (Los) of *D. quinqueramus* (cn), approximately 8.10 Ma to 5.23 Ma, respectively. This boundary might be linked to a brief episode of sea level drop during the late Tortonian period, roughly around 8.4 million years ago. By considering the biomarker correlation with the sea-level curve, a preliminary age estimation of approximately 8.4 million years (Ma) is proposed for the Top UCF (figure 4.3). This age corresponds to the initiation of the global sea-level fall (Miller *et al.*, 2020). Detailed age determination is discussed in chapter 5.

#### 4.2. Well to Well Correlation

Based on the deposition age scheme established in well SD-1, well-to-well correlation was conducted across all available wells (figure 4.4). The initial correlation was carried out along an arbitrary line in the five wells that have biostratigraphic data (line A in fig. 4.4). In correlation line A, the Baturaja Formation (from Top TAF to Top BRF) can be easily distinguished by its low gamma ray log and blocky appearance. The base of the Baturaja Formation (Top TAF) is characterized by the presence of Los *C. abisectus* (cn) (GGG-1, SD-1, and SZ-1), indicating that the onset of Baturaja carbonate growth occurred within a relatively similar timeframe (approximately 23.04 Ma). In well GGG-1, the occurrence of Los from *G. altiapertura* (pf) and Los from *T. carinatus* (cn) also suggests the top BRF deposition age is relatively consistent with the one proposed in well SD-1 (approximately 22.2 Ma). The presence of characteristic species indicating the deposition age in well GGG-1 is significant because the

location of well GGG-1, situated in a basement high area, further supports the understanding that the BRF development in the study area occurred within a similar timeframe.

Correlating the Top Massive proved to be challenging because initially, the massive unit was defined as a lithostratigraphic unit where there was a thick-enough sandstone bed at the beginning of the UCF deposition. The available biostratigraphic data in the five wells along well to well cross-section A (figure 4.4) also indicate confusing deposition ages. For example, in well GGG-1, the presence of *H. obliqua* (Los and Fos) below top TAF marker suggesting the possibility of sample mixing during drilling operation. Regarding the distribution of taxa species, we favored the species identification within side-wall cores against the ones from ditch cuttings, which could potentially involve sample mixing.

We placed the Top Massive marker in well SZN-1 in a position that appears younger than the Los of *S. heteromorphus* (Los at 13.5 Ma) and Los of *G. Mayeri* (Los at 10.46 - 11.63 Ma). Although both of these species indicate a relatively younger age, the presence of Los *G. cf. sicanus* and Fos *H. ampliaperta* suggests an age relatively consistent with the interpretation in well SD-1 (16 Ma). Therefore, we retained the marker in that position. The Top Massive marker in well GGG-1 is placed above Los *S. belemnos*, in well SZ-1, it positioned near Los *G. diminuta*, while in BEN-1, it was situated close to Los *H. obliqua* and within the range of Los and Fos *S. heteromorphus*. The presence of these species supports the interpretation of the age of the Top Massive as approximately 16 Ma (figure 4.3).

To correlate the Top UCF marker, the presence of Los *D. calcaris* in well SZ-1 can strengthen the interpretation of the age in SD-1 (8.4 Ma). However, in wells other than SZ-1, there is no biostratigraphic data analyzed in this interval. Therefore, the correlation of the Top UCF relies entirely on wireline logs, characterized by the base of carbonate deposition in the Parigi Formation.

After establishing the correlations and deposition ages in the five wells with biostratigraphic data, we continued to correlate each marker in all the wells. This was achieved by using three north-south-oriented correlation lines (NS-1, 2, and 3 in figure 4.4) and three east-west-oriented correlations (EW 1, 2, and 3 in figure 4.4).

In the North – South correlations (figure 4.5, 4.6 and 4.7), a relatively significant thickening pattern is observed within the TAF interval (figure 4.5). This pattern characterizes how the rifting tectonics during the TAF deposition controlled the distribution of TAF

sedimentation. However, a different pattern is evident in the younger formations compared to the TAF, as they show less significant variations in thickness, suggesting that the rifting activity had weakened or ceased. An anomaly in the wireline log of well SK-1 (indicated by a flat gamma-ray response and left-shifting of NPHI RHOB) at a depth of 1219.2 – 1524 m (4000 – 5000 ft) is attributed to the well intersection with a normal fault at that depth, leading to the apparent disappearance of the BRF in well SK-1 (fig 4.5). In areas distant from the boundary fault, as represented by the NS 2 correlation line (figure 4.6), the thickness of each formation remains relatively consistent from north to south. However, at the western area, as shown by the NS 3 correlation (figure 4.7), thickening of the TAF is also evident in wells NI-4, AAA1, and Z-1. This indicates that this area is also influenced by normal faulting, which resulted from the rifting during the deposition of the TAF.

The significant differences in thickness are clearly visible in the east-west well correlation profiles (figure 4.8, 4.9, 4.10). Particularly, substantial thickening can be observed in wells located in the depocenter (SD-1 and SH-1) (figure 4.9). These cross-sections reveal the development of two sub-basins within the study area: the Asri sub-basin, represented by wells NI-4, AAA-1, and Z-1, and the Ardjuna sub-basin, represented by wells SH-1, SD-1, SK-1, and SZ-1. The highest well location is well O-1. In this well, the TAF and BRF formations did not develop or are absent, resulting in direct contact between the UCF and the basement (figure 4.10).



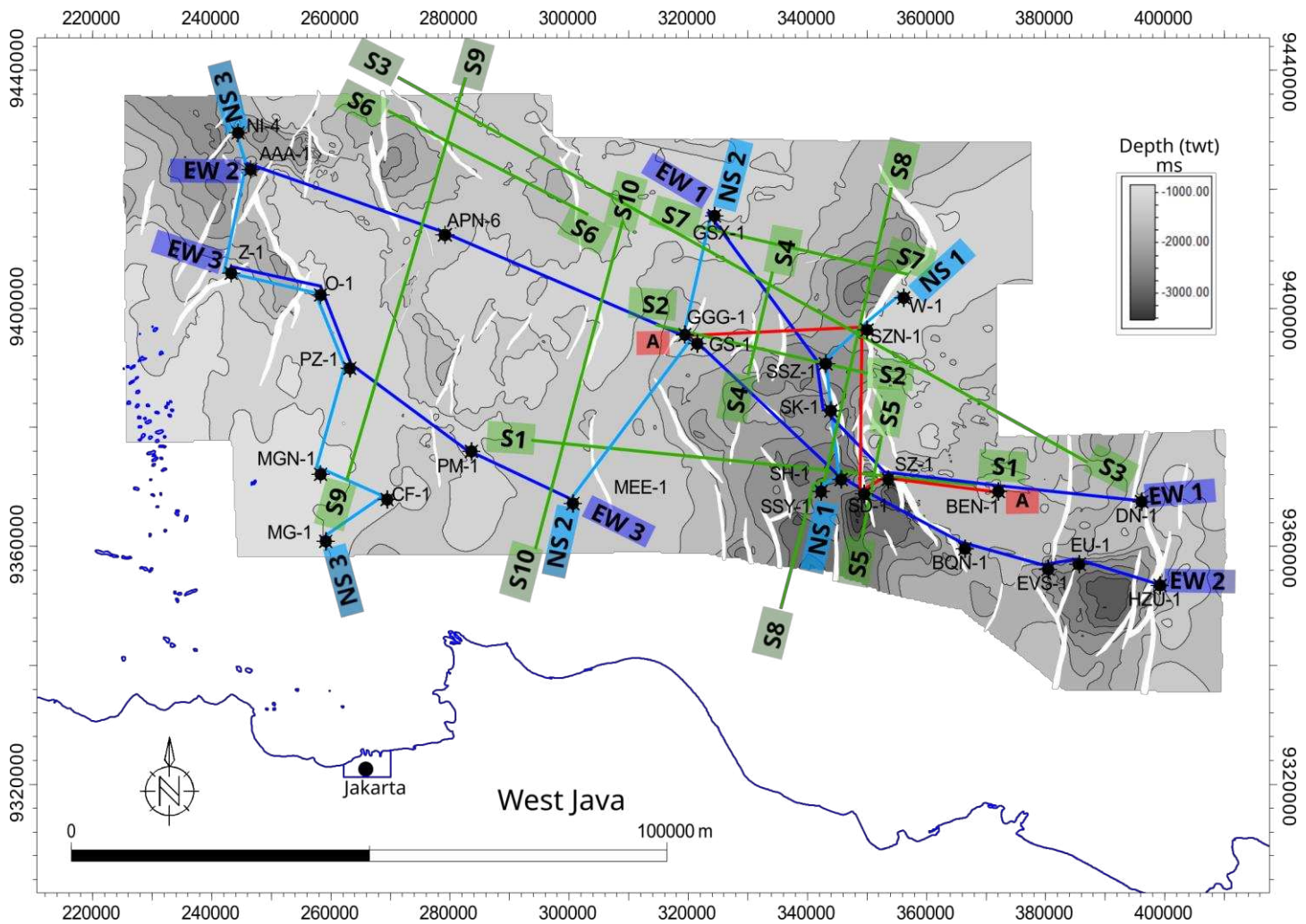


Figure 4.4 Well to well correlation line and selected seismic base map used in this report. The map in the background is seismic interpreted basement map.

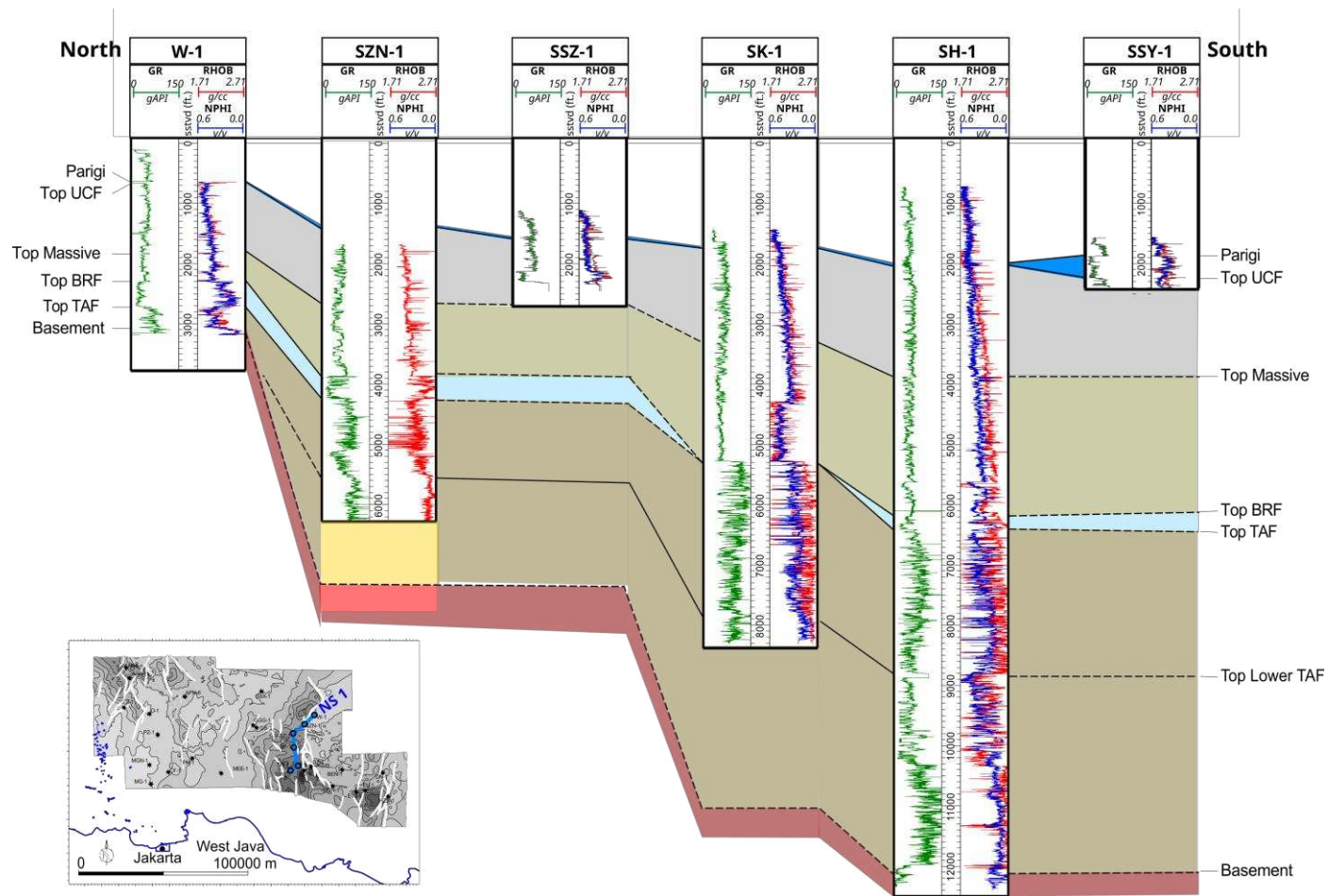


Figure 4.5 North South correlation (NS 1 line in fig 4.4)



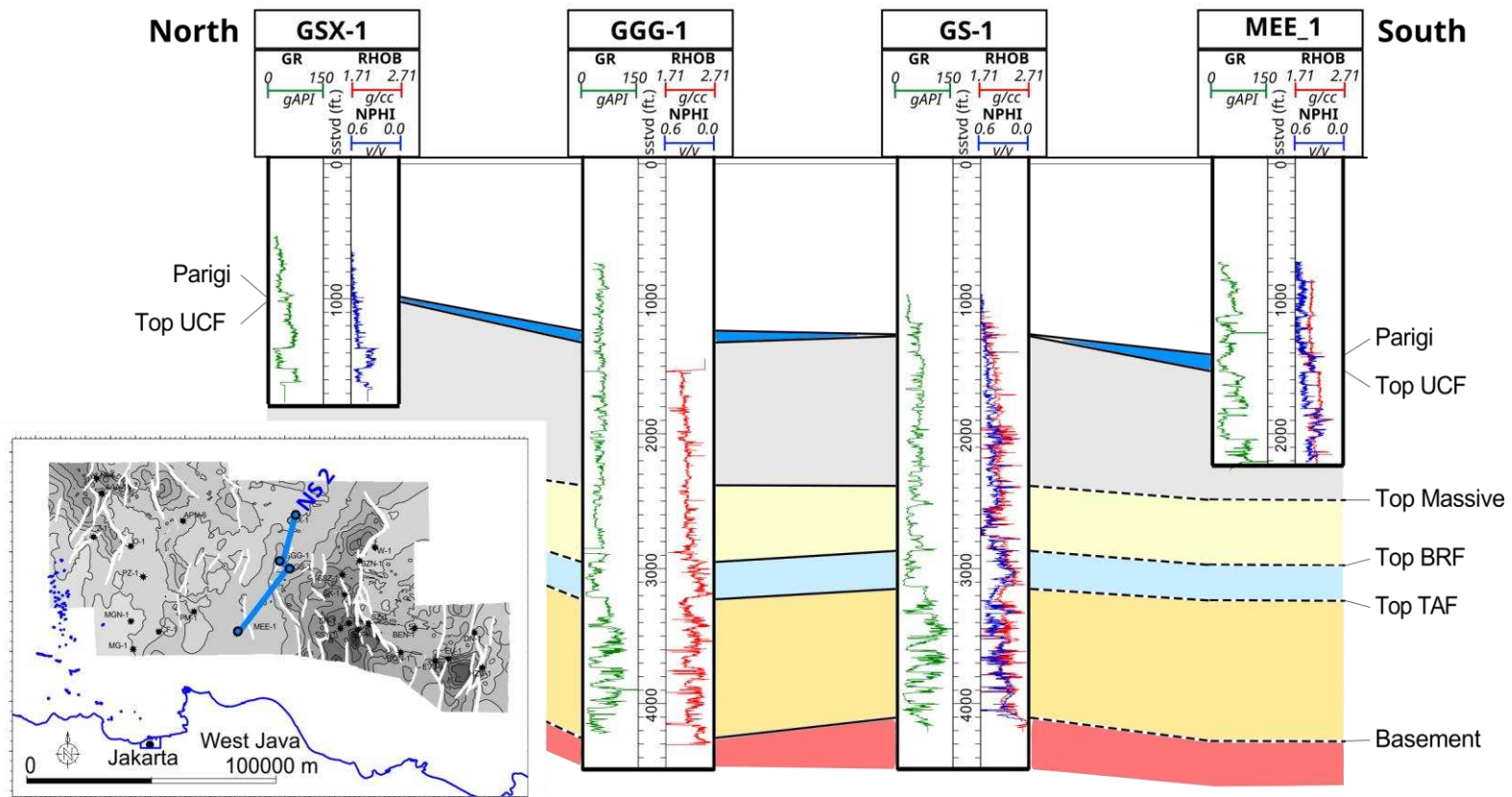


Figure 4.6 North South correlation (NS 2 line in fig 4.4)

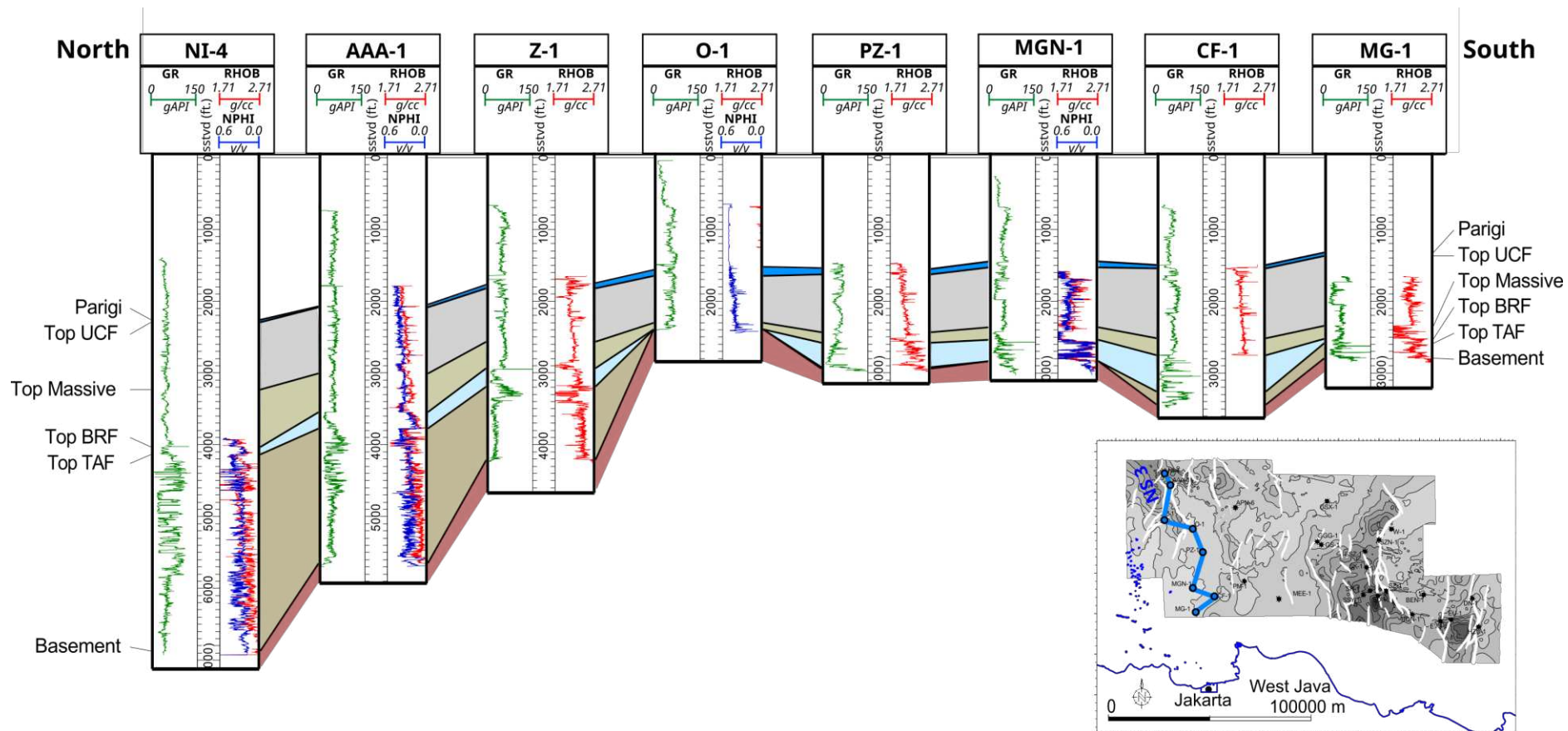


Figure 4.7 North South correlation (NS 3 line in fig 4.4)

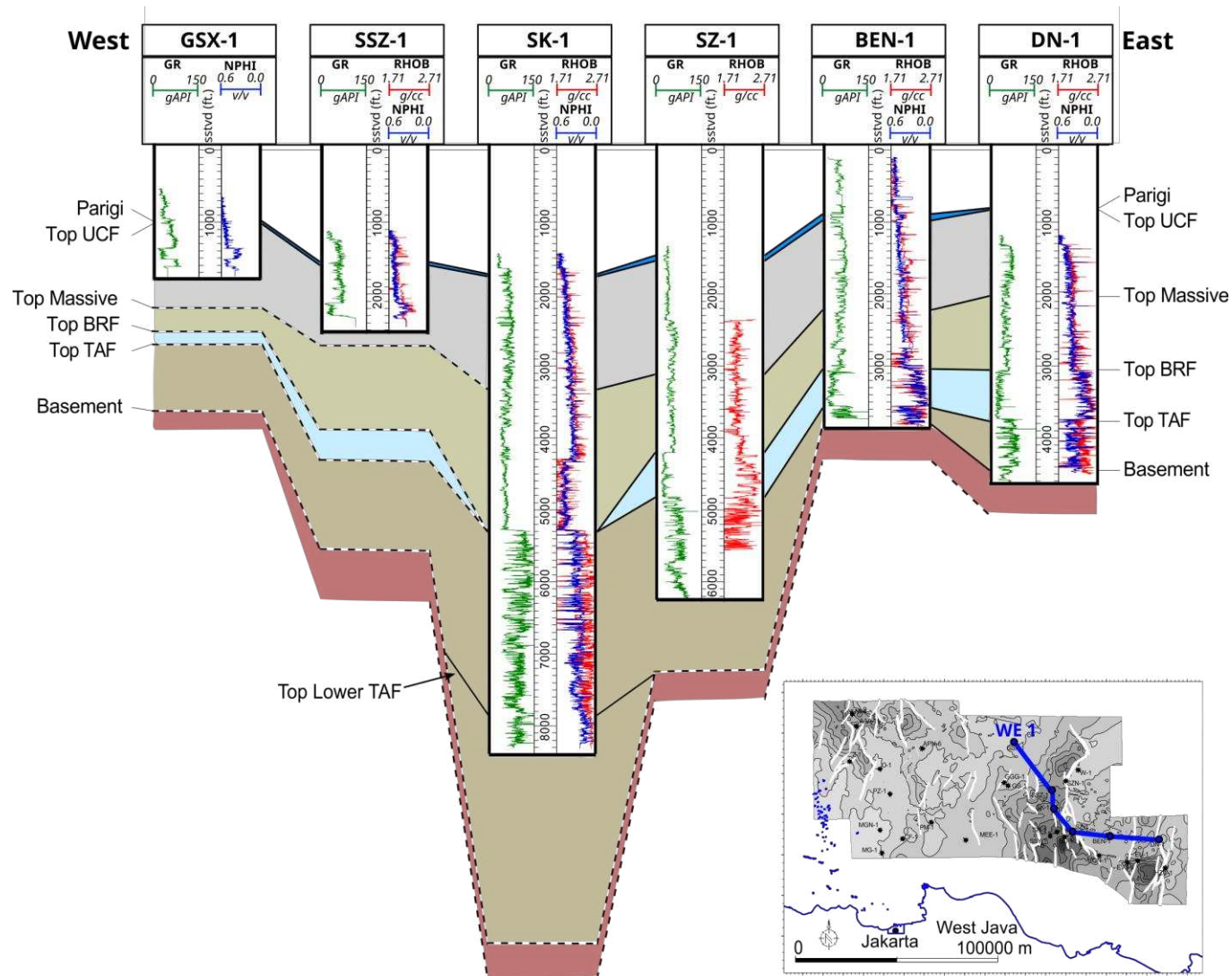


Figure 4.8 West East correlation (WE 1 line in fig 4.4)

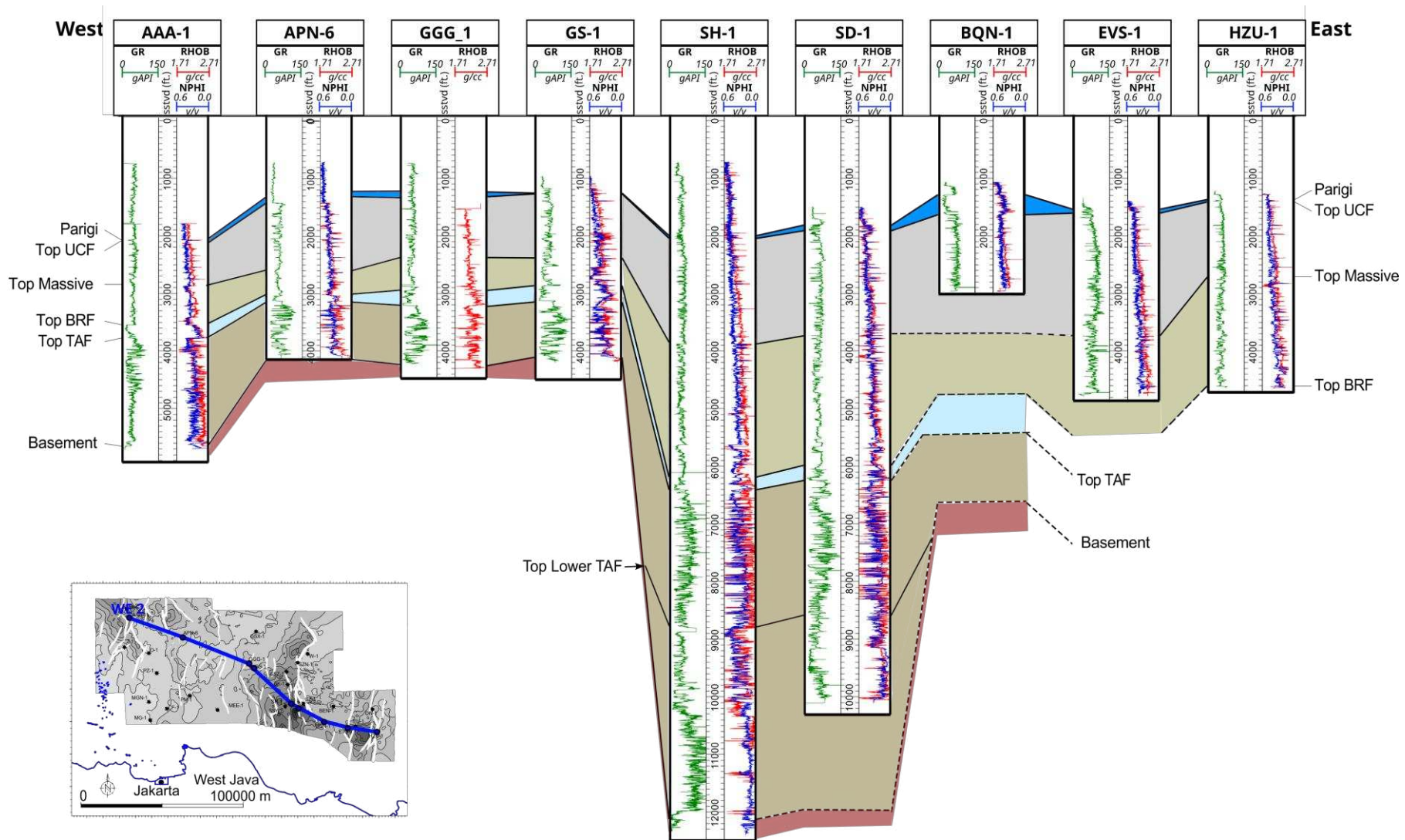


Figure 4.9 West East correlation (WE 2 line in fig 4.4)



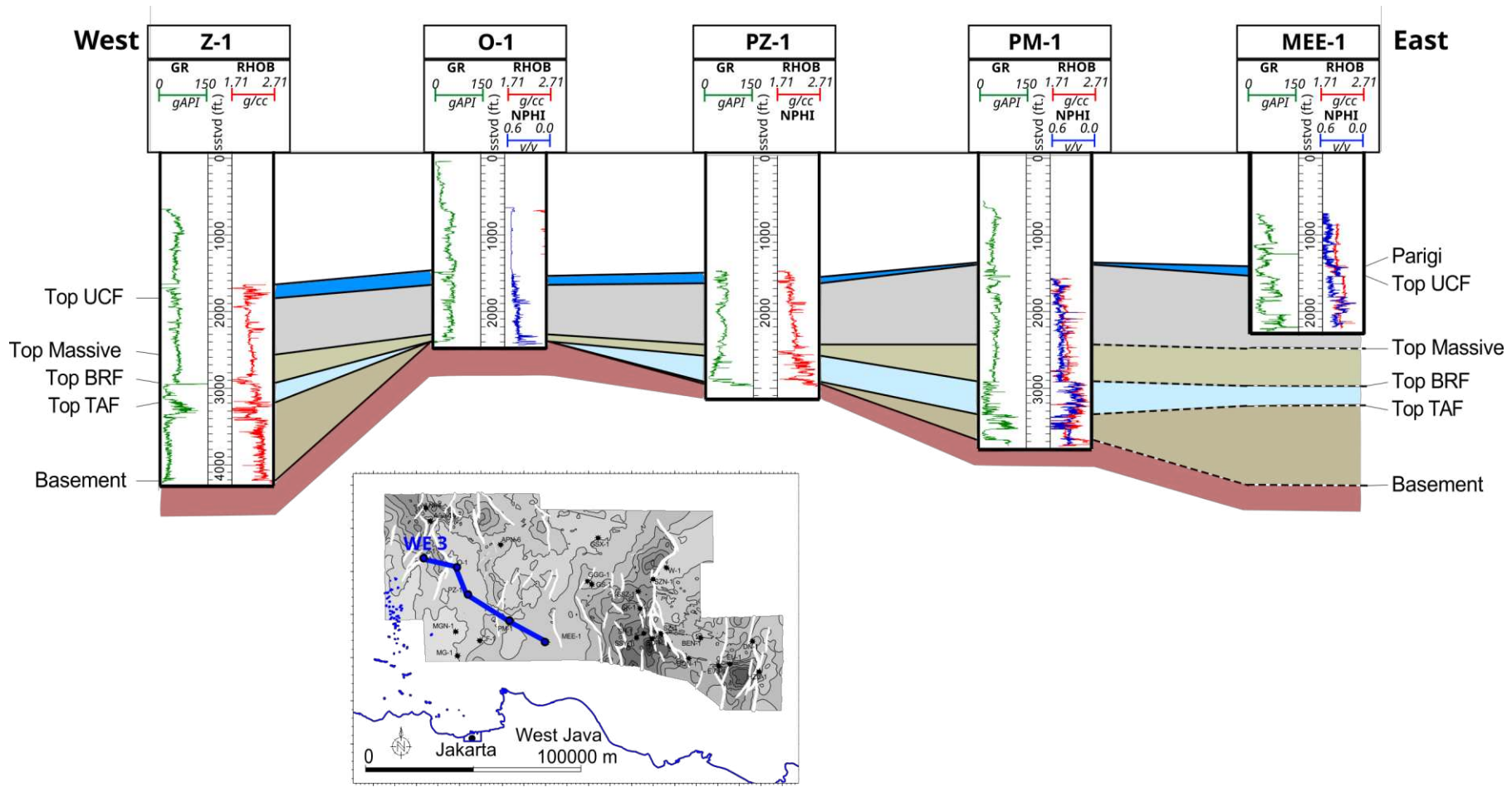


Figure 4.10 West East correlation (WE 3 line in fig 4.4)

### 4.3. Seismic interpretation

#### 4.3.1. Well to Seismic Ties

Based on the analysis of well-to-seismic ties using available checkshot data (figure 4.11), it can be determined that, in general, the basement horizon typically aligns with the initial seismic troughs following a chaotic interval on the deeper seismic zones, which serves as a distinctive marker for the basement itself. The top of the TAF and UCF horizons are likewise associated with peak events, while the upper boundaries of the BRF and Parigi formations are consistently observed at seismic troughs (table 4.4, figure 4.12, 4.13). The straightforward identification of these five seismic events across all seismic sections can be attributed to the lithological difference present in the rock layers. These disparities are particularly evident when transitioning from the basement to the TAF, TAF to BRF, BRF to UCF, UCF to Parigi, and Parigi to Cisubuh. The sharp contrasts in lithology offer a clear distinction between these seismic horizons. Furthermore, the horizontal consistency exhibited by these five primary seismic horizons increase the confidence in the accuracy of our seismic interpretations. The good established continuity of these horizons provides a robust foundation for our broader geological and stratigraphic analyses.

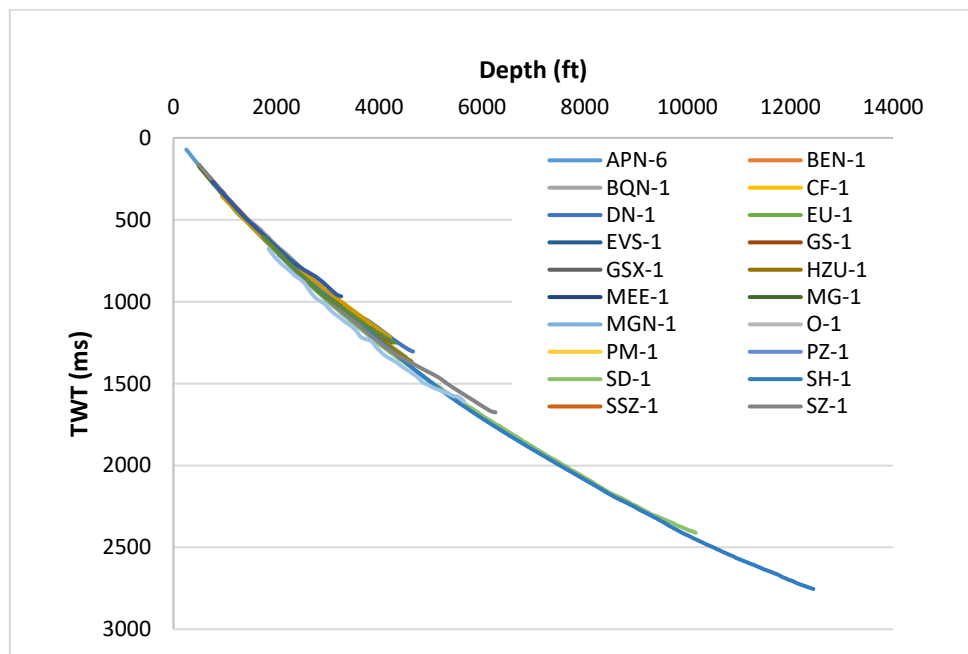


Figure 4.11 Available check shot data used for well to seismic ties

The UCF is divided by two stratigraphic units, Massive unit at the lower part and Main unit in the upper part. Interpreting the top Massive unit horizon was challenging due to the less distinct seismic horizon continuity. The lithology compositions that make up UCF does not exhibit significant variations, the Massive unit comprises shale with slightly thicker sandstone layers, while the Main unit consists of shale with less sandstone with limestone intercalation. The similar lithology of its constituents results in less contrasting seismic impedance differences, which makes the interpretation less straightforward. The presence of active faults also raises several questions about the horizon continuity (figure 4.12, 4.13). Nevertheless, the availability of wellbore data across the entire study area and its distribution greatly aids in the interpretation of this horizon by providing the correct position near the well data.

Table 4.4 Dominant lithology of major formation and seismic reflectors events tied into the seismic data

Age	Formation	Dominant lithology	Seismic event
Pliocene - Pleistocene	Cisubuh	Shale	<i>Troughs</i>
Late Liocene - Pliocene	Parigi	Carbonate	<i>Peak</i>
Early - late Miocene	Upper Cibulakan	Main Shale with minor sand and carbonate intercalation, in several high area carbonate appear as a reef built up	<i>Troughs</i>
		Massive Shale with thick sandstone layer	<i>Troughs</i>
Late Oligocene - Early Miocene	Baturaja	Carbonate	<i>Peak</i>
Late Eocene? - late Oligocene	Talang Akar	Sandstones, shale, coal and carbonate	<i>Troughs</i>
	Basement		



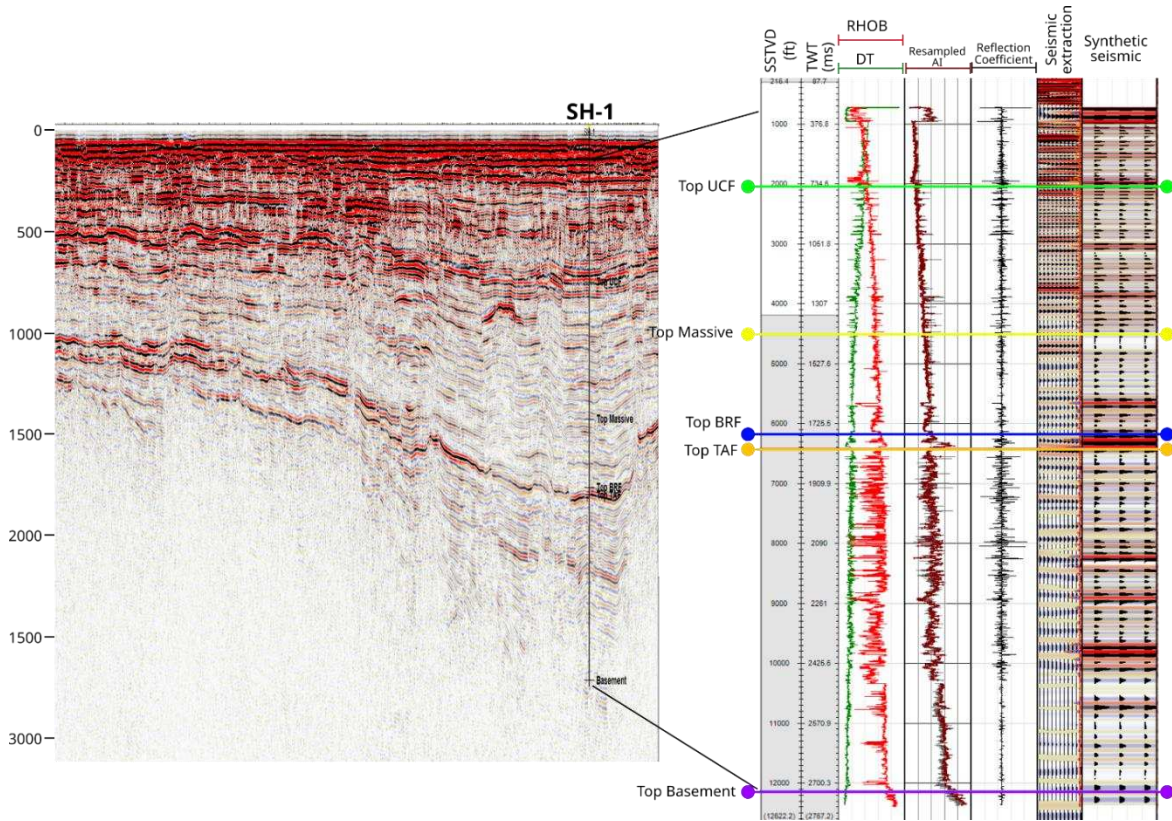


Figure 4.12 SH-1 well to seismic ties analysis (line S1 in fig. 4.4). SH-1 location is 500 m to the south of seismic line.

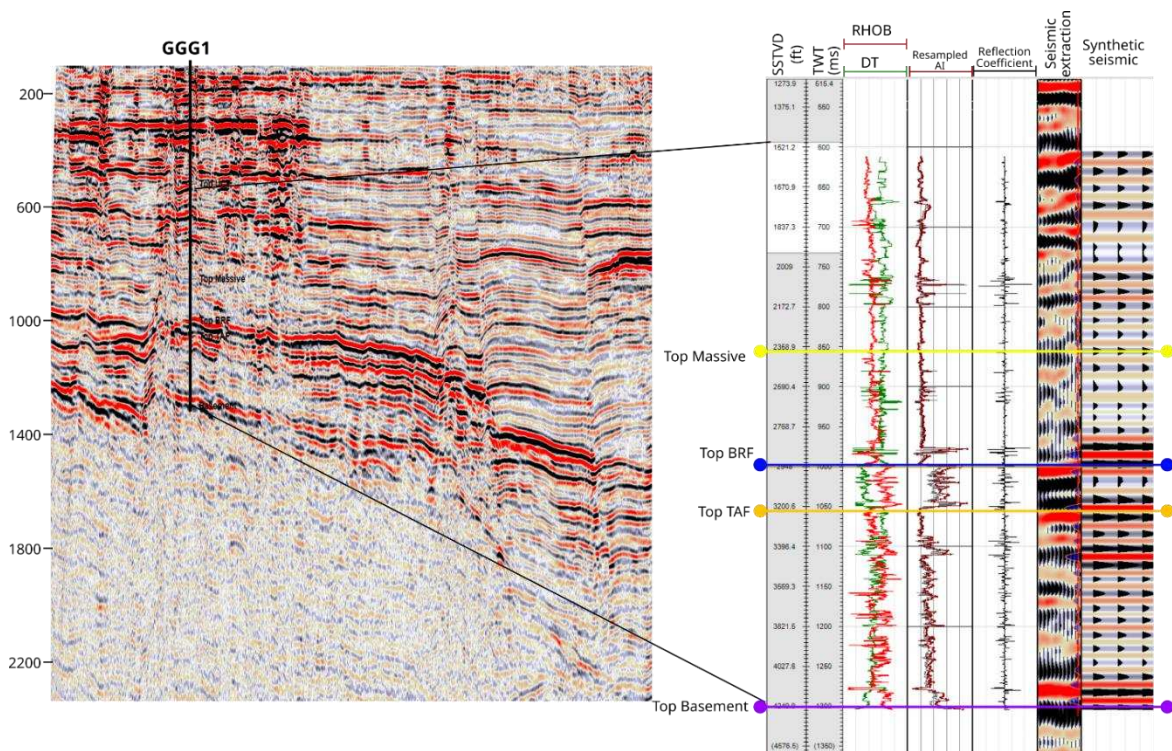


Figure 4.13 GGG-1 well to seismic ties analysis (line S2 in fig. 4.4).



### 4.3.2. Fault interpretation

Structural development of the study area is dominated by series of normal faults with some locally observed folds. In most of seismic sections, faults geometries are characterized by high to moderate dips defining half grabens and horst structures. The structural geology of North West Java Basin can be observed clearly along the NW-SE seismic line (figure 4.14). It is dominated by N-S trending normal fault that was probably related to the Eocene rifting which occurred predominantly at the Ardjuna sub-basin (Hall, 2002; Pubellier and Morley, 2014). The main fault, called Ardjuna fault (Koesoemadinata and Pulunggono, 1974), occurred toward the eastern border of the Ardjuna sub-basin, forming an asymmetric half graben basin (figure 4.15). In figure 4.16, the geometry of each fault intersecting the basement horizon in this area can be observed. It is evident that the morphology of the basement is strongly influenced by the north-south trending faults. These faults, particularly the Ardjuna fault and other major faults, exhibit geometries characterized by horizontally segmented faults separated by a northwest-southeast trending relay zone. The Ardjuna Fault is characterized by west dipping fault segments oriented in the NW-SE and NE-SW directions, indicating that the rifting in this area occurred in multiple events or over imprinted over an inherited structure. These interconnected fault segments collectively form a larger fault zone, which involves the basement to the Parigi Formation, suggesting the fault movement is active until the end of Parigi deposition. This fault shows a displacement of up to 1.5 km (788 ms) in the southern area, progressively decreases towards the north, terminating at the northern end of the research block. To the west of the border fault, several minor isolated faults with opposite dip directions can be observed, which are referred to as antithetic faults.

Combination of progressive faulting and sediment filling during synrift period in this area produce a wedge shaped sediment fill in Talangakar Formation in which the sediment thicken towards Ardjuna fault, decreasing towards younger layer (figure 4.14). In the seismic section (figure 4.14), we can observe variations in basement elevation, with the highest structures located in the western part and the lowest point (depocenter) situated in the central area of the block. Notably, the thickness of sedimentary rocks in the lowest part of the basin can exceed 3800 meters (12,500 ft), as evidenced in well SH-1.

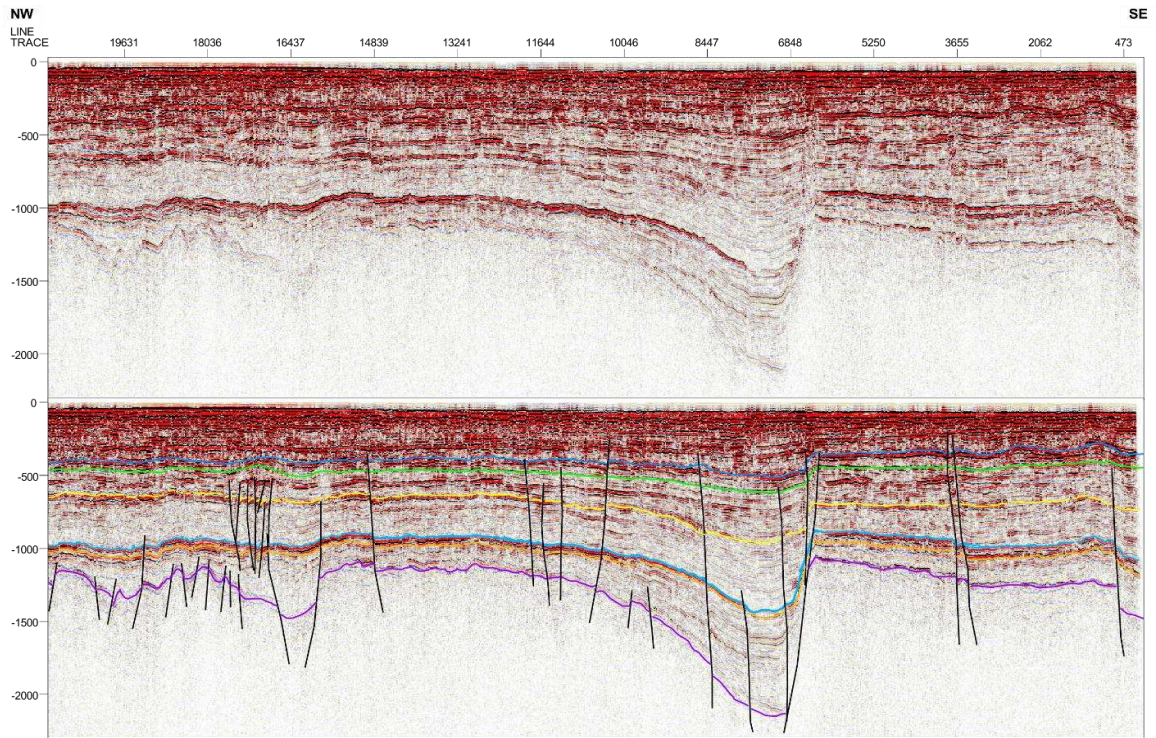


Figure 4.14 Horizon and fault interpretation on NW – SE Seismic line (line S3 in fig. 4.4).

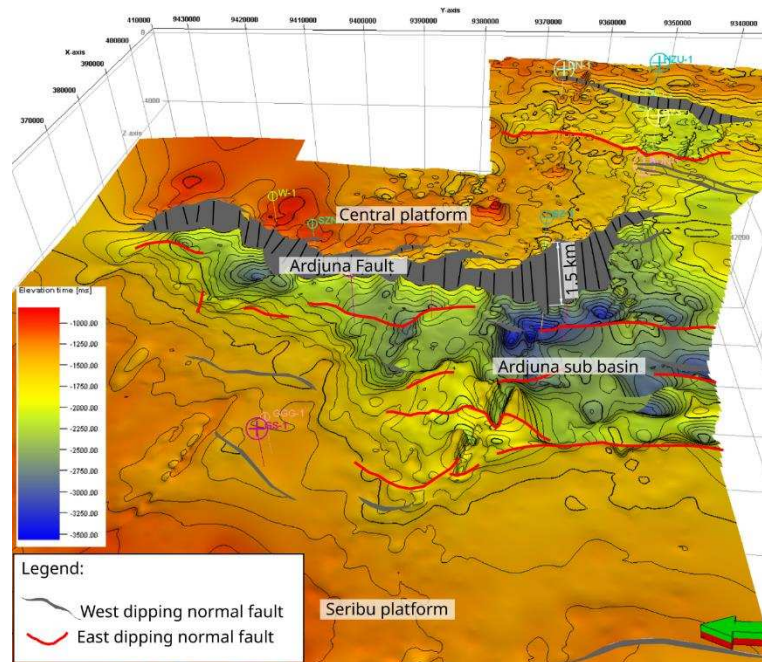


Figure 4.15 3D view of the top basement grid with faults showing the N – S trending normal fault developed in Ardjuna sub basin

### 4.3.3. Horizon Interpretation

The interpreted horizons include top basement, top TAF, top BRF, top Massive, Top UCF, and Top Parigi. The results of horizon mapping are presented in [fig. 4.16 to 4.21](#). Several seismic reflection configuration and termination can be seen in the seismic database and are presented in [figure 4.22](#). The selected interpreted W-E seismic line interpretation can be seen in [figure 4.14, 4.22, and 4.23](#) while the N-S seismic line are presented in [figure 4.24, and 4.25](#).

As mentioned earlier, top Basement is identified at the initial seismic troughs event following chaotic reflector configuration ([figure 4.22](#)). This chaotic seismic facies is consistent in almost all available seismic cross-section data, with exceptions where seismic reflectors multiple indicating pseudo-layers are present in the interval below the seismic interval. For such facies, we disregard these seismic reflectors and rely on well data that penetrate down to the basement and seismic lateral continuity.

Two sub-basins can be distinguished from the basement structure map ([figure 4.16](#)), separated by a basement high area, called Seribu platform ([Koesoemadinata and Pulunggono, 1974](#)) ([figure 4.15](#)). The Ardjuna sub-basin, bounded by Ardjuna fault, is the primary sub-basin located in the North West Java Basin region. The Sunda sub-basin lies to the west of the studied area. Similar to the Ardjuna sub-basin, the Sunda sub-basin is also bounded by a north-south-oriented fault with a westward dip direction. Sunda sub-basin features greater depth to the west of the studied area, which is not covered by the current dataset.

The thickness of the Talangakar Formation indicates up to 1500 ms in the deepest part of the Ardjuna sub-basin, ranging from 50 to 100 ms in the upthrown area, called Central platform ([Koesoemadinata and Pulunggono, 1974](#)), decreasing to the southwest of the study area (around wells MGN-1 and MG-1) ([figure 4.26](#)). In the Seribu platform and Central platform areas ([figure 4.15](#)), the deposition of the Talangakar Formation is characterized by a parallel to sub-parallel seismic configuration with southward-directed downlap reflector termination ([figure 4.22](#)). In contrast, in the Ardjuna sub-basin, the deposition of the Talangakar Formation is predominantly marked by a divergent seismic configuration, with erosional toplap terminations found at the basin edges and apparent onlap directly adjacent to the basement.

The Baturaja Formation has a maximum thickness of 500 ms in the southeast region, and exhibits relatively homogeneous thickness in the central high area (60 – 100 ms), thinning in the Ardjuna sub-basin ([figure 4.27](#)). The thickness variations are evident in the W-E oriented

seismic section (figure 4.22), where carbonate thickening is observed in the high areas, while in the sub-basin region, this carbonate growth is not apparent. In seismic sections, the upper and lower boundary of Baturaja Formation is characterized by high-amplitude continuous reflectors, with a hummocky seismic configuration in the internal carbonate reef (figure 4.22). In the Ardjuna sub-basin area, the Baturaja Formation can be identified by concordant parallel to sub-parallel reflectors with continuous high amplitude contrast (figure 4.23).

The Massive unit (lower part of UCF) is characterized by a parallel to sub-parallel reflector configuration (figure 4.23), generally exhibiting low to medium amplitudes. In the northern part of the study area, several oblique progradational reflectors with a North-South orientation can be observed, indicating the direction of sediment input during the deposition of the Massive unit (figure 4.22b). Meanwhile, in the downthrown area from the Ardjuna fault, some progradation is also noticeable in the North-South-oriented seismic section. This progradation has a sigmoidal progradational geometry (figure 4.22c). The seismic configuration mapping is discussed further in Chapter 5. The thickness of the Massive unit again shows significant differences between the basin and high areas, reaching 550 ms in the Ardjuna sub-basin and thinning to 80 ms in the Central platform and Seribu platform areas (figure 4.28).

Similar to the Massive unit, the Main unit (upper part of UCF) is characterized by a parallel-sub-parallel reflector configuration (figure 4.22) with medium amplitudes. In the Main unit, progradation is no longer observed, but mounded geometries (figure 4.22) indicative of reef-like carbonate structures can be observed in many places, especially in the southern part of the Ardjuna sub-basin. The total thickness of the Main unit is slightly more uniform compared to the Massive unit below. The average thickness in the Ardjuna sub-basin ranges between 350 and 400 ms, while it is 150 to 250 ms in the high areas (figure 4.29).

The Parigi Formation is characterized by high-contrast amplitudes above the UCF horizon (figure 4.22). Mounded formations are frequently found in the southeastern part of the study area, oriented in a north-south direction. The distribution of carbonate geometries can be easily observed on the thickness map of the Parigi Formation, where there are areas with thicknesses of 150-250 ms exhibiting elongated shapes with the long axis oriented north to south (figure 4.30). In thinner areas, these elongated formations are no longer present. On seismic sections, this area is characterized by a sub-parallel configuration with high amplitudes.



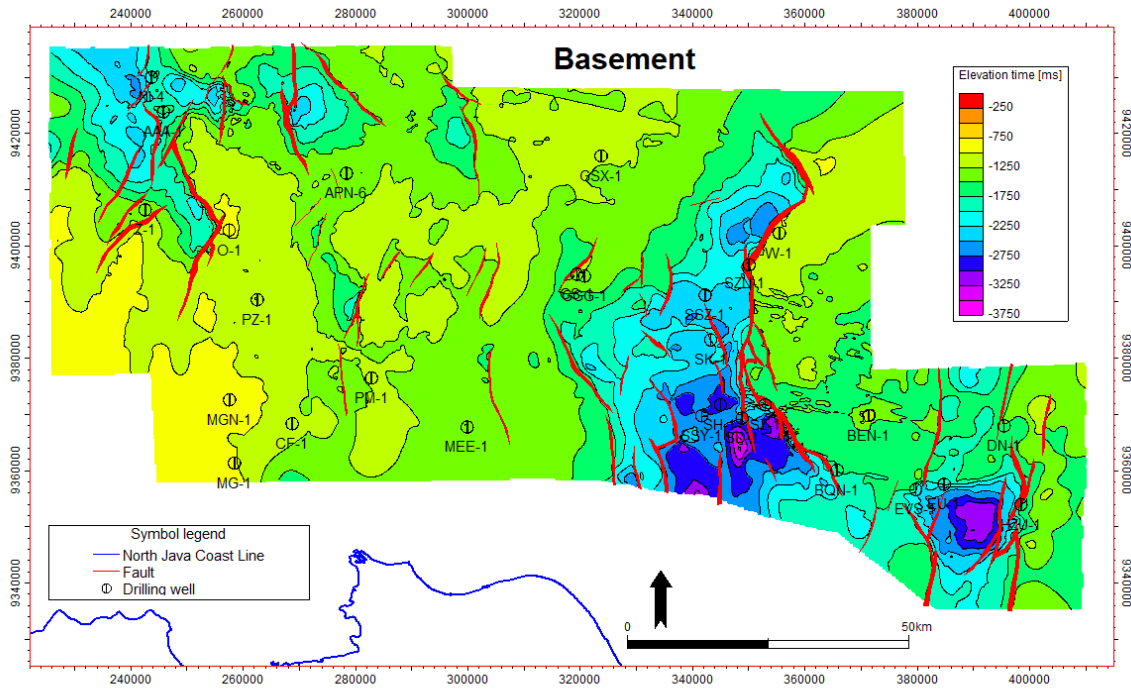


Figure 4.16 Top Basement time structure map

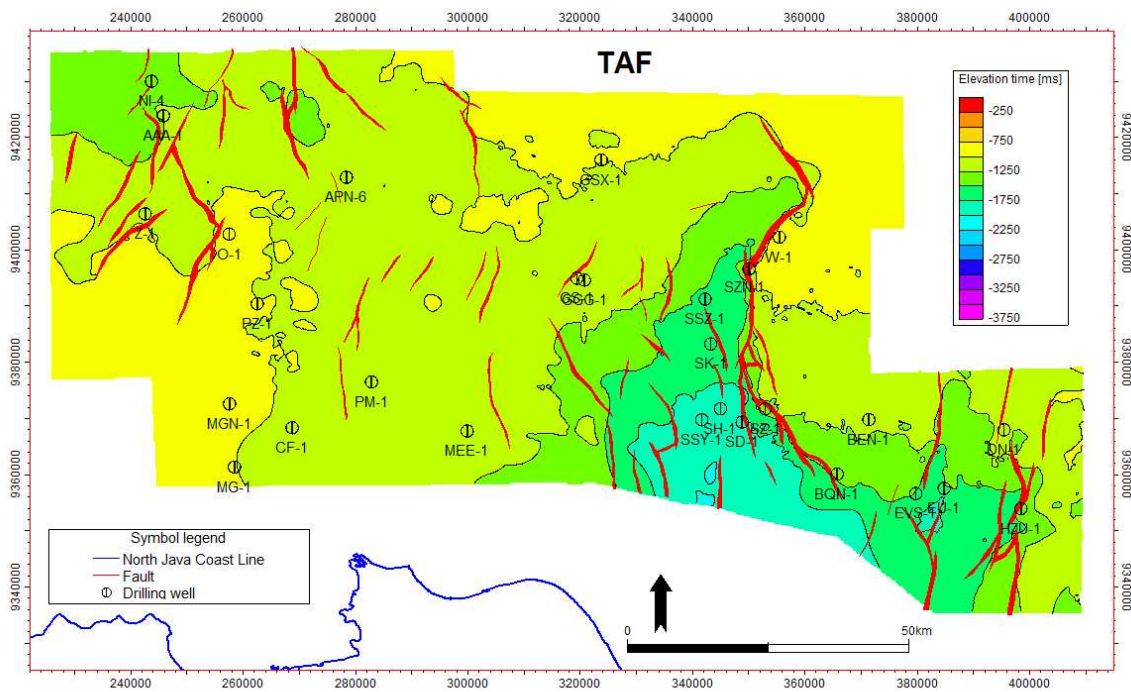


Figure 4.17 Top Talangakar Formation time structure map

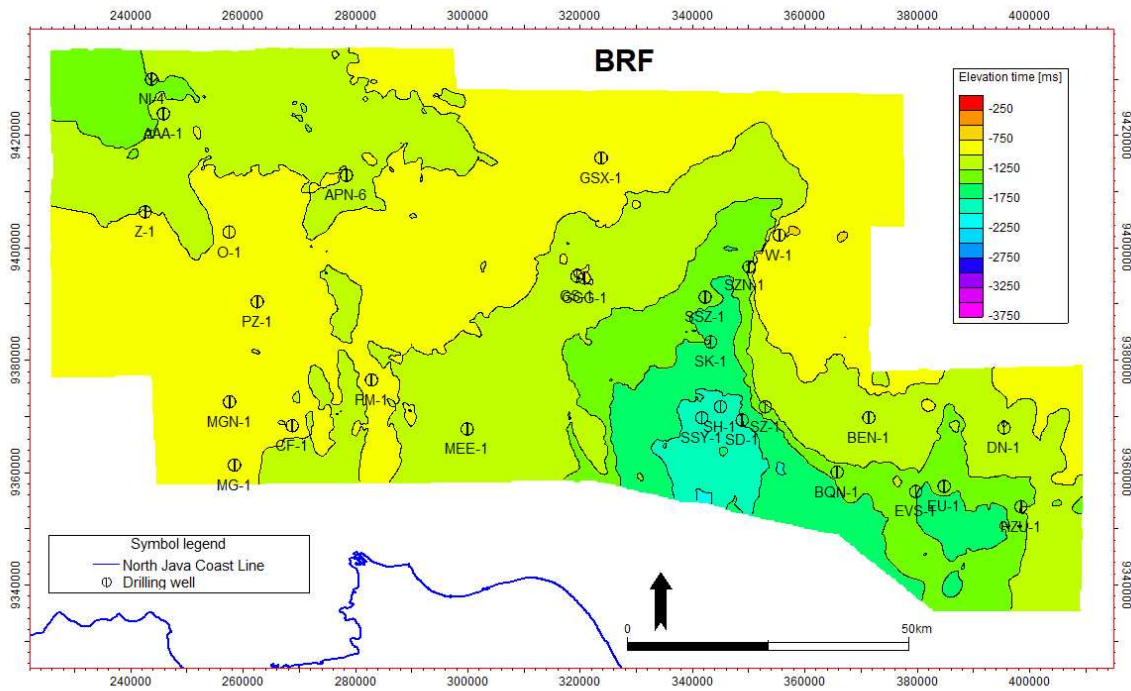


Figure 4.18 Top Baturaja Formation time structure map

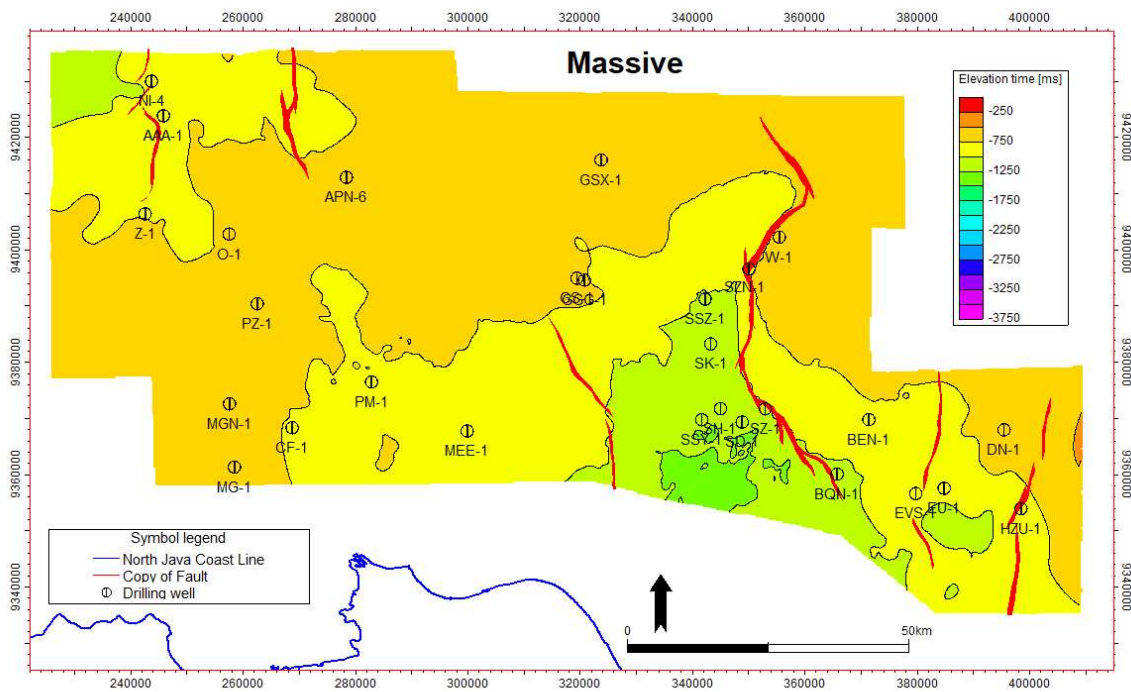
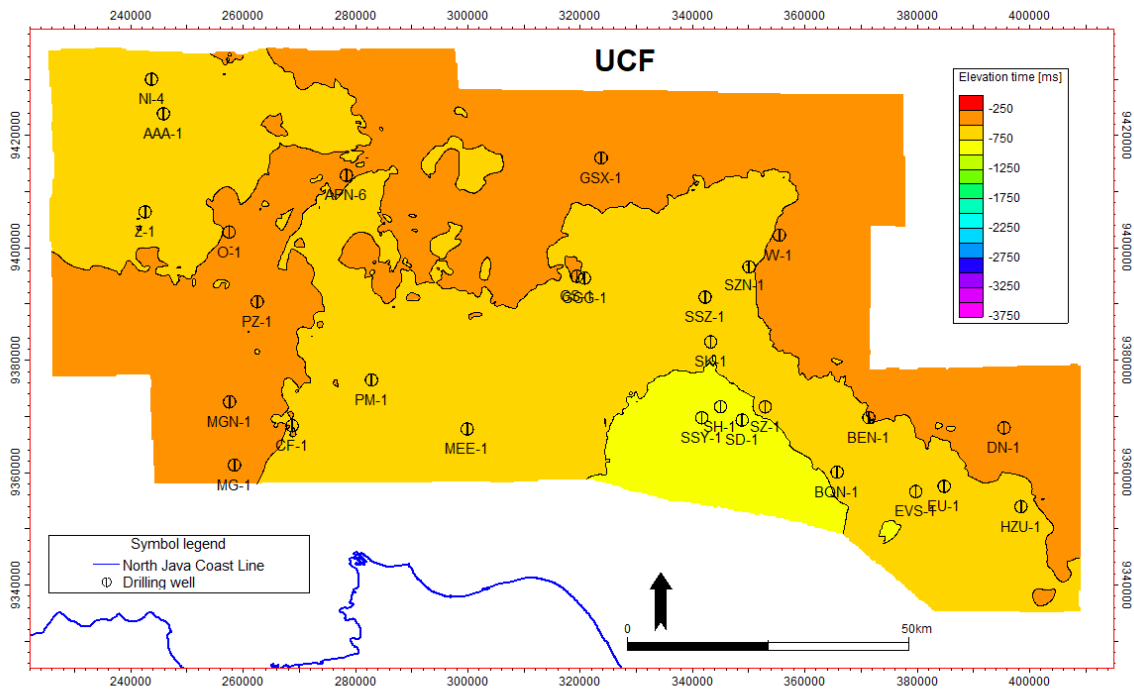


Figure 4.19 Top Massive unit time structure map



10

Figure 4.20 Top Upper Cibulakan Formation time structure map

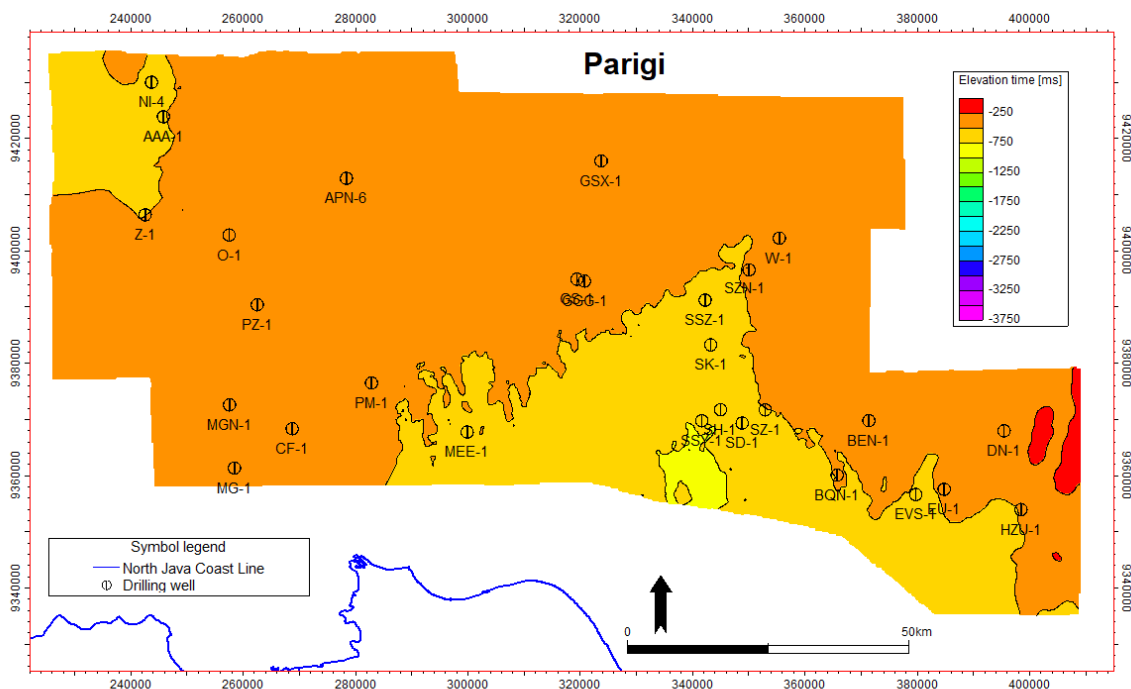


Figure 4.21 Top Parigi Formation time structure map



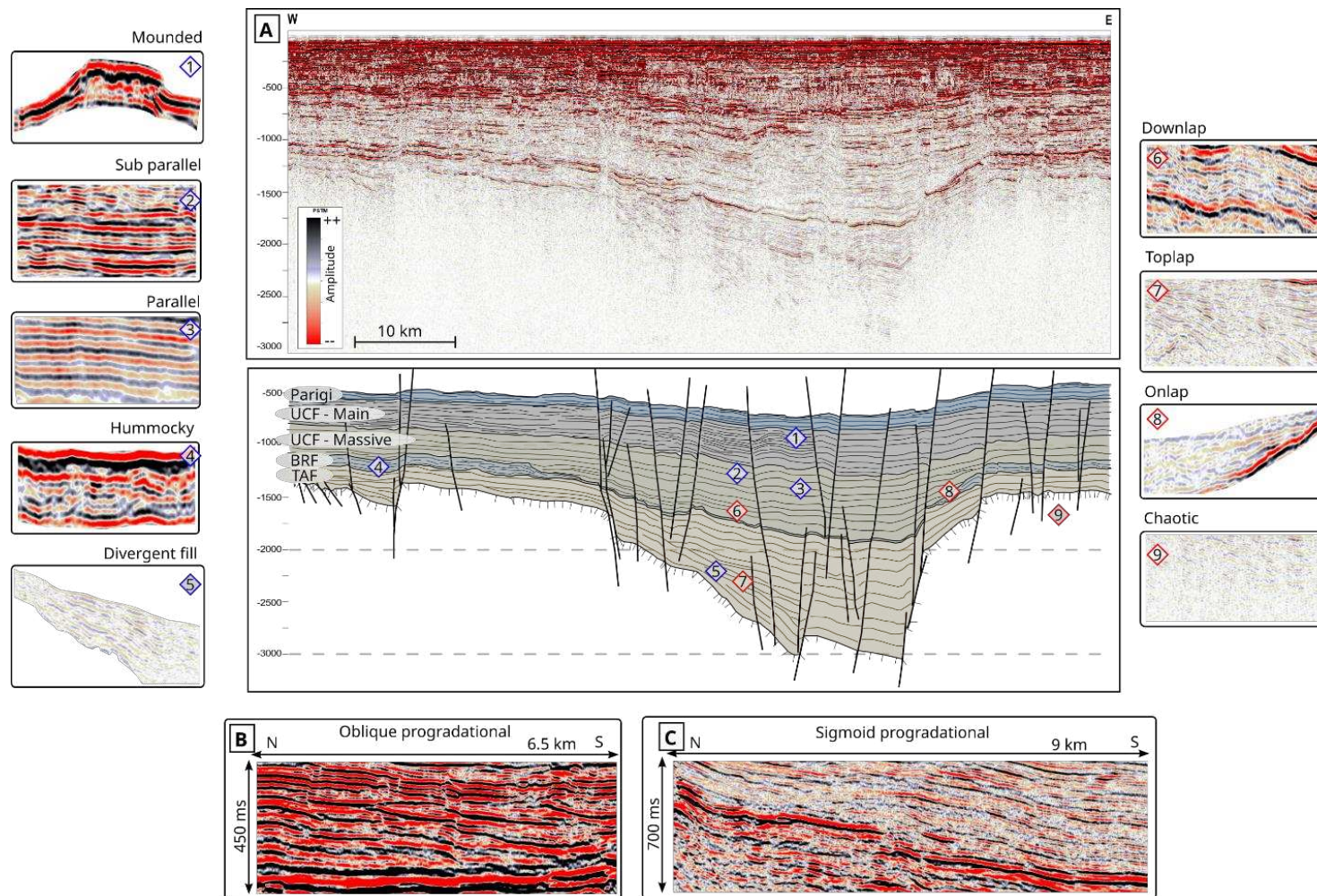


Figure 4.22 A) Un-interpreted (up) and interpreted (down) seismic line S1 showing representative seismic reflection configuration and termination found in the studied area. B) Oblique progradational configuration in line S4. C) Sigmoid progradational in line S5. See fig.4.4 for line location



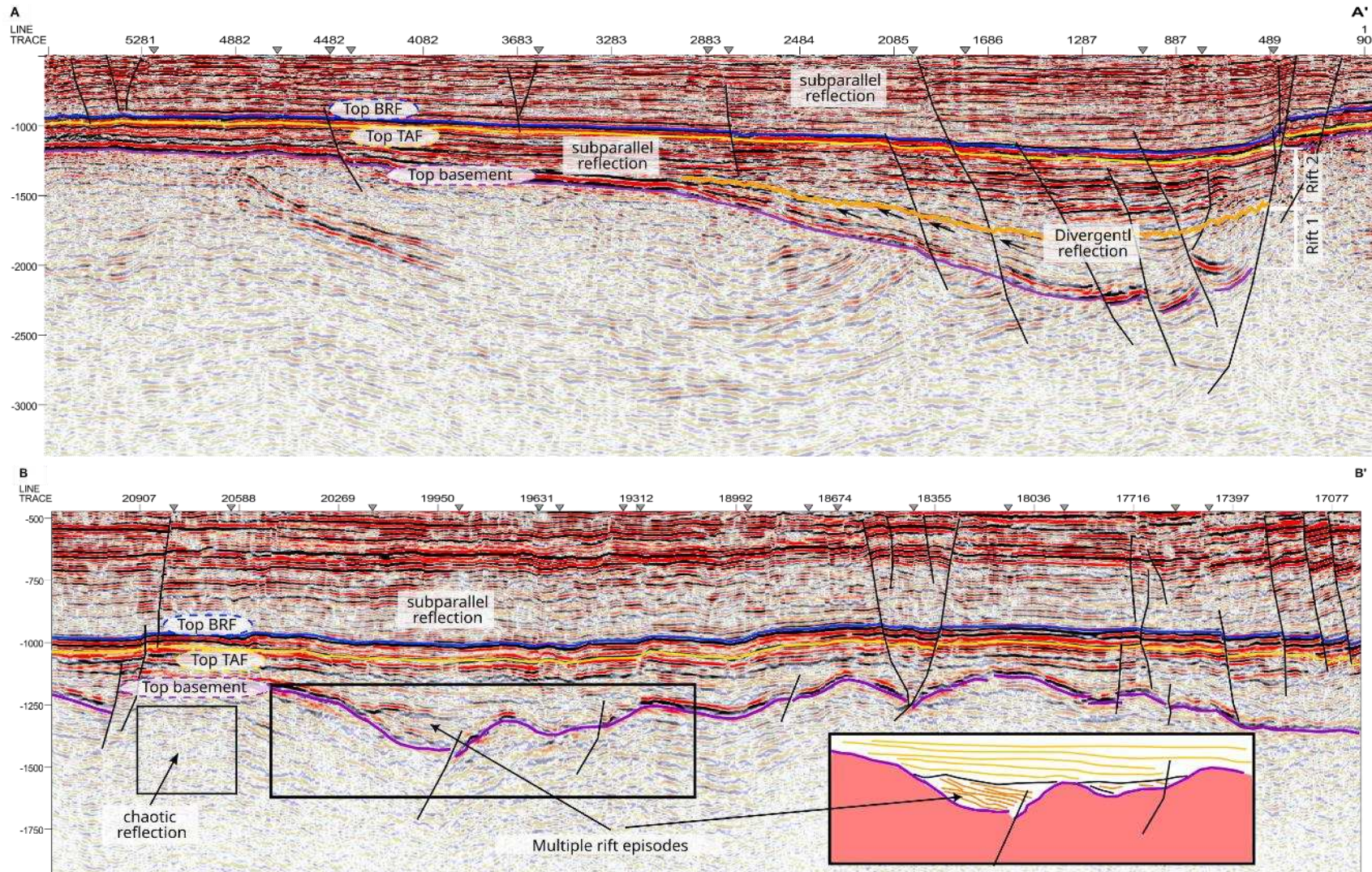


Figure 4.23 2D seismic line S7 (A) and S6 (B) showing dominant seismic configuration in each of the formation. Two rift episodes are identified in Talangakar Formation. See fig.4.4 for line location



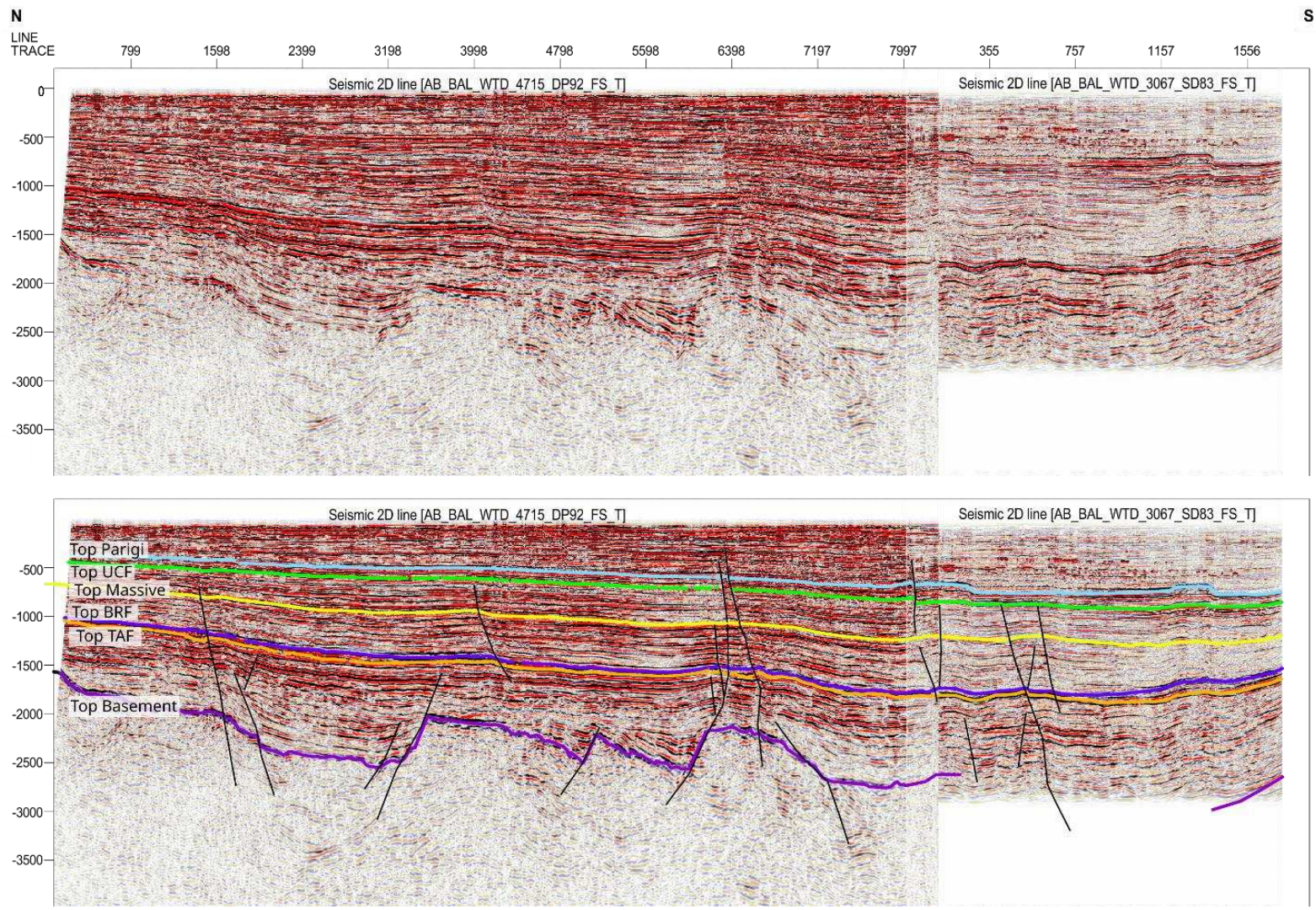


Figure 4.24 Un-interpreted (up) and interpreted (down) N – S seismic line S8 showing seismic interpretation in the Ardjuna sub basin. See fig.4.4 for line location



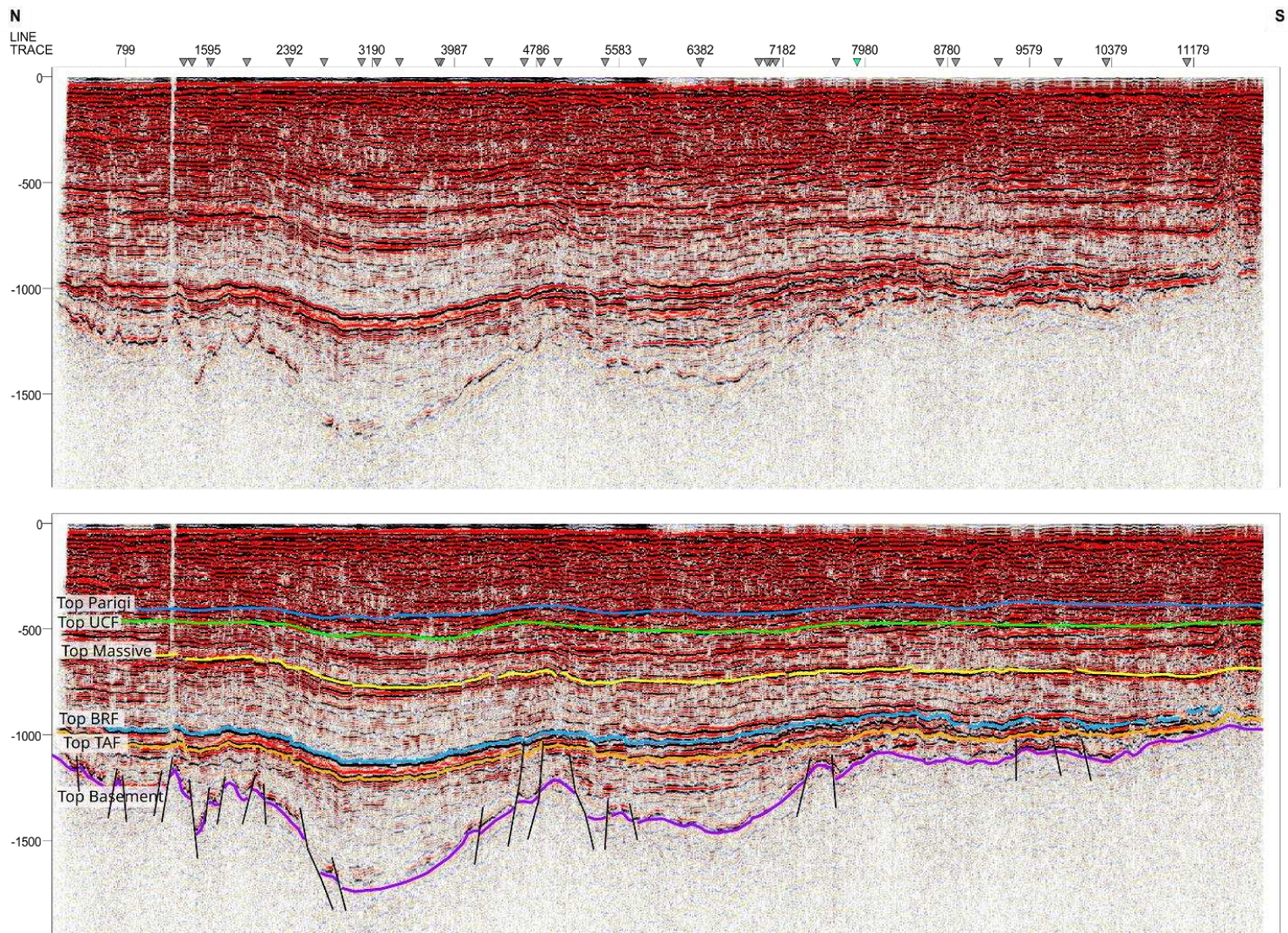


Figure 4.25 Un-interpreted (up) and interpreted (down) N – S seismic line S9 section showing seismic interpretation in the Seribu platform.  
See fig.4.4 for line location



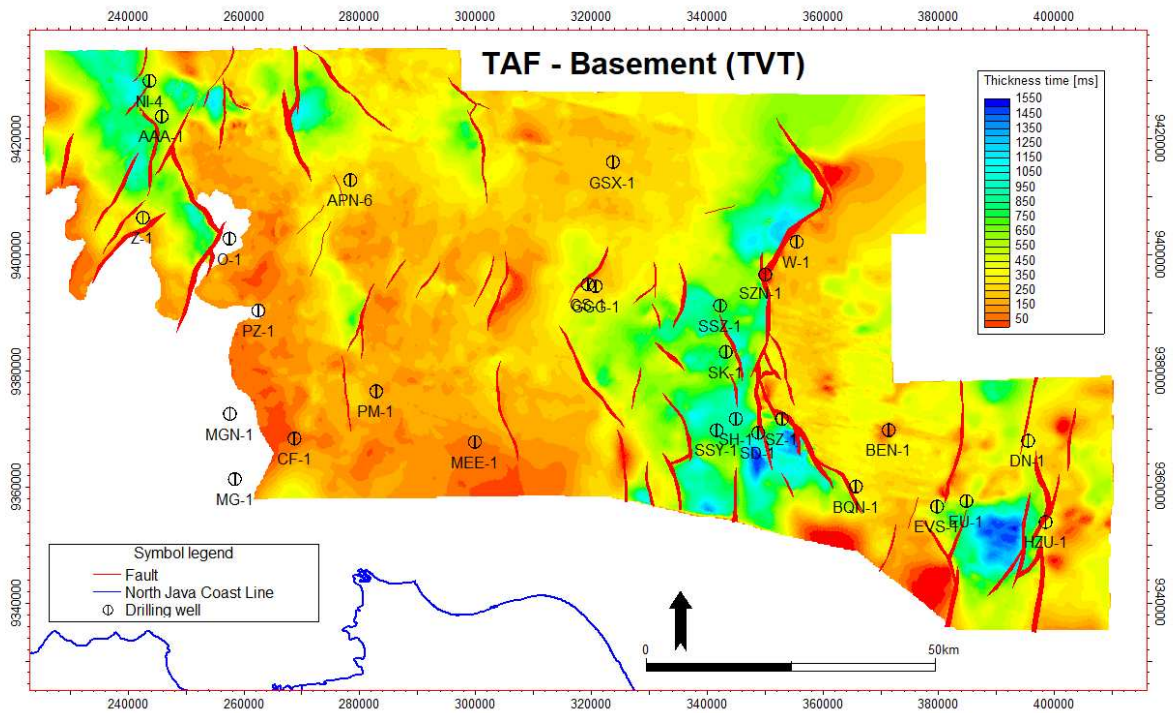


Figure 4.26 Talangkar Formation thickness map derived from seismic interpretation.

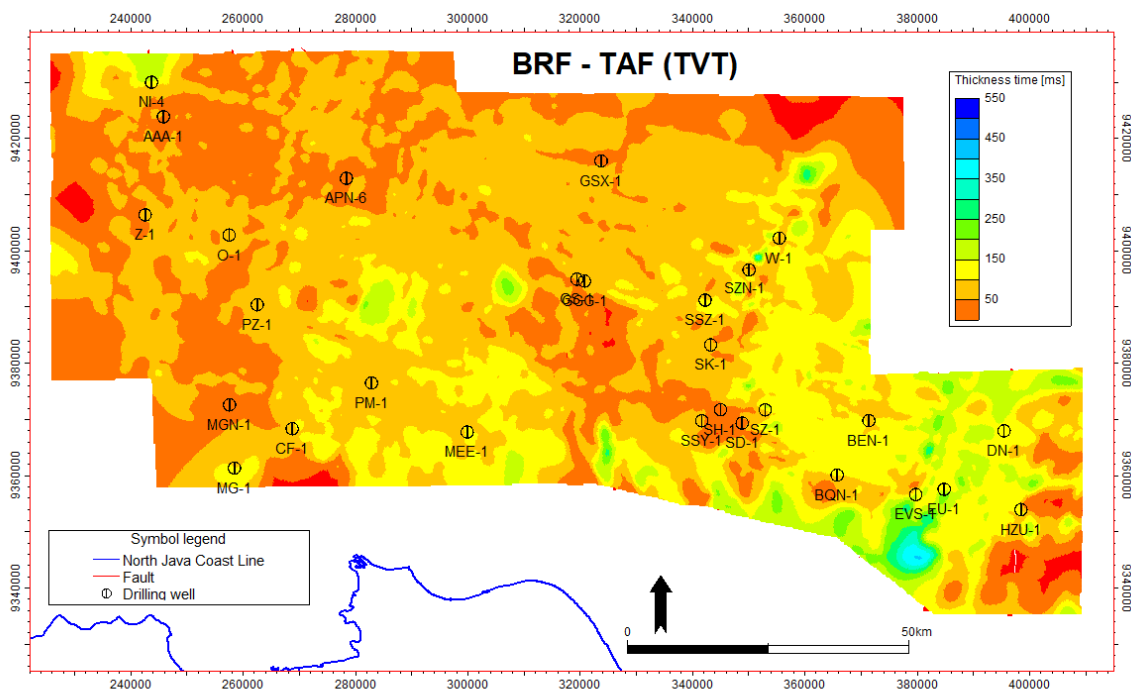


Figure 4.27 Baturaja Formation thickness map derived from seismic interpretation.

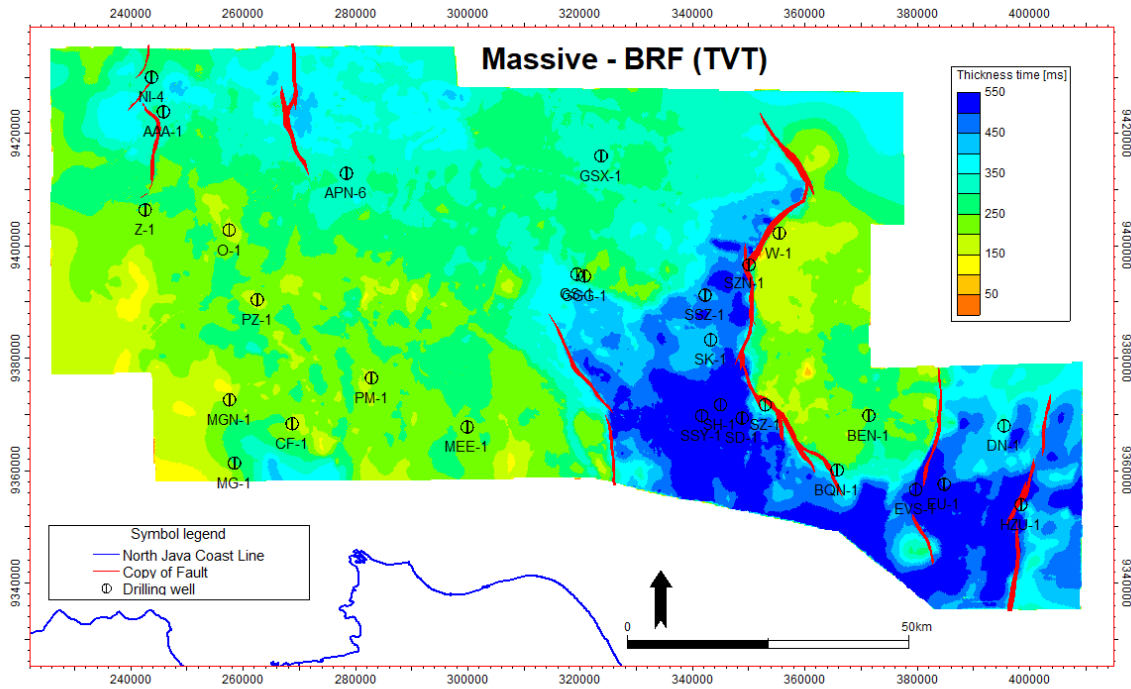


Figure 4.28 Lower part of Upper Cibulakan Formation (Massive unit) thickness map derived from seismic interpretation.

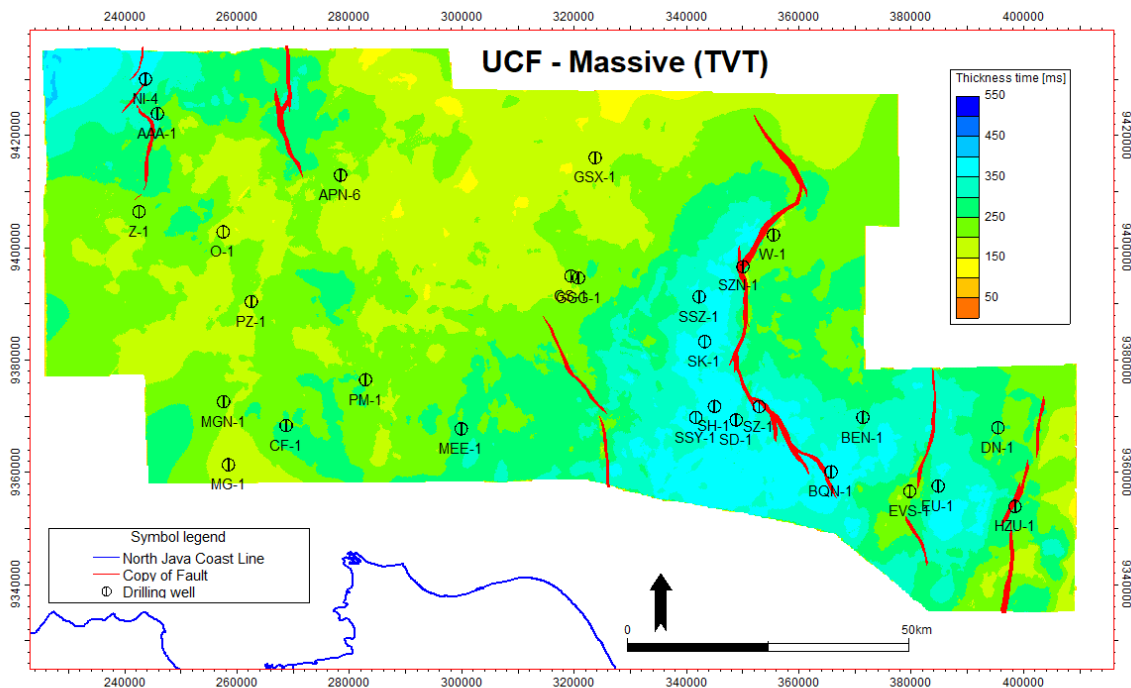


Figure 4.29 Upper part of Upper Cibulakan Formation (Main unit) thickness map derived from seismic interpretation.

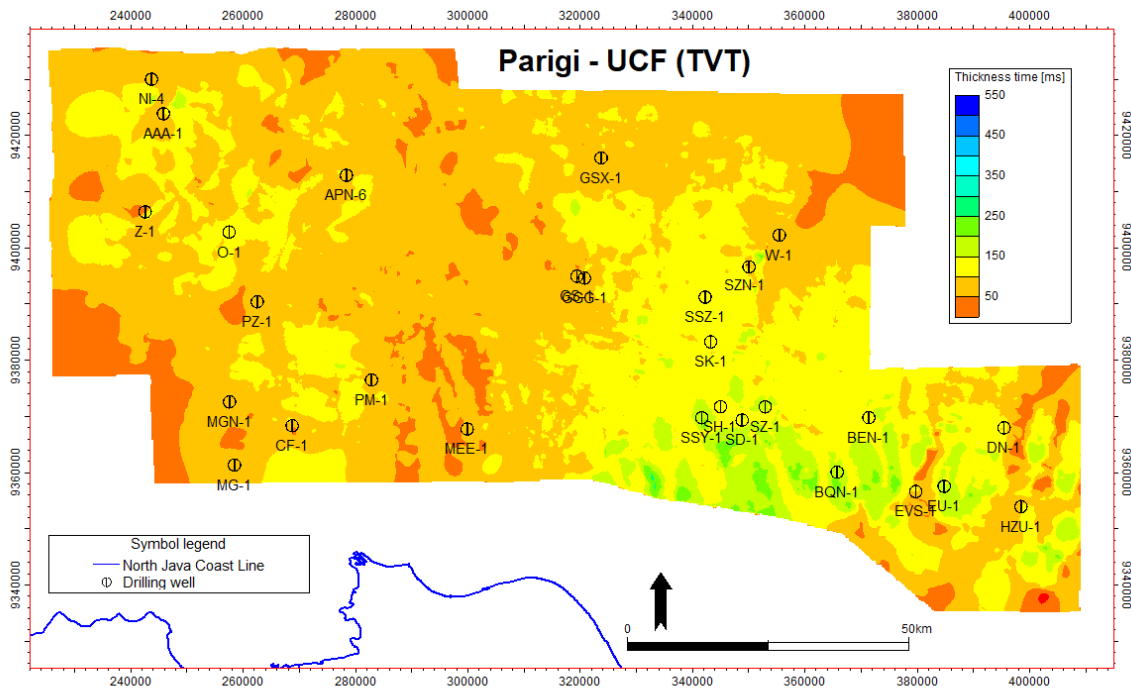


Figure 4.30 Parigi Formation thickness map derived from seismic interpretation.

## 4.4. Discussion

### 4.4.1. Paleogeographic reconstruction

Nine wells (AAA-1, APN-1, BEN-1, GS-1, NI-4, PM-1, SZN-1, W-1, and Z-1) penetrated the basement. Most of the samples were characterized as low-grade metamorphic rocks, such as chlorite schist, metaquartzite, and phyllite. However, one particular sample from the PM-1 well was identified as gneiss.

The thickness of Talangakar Formation in the study area reaches up to 1700 m (5577.5 ft), particularly in the deepest part of the basin. Biostratigraphic studies conducted on the SD-1 (Noon *et al.*, 1993) well reveal the progressive shifts in the depositional environment, transitioning from terrestrial (supra-littoral) in Early Oligocene to transitional marine conditions (outer littoral) in the late Oligocene. In the gamma-ray well log data, this environmental transition is characterized by a shift from blocky sandstone in the lower section to laminated sandstone-shale with the present of several coal layers in the upper section (figure 4.31). The presence of multiple coal seams and the repeated progradation stacking pattern within the upper section point to a transitional environment, specifically a deltaic setting. The boundary between Lower Talangakar Formation (LTAF) and Upper Talangakar Formation (UTAF) is easily recognizable based on lithology, in wells SH-1 and SD-1: the top of the LTAF is identified at a depth of approximately 2740 m (9000 ft) (figure 4.9).

On the 2D seismic sections, the top of the LTAF can be correlated with erosional unconformity in the Talangakar Formation interval identified in the Ardjuna sub-basin and other deeper areas of the North West Java Basin (figure 4.22 and 4.23). This seismic configuration in the TAF interval points to the deposition during a syn-rift period, where subsidence significantly influenced the sediment distribution patterns. In the W-E seismic cross-section along northern region (figure 4.23), two repetitions of divergent configurations can be observed, separated by erosional unconformity (toplap), indicating that the rifting process during the deposition of the Talangakar occurred at least twice. Gresko *et al.* (1995) stated that the deposition below this unconformity belong to the Jatibarang Formation (figure 2.9), but the lithological description in SK-1 and SH-1 does not shows any volcanoclastic lithology, therefore, we tentatively include it as part of Talangakar Formation. Further analysis is needed to describe this deposition.

The gamma-ray log patterns in the western part of the study area, represented by wells NI-4, AAA-1, and Z1, also exhibit a similar configuration, with thick massive low gamma-ray sandstone at the bottom and alternating layers of sandstone and coal at the top (figure 4.7, 4.31). Despite the biostratigraphic analysis results in well NI-4 (Geoservices [LTD], 1999) indicating a similar depositional environment (starting with lacustrine and transitioning to littoral), the deposition began in the Late Oligocene. If these analysis results are accurate, then it suggests that Early Oligocene sediments did not develop in the NI-4 surrounding area and might have been deposited in deeper parts further west to NI-4. Furthermore, the rift activity during this second episode was not sufficient to submerge the entire NWJB area, and the elevated area in the Seribu platform were still acting as a barrier to marine waters in the NI-4 and surrounding areas. Therefore, at the onset of deposition in Late Oligocene, even though the Ardjuna sub-basin area has transitioned into marine environment, the structurally higher part at the northwest of Seribu platform remained in the lacustrine environment and gradually submerged.

In summary, the Talangakar Formation in the study area was deposited during the Early Oligocene to the Earliest Early Miocene, transitioning from a lacustrine to a shallow marine transgressive environment. The general paleogeographic reconstruction map are shown in figure 4.32.

The Baturaja Formation is a lithostratigraphic unit consisting of massive limestone deposits overlying the Talangakar Formation. In borehole data, it is characterized by blocky-low gamma ray values accompanied with high density and low neutron porosity values. In the well data available for this study, the Baturaja Formation can be easily identified, especially in wells located in the high areas (Seribu platform and Central platform) (e.g., GGG-1, SZN-1, SZ-1, and BEN-1). In contrary, in the wells located within the depocenter of the basin, the Baturaja Formation is recognized by alternating layers of limestone and shale. When relying solely on well log data, this formation may not be readily distinguishable; therefore, the interpretation of the top of the Baturaja Formation should be aided by lithology description in the mud log or sidewall core data. Based on the thickness map of the Baturaja Formation from our seismic interpretation and several wells, we develop a paleogeographic map that divides the carbonate on Baturaja Formation based on bulk thickness (figure 4.33).



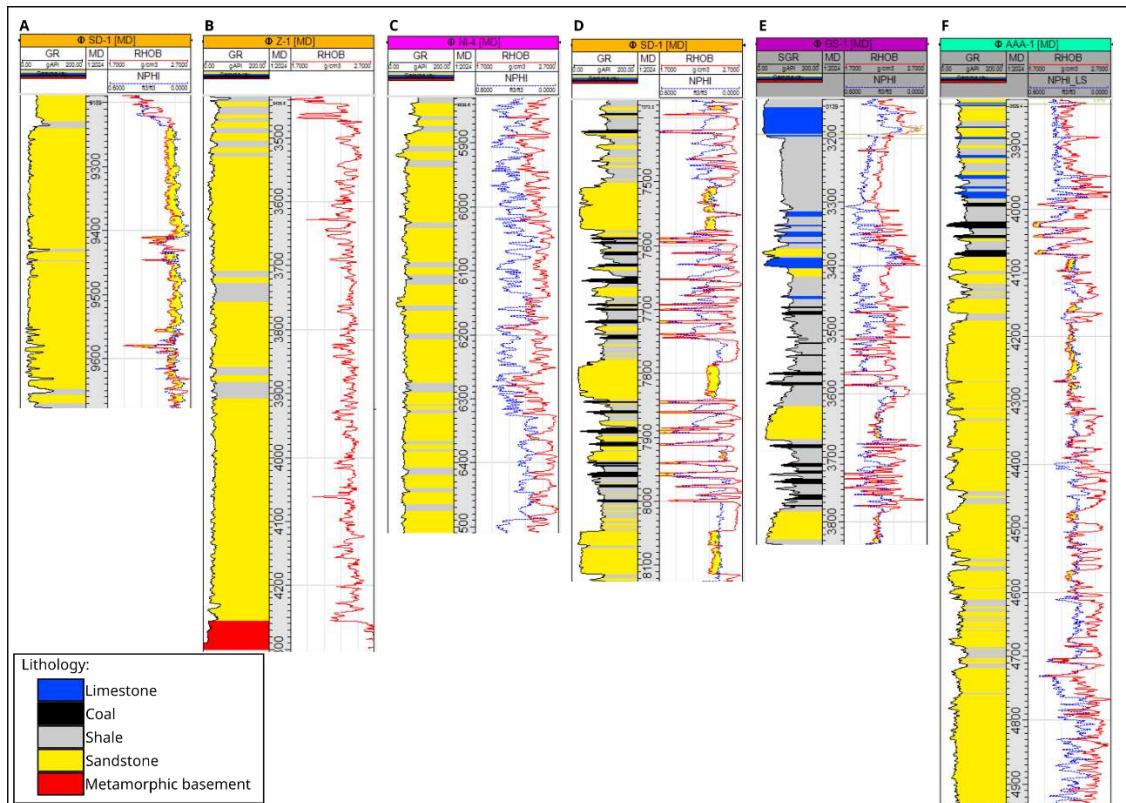


Figure 4.31 typical gamma ray log response in Talangakar Formation. Different thick blocky and serrated log response in Lower TAF showing the fluvial – lacustrine facies (a,b,c); Blocky and bell log shapes with coal intercalation in upper TAF showing littoral/deltaic facies (d); typical deepening up parasequence in upper TAF from littoral to marine environment (e); and complete facies transition in TAF from continental to marine (f).

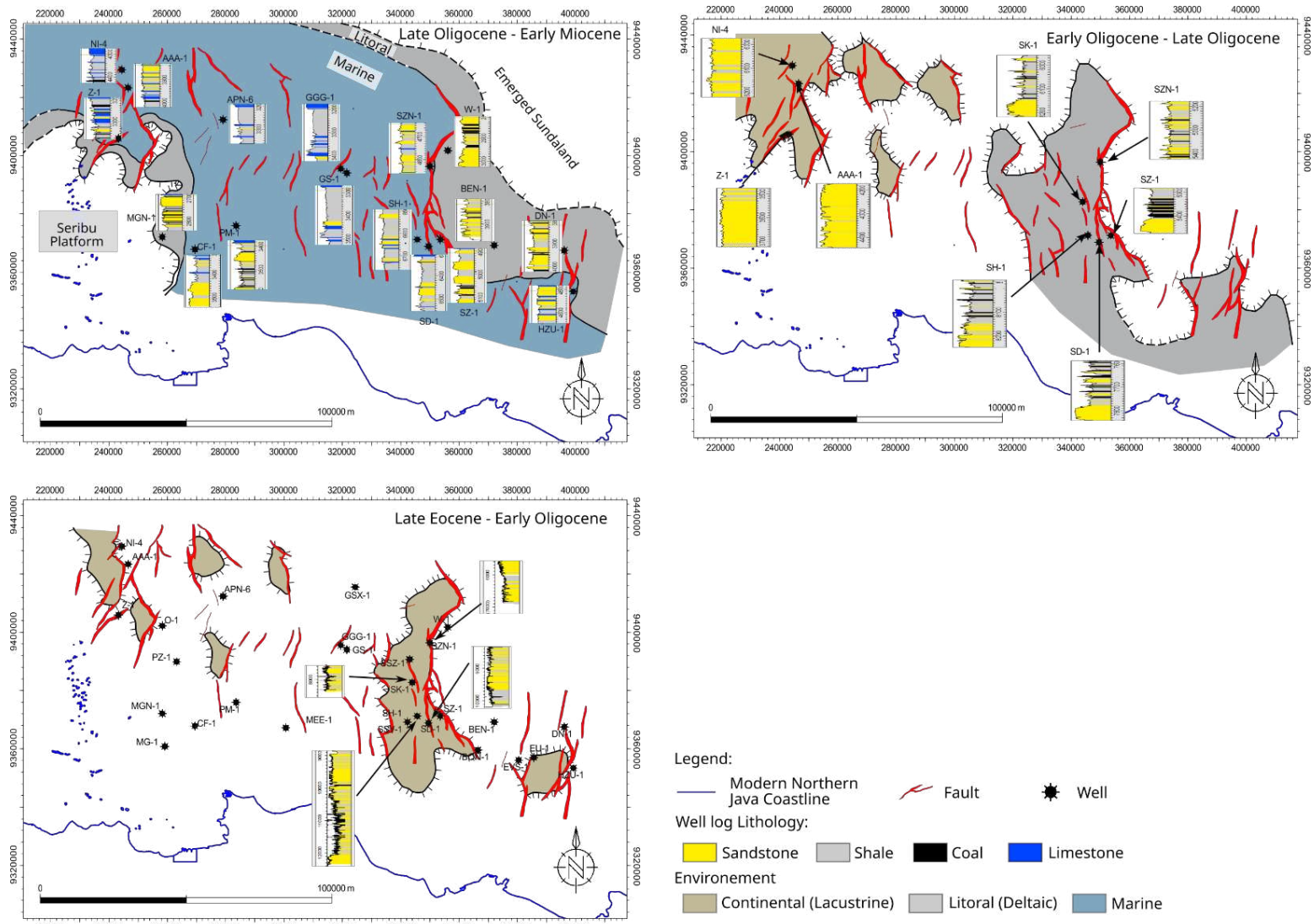


Figure 4.32 General paleogeography reconstruction of Talangakar Formation

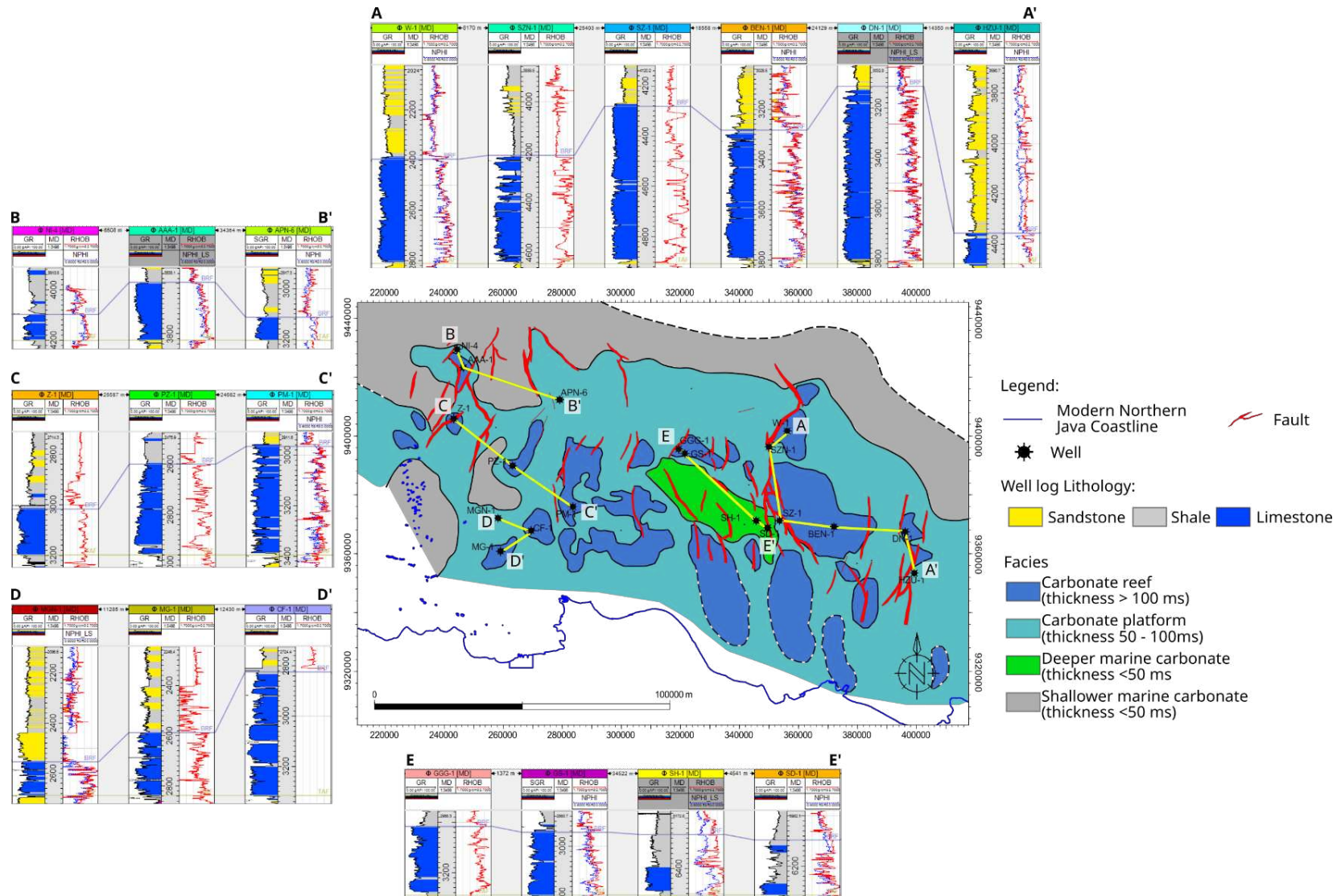


Figure 4.33 Gamma-ray log response and paleogeography reconstruction during the Baturaja Formation

The end of the deposition of the Baturaja Formation is marked by a falling of regional sea level which can be observed in biostratigraphic data of SD-1 Well (Noon *et al.*, 1993). At this time, sediment supply increases, as shown by the development of a thick, multiple-stacked layer of sandstone in the lower part of the Upper Cibulakan Formation. The Massive unit, named after Burburry (1997), constitute the lower part of the Upper Cibulakan Formation, occurring in the Early Miocene. In the deepest part of the basin, this unit encompasses approximately 650 meters (2132.5 ft) of interbedded sandstones, siltstones and shales. Regional evidence suggests the sediments are shelfal/deltaic in origin, and deposited during the Early Miocene when delta lobes prograded south into the Ardjuna sub-basin (Arpandi and Patmosukismo, 1975; Atkinson, 1993; Purantoro *et al.*, 1994; Posamentier, 2002). The upper part of the Upper Cibulakan Formation, named Main unit, comprises intercalated sandstone, siltstone, and shale with several carbonate build-up bodies developed in structurally selective areas at two stratigraphic levels. In contrast to the Baturaja Formation, these carbonates are not widespread but occur as isolated build-ups grading laterally into deeper marine silts and muds with limestone intercalations. The two stratigraphic levels are named Mid-Main carbonate and Pre-Parigi carbonate.

From the mudlog and core description data available, the massive unit is generally composed of interbedded sandstone, siltstone, and clay. Carbonate layers are rarely found. If there is a thin layer of carbonate, it is usually located at the very bottom of the massive unit and may be clastic rework from the Baturaja Formation. The sandstone present is fine to very fine-grained, dark gray, with angular to subangular shapes and medium sorting. It is slightly calcareous and contains a small amount of glauconite. The mudstone and clay also have relatively similar descriptions. In the Main unit, the sandstone is fine to very fine-grained, dark gray, with similar sorting and texture. However, it tends to be more calcareous. Carbonate layers and beddings become more prevalent towards the upper part. In some wells, these carbonate layers appear exceptionally thick, reaching up to 90 meters (295 ft) in the MGN-1 well. This thick limestone presence is also observed in MG-1, PM-1, MEE-1, GSX-1, and SSZ-1. The occurrence of thick limestone in the upper part of the Main unit suggests a relative sea level deepening during deposition of Main unit. This is further supported by biostratigraphic analysis (Noon *et al.*, 1993), indicating a deepening of bathymetry from littoral conditions in the upper Massive unit to sublittoral conditions in the Main unit.

Well and seismic interpretation in the Seribu platform area reveals the stratigraphic position of the Middle Main Carbonate (MMC) and Pre-Parigi Carbonate within the Main unit



(figure 4.34 and 4.35). The seismic cross-section illustrates that the Middle Main Carbonate is present at the lower part of the Main interval. Among the accessible data, only seismic data from the region south of the MEE well displays this MMC carbonate.

Based on wireline data (figure 4.34) and taking into account of previous research, an interpretation of the depositional environment of Upper Cibulakan Formation could be made (figure 4.36). Considering the thickness of sandstones within the Massive unit and the evidence of a shallowing up sea level observed in biostratigraphy, leading to the interpretation that these thick sandstone deposits can be linked to the period of regressive sea levels. Strong evidence shows that the massive unit interval is most likely deposited in a delta system with a N-S oriented progradation. The rise in sea level and a decline in sediment supply likely occurred during the Middle Miocene, as indicated by presence of thick shale with thin intercalations of sandstone and limestone within the Main Member. This scenario probably resulted in the reworking of sediments in the shoreline area to the North, subsequently deposited as sandstones in the Main Member. The detailed interpretation of UCF is discussed in Chapter 5.

#### **4.4.2. Impact of the fault on the architecture of the sedimentary filling and thickness distributions**

Among the wells that penetrate the Talangakar Formation, a substantial difference in thickness is evident between low and high areas. Notably, in certain wells like PZ-1 and MG-1, the Talangakar Formation appears to be absent, with the Baturaja Formation directly covering the basement (figure 4.7). Seismic interpretation of the Talangakar Formation also reveals an onlap pattern toward the basement, supporting this observation (figure 4.22 to 4.25). The BEN-1 well, representing the Central platform area, indicates that sediment deposition initiated in the Early Miocene within a littoral environment. This suggests that Oligocene sedimentation primarily occurred in structurally low areas, while at the high area especially the Central platform experienced either non-deposition or erosion.

In the Early Miocene, a tectonic quiescence phase was observed in various back-arc basins across Indonesia, including the North West Java Basin, (Burbury, 1977; Martodjojo, 1984; Satyana, 2005). In our study area, this quiescence phase is characterized by the extensive carbonate development of the Baturaja Formation. The thickness of the Baturaja Formation in the study area can be categorized into three regions: the Central Platform, the Ardjuna sub-basin, and the Seribu Platform area.

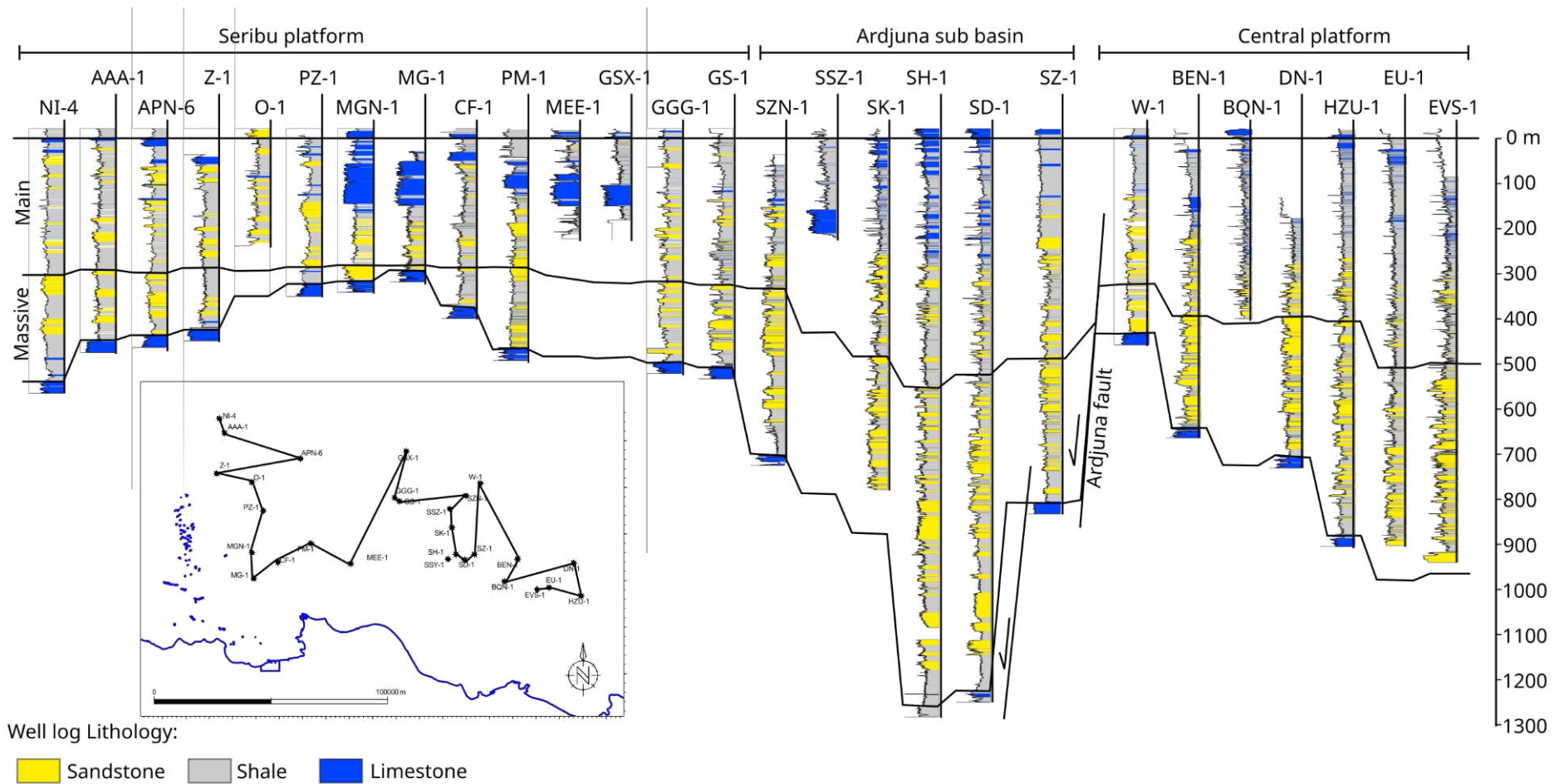


Figure 4.34 Arbitrary line correlation in the Upper Cibulakan Formation.

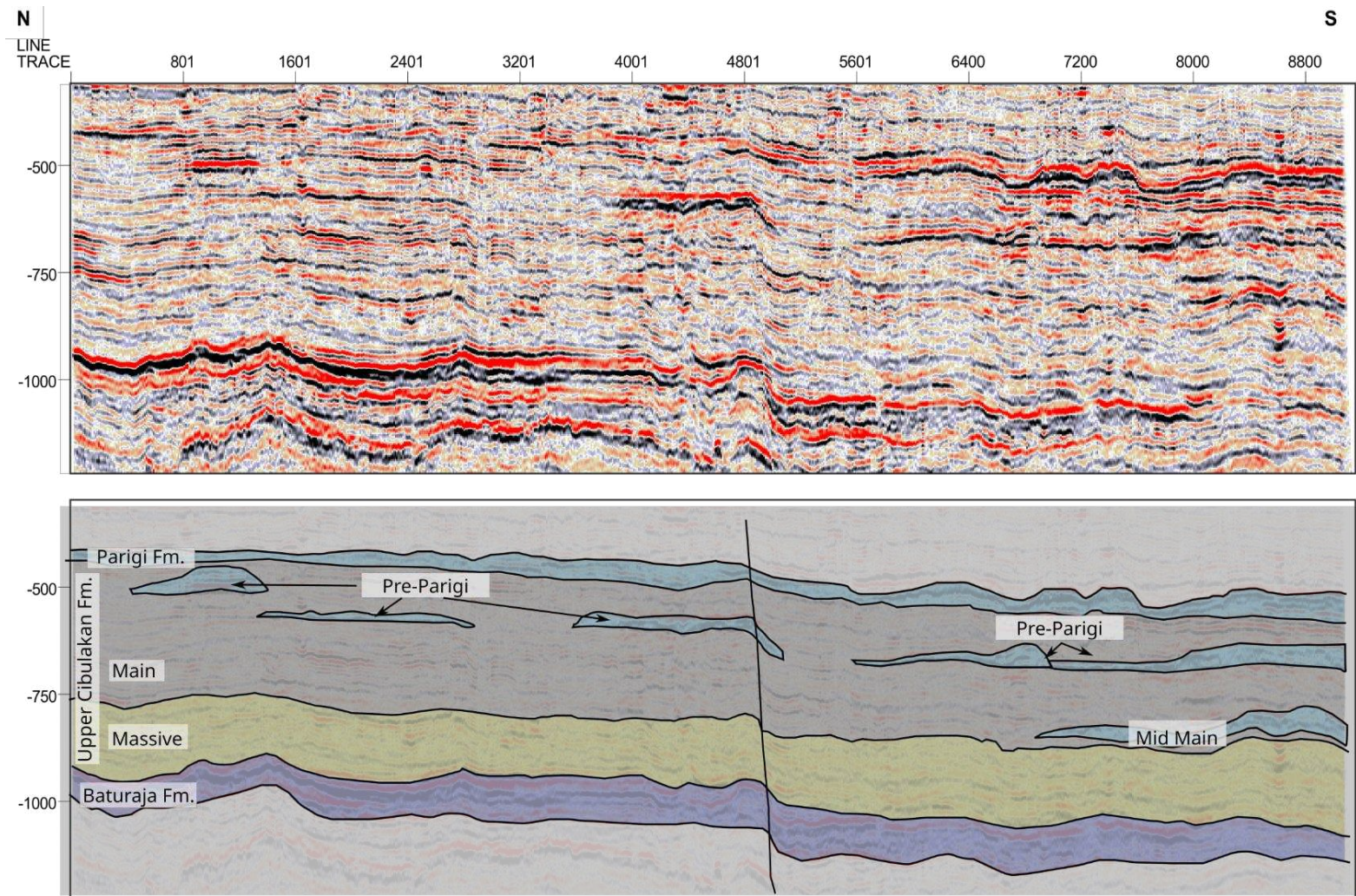


Figure 4.35 Un-interpreted (up) and interpreted (down) N – S seismic line S10 section showing seismic interpretation in the Seribu platform area. Middle main carbonate can be seen in the lower part of the Main unit, and Pre Parigi carbonate in the upper part. See fig.4.4 for line location



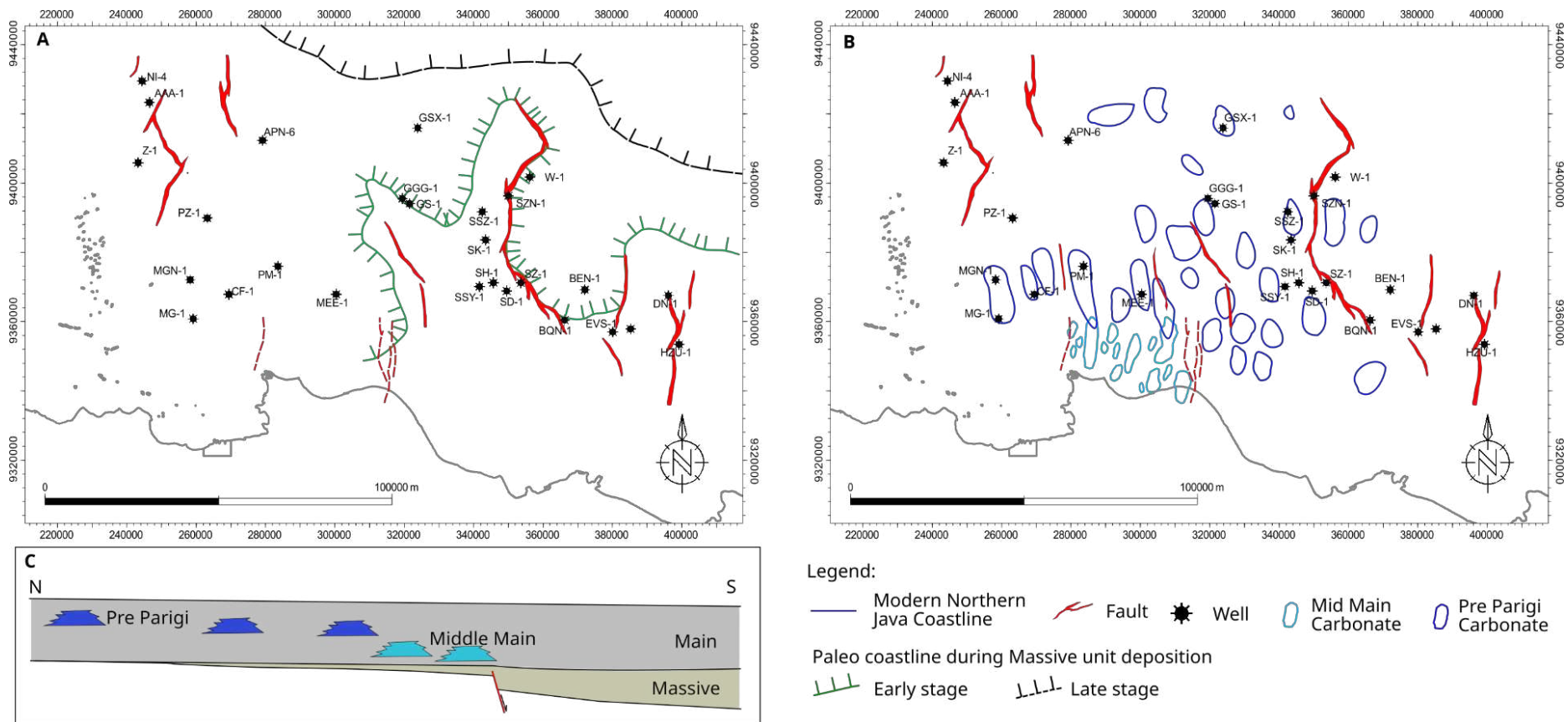


Figure 4.36 Paleogeography reconstruction of Upper Cibulakan Formation. The northward evolution of paleocoastline during the Massive unit deposition (a); the Middle Main carbonate distribution are bounded by the fault in the southern area, while the Pre Parigi carbonate are more widespread (b); and schematic NS cross section showing the distribution of stratigraphic unit in Upper Cibulakan Formation (c). Some southern data (fault (dashed line) and Mid Main Carbonate distribution) are taken from Ratkolo, 1994.



The highest thickness is observed in the Central Platform region, reaching up to 200 meters in wells SZ-1 and DN-1 (figure 4.33). This suggests that this area is particularly conducive to carbonate growth. The gamma-ray log patterns also indicate relatively clean carbonate development with minimal shale intermixing, especially close to Ardjuna fault, as represented by wells SZ-1 and SZN-1 (figure 4.33). Seismic interpretation in the Central Platform area reveals the presence of an extensive carbonate reef platform with relatively uniform thickness that thins towards the Ardjuna fault (figure 4.22).

In the deeper Ardjuna sub-basin, carbonate reefs did not develop in the area close to Ardjuna fault. This suggests that this area was not suitable for the carbonate to develop. Gamma-ray logs in wells SD-1 and SH-1 reveals thin and blocky carbonate facies at the base, transitioning into shaly facies (figure 4.33). This indicates that during the early deposition of the Baturaja Formation, carbonate facies might have initially developed (or deposited) in this area, but carbonate deposition ceased, possibly due to rapid submergence that halted carbonate growth. This is supported by the gamma-ray pattern in well SD-1, showing a fining-upward pattern indicative of a gradual lithological transition from carbonate to shale.

Northwest of SD-1, wells GGG-1 and GS-1 shows a carbonate deposition similar to those in the Central Platform area, but with smaller thickness. Seismic sections illustrate that the growth of carbonate in this area is controlled by pre-existing faults (figure 4.13). This indicates that even though tectonic activity in the NWJB area are generally considered inactive during the deposition of the Baturaja Formation, the location of these faults still influences the carbonate growth.

South of well SD-1, seismic interpretation reveals three locations with significant thickness in the NW-SW direction (figure 4.33). While we lack well data that penetrates these thickness areas, their geometry suggests the formation of carbonate reef facies oriented relatively perpendicular to the coastline at that time.

In the Seribu Platform area, when examining the thickness map resulting from seismic interpretation, the Baturaja Formation appears relatively uniform. There are narrow, isolated areas with higher thicknesses in arbitrary directions. The maximum thickness from well data reaches 150 m in well CF-1 (figure 4.33) with blocky serrated pattern with intercalation of thin layers of high gamma-ray facies (shale or fine-grained limestone). This aligns with the findings of Widodo (2018).

From the available wellbore data, thickness variations of the Massive unit are evident among the Seribu platform, Ardjuna sub-basin, and Central platform (figure 4.34). In the Seribu platform region, the thickness variations of the Massive unit appear to cover the adjacent morphological features formed towards the end of the Baturaja Formation deposition. This discrepancy is observed in wells such as PZ-1, MGN-1, MG-1, and CF-1, where the Massive unit is thinner compared to neighboring wells. Conversely, in wells like PM-1, GGG-1, and GS-1 within the same region, the thickness of the Massive unit appears relatively uniform. This suggests that the deposition of the Massive unit in the Seribu platform is not significantly influenced by the existing fault movements in the area. However, in the Ardjuna sub-basin area, the well correlation section reveals that the Massive unit thickens towards the Ardjuna Fault. This thickening is most prominent in wells SH-1 and SD-1, located closer to the Ardjuna Fault. While south to the central platform area, well correlations reveal thickness variations similar to those in the Ardjuna sub-basin. The thickness of the Massive unit appears to increase towards the southern area and reaches its maximum in the wells EU-1 and EVS-1.

The thickness variations are also clearly observed in the seismic cross-section (figure 4.22). The Massive unit seems to have been deposited on the existing low topography, showing divergent reflector configuration and onlaps towards the high areas. The thickness map of the Massive unit (figure 4.28) provides a broader overview of the thickness variations. It is evident that the Massive unit exhibits significant thickness differences among the three mentioned regions. In the Ardjuna sub-basin, the orientation of thickness appears to follow the direction of the north-south Ardjuna Fault, leading to the interpretation that during the deposition of the Massive unit, there was still a significant movement, possibly due to sagging processes indicating that the basin was in the post-rift phase. Alternatively, it could be attributed to tectonic events causing fault movement over a brief period during deposition indicating the basin was still in the syn to post rift transition. Our analysis suggests that the latter interpretation is more fitting to explain these thickness variations. Further details are discussed in Chapter 6.

In the Main unit, although there are still thickness variations, the differences are not so significant. We interpret this as a result of sagging processes, causing the deeper parts to have slightly greater thickness.

#### 4.4.3. Mid-Main, Pre-Parigi, and Parigi Carbonate distribution

To gain a comprehensive view of MMC distribution, we referred to the distribution map by [Ratkolo \(1994\)](#). The map indicates that the distribution of MMC is limited to the Rengasdengklok high region (refer to [figure 2.11](#) for the position of Rengasdengklok high). For the distribution of Pre-Parigi carbonate, we conducted a detailed mapping of its geometry in the seismic data ([figure 4.36](#)). The distribution map reveals distinct differences in the long-axis orientation of each carbonate reef body. In the MMC, the orientation is observed to be 5° clockwise, following the orientation of the faults forming the Rengasdengklok high. On the other hand, the Pre-Parigi carbonate has a distribution of approximately 10° counterclockwise. This distribution also appears to follow the orientation of the surrounding faults. In the Ardjuna sub-basin, carbonate bodies exhibit a more circular shape, while in the Central Platform, two reef bodies are present, and their long-axis orientation follows the Ardjuna Fault. The difference in orientation indicates that the pre-existing fault orientation controlled the direction of carbonate reef body distribution. This phenomenon may be attributed to sagging tectonics influencing variations in sea depth during that period.

The Parigi Formation is defined as a carbonate growth during the second tectonic quiescence episode in the late middle Miocene ([Burbury, 1977](#); [Martodjojo, 1984](#)). Based on our analyzed data, it appears that this formation was deposited conformably above the Upper Cibulakan Formation (UCF). A review of biostratigraphic data indicates that this event occurred at a younger age, specifically at 8.4 Ma (late Miocene). Seismic mapping of the Parigi Formation reveals a thick distribution in the southern part of the Ardjuna sub-basin, with the long-axis orientation of each reef trending approximately 10° counterclockwise. The distribution of each reef (thickness >150 ms in [figure 4.30](#)) seems to be minimally or not influenced by fault orientations. This supports the notion that the tectonic quiescence event occurred during the deposition of the Parigi Formation.

**CHAPTER 5: SEQUENCE STRATIGRAPHY OF THE UPPER  
CIBULAKAN FORMATION**



## 5.1. Introduction

A detailed analysis is provided to describe the stratigraphic sequences in the Upper Cibulakan Formation. Firstly, the focus will be on explaining the stratigraphic sequences in a key well, SD-1. Secondly, we have conducted an analysis of electrofacies based on wireline log data, ditch cutting and core descriptions, as well as a review of dip meter data. Subsequently, seismic stratigraphic analysis will be discussed based on several seismic cross-sections. The discussion will conclude with an overview of the development of stratigraphic sequences based on the analyses conducted.

The chosen area for the stratigraphic sequence analysis is the Ardjuna sub-basin, considering it to be the thickest sub-basin where the Upper Cibulakan Formation sediment is deposited most extensively. The selected block location covers an area of 6500 km<sup>2</sup> (figure 5.1). Seven wells are used for this analysis, including W-1, SZN-1, SK-1, SH-1, SD-1, GGG-1, and BEN-1. With the same considerations discussed in chapter 4, SD-1 is chosen as the key well for the depositional sequence analysis. The Upper Cibulakan Formation is deposited conformably above the Baturaja Formation. To gain a comprehensive understanding of the Upper Cibulakan Formation, our stratigraphic sequence analysis initiates from the base of the Baturaja Formation.

Based on literature review and our geological investigation, we emphasized the influence of sediment input from the northern direction during the deposition of the Upper Cibulakan Formation. The correlation, thickness variations, and seismic interpretation in the Massive unit and the subsequent Main unit consistently point towards a northern sediment source, providing a foundational understanding of the paleogeographic context that will continue to shape our interpretations in the sequence stratigraphic interpretation.

## 5.2. Electrofacies Determination

Facies analysis is based on gamma-ray log value and shape, stacking patterns, dip meter analysis, as well as cutting and sidewall core description of seven wells. Firstly, we correlated petrophysical wireline logs, particularly gamma-ray, resistivity, density, and neutron logs, to determine lithology using the standard method by [Asquith \*et al.\* \(2004\)](#), across all well data. The resulting lithology was then calibrated with available mudlog and core descriptions. Based on the analysis, we categorized it into three common lithologies: sandstone, shale (including silt and clay), and limestone.



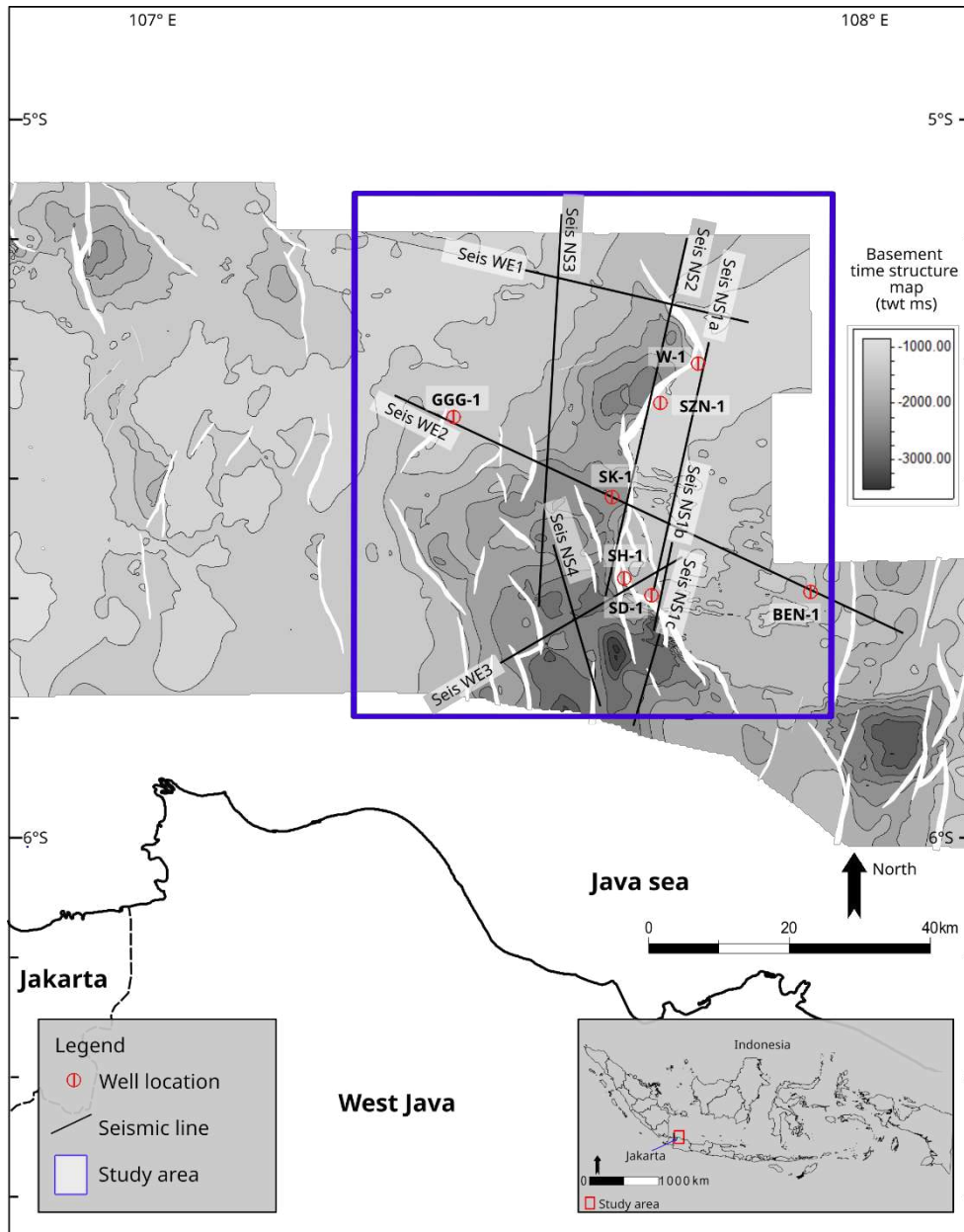


Figure 5.1 Generalized location map of North West Java sea showing the study area, well and seismic data used in the analysis.

Secondly, a visual inspection was carried out on the stacking pattern following the standard method by [Rider and Kennedy \(2011\)](#), particularly focusing on the gamma-ray log. Corresponding dip pattern were interpreted based on classification by [Donselaar and Schmidt \(2005\)](#) and [Höcker et al. \(1990\)](#) to determine potential depositional facies. In this context, we refer to it as the Gamma Ray Facies (GRF). Nine Gamma-Ray Facies (GRF) has been identified which correspond to depositional architecture elements ([table 5.1](#)). Afterward, the nine gamma-

ray facies were regrouped into four facies associations: delta plain (FA1), delta front and prodelta (FA2), shelf marine (FA3), and reefal carbonate (FA4).

### 5.2.1. **Facies Association 1: Distributary channel and point bar facies deposited in delta plain**

#### 5.2.1.1. **Gamma-ray facies 1 (GRF1):**

This facies is characterized by thick (average thickness ~25m), low blocky gamma ray log, marked by a sharp-base. Ditch cutting samples in a sandstone interval shows that this facies corresponds to dark to light grey, medium to fine grained, sub-angular to sub-rounded, glauconitic, non-calcareous, sandstones. [Figure 5.2a](#) shows an example of the response of the dip meter log in the SZN-1 well. In the figure, we can see dip patterns which are valuable for sedimentary facies interpretation. Increasing up dip stacking pattern indicated by blue line can be seen in the GRF1 with the large scattered dip direction. The seemingly randomly distributed dip directions can be zoomed in and further sub divided into small, 1 – 2 meters (3 – 6 ft). thick intervals with unidirectional dips and dip direction ([figure 5.3](#)). The gradually changing dip with unidirectional distribution are interpreted as the representation of cross beds. Furthermore, the dip direction clockwise rotation can indicate the lateral accretion of each bed or the migration of the channel. Shales underlying sandstones in [figure 5.2b](#) show a consistent dip at  $<5^\circ$  (green line) in a west dip direction that indicates a regional stratigraphic dip. In the sandstone with a blocky gamma-ray pattern, a higher dip ( $30^\circ$ ) can be observed, interpreted as west-oriented crossbeds. The gamma-ray pattern with this dip meter character is interpreted as a point bar deposit with crossbeds sedimentary structures.

GRF1 is mostly observed within the proximal wells (W-1 and SZN-1). Micropaleontological evidence indicates a littoral environment associated with this electrofacies. We interpret GRF1 as amalgamated channel or point bar deposits.

#### 5.2.1.2. **Gamma-ray facies 2 (GRF2):**

This facies is characterized by a sharp base, a general fining upward trend (the gamma-ray curve defines a bell-shape) with thickness of 50 – 80 m (164 – 262.5 ft). Ditch cutting description shows that this facies consists of fining upward successions of quartz rich, predominantly medium to fine grained sandstones at the bottom to very fine sandstones on the top, containing angular to sub angular, and moderately sorted grains.

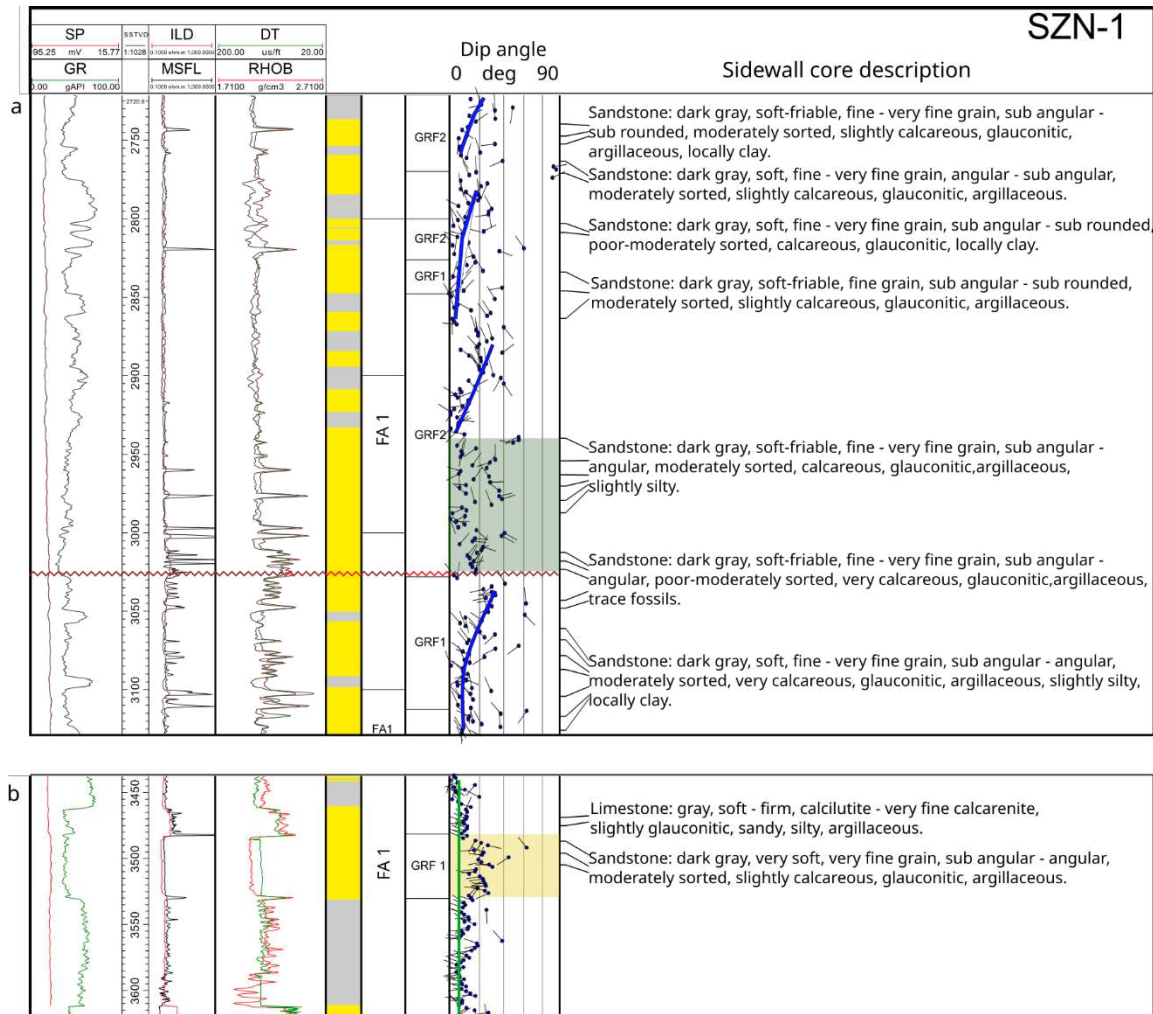


Figure 5.2 SZN-1 composite log showing example of blocky and bell gamma ray facies (GRF1 and GRF2) at 2750 – 3100 ft depth (a), and 3450 – 3600 ft depth (b). The green shaded region in fig a, indicates a randomly oriented tadpole zone. The blue lines showing the increasing up dip tadpole pattern. Note the clear dip shift in figure (a) at 3030ft, indicate an erosional unconformity. The green vertical color in the figure b indicates the regional stratigraphic dip. The GRF1 and GRF2 is characterized by higher depositional dip pattern indicates the crossbed structure. The tadpole data are based on high-resolution four-arm dipmeter logs (HDT) interpreted by Schlumberger (1983).

GRF2 has a same dip meter response compared to GRF1. In [figure 5.2a](#), the steepening upward dip can still be observed, although this trend is somewhat challenging to interpret because the dip and dip direction values are not as clear as those in GRF1. However, the apparent direction can still be discerned and is indicated by the blue line. Micropaleontological occurrences show a decreasing in species diversity and abundance leading to shallower environment (outer littoral to inner sublittoral). We interpret GRF2 as a distributary channel fill in delta plain. This facies is mostly observed within Massive unit.

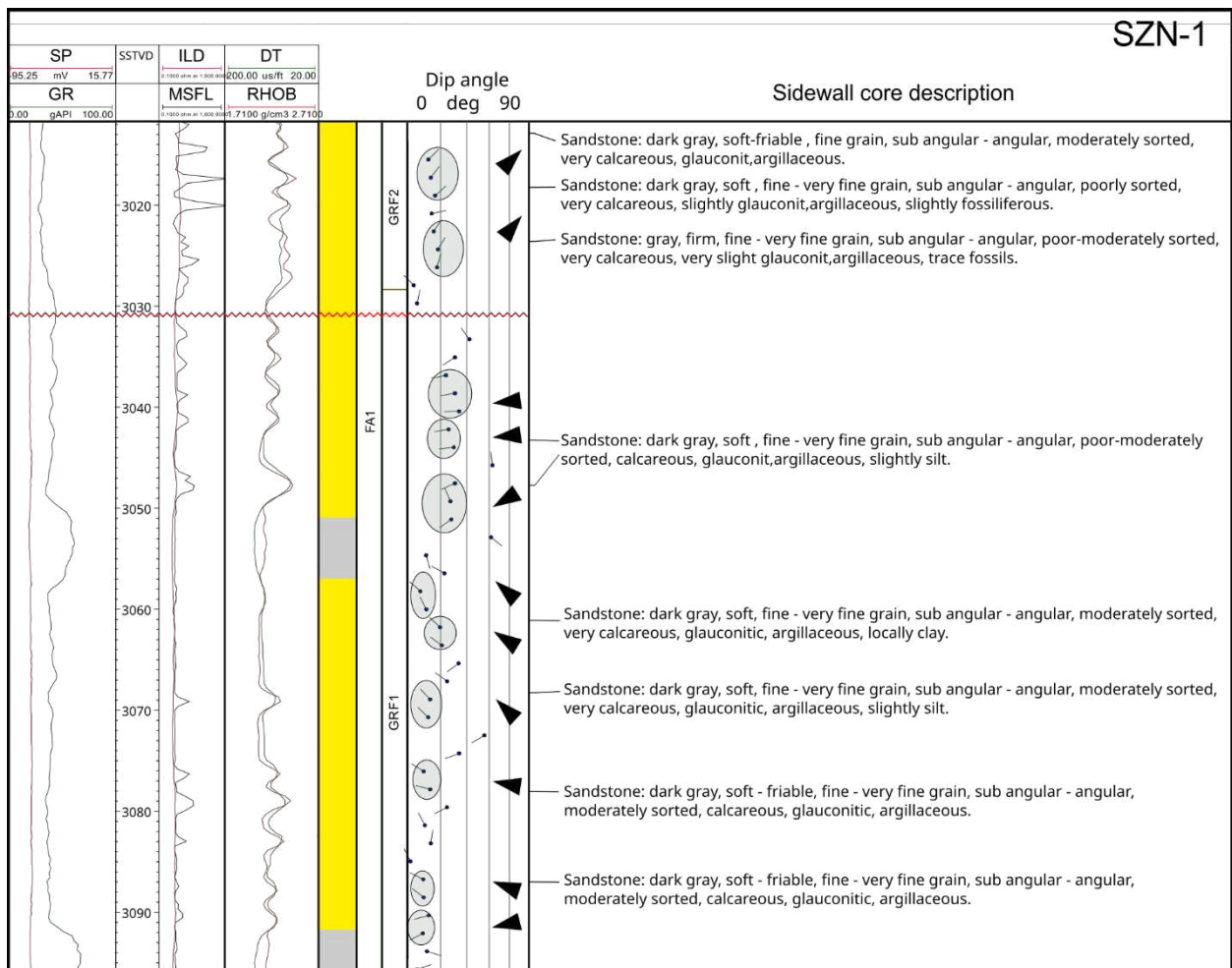


Figure 5.3 Zoom in of SZN-1 composite 3280 – 3365 ft. the tadpole in fig 5.2 are grouped in 3 – 6 ft (1 – 2 m) thick package with unidirectional dip. black rotated triangle is a dominant dip direction of each bed showing the clockwise rotation of dip direction. The tadpole data are based on high-resolution four-arm dipmeter logs (HDT) interpreted by Schlumberger (1983).

## 5.2.2. Facies Association 2: Delta front to prodelta environment with tidal influenced mouth bar or shelf ridge

### 5.2.2.1. Gamma-ray facies 3 (GRF3):

This facies is characterized by thick (average thickness ~30m (~98.5 ft)), individual coarsening upward trend (funnel-shape in the gamma-ray curve). The succession involves a vertical transition from shales into increasingly cleaner sandstones. Ditch cutting and sidewall core samples in a sandstone interval shows that this facies corresponds to dark to light grey, medium to fine grained, sub-angular to sub-rounded, glauconitic, slightly calcareous, sandstone. The dip meter log response in GRF 3 (figure 5.4) shows a both decreasing and increasing up dip stacking pattern that could indicate cross beds associated with compactional

draped. This dip meter pattern could indicate deposition influenced by tidal currents. GRF3 is mostly observed within the lower part of Massive unit and lower part of Main unit. Micropaleontological evidence indicates a marine environment (inner sublittoral) associated with this electrofacies (Noon *et al.*, 1993; Romein *et al.*, 1987). We interpret GRF3 as delta front/mouth bar deposits.

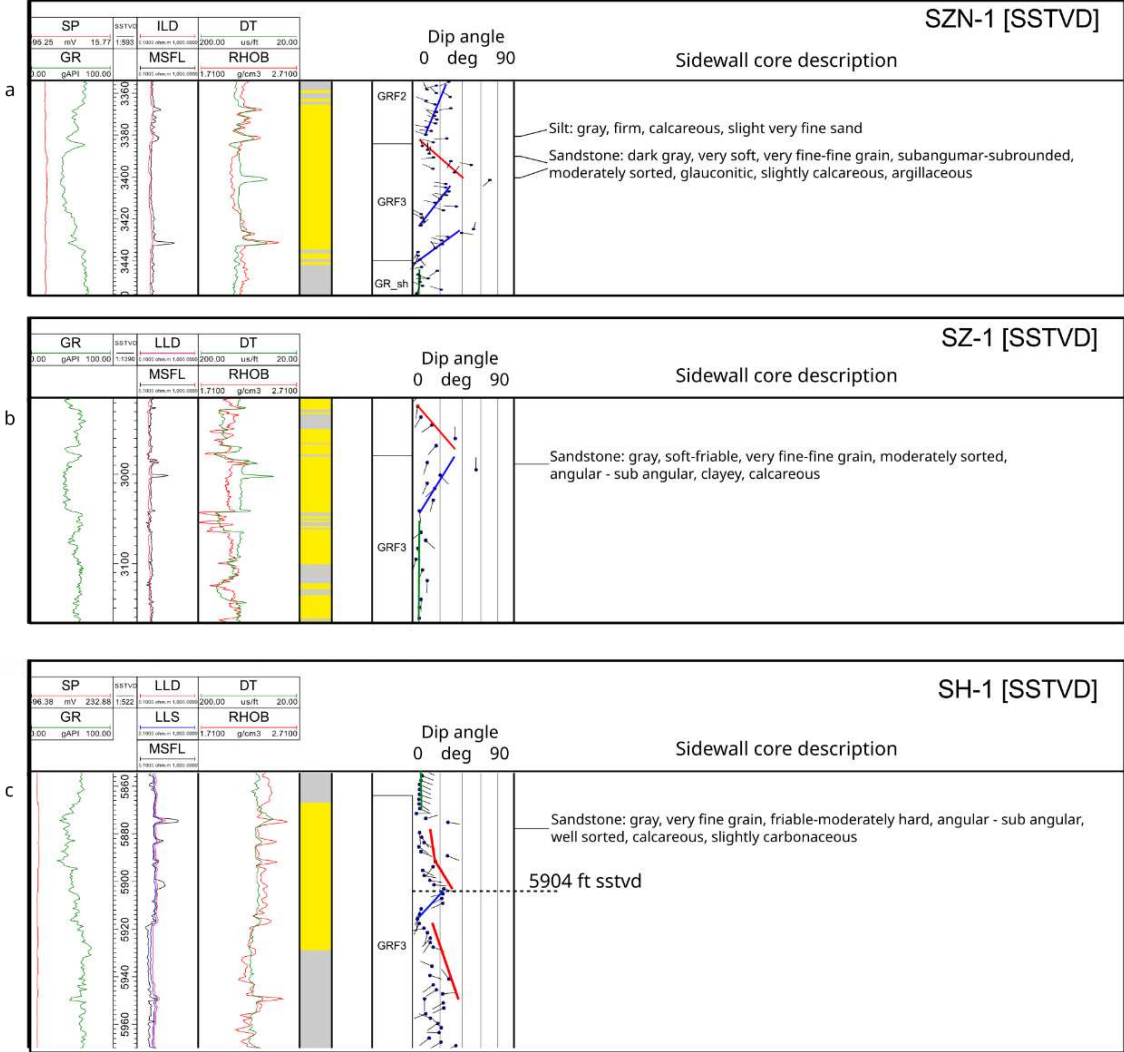


Figure 5.4 Composite log showing example of funnel gamma ray facies (GRF3).SZN-1 well at 3360 – 3440 ft depth (a), SZ-1 well at 2950 – 3150 ft depth (b), and SH-1 well at 5860 – 5960 ft depth (c). The blue lines showing the increasing up dip tadpole pattern, the green vertical color indicates the regional stratigraphic dip, and the red lines indicate the decreasing up dip. The GRF3 indicate by both decreasing and increasing up dip pattern. Note the sudden change in dip direction at 5904ft indicate the major shift in depositional trend (i.e. sequence boundary). The tadpole data are based on high-resolution four-arm dipmeter logs (HDT) interpreted by Schlumberger in 1983 (SZN-1), 1979 (SZ-1); and formation micro scanner (FMS) interpreted by Schlumberger in 1992 (SH-1).



### 5.2.2.2. Gamma-ray facies 4 (GRF4):

This facies, marked by a sharp-base, is made up of 20-50 m (65.5 - 164 ft) thick of blocky serrated GR trend characterized by relatively constant GR value and is related to aggradation of fine sand sediments, capped by transition back to shales. The base of GRF2 is generally erosive into the underlying sediments, which are most often shales. Ditch cutting sample shows a quartz rich fine sandstones similar to GRF3. The dip meter log response in GRF 4 (figure 5.5) shows a relatively uniform low dipping value.

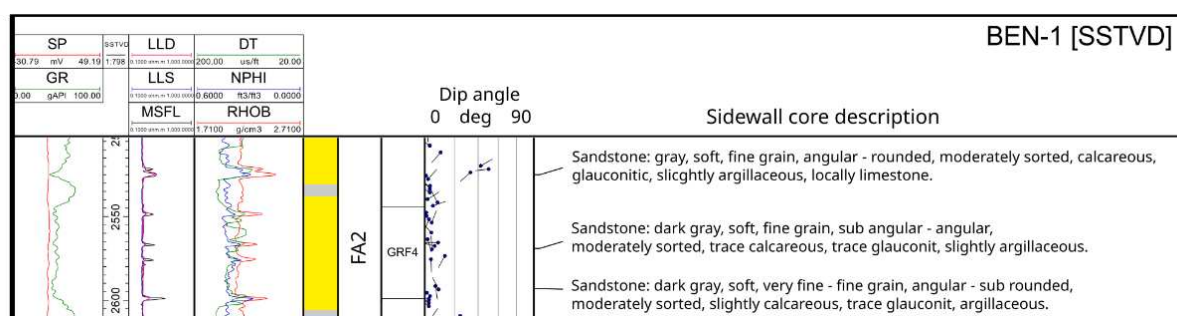


Figure 5.5 Composite log showing example of blocky serrated gamma ray facies (GRF4). BEN-1 well at 2500 – 2620 ft depth. The dip meter tadpole shows a relatively uniform dip at  $<10^\circ$ . The tadpole data are based on formation micro scanner log (FMS) interpreted by Schlumberger (1993).

This facies is generally observed within the lower part of Massive unit. Micropaleontological evidence in SD-1 indicates slightly deeper marine environment (deep inner to outer sublittoral). We interpret GRF4 as a stacked proximal mouth bar.

### 5.2.2.3. Gamma-ray facies 5 (GRF5):

This facies shows amalgamated coarsening upward sandstones (amalgamated funnels-shape in the GR curve) with thickness varying from 50 to 80 m (164 to 262.5 ft). Well cuttings show a dark grey, fine to very fine grain, sub angular to sub rounded, moderately sorted sandstone. The dip meter log response in GRF 5 (figure 5.6) shows a randomly oriented dip direction that could indicate that the bedding was disturbed by post sedimentary process. Atkinson (1993), describing the core data from the B field south to the study area, found that most of sandstone in the Main interval was strongly bioturbated. The dip meter response in this facies could be correlated to this bioturbated sandstone facies. Micropaleontological evidence shows a similar environment than GRF4 (outer littoral to inner sublittoral). This facies is



commonly observed in the upper part of Massive unit. We interpret GRF 5 as a stacked mouth bar in delta front, or shoreface environment.

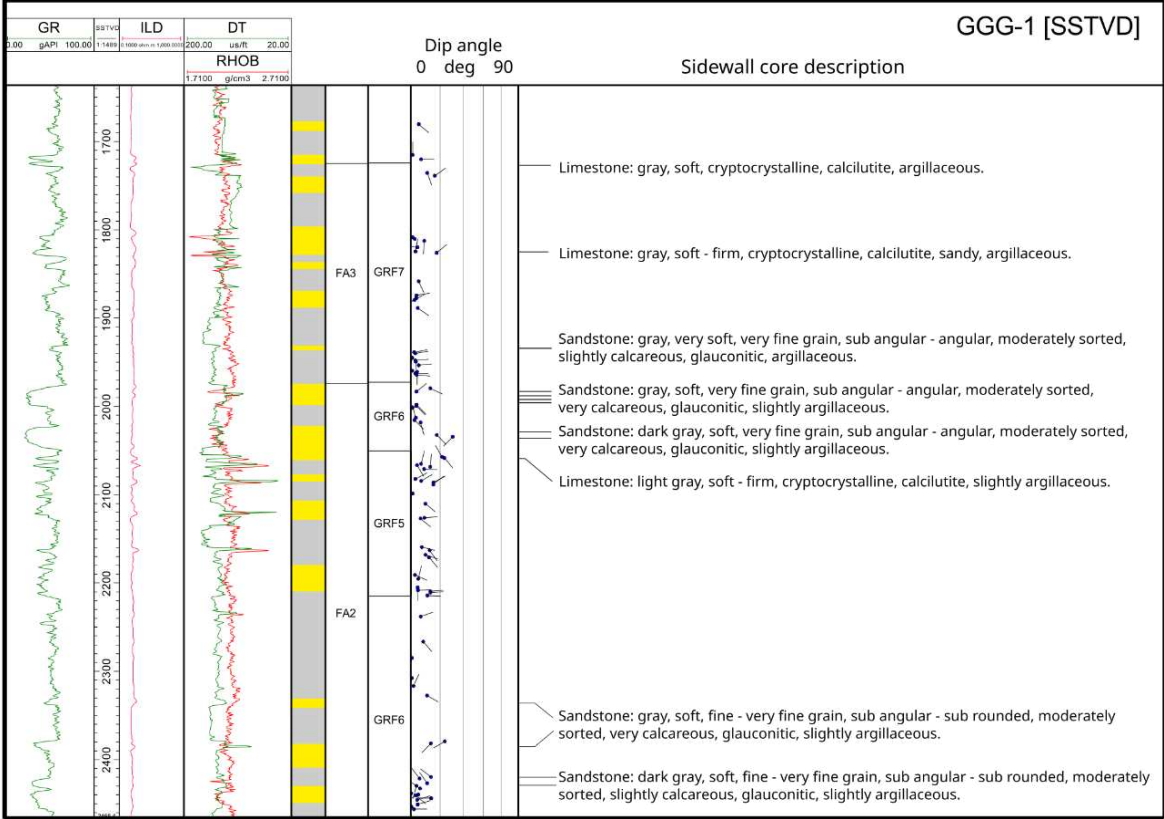


Figure 5.6 Composite log showing example GRF5, 6, and 7 at GGG-1 well. The dip meter tadpole shows a relatively uniform dip at  $<10^\circ$  with a randomly oriented tadpole could indicate that the bedding is disturbed by post sedimentary process. The tadpole data are based on high-resolution four-arm dipmeter logs (HDT) interpreted by Schlumberger (1974).

**5.2.2.4. Gamma-ray facies 6 (GRF6):**

This facies shows repeated coarsening upward trends (stacked funnels) similar to GRF3 with higher GR values. The shales, associated with one or more siltstone layers, vertically grade into thin sandier siltstones (generally 10 – 15m (32.5 to 49 ft) thick). A ditch cutting sample shows a grey, silt and very fine grained sediment similar to GRF3 and 4. This facies have the same dip meter response than GRF 5 (figure 5.6). GRF6 is generally observed within lower part of Massive unit and lower part pf main unit. Micropaleontological data show a similar environment than GRF3 (inner sublittoral). We interpret GRF6 as a proximal mouth bar.

#### 5.2.2.5. **Gamma-ray facies 7 (GRF7):**

This facies exhibits a serrated hourglass trend which combines fining and coarsening upward trend, consisting of mixed layer of claystone, sandstone with the occurrence of limestone layer. GRF7 is closely associated with the middle part of Main unit. Ditch cutting description shows a grey to brown, fine to very fine grain, calcareous sandstone with intercalated claystone and mudstone. This facies have the same dip meter response than GRF 5 (figure 5.6). Micropaleontological evidence shows an open marine environment (inner littoral) (figure 5.7). We interpret GRF7 as a tidal bar or a mixed tidal flat.

### 5.2.3. **Facies Association 3: Reworked or clastic carbonate in a storm dominated marine environment**

#### 5.2.3.1. **Gamma-ray facies 8 (GRF8):**

This facies shows an aggrading blocky pattern with thin spikes of GR values (spiky) corresponding to limestones layers. Intervals marked by GRF8 are predominantly made of silty claystone with intercalation of limestones. Ditch cutting description shows a hard, dense crystalline limestone with some foraminiferal mudstone, wackestone to packstone, with grey to brown color. Micropaleontological evidence shows deeper marine environment compared to GRF7 (deep inner littoral to outer littoral) (figure 5.7). We interpret GRF8 as a reworked clastic limestone in a shelf marine (storm dominated). GRF8 is closely associated with the upper part of Main unit.

### 5.2.4. **Facies Association 4: Reefal carbonate**

#### 5.2.4.1. **Gamma-ray facies 9 (GRF9):**

This facies exhibits a blocky pattern with limestone lithology. Intervals characterized by GRF9 predominantly consist of white to grey dolomitic limestone, ranging from floating biogenic fragments, fine to medium-grained calcarenite, to crystalline. It appears to have been deposited in a clean, low-energy environment with a biostromal structure, rather than a high-energy biostromal type environment (W-1 well core description), in line with Widodo (2018). We interpret GRF9 as a reefal carbonate in the Baturaja and Parigi Formations.

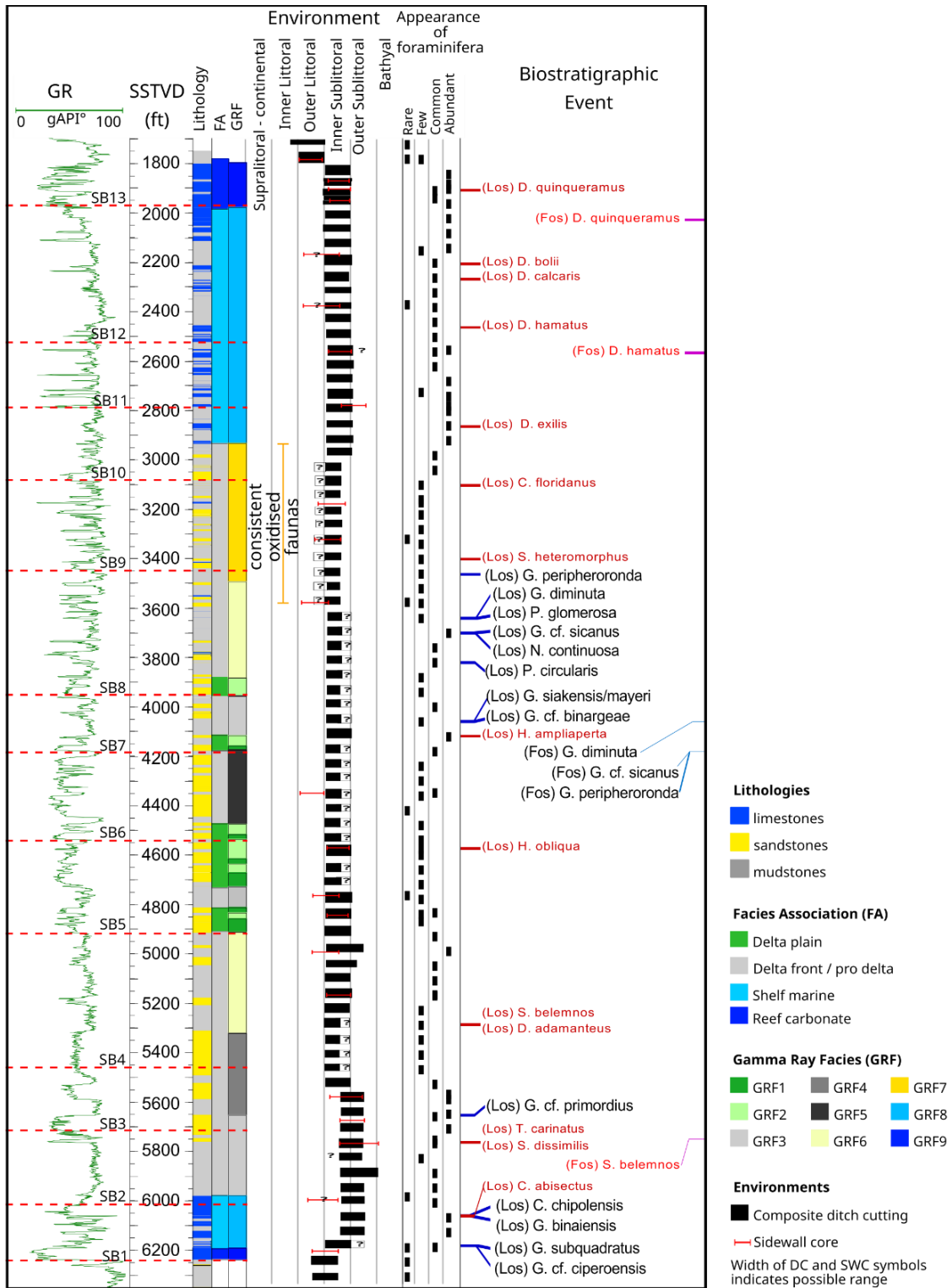


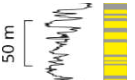





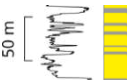

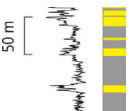

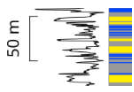

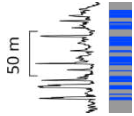

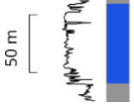



Figure 5.7. SD-1 well sequence stratigraphic interpretation with biostratigraphic report (modified from Noon et al, 1993).

Table 5.1 Gamma ray log facies (GRF) observed in Baturaja, Upper Cibulakan, and Parigi Formation. The stacking patterns associated with these gamma-ray logs trends are illustrated as a black triangle for fining-upwards patterns, an inverted black triangle for coarsening-upwards patterns and a black rectangle for aggrading patterns.

<b>Facies Association</b>	Gamma ray log Facies	GR Log type	GR shape	Stacking pattern	Lithology composition	Interpretation	Distribution
<b>FA 1</b>	GRF 1		Blocky		Intercalation of sandstone and shale with minor limestone layers characterizes the Upper Cibulakan Formation. The sandstone exhibits a light brown to grey color, is soft to friable, and varies from very fine to medium grain. It is medium sorted with an angular to sub-angular shape. The calcareous content in the sandstone increases upward. The limestone layer thickens and becomes more common upward. Thicker limestone layers (>5m) typically appear as grey to brown foraminifera wackestone to packstone. In cases where thin spiky gamma-ray	Amalgamated channel / point bar	Massive unit especially in the W-1 and SZN-1 (proximal well)
	GRF 2		Bell			Delta plain/ distributary channel	Evenly distributed in Massive unit
<b>FA 2</b>	GRF 3		Funnel			Delta front / mouth bar deposit	Lower part of massive unit and lower part of main unit
	GRF 4		Blocky serrated			Stacked proximal mouth bar	Lower part of massive unit
	GRF 5		Amalgamated funnel			Stacked Mouth bar	Upper part of massive unit
	GRF 6		Stacked funnel			Delta front, shoreface, and proximal mouth bar	Lower part of massive unit and lower part of main unit

	GRF 7		Hourglass serrated		signatures are present, they are usually associated with hard, dense crystalline limestone.	Tide dominated shelf ridge	Middle part of Main Unit
<b>FA 3</b>	GRF 8		Spiky			Reworked carbonate in storm dominated shelf system	Upper part of Main unit
<b>FA 4</b>	GRF 9		Blocky		White to grey dolomitic limestone, varying from floating biogenic fragment, fine to medium grained calcarenite, to crystalline. Appears to have been deposited in a clean low energy environment (W-1 well core description).	Reef carbonate	Baturaja and Parigi Formation

### 5.3. Sequence Stratigraphy Interpretation

Thirteen third order sequences have been interpreted within the SD-1 well, from BRF to Parigi formations. This interpretation is primarily based on the stacking pattern of gamma-ray and lithology variation (figure 5.8). Additionally, consideration has been given to the biostratigraphic report conducted by Noon *et al*, 1993, which has been reviewed and integrated into our interpretation (figure 5.7). Most of those third order sequences, delimited by sequence boundaries, have been recognized on the seismic lines. The age of each sequence boundary is then assigned based on the combination of biomarker fossils and the global sea level curve (Miller *et al.*, 2020). Special attention was given because most of the fossil retrieved came from ditch cuttings in which down casing often occurs.

The SD-1 well is one of the deepest wells in the research dataset and has the most comprehensive dataset compared to other wells. Additionally, considered to be far from fault zone, minimizing the effects caused by faults, we have decided to use the SD-1 well as the key well for sequence stratigraphy interpretation. First, we placed sequence boundaries candidate based only on SD-1 data. After completing the analysis, the correlation of sequence boundaries was carried out for all available wells (figure 5.9 and 5.10). At this stage, the sequence boundary established in SD-1 could be modified to accommodate the data in other wells.

#### 5.3.1. Sequence 1

Sequence 1, observed in all the wells, is characterized by blocky GR (GRF9) transitioning to spiky GR stacking pattern (GRF8) in the wells that penetrate the deeper area of the basin (SH-1 and SD-1) and massive blocky GR (GRF9) in the shallower area (W-1 and SZN-1). This sequence predominantly consists of limestone with minor shale beds. The base limit of sequence 1 is characterized by a sharp base interpreted as sequence boundary (SB 1) and is coincident with the base of BRF (23.04 Ma). The decision to place SB 1 precisely at the boundary between the Talang Akar Formation (TAF) and Baturaja Formation (BRF) is based on the GR log pattern, which exhibits a fining-upward trend in TAF. It consistently shows high GR values at the upper boundary of TAF, abruptly shift to very low, forming a sharp contact at the lower boundary of BRF (figure 5.9 and 5.10). This is consistent with Widodo (2018) who claimed that the lower part of Baturaja was deposited during a rapid transgressive event above sequence boundary at the end of TAF deposition. Additionally, a brief sea-level drop during



the Chattian-Aquitainian transition (23.04 Ma) (Miller *et al.*, 2020) could be responsible in shaping this sequence boundary.

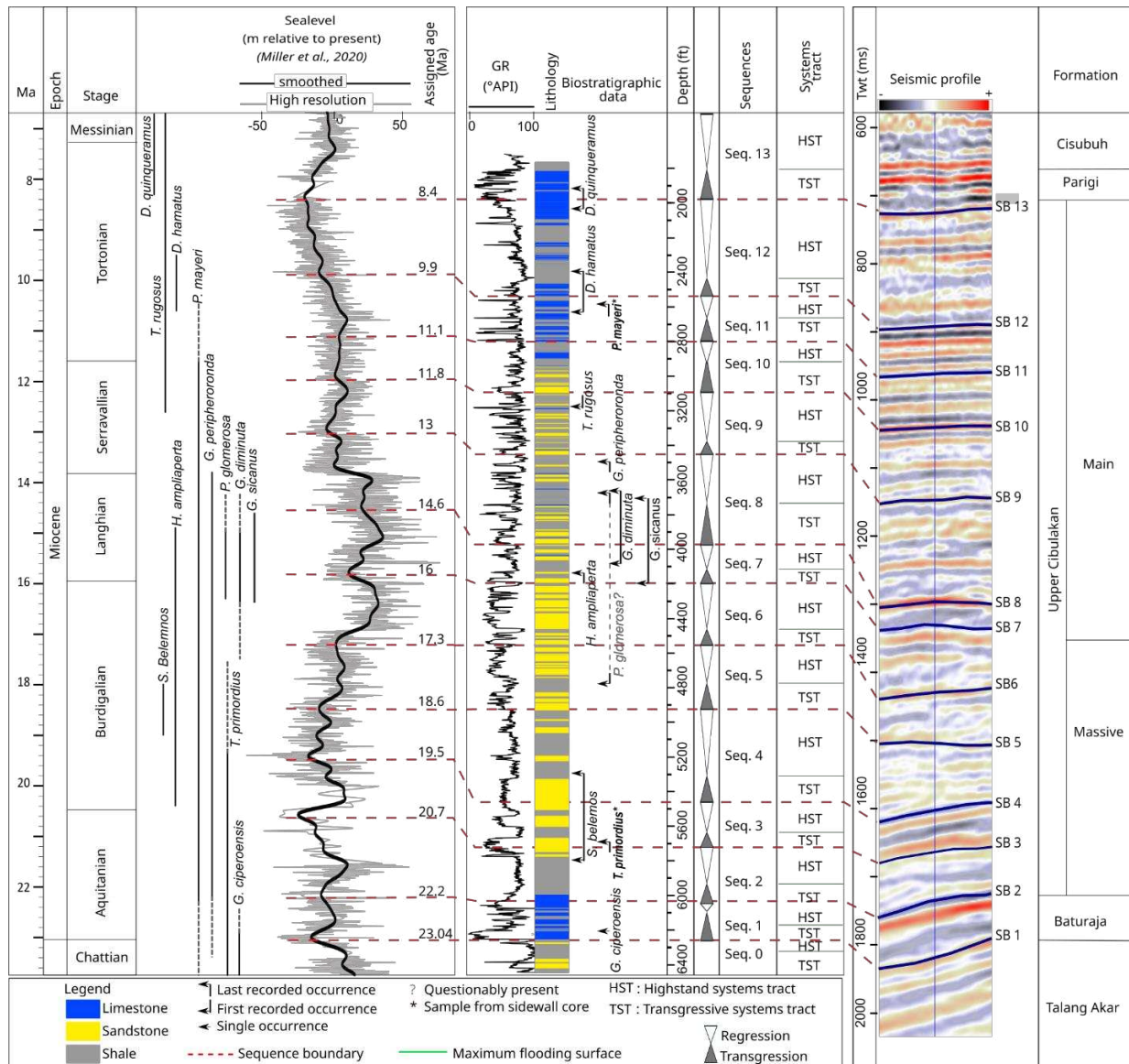


Figure 5.8. The general sequence stratigraphic chart of the Ardjuna sub basin NWJB based on the analysis of the SD-1; selected calcareous nannofossils and planktonic foraminifera data are based on (Noon *et al.*, 1993), refer to figure 5.7 for complete species. The apparent age of sequence boundary is determined from combination of global bio event in GTS 2020 (Gradstein *et al.*, 2020) and global sea level event (Miller *et al.*, 2020).

We interpret the timing of the initial development of the BRF (sequence 1) at the Chattian-Aquitainian transition. This interpretation is in line with Purantoro *et al.* (1994) and Atkinson (1993), while some researchers, i.e. Burbury (1977), placed the onset of the BRF older in the Rupelian, and Arpandi and Patmosukismo (1975); Noble *et al.* (1997, 1991) placed it younger in the mid-Burdigalian.

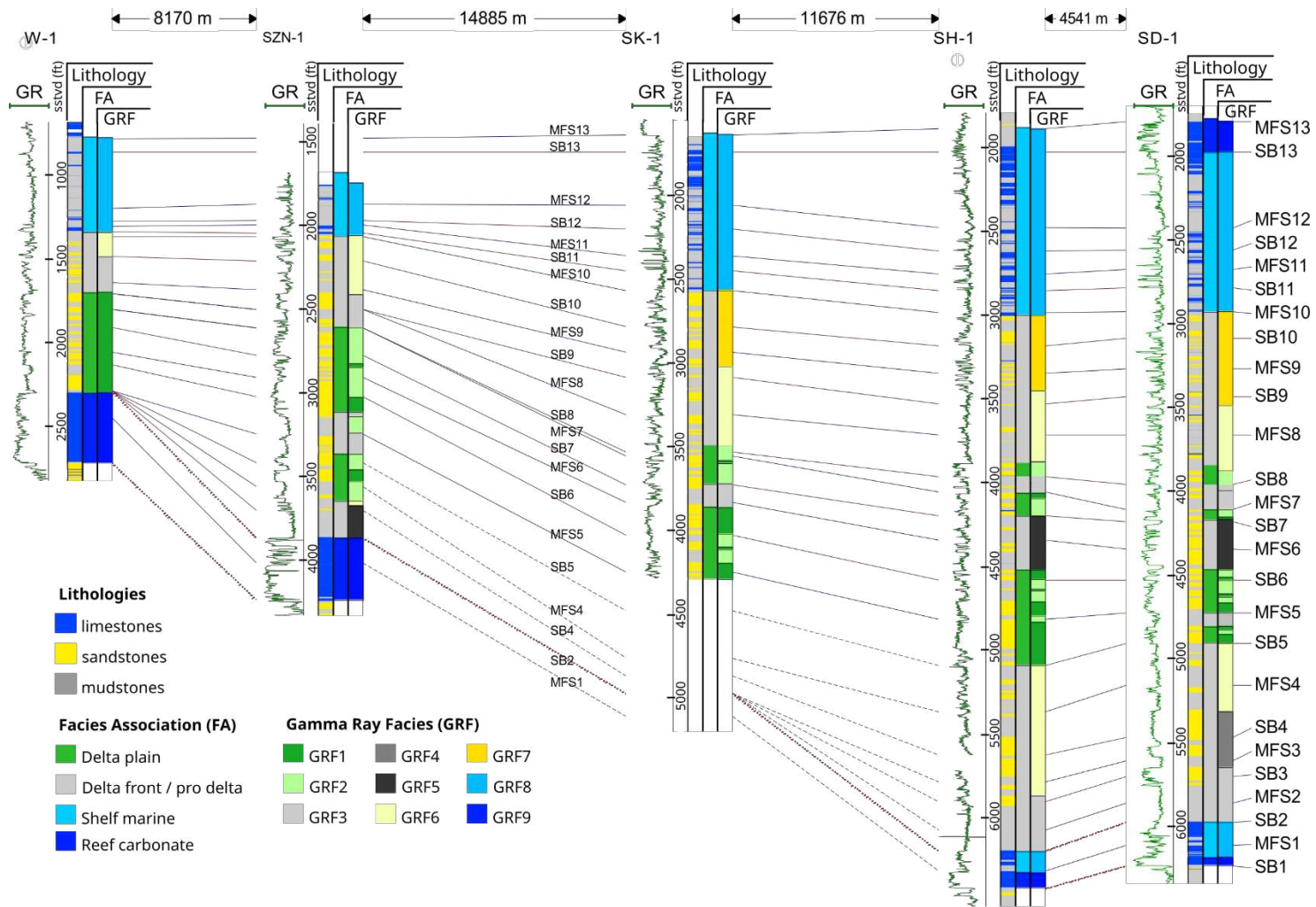


Figure 5.9. North – South sequence stratigraphic. The wells are flattened on datum (SB13).

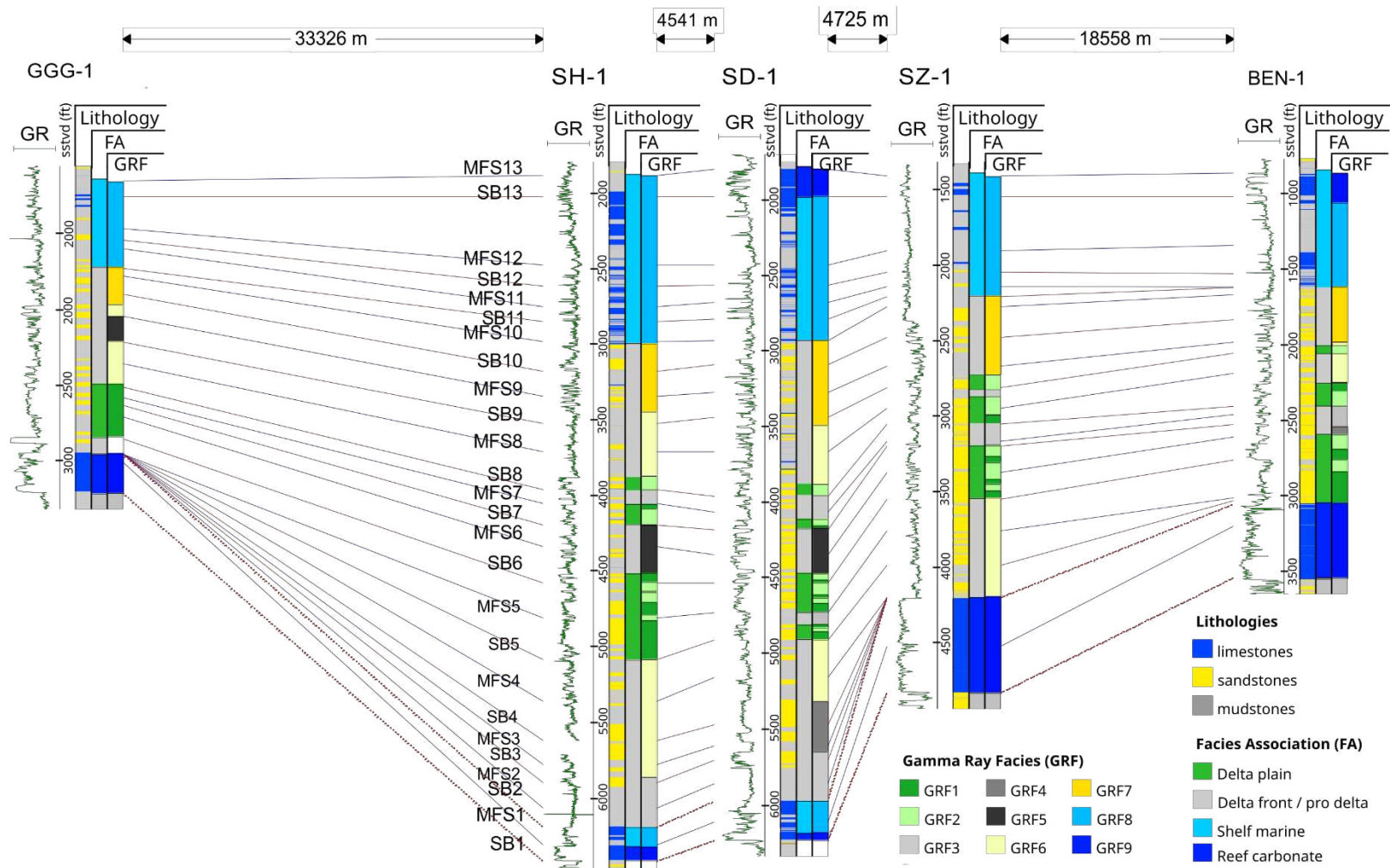


Figure 5.10. West – East sequence stratigraphic. The wells are flattened on datum (SB13)

This difference may occur due to the diachronic nature of BRF that developed in relative marine transgression (Burbury, 1977; Clements and Hall, 2007), they could develop and demise earlier in deeper basin area and later in structurally high areas. The end of BRF deposition can be recognized lithologically above the last occurrence of thick carbonate beds. In this case, we place it as SB 2 (Early Aquitanian). Almost all of the researchers mentioned above reported the end of the BRF at the Burdigalian-Langhian transition (near SB7 in figure 5.7). However, our biostratigraphic data does not support those interpretations, therefore it is possible that BRF was still being developed in other structurally higher areas outside the study area and co-evolved with the lowermost part of the UCF.

### 5.3.2. Sequence 2

Sequence 2 is characterized by a fining-up GR stacking pattern and comprises thin limestone layers gradually transitioning to claystone in its upper part. It exhibits a northward thinning trend, approaching a basement high, and eventually thins out at W-1 (figures 5.9 and 5.10). This sequence is notably present in wells SH-1 and SD-1, marking the beginning of a substantial clastic supply as the Massive unit overlays the Baturaja Formation (figures 5.7 and 5.9). The interpretation of the gamma-ray stacking pattern indicates that sequence 2 begins with a transgressive system tract (TST) above the BRF, characterized by a fining-upward stacking pattern, followed by a highstand system tract (HST) marked by a coarsening-upward stacking pattern. The gradual transition from BRF to UCF makes it challenging to determine the basal limit of sequence 2.

Despite the absence of a distinct response in the logs of both wells at the base of sequence 2 (figures 5.9 and 5.10), the lack of response suggests the likely absence of lowstand sediments in wells SD-1 and SH-1, indicating a shelf bypass. The transgressive system tract is observed to be directly deposited above the Baturaja Formation. The interpretation is supported by a non-deposition unconformities at the top of the Baturaja Formation in GGG-1 well, indicated by the younger age of the UCF (N5 – N6; *Globigerinoides altiapertura*) compared to deeper well (SD-1), as well as The rapid change in thickness of the Baturaja Formation, showing a thick blocky gamma-ray pattern (GRF9) in SZ-1 (indicative of reef facies), compared to thinner intervals in SH-1 and SD-1 wells, implies a significant paleotopographic difference between the Ardjuna sub-basin and the Central High (figure 5.11). Furthermore, the patterns of porosity indicator log (RHOB,



NPFI, and Sonic) in W-1 and SZ-1 show an increasing trend towards the top of the Baturaja Formation, suggesting the upper part of BRF might have experienced dissolution and subaerial exposure at the end of its deposition (figure 5.11). Coring operations captured only 25% of the total core length, obtaining soft, earthy, and crumbling rubble samples (core description sheet well W-1, Pertamina, 1973; unpublished). This phenomenon likely occurred due to natural caving in W-1, and it is highly probable that during the deposition of sequence 2, there was a significant drop in sea level, making the top of BRF a suitable sequence boundary.

The base limit of Sequence 2 (SB 2) occurs 40 meters (131 ft) above the occurrence of *G. ciproensis* (LOs at 22.9 Ma) and can be associated with the short-term sea-level fall during the Aquitanian (22.2 Ma). Therefore, we assign the age of SB 2 to approximately 22.2 Ma.

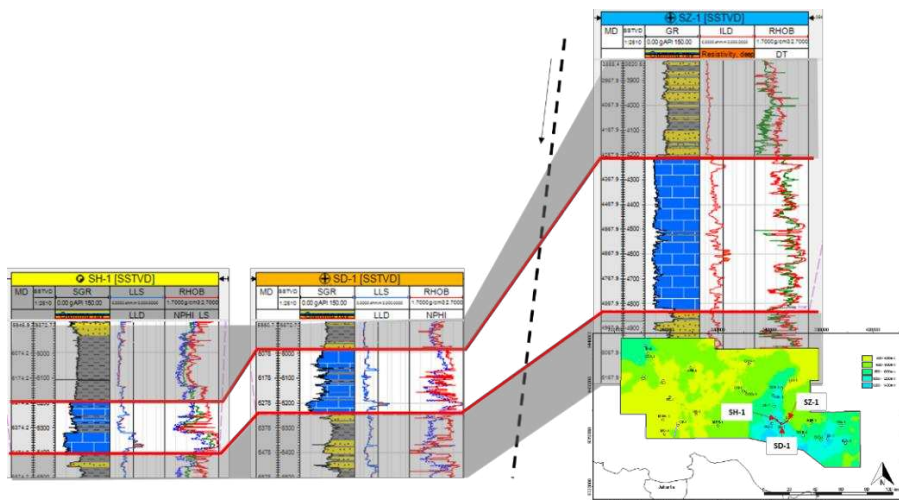


Figure 5.11. Correlation on SH-1; SD-1; and SZ-1 well showing the different features in the Baturaja Formation

### 5.3.3. Sequence 3

Sequence 3 is characterized by blocky to fining up GR stacking patterns at its base and is followed by a coarsening up stacking pattern. Its thickness varies from 80 m in the basinal area and is absent on the structural high area towards the Central Platform (W-1, SZ-1, and BEN-1) (see figure 4.15 for the location of Central platform).

In wells SD-1 and SH-1, this sequence is characterized by the first thick sandstone layer with a coarsening-upward pattern (GRF3) in the Massive unit (figure 5.9 and 5.10). The decision to

place a sequence boundary at the base of this sandstone primarily relies on the gamma-ray log pattern, supported by dip meter analysis in well SH-1. In this well, a southwestward dip direction ( $225^{\circ} - 270^{\circ}$ ) is observed in the lower interval, abruptly shifts at a depth of 1800 m (5904 ft) sstvd towards the southeast ( $90^{\circ} - 135^{\circ}$ ) (figure 5.4c and 5.12). Although the dip angle values in the upper interval are relatively small ( $<7^{\circ}$ ), making the dip direction less reliable due to the difficulty in determining layering direction in relatively flat layers, the dominance of the dip direction shows a uniform trend and increases the confidence level in the interpretation of dip and dip direction in this interval. We interpret this abrupt change in dip direction as a sequence boundary resulting from a shift in sedimentation patterns.

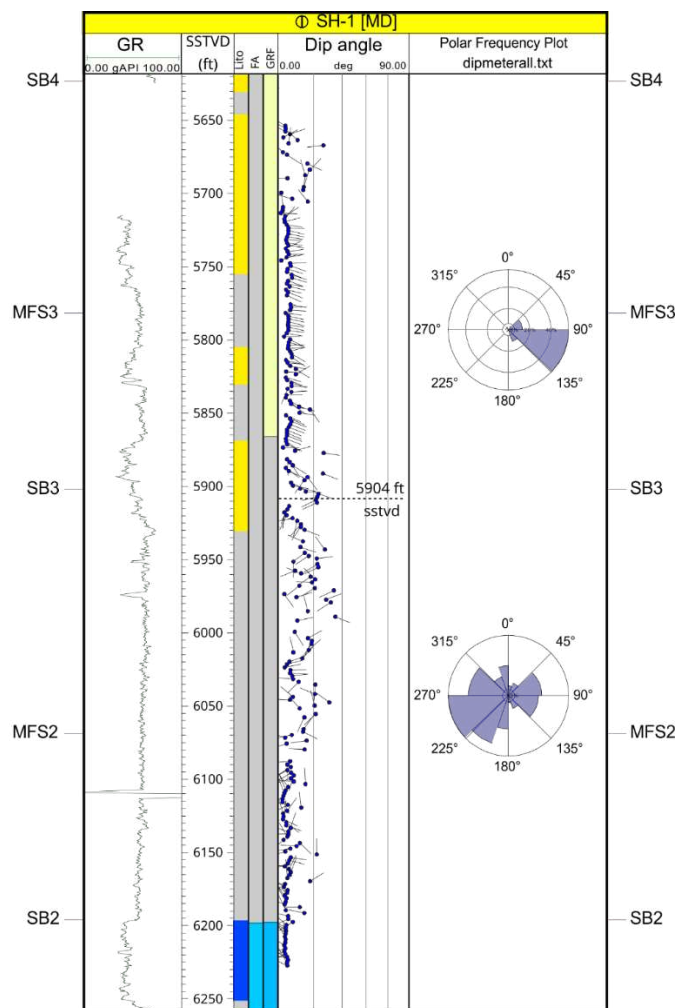


Figure 5.12. Dip meter and frequency plot of the dip direction in SH-1. The lower interval data showing southwest direction while the upper interval shows a southeast trend. Refer to figure 5.4c for detailed view in 5860 – 5960 ft depth. The tadpole data are based on formation micro scanner log (FMS) interpreted by Schlumberger (1992).



Basal limit of sequence 3 (SB 3) occurs 15 meters (49 ft) below the occurrence of *T. primordius* retrieved in a sidewall core (LOs at 17.54-19.3 Ma, Spezzaferri *et al.*, 2018), and *S. belemnos* (FOs at 19.01 Ma – LOs at 17.94 Ma). Fossil markers suggest an age of SB 3 within *S. belemnos* time interval (19.01 Ma – 17.94 Ma, but retrieved within cuttings). This limit, defined by thin blocky sandstone in GR, is a good candidate for the major sea-level fall known in late Aquitanian (20.7 Ma), before the occurrence of *T. primordius*. Thus, SB3 is tentatively assigned at ~20.7 Ma.

#### 5.3.4. Sequence 4

Sequence 4 is characterized by blocky fine sandstone beds at the base, grading to a long fining up stacking pattern (figure 5.9 and 5.10). Similar to the previous sequences, deposition in sequence 4 are confined to the basinal area, where its thickness reaches 140 m (459 ft), and are absent in the platform regions. The interpretation of a sequence boundary in this interval begins with the observation of a sudden sea-level drop recorded in the biostratigraphic report (figure 5.8). The thick sandstone at a depth of 1694 m (5560 ft) indicates an inner sublittoral to deep outer sublittoral environment, transitioning abruptly to an outer littoral – shallow inner sublittoral environment immediately above. We place the sequence boundary at a depth of 1664.2 m (5470 ft), precisely at the base of the thick blocky sandstone deposited in a shallower environment compared to the 1694 m (5560 ft) sandstone.

The sequence boundary marker falls within the *S. belemnos* (cn) LOs at 18 Ma and FOs at 19 Ma intervals. Initially, our tentative age estimate was based on this range. However, upon revisiting the biostratigraphic report, which indicates that the marker corresponds to a significant change in the depositional environment, we prefer to correlate it within a regional regressive event. We assign the base limit of sequence 4 (SB 4) an age of ~19.5 Ma, based on the assumption that it can be related to the short-term sea-level fall at early Burdigalian (19.5 Ma), being the lowest regional sea-level drop at that time.

#### 5.3.5. Sequence 5

Sequence 5 is characterized by fining up GR stacking pattern with increasing sandstone proportion compared to previous sequences. Unlike sequences 3 and 4, sequence 5 is present in all the studied wells, indicating its widespread presence within the area. This sequence is characterized by the onset of delta plain facies association (FA1) occurrences, which can be seen in all of analyzed wells. This indicates that during the deposition of sequence 5, the

Ardjuna sub-basin was dominated by prograding delta facies. Consequently, we place a sequence boundary below the first delta facies sandstone. This interpretation is further supported by biostratigraphic reports (Noon *et al.*, 1993), which indicate a decrease in the quantity of foraminifera fossils in many samples in this interval (figure 5.7).

Consequently, the absence of a clear fossil marker at the base of sequence 5 prevented the precise determination of the age of sequence boundary 5 (SB 5). A tentative age of ~18.6 Ma has been assigned to the base limit of sequence 5, in relation to a short-term sea-level fall (Miller *et al.*, 2020). Further investigations and additional data are required to refine the age determination for SB 5.

#### 5.3.6. Sequence 6

Sequence 6 is characterized by dominantly blocky gamma ray (GR) intercalated by several thin fining upward stacking pattern. The lithology within this sequence mainly consists of medium to fine-grained sandstone with intercalated shale layers. In the study area, sequence 6 thickens from 60 meters to 100 meters (196.5 to 328 ft) as it extends southward. The interpretation of the sequence boundary in this interval is mostly based on the observation of gamma-ray log, which shows the dominance of bell-shaped gamma-ray facies (GRF2), that eroded the underlying sandstone. This phenomenon is observed in all wells, especially in well SZN-1, supported by dip meter data showing a sudden shift in dip values (see depth 924 m (3030ft) in figure 5.2), suggesting that this erosion may have occurred regionally. Therefore, we place a candidate sequence boundary just below this sandstone.

The base limit of sequence 6 (SB 6) is observed approximately 10 meters (32.5 ft) above the occurrence of *H. ampliaperta*, with first occurrences (FOs) at around 20.43 Ma and last occurrences (LOs) at around 14.86 Ma in SZN-1. In SD-1, SB 6 is located about 125 meters (410 ft) below the last occurrence of *H. ampliaperta*. The GR trend within sequence 6 displays two successive transgressive-regressive packages. Comparing these patterns to the Miller *et al.* (2020) curve, a tentative age assignment of approximately 17.3 Ma is proposed for SB 6.

#### 5.3.7. Sequence 7

Sequence 7 is characterized by a fining upward stacking pattern, and is primarily composed of sandstone - shale intercalations. The thickness of this sequence varies between 30 meters and 95 meters (98.5 to 311.5 ft) within the study area. The determination of the sequence

boundary in this interval relies on observation from gamma-ray logs, lithology variations, and fossil content which mark facies associations. The occurrence of delta plain facies association (FA1) above the delta front facies association (FA2) in wells SH-1, SK-1, and SD-1 could indicate a sea-level fall. Therefore, we place a sequence boundary candidate just below the delta plain facies association of the next sequence.

The base limit of sequence 7 (SB 7) coincides with the first occurrence of *G. diminuta* (FOs at 16.38-17.54Ma, Kennett and Srinivasan, 1983), and *G. sicanus* (FOs at 16.4 Ma, Kennett and Srinivasan, 1983). Considering the sea-level fall observed at approximately 16 million years ago, a tentative age assignment of around 16 Ma is given to SB 7. The decrease in sandstone proportion observed from sequence 6 to sequence 7 is evident in the overall change in the gamma-ray stacking pattern and the lithological composition, which is rich in shale. This change is interpreted as a result of a maximum flooding event that occurred during the mid-Langhian period, estimated to be around 15.3 Ma (Miller *et al.*, 2020).

#### 5.3.8. Sequence 8

Sequence 8 is characterized by a fining upward stacking pattern followed by a coarsening pattern. Within this sequence, there is an intercalation of sandstone – shale layers with minor occurrences of limestone. The thickness of this sequence ranges between 55 m and 160 m (180.5 to 524.9 ft) in the wells (figure 5.9). Determination of the sequence boundary is also based on the analysis of gamma-ray logs, lithology variations, and fossil content represented through facies interpretation. In this sequence, there is a repetition of delta plain facies association above the delta front facies association from the underlying sequence 7, leading us to place a sequence boundary below the delta plain sandstone.

The base limit of sequence 8 (SB 8) falls within the range of the first occurrences of *G. diminuta* and *G. sicanus*. Based on the age assignment of SB 7 at approximately 16 Ma, SB 8 is tentatively assigned an age around 14.6 Ma. This determination places SB 8 after the mid-Langhian maximum flooding event.

#### 5.3.9. Sequence 9

Sequence 9 is characterized by a serrated coarsening up stacking pattern. It primarily consists of sandstone-shale intercalations, with an increasing proportion of limestone layers towards the top of the sequence. The thickness of sequence 9 increases towards the South,

ranging from 20 meters to 160 meters (65.6 to 524.9 ft) across the wells. Similar to sequence 8, the repetition of delta front facies association from the underlying sequence 8 to delta plain facies also occurs in this sequence, particularly observed in wells SZ-1 and BEN-1 (figure 5.10). Therefore, we also place a candidate for the sequence boundary precisely below the sandstone of delta plain facies.

The base limit of sequence 9 (SB 9) aligns with the approximate last occurrence of *G. peripheroronda*, estimated to be around 13.91 Ma. Considering the significant Early-Serravallian sea-level fall that occurred at approximately 13 Ma, a tentative age assignment around 13 Ma is assigned to SB 9.

#### 5.3.10. Sequence 10

Sequence 10 is characterized by an overall fining up stacking pattern. It is composed of intercalations of sandstone, shale, and limestone, with an increasing abundance of limestone towards the top of the sequence. Thickness of sequence 10 also increases in a southerly direction, ranging from 40 m to 100 m (131.2 to 328 ft). Determination of the basal limit of this interval is supported by the observation of gamma-ray logs, indicating the presence of hourglass serrated gamma-ray facies (GRF7; figure 5.9 and 5.10). The lower part of this facies is marked by a fining-upward gamma-ray trend, followed by a coarsening-upward pattern. We interpret this gamma-ray pattern as indicative of a tide-dominated shelf ridge where the lower part may represent a step of embayment mouth, thus we place a sequence boundary below the fining upward sandstones.

The base limit of sequence 10 (SB 10) occurs few meters above the first occurrence of *T. rugosus* (FOs at 12.67 Ma). As a result, we assigned the age of SB 10 to ~11.8 Ma where a sea-level fall is documented (Miller *et al.*, 2020).

#### 5.3.11. Sequence 11

Sequence 11 is characterized by serrated stacking pattern, and consists of limestone – shale alternations, with a thickness ranging from 45 m to 75 m (147.6 to 246.1 ft) in the wells. The gamma-ray log pattern in this sequence does not indicate the development of a new sequence after sequence 11. Interpretation of sequence 11 is mainly based on 1) the lithological content indicating the occurrence of a thick limestone-rich interval in the well, supported by 2)

the seismic stratigraphic interpretation revealing the formation of carbonate mound structures in this interval. Further discussion on this will be elaborated in the seismic stratigraphy section.

Due to the absence of fossil markers near the base of sequence 11, we were unable to precisely determine its age. However, we can infer that SB11 must be older than *D. hamatus* (FOs at 10.57 Ma) and *P. mayeri* (LOs at 10.54 Ma). Considering the increasing trend of limestone layers in the sedimentary record, which is likely associated with a short-term sea-level fall, we tentatively assign an age of ~11.1 Ma to SB11 coinciding with slight sea-level fall (figure 5.7).

#### 5.3.12. Sequence 12

Sequence 12 begins with an interpreted fining-up stacking pattern followed by a coarsening up trend. This sequence comprises limestone - shale intercalations, with the thickness of limestone layers increasing towards the top (figure 5.9 and 5.10). The thickness of sequence 12 varies from 110 m to 190 m in the study area.

The base limit of sequence 12 (SB 12) is few meters above the last occurrence of *P. mayeri* (LOs at 10.54 Ma), and falls within the range of *D. hamatus* (first occurrence at 10.57 Ma and last occurrence at 9.61 Ma). Within this timeframe, we assign an age of ~9.9 Ma to SB 12 coinciding with a sea-level fall. As for sequence 11, the top of sequence 12 is marked by a seismic reflector marking an erosive surface.

#### 5.3.13. Sequence 13

Sequence 13 is incomplete in the study area but initiates with thick, blocky to fining-up gamma-ray trends. This sequence predominantly consists of thick limestone layers with minor shales. The sequence boundary of sequence 13 coincides with the marker top of the Upper Cibulakan Formation. It is characterized by the presence of thick limestone in well SD-1, deposited above shale dominated interval and intercalated with limestone.

The base limit of sequence 13 (SB 13) falls within the range of *D. quinquerramus* (FOs at 8.10 Ma and LOs at 5.23 Ma). Characterized by fining upward gamma-ray stacking pattern with a sharp contact, the base limit of sequence 13 (SB 13) coincides with the base of the Parigi Formation, which is assigned an age of approximately 8.4 Ma.

## 5.4. Seismic Stratigraphy Interpretation

### 5.4.1. Seismic Facies

Nine seismic facies were identified in the available seismic data (table 5.2). Seismic facies 1 (SF1) is characterized by parallel; generally continuous strong contrast high amplitude, and low frequency reflectors. This facies can be found in both the sequence 1 (Baturaja Formation) and in sequence 13 (Parigi Formation). Within the sequence 1, this seismic facies occurs in low areas of the Ardjuna sub-basin, suggesting regions with clastic deposition or reworked carbonate in deeper sea levels. In sequence 13, SF1 can be found in areas that are proximal to the reef facies of the Parigi Formation, indicating deposition in inner platform. Well bore data shows that SF1 displays a blocky gamma-ray stacking pattern in a carbonate facies (GRF9) grading to spiky with limestone – shale intercalations (GRF8).

Seismic facies 2 (SF2) is characterized by high amplitude of seismic reflector at the top, with irregular internal architecture that shows a contorted, semi-continuous reflector, and high to moderate frequency. This facies can be found in both sequence 1 (Baturaja Formation) and sequence 13 (Parigi Formation). In sequence 1, SF2 is found in high areas (Central and Seribu platforms), while in the sequence 13 it can be found in the Southeastern area where the reefal complex of Parigi Formation is found. Some mounded internal structures are observable both in BRF and Parigi Formation, especially where the facies is thick. The well drilled in this facies displays a blocky thick gamma-ray log pattern (GRF9), predominantly composed of limestone with minor shale layers. Based on the reflectors configuration and lithological variation, SF2 is interpreted as carbonate developed in a barrier or platform interior.

Seismic facies 3 (SF3) is characterized by mounded reflector configuration with high amplitude reflectors at the top. The internal structures of this facies shows contorted to chaotic reflectors. This seismic facies is exclusively found in sequences 11 and 12 (pre Parigi carbonate), particularly in the central to southwest region of the research area, exhibiting an elongated geometry trending northwest-southeast. Well SSZ-1 was drilled specifically to penetrate this facies (figure 4.34), revealing that the gamma-ray stacking pattern displays a blocky thick gamma-ray log pattern (GRF9) with limestone lithology. Based on the seismic facies geometry, lithological and gamma-ray characteristics, this facies is interpreted as a carbonate reef-bound shelf margin.



Seismic facies 4 (SF4) is characterized by sigmoid progradational, discontinuous, medium to low amplitude with high frequency reflectors. This seismic facies can be identified in sequences 2 to 7, concentrated in the downthrown area of the Ardjuna fault. The limited distribution of this facies suggests that during the deposition of sequences 2 to 7, there was a difference in elevation causing sediment- supply from the central platform into the Ardjuna sub-basin with sigmoidal progradational geometry. Well data that penetrated this seismic facies reveals a series of deltaic facies from GRF1 to 6. Based on seismic and well observation, SF4 is interpreted as clastic delta progradation driven by sediment supply, in a in gentle to moderate slope area.

Seismic facies 5 (SF5) is characterized by oblique progradational, discontinuous, medium to high amplitude with medium frequency reflectors. This seismic facies is also present in sequences 2 to 7, in the northern part of the study area. A significant difference from SF4, as seen in the seismic section, is the slope during its deposition. In contrast to SF4, this obliquely prograding facies is deposited in a relatively flat area in the northern part of the study area. Seismic interpretation indicates that the progradation direction of this facies is from north to south, indicating the depositional direction during the deposition of sequences 2-7. Well SZN-1 penetrates the distal part of this seismic facies and shows the same gamma-ray facies as observed in SF4. Based on the geometry observed in seismic data and the lithology variation in the well data, this seismic facies is interpreted as clastic delta progradation driven by sediment supply, within a flat to very gentle relief.



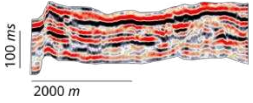

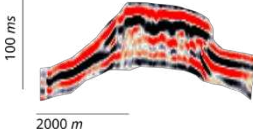

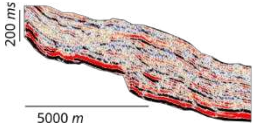

Seismic facies 6 (SF6) is characterized by subparallel, semi continuous high amplitude and high frequency reflectors, with onlap termination. This seismic facies can be found in sequences 8 and 9, particularly in the northern area. The well data that penetrated into this seismic facies show a dominance of amalgamated funnel pattern characteristics of GRF6 and serrated gamma-ray stacking pattern of GRF7. Based on seismic and well observation, SF6 is interpreted as clastic delta progradation driven by sea level fall.

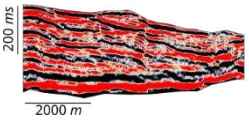

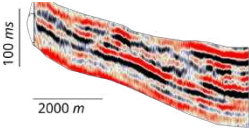

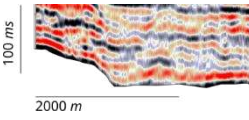

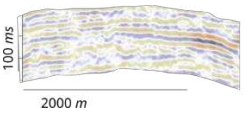

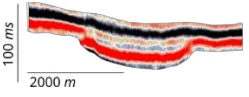

Seismic facies 7 (SF7) is characterized by subparallel to chaotic, discontinuous, with low amplitude and high frequency reflectors. This seismic facies can be found in sequences 10 and 11, particularly in the northern area similar to SF6. Well data that penetrated into this seismic facies consists of GRF6 and GRF7. Based on seismic and well observation, SF7 is interpreted as retrogradation of delta facies (backstepping) driven by relative sea-level rise.

Seismic facies 8 (SF8) is characterized by parallel to subparallel continuous reflectors, with low amplitude and high frequency. This seismic facies is found throughout all the sequences of the Upper Cibulakan Formation. It is generally located in relatively distal areas compared to SF4 to SF7. Well data penetrating this seismic facies indicates that it is composed of intercalations of sandstone, shale, and limestone, as indicated by GRF3 to 7. Based on seismic and well observation, SF8 is interpreted as clastic deposits in a distally deltaic to marine environment (prodelta to shelf).

Seismic facies 9 (SF9) is characterized by hummocky, semi continuous reflectors, showing channel like feature, with high amplitude and high frequency reflection. This seismic facies can only be identified in sequence 10 in the northern area. The distribution of this seismic facies cannot be clearly mapped on seismic sections and is only found in a few west-east-oriented seismic sections. No wells penetrate this seismic facies, and its interpretation is solely based on the geometric shape observed on seismic sections. This seismic facies is interpreted as a channel fill and levees in delta environment (distributary channel).

Table 5.2 Seismic facies (SF) observed in Baturaja, Upper Cibulakan, and Parigi Formation.

Name	Seismic example	Line drawing	Description	Interpretation	Distribution
SF1			Parallel continuous, high amplitude with low frequency	Clastic carbonate deposit in the inner/peripheral platform	Deeper part of the Ardjuna sub-basin in Sequence 1 (BRF); and in the central to northern area of Sequence 13 (Parigi)
SF2			High amplitude contrasts at the top with internal structures showing contorted semi-continuous high to moderate amplitude, and frequency; some mounded internal structures are observable	Reefal carbonate in platform margin	Platformal region in Sequence 1 (BRF); and in the southern area of Sequence 13 (Parigi)
SF3			Mounded configuration with high amplitude at the top. Internal structures show contorted to chaotic reflectors	Reef-bound shelf margin	Sequence 11 and 12 (Upper Main)
SF4			Sigmoid progradational, discontinuous medium to low amplitude with high frequency	Clastic delta progradation driven by sediment supply, in a gentle to moderate slope area	Sequences 2 - 7 (Massive unit) in the downthrown area close to the Ardjuna fault

Name	Seismic example	Line drawing	Description	Interpretation	Distribution
SF5			Oblique progradational, discontinuous medium to high amplitude with medium frequency	Clastic delta progradation driven by sediment supply, within a flat to very gentle relief	Sequences 2 - 7 (Massive unit) in the northern area
SF6			Subparallel continuous high amplitude and high frequency, with on lap termination	Clastic delta progradation driven by sea level fall	Sequence 8 - 9 (Lower Main) in the northern area
SF7			Subparallel to chaotic discontinuous with low amplitude and high frequency	Retrogradation (backstepping) driven by relative se-level rise	Sequence 10 - 12 (Upper Main) in the northern area
SF8			Parallel to subparallel continuous with low amplitude and high frequency	Clastic deposit in a distal delta to marine environment (prodelta to shelf)	Sequence 2 - 12 (Massive and main) usually next to SF4 to 7
SF9			Hummocky semi continuous showing the channel like feature, high amplitude and high frequency	Channel fill and levees in a delta plain (distributary)	Sequence 10 in the northern area

#### 5.4.2. Third Order Sequence Seismic horizon interpretation

Fourteen seismic horizons including SB1 to SB13 and the top Parigi have been interpreted on the seismic section to map their distribution throughout the study area. Our well log and biostratigraphic analysis revealed that these limits, spanning 0.7 – 1.6 Ma, delineate boundaries of third-order sequences. These sequences displaying specific internal geometrical patterns and characteristics resulting from variations in accommodation space and sedimentary supply. In the sequence stratigraphy interpretation, the top Talang Akar is defined as sequence boundary (SB)1, top Baturaja as SB2, top Massive as SB7, and top Upper Cibulakan Formation as SB13. As for the top Parigi horizon, it is an interpretation based on lithostratigraphy where we placed the horizon at the most contrasting amplitude above the interpreted carbonate geometry. During seismic interpretation, this horizon shows a tendency to cross the reflectors continuity due to lateral facies change. Meanwhile, the more continuous shale horizon, interpreted as MFS13, exists above this lithostratigraphic horizon, thus the MFS13 serve as the sequence stratigraphic marker (figures 5.9 – 5.10).

Nine 2D seismic lines are included in this report to illustrate the distribution of sequence boundary horizons in each area of the study site (figure 5.1), divided into six North-South (dip direction) seismic lines representing the western, central, and eastern boundaries (figures 5.13 – 5.17), as well as three West-East (strike direction) seismic lines in the northern, central, and southern regions of the study area (figure 5.18 – 5.20).

Sequence 1 (bounded by SB 1 at the base and SB 2 at the top) is characterized by high amplitude seismic reflectors overlying syn-rift strata with low to moderate amplitude reflectors. The seismic interpretation indicates that the distribution of sequence 1 or the Baturaja Formation extends throughout the study area, with the thickest section located in the Central platform and Seribu platform regions (figures 5.13, 5.19), dominated by the reefal carbonate seismic facies (SF2). It thins towards the Ardjuna sub-basin (figures 5.14, 5.16, and 5.19), evolving to clastic carbonate seismic facies (SF1). This thinning can also be observed in the northern area, as shown by seismic line WE1 (figure 5.18) that shows the relatively flat-thin Baturaja deposits, dominated by SF1, while SF2 is no longer present. This North direction thinning distribution is observed consistently in both the basinal and platformal areas, indicating that the northern part of the study area was close to the paleo shoreline during the deposition of sequence 1.



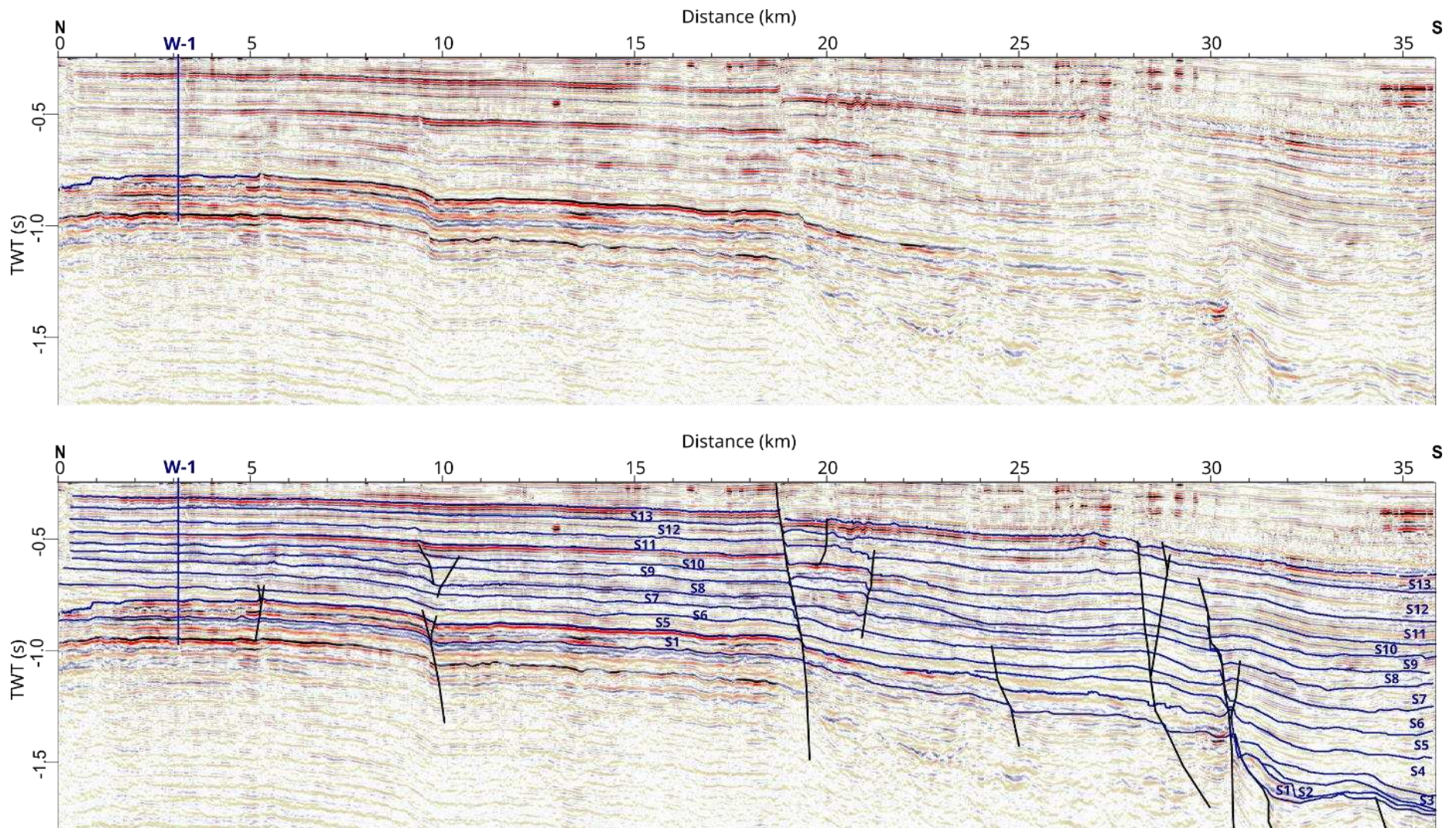


Figure 5.13. Sequence boundary interpretation on seismic line NS1a representing the dip line interpretation in the Central platform to Ardjuna sub basin. S1 – S13 denote the sequence number based on their description in the wells.



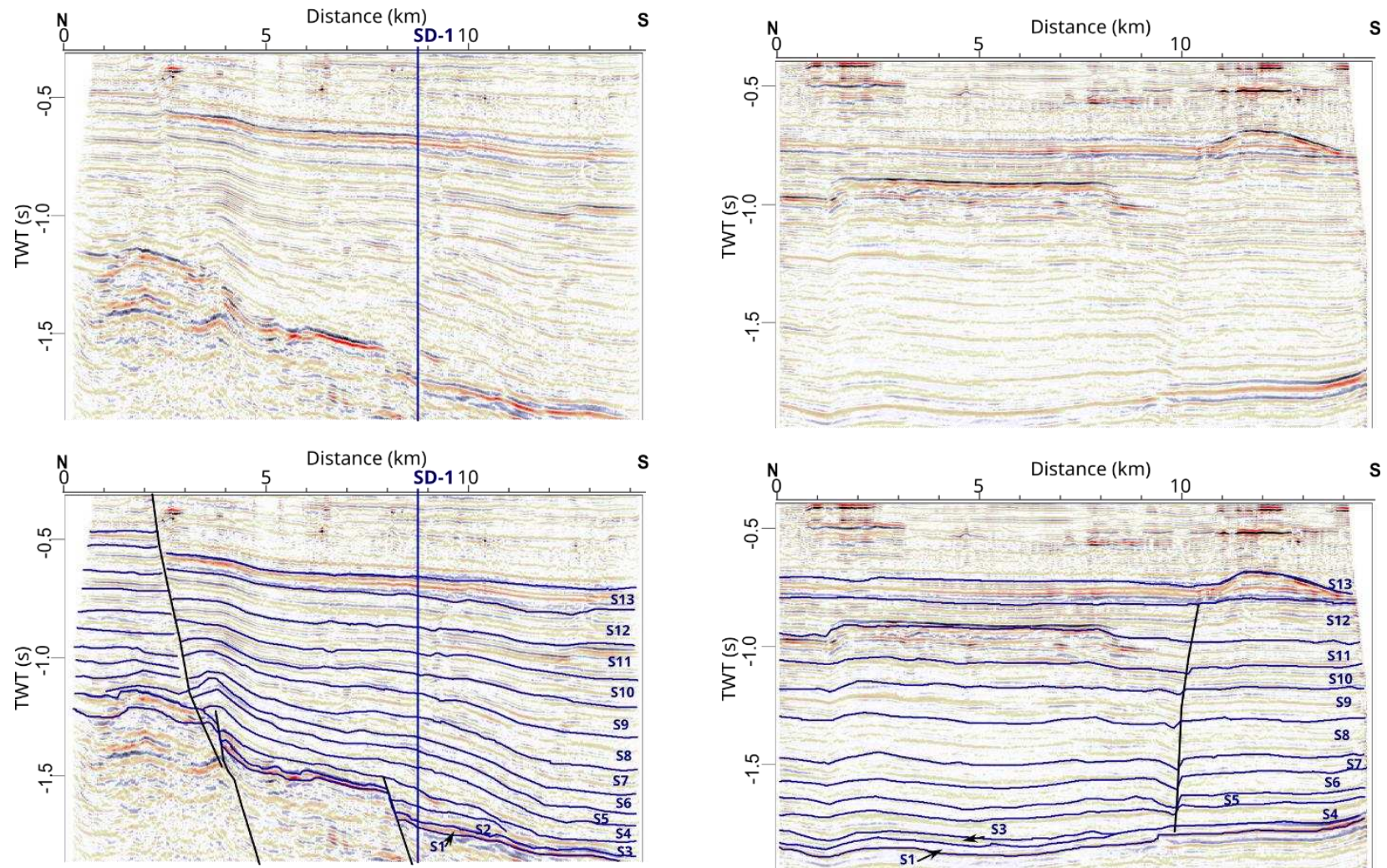


Figure 5.14. Sequence boundary interpretation on seismic line NS1b (left) and NS1c (right) representing the dip line interpretation in the Western margin of Ardjuna sub basin. S1 – S13 denote the sequence number based on their description in the wells.



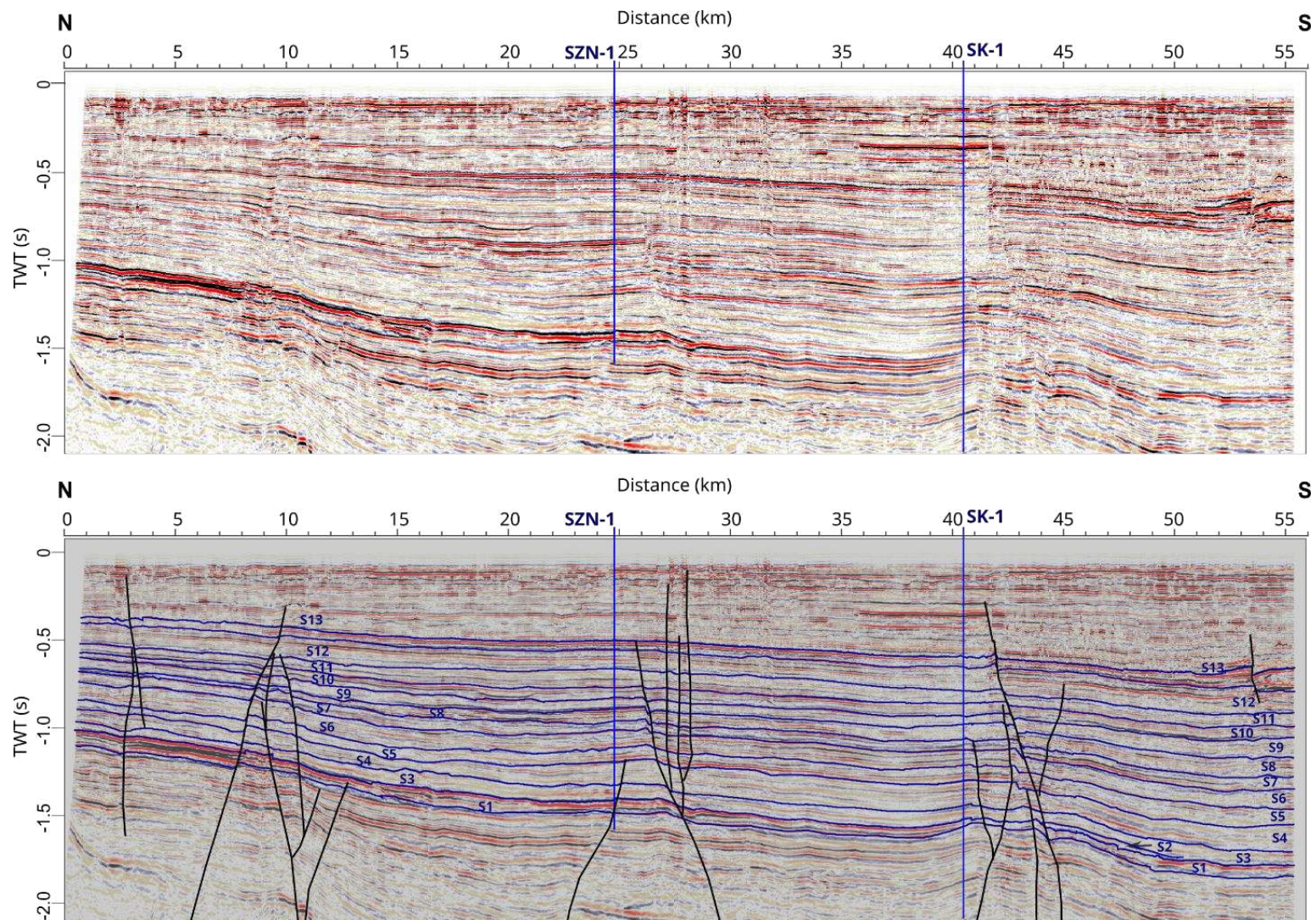


Figure 5.15. Sequence boundary interpretation on seismic line NS2 representing the dip line interpretation in the Ardjuna sub basin. S1 – S13 denote the sequence number based on their description in the wells.



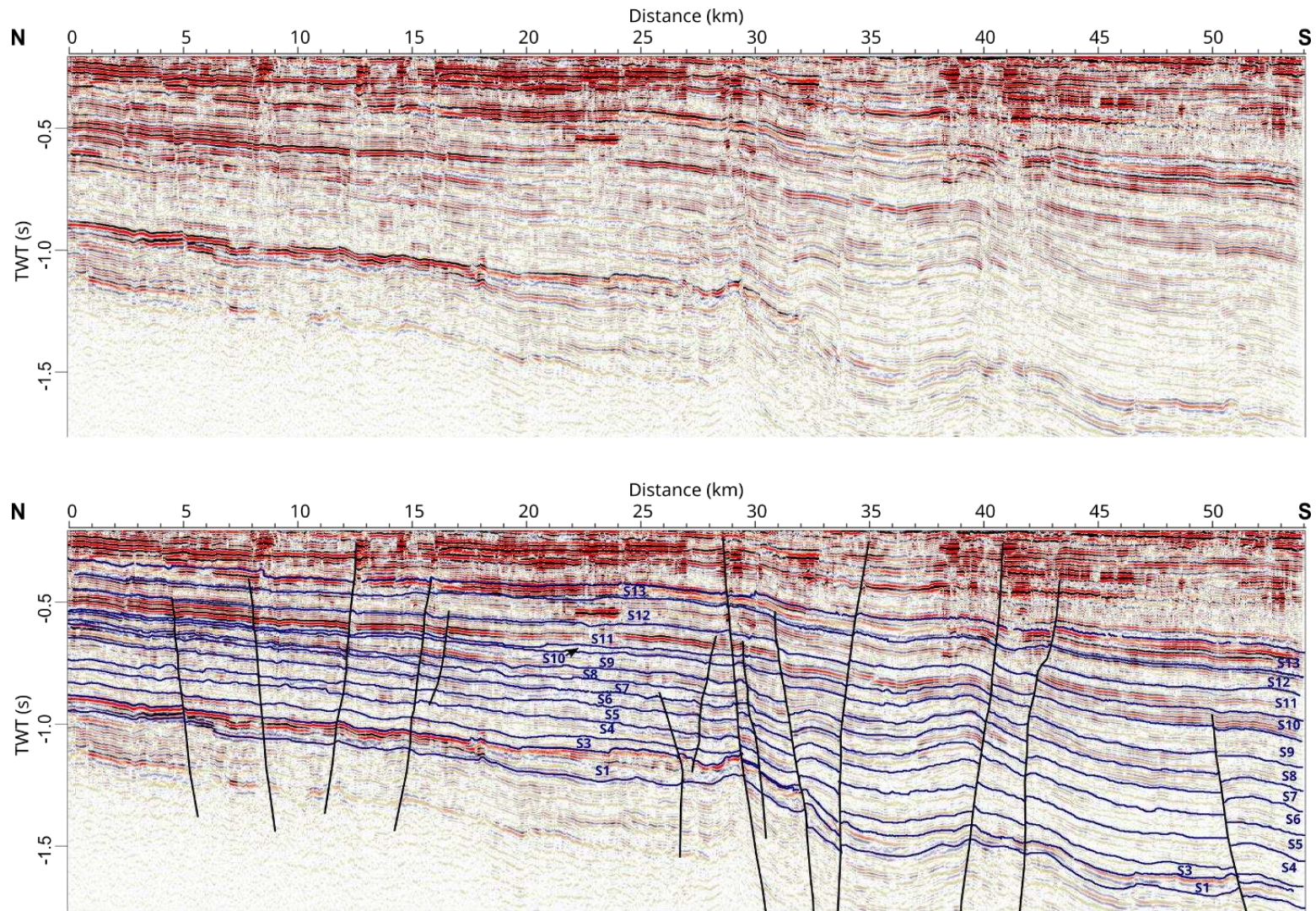


Figure 5.16. Sequence boundary interpretation on seismic line NS3 representing the dip line interpretation in the Western margin of Ardjuna sub basin. S1 – S13 denote the sequence number based on their description in the wells.



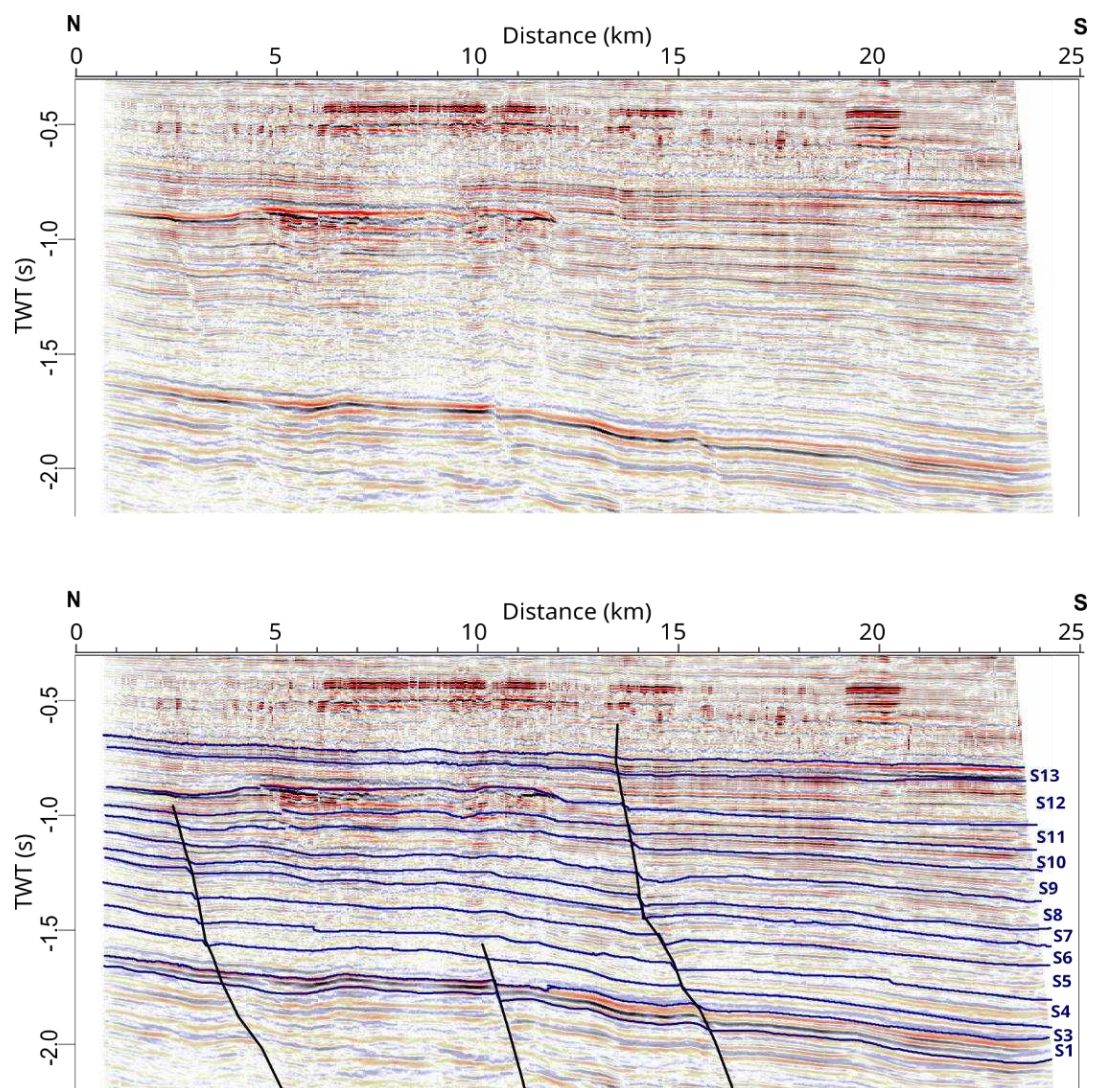


Figure 5.17. Sequence boundary interpretation on seismic line NS4 representing the dip line interpretation in the deeper area of Ardjuna sub basin. S1 – S13 denote the sequence number based on their description in the wells.



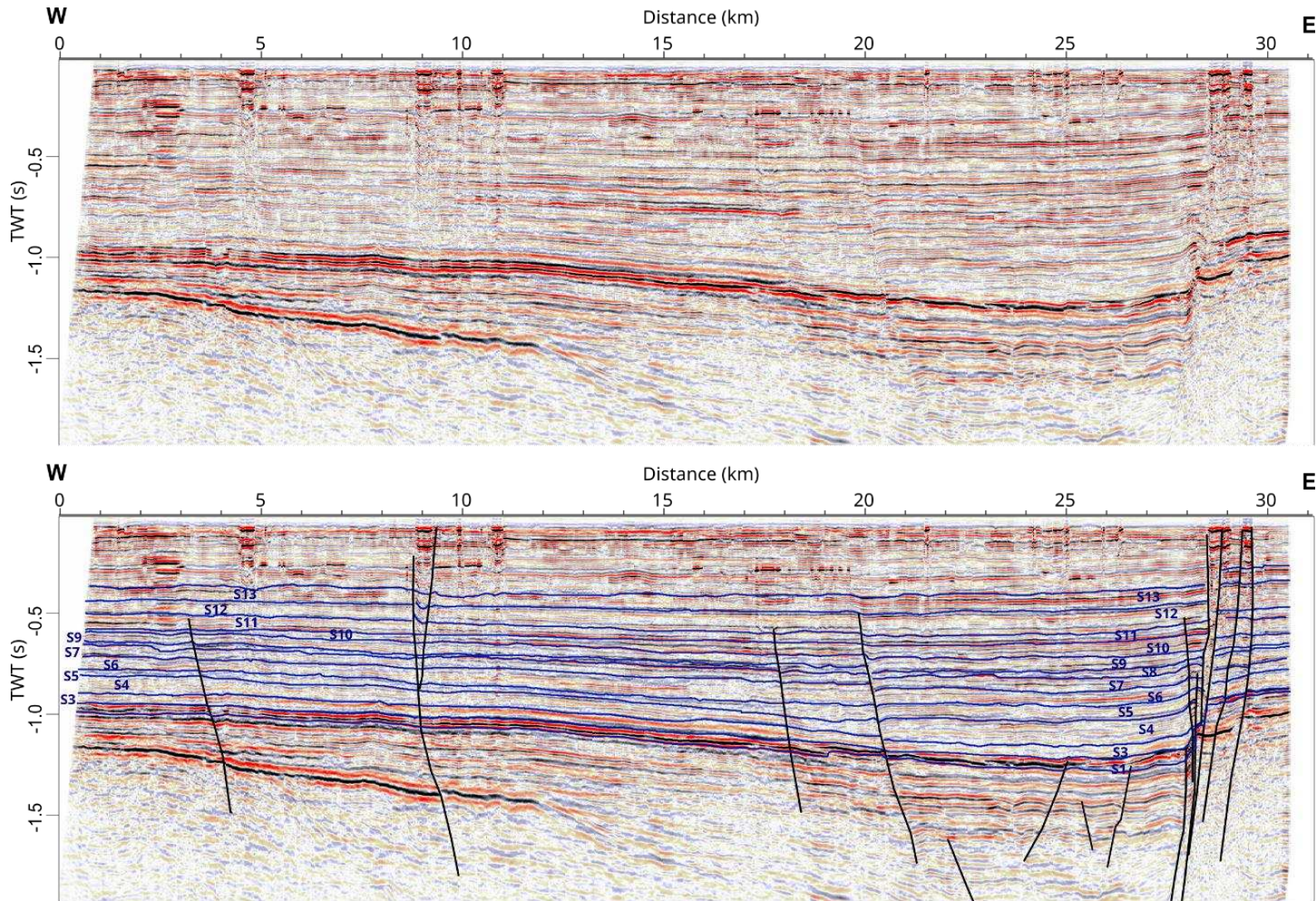


Figure 5.18. Sequence boundary (SB) interpretation on seismic line WE1 representing the strike line interpretation in the north area of Ardjuna sub basin. S1 – S13 denote the sequence number based on their description in the wells.



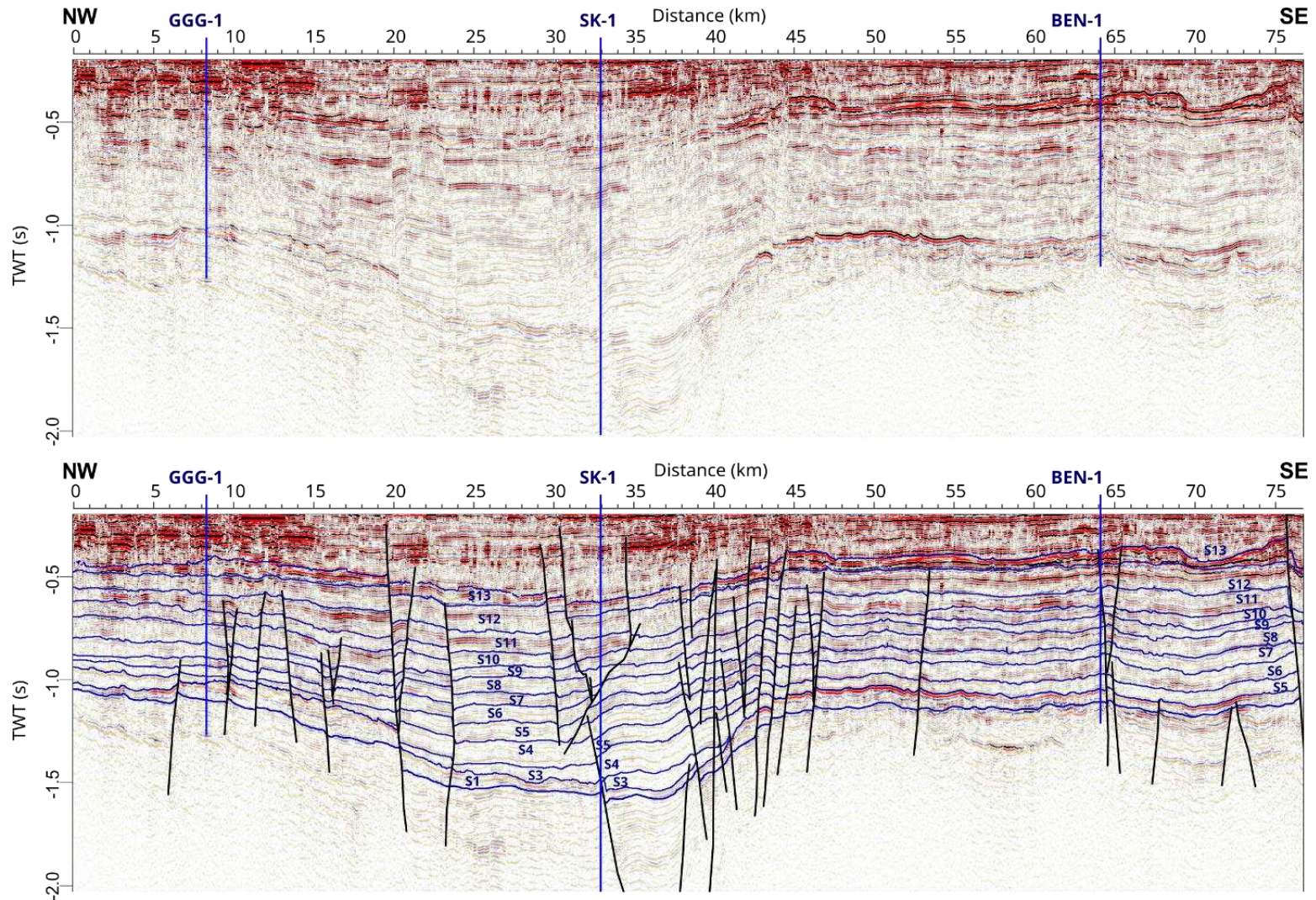


Figure 5.19. Sequence boundary interpretation on seismic line WE2 representing the strike line interpretation in the central area of Ardjuna sub basin. S1 – S13 denote the sequence number based on their description in the wells.



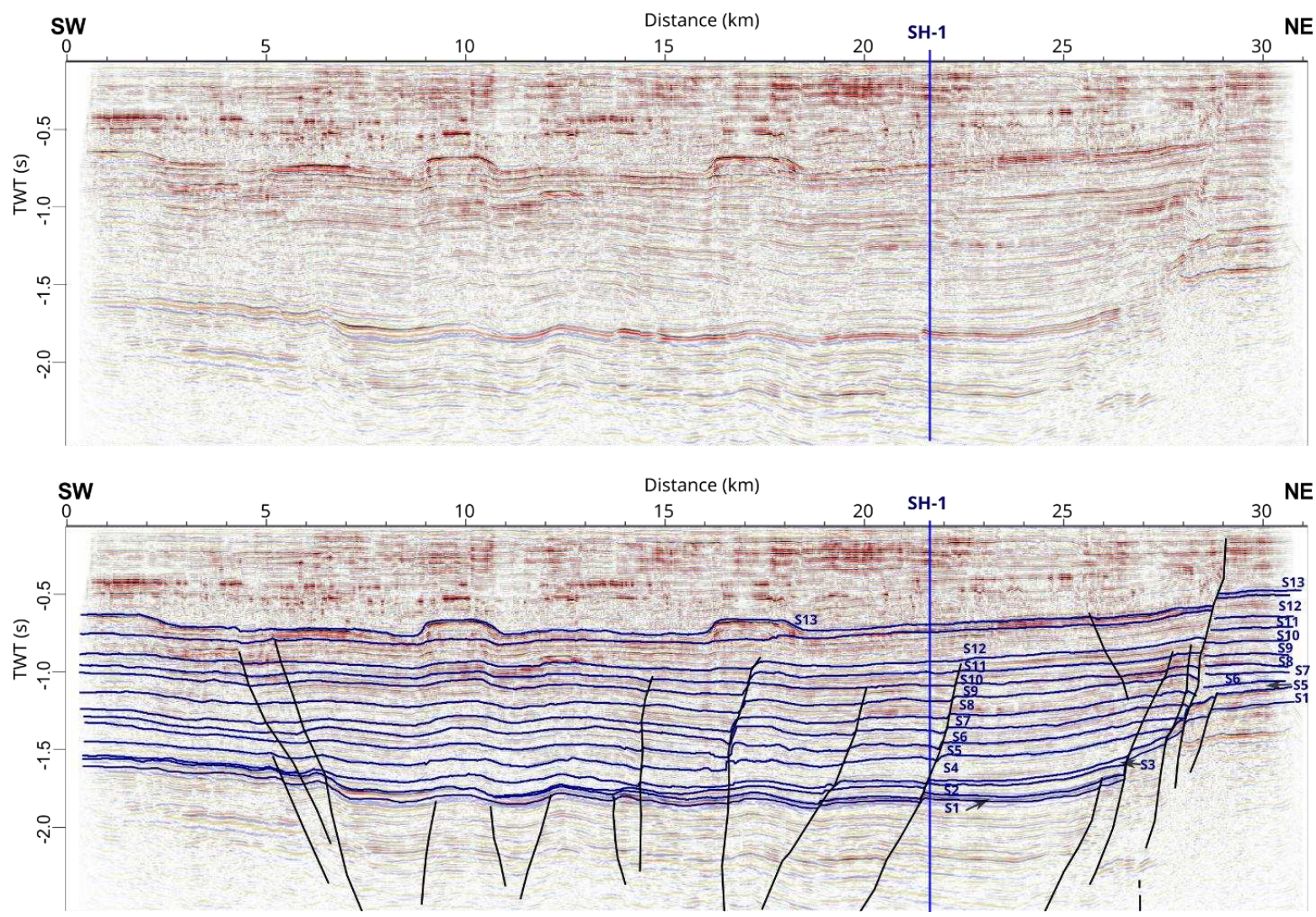


Figure 5.20. Sequence boundary interpretation on seismic line WE3 representing the strike line interpretation in the southern area of Ardjuna sub basin. S1 – S13 denote the sequence number based on their description in the wells.

Sequence 2 (bounded by SB 2 at the base and SB 3 at the top) represents the first siliciclastic deposits shedded in the Ardjuna sub-basin after the deposition of the Baturaja Formation. The distribution of this sequence is limited only to the southern part of the Ardjuna sub-basin and appears to be absent on the Central platform and Seribu platform (figures 5.13 and 5.14). Seismic line NS2 (figure 5.15) indicates that this sequence extends up to 7 km long from the central to the southern Ardjuna sub-basin, while in the west-east direction, its lateral extension can reach up to 12 km, as observed on seismic line WE3 (figure 5.20). On seismic line WE3, the seismic reflectors are onlapping onto the Ardjuna fault, and downlap towards the basin, forming sigmoidal progradation seismic facies (SF4).

Sequence 3 and sequence 4 (bounded by SB 3 at the base and SB 5 at the top) are distributed across the entire Ardjuna sub-basin and are absent in the platform areas (figure 5.19). To the West, both sequences terminate directly above SB 2, while to the East, they terminate at the Ardjuna fault. These two sequences show a thickening to the south as observed on seismic line NS2 (figure 5.15), reaching their maximum thickness at the southern margin of the study area, as seen on seismic line NS4 (figure 5.17). Sigmoidal progradation seismic facies (SF4) develops along the Ardjuna fault boundary, extending toward the Ardjuna sub-basin (figure 5.14, 5.21), while oblique progradational seismic facies (SF5) develops in the northern area of the Ardjuna sub-basin with a north to south orientation (figure 5.21). Both of these seismic facies transition into parallel to subparallel seismic facies (SF8) towards the distal direction (figure 5.21).

Sequence 5 and sequence 6 (bounded by SB 5 at the base and SB 7 at the top) mark the widespread distribution of the sediment input covering the entire study area, with a thicker characteristic observed in the Ardjuna sub-basin (figure 5.19). Sigmoidal progradation seismic facies (SF4) is still evident at the Ardjuna fault boundary (figure 5.14), while oblique progradational seismic facies (SF5) occurs in the northern area of the Ardjuna sub-basin. Similar to Sequences 3 and 4, both seismic facies (SF4 and SF5) evolves into SF8 towards the deeper part of the basin (figure 5.21).

Sequence 7 to sequence 10 (bounded by SB 7 at the base and SB 11 at the top) exhibit similar characteristics, demonstrating thickening in the Ardjuna sub-basin, especially near the Ardjuna fault. In sequence 7 (SB 7 – SB 8), mostly characterized by the development of SF5 in the northern to central areas, transitioning into SF8 towards the south, SF4 is no longer present.



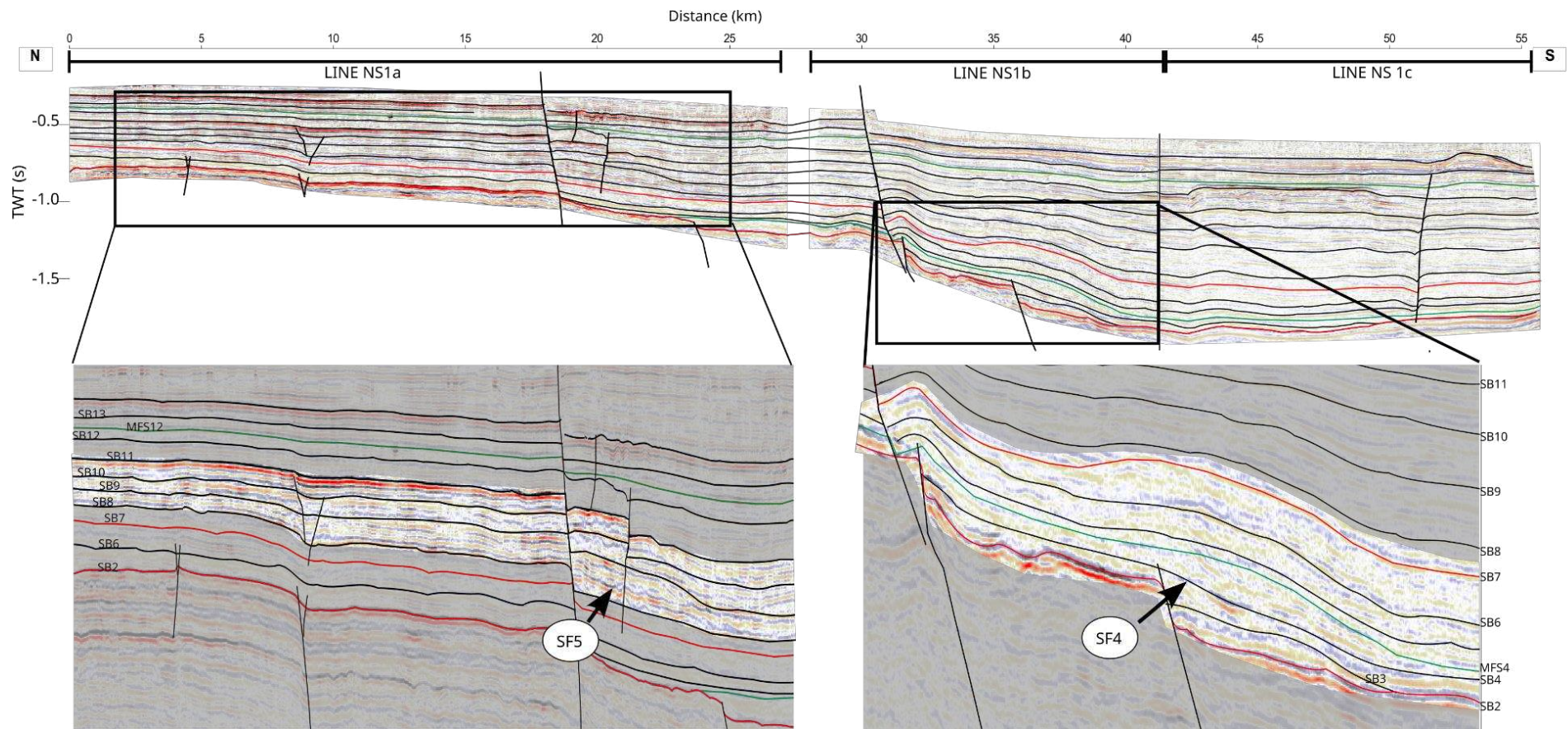


Figure 5.21. Sequence boundary interpretation in composite line NS1abc. The shift from seismic facies SF4 below SB7 to SF5 above SB7 is noticeable. Landward lateral shift of this seismic progradation facies indicates a transgressive event occurring above SB7.

In sequences 8 and 9 (SB 8 – SB 10), clastic progradation seismic facies with onlap termination (SF6) are observed in the northern area (figure 5.22), which transitions into SF5 towards the south. In sequence 10 (SB 10 – SB 11), SF6 is replaced by retrogradation seismic facies (SF7) which also transition into SF5 to the south. A unique feature is observed in sequence 10, where there is an incised valley (SF9) (figure 5.22). The overall distribution of seismic facies SF5 to SF9 is visible in all north-south-oriented seismic profiles, aiding in interpreting the development of the depositional sequences in the study area.

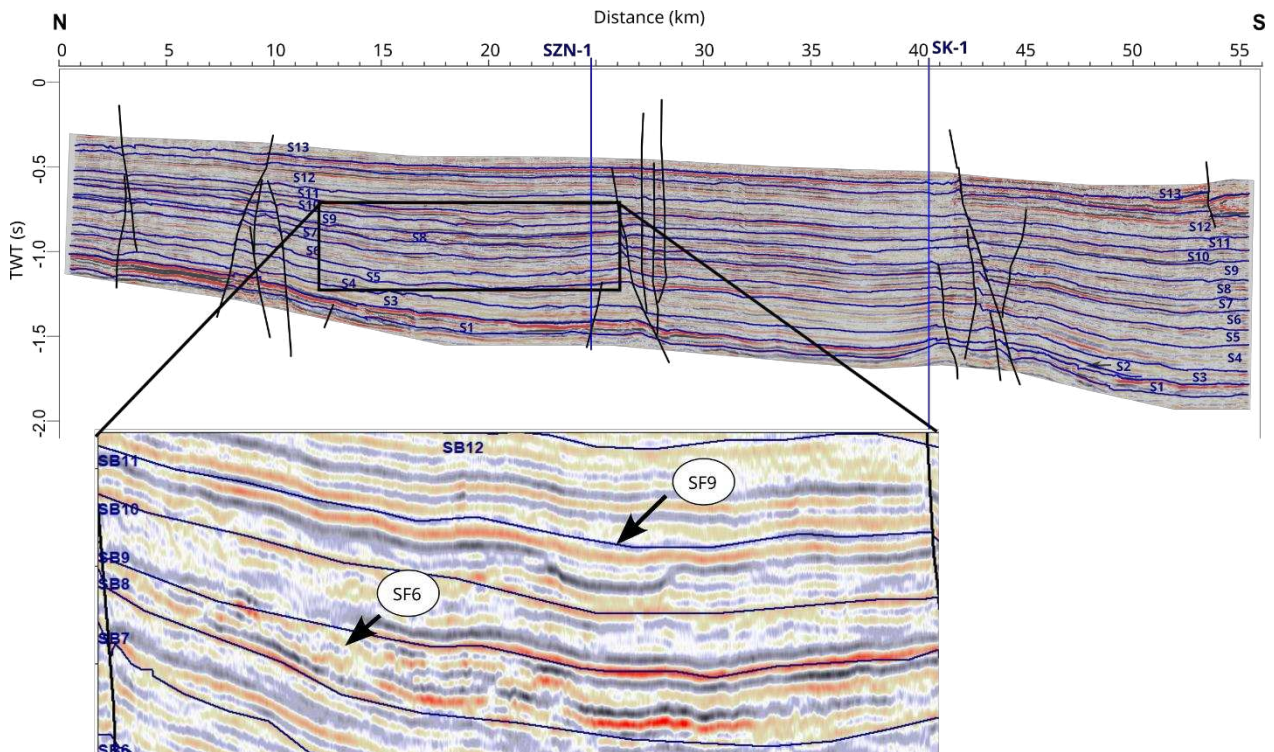


Figure 5.22. Zoom on the interpreted seismic line NS2 showing the location of SF5 and SF9.

Initially, sequences 11 and 12 (bounded by SB 11 at the base and SB 13 at the top) could not be precisely defined in the well correlation. However, seismic stratigraphic interpretation revealed a horizon with contrasting amplitude above sequence 10. In the proximal areas, this horizon is onlapped by seismic reflectors. Furthermore, mounded features characterized by seismic facies (SF3) and interpreted as reef bodies, are particularly occurring in the southern part of the study area (figures 5.23). These carbonates are part of the pre-Parigi carbonate presented in Chapter 4. In sequence 11, alongside SF3, another observable seismic facies is parallel to sub-parallel reflectors (SF8), while seismic facies indicating clastic sediment progradation is no longer identified. Sequence 12 is characterized by the dominance of SF8, with fewer occurrences of SF3 compared to sequence 11 in the southern part, as illustrated in



seismic profile WE3 (figure 5.20). Sequence 12 is delimited at the top by SB13 or the Top Upper Cibulakan Formation, which, in seismic sections, is characterized by high-contrast amplitude, indicating the lower boundary of carbonate facies SF 2 in the Parigi Formation.

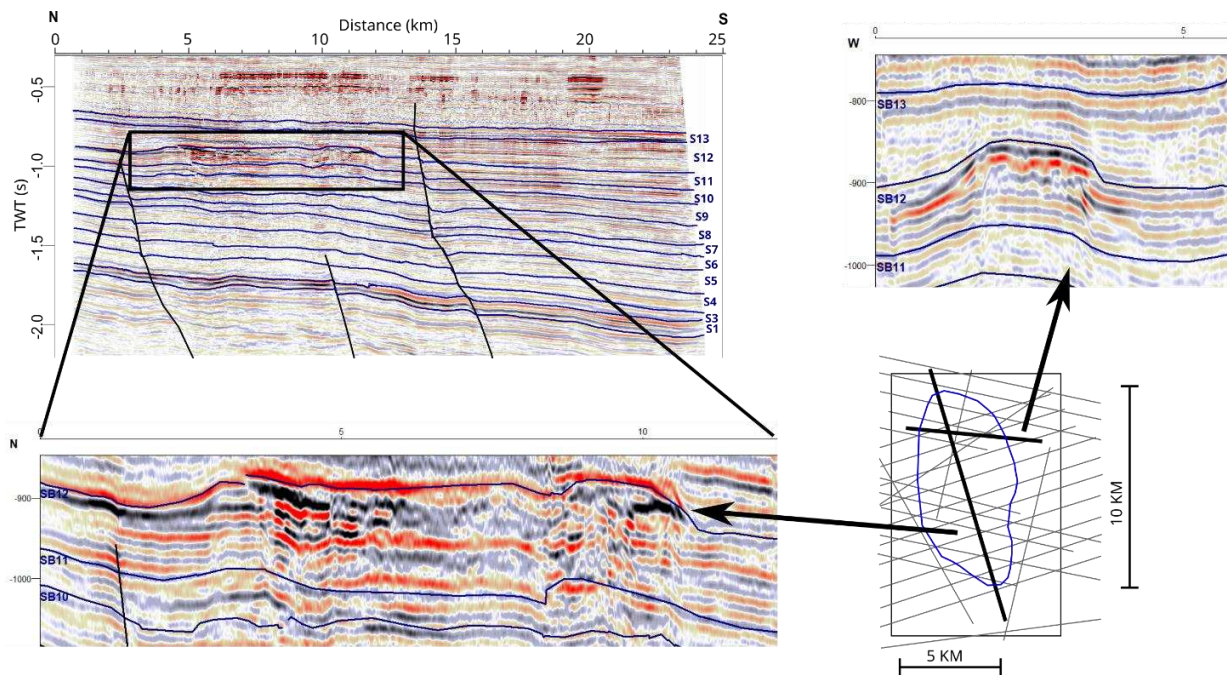


Figure 5.23. Zoom into the interpreted seismic line NS4 showing the location of SF3. The blue polygon shows approximately a 10km-long to 5 km-wide elongated structure oriented NW-SE. The carbonate geometry mapping was controlled by 2D seismic data (grey line).

#### 5.4.3. Second order sequences

Our analysis indicates a major sea-level fall occurring at the end of the deposition of sequence 1, marked by the SB2, resulting in the demise of the Baturaja Formation carbonate reefs in high areas, especially the Seribu platform and central platform. Similar phenomena were observed in the onshore North West Java Basin area (Widodo, 2018), indicating that this unconformity is regional. We interpret the top of the Baturaja Formation as the boundary for the 2<sup>nd</sup> order sequence. Consequently, we define the Baturaja Formation as the oldest incomplete HST within the second-order sequence.

##### 5.4.3.1. Aquitanian – Early Burdigalian (early Miocene Transgressive System Tract)

The early Miocene is marked by an overall fining upward trend of gamma-ray logs starting from SB2 to MFS4, a deepening stacking pattern of gamma-ray facies and a landward



evolution of onlap seismic reflector (figure 5.24, 5.25). Those features are certainly the result of a 2<sup>nd</sup> order transgressive sequence. We therefore combine the deposition of sequence 2, 3 and the transgressive system tract of sequence 4 (TST4) into one depositional package, the early Miocene TST (figure 5.24).

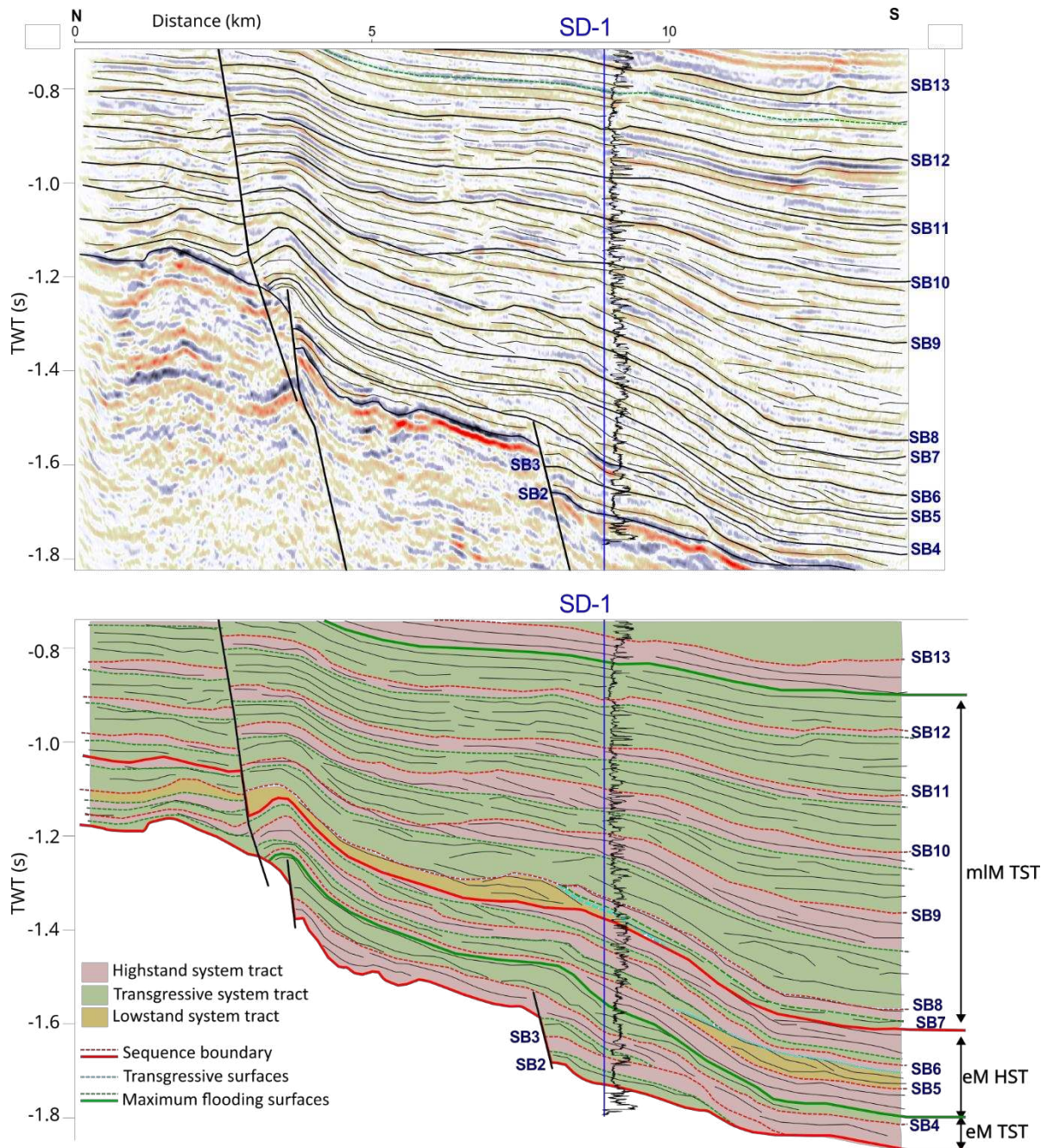


Figure 5.24. Sequence stratigraphic interpretation of the NS1b line. The first 2<sup>nd</sup> order sequence (bounded by straight red line SB2 and SB7) is characterized by sigmoid progradation seismic facies (SF4), while the latter 2<sup>nd</sup> order is dominated by parallel to subparallel seismic facies (SF8). eM: early Miocene; mIM: middle – late Miocene



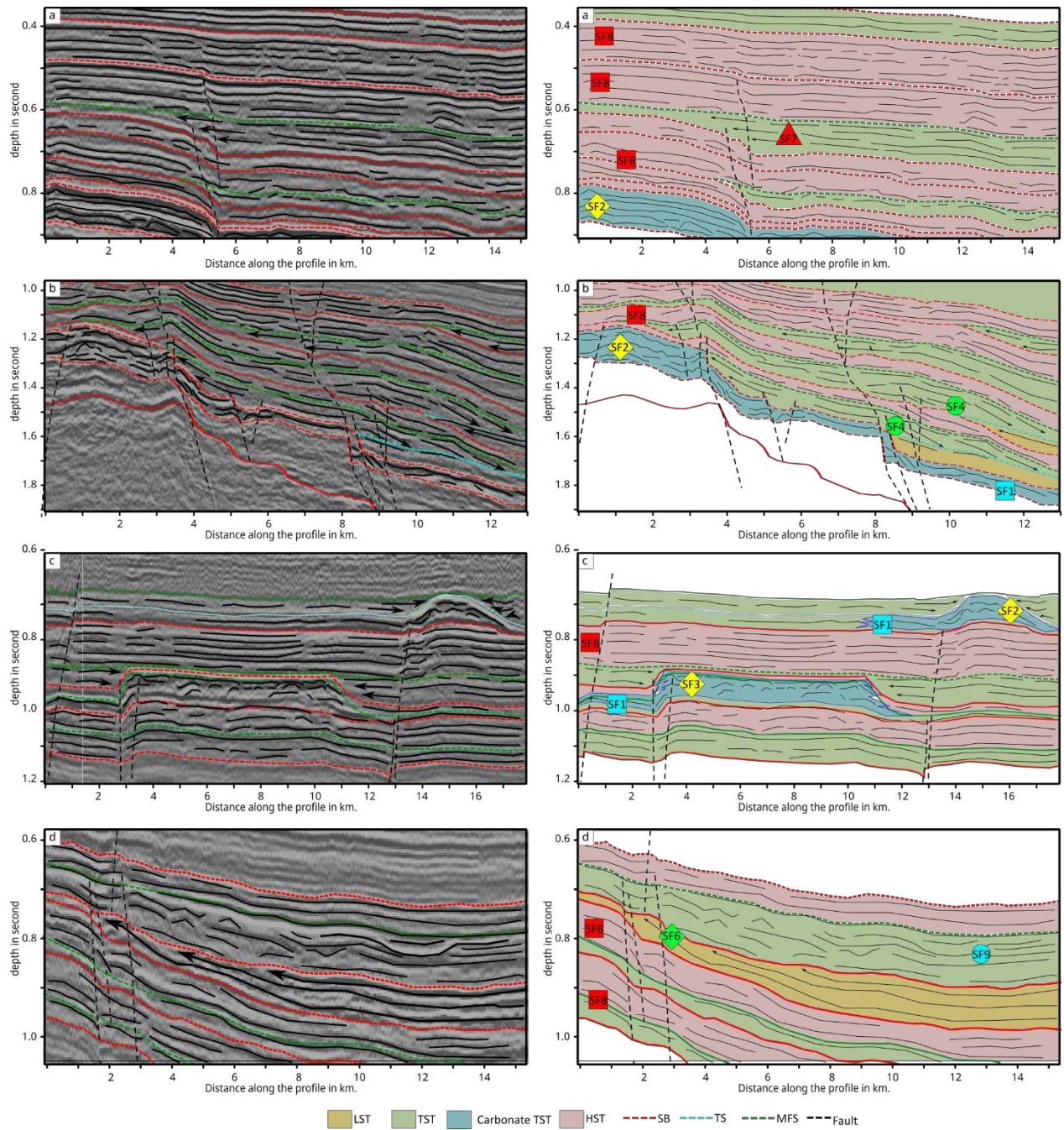


Figure 5.25 Line drawing interpretation and sequence stratigraphic interpretation in Upper Cibulakan formation. (a) line NS2; (b) line NS1a; (c) line NS1c; (d) line NS3. SF – seismic facies.

The interpreted seismic profiles show that the Ardjuna fault were already established and continued to develop during the early Aquitanian (top BRF), forming a N-S oriented embayment in the North Ardjuna sub-basin. Prior rifting tectonic provides high accommodation space at the downthrown area of the Ardjuna fault. In addition, the former reef topography of the BRF throughout the high relief area also contributes into providing accommodation space.

The Aquitanian - early Burdigalian isopach map shows the sediments thicken towards the border fault of the eastern part of the N-S oriented embayment, they disappear to the east at the footwall block, and thin out to the west towards the BRF reef facies (figure 5.26). A thinning trend can also be seen to the north where the sediment supplies most certainly came from an emerged area (Abdurrokhim and Ito, 2013; Atkinson, 1993; Clements and Hall, 2011).

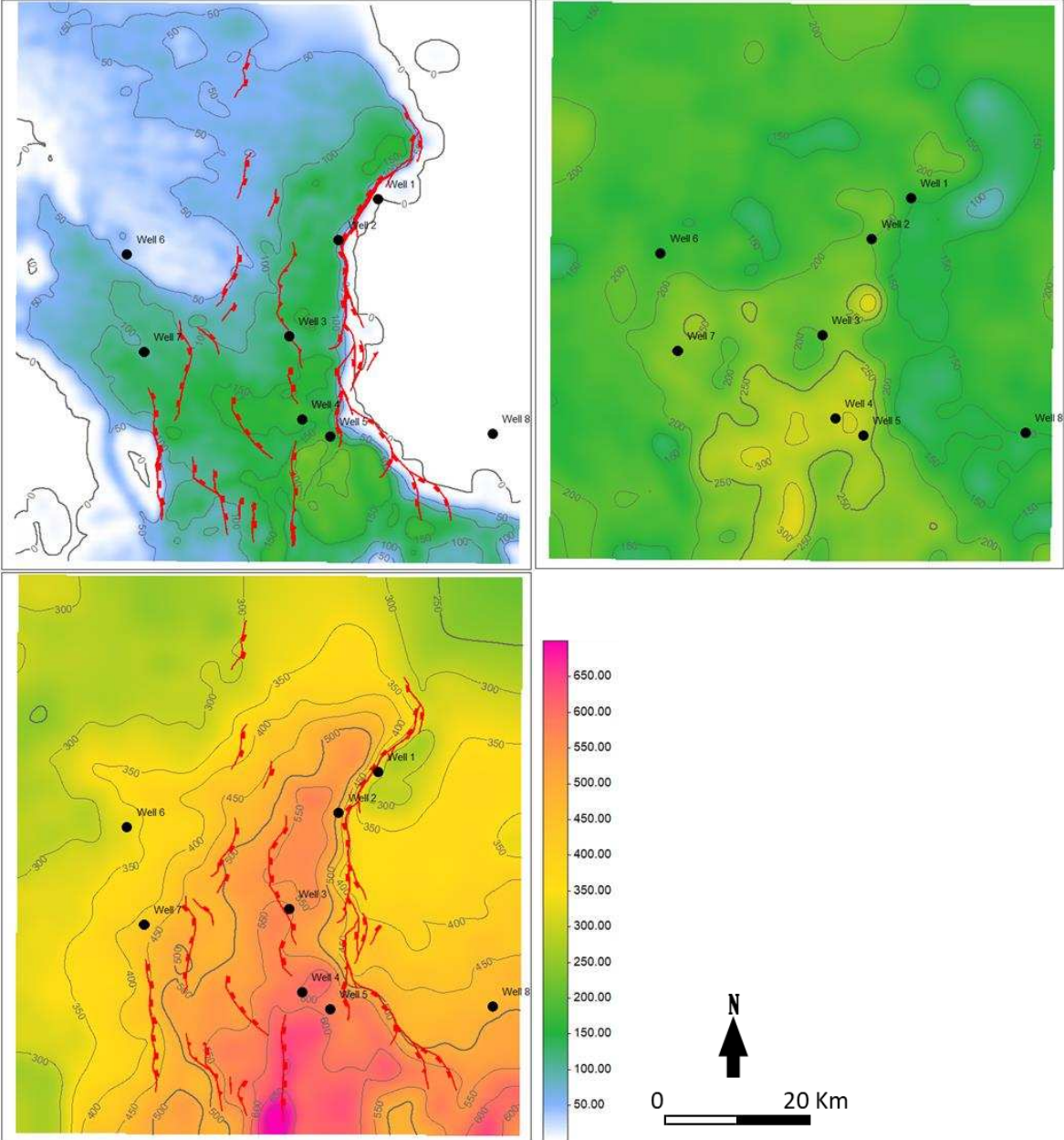


Figure 5.26 thickness maps in time domain at three deposition time intervals. (top left) early Miocene TST in the Aquitanian - e. Burdigalian; (top right) early Miocene HST in the Burdigalian - e. Langhian; (bottom left) middle - late Miocene TST in the Langhian - Tortonian.



The relative sea level rises characterizing the Early Miocene must have been induced by the extensive basin subsidence during this period. Global sea level curve (Miller *et al.*, 2020), which shows an aggradational trend during the Early Aquitanian-Burdigalian period, featuring two major floods (MFS2 ~ 21.6 Ma and MFS3 ~ 20.2 Ma) with a maximum sea level rise of 35 m (115 ft) at MFS3, could not accommodate the maximum sediment thickness (250 m (820 ft) in SH-1). Although the general consensus is that rift tectonic have ceased since the deposition of the BRF (Adnan *et al.*, 1991; Clements and Hall, 2007), basin subsidence plays a significant role in this area. Our results indicate that some major structures have experienced tectonic re-activation and were continued during sedimentation. In addition, the transgression characteristics recorded in the log, lithology and seismic data also indicate that the sediment supply failed to surpass the rate of accommodation generation (positive accommodation). This is also supported by the appearance of seismic facies 3 and 4, indicative of areas with positive accommodation (figures 5.21 and 5.22).

#### 5.4.3.2. Burdigalian – Early Langhian (early Miocene Highstand System Tract)

An overall coarsening upward trend of gamma-ray logs starting from MFS4 to SB7, combined to a shallowing up stacking pattern of gamma-ray facies and a seaward shift of onlap seismic reflectors mark an overall highstand period from Burdigalian to early Langhian. Those criteria argue in favor of a 2<sup>nd</sup> order highstand system tract sequence, combining the deposition of the 3<sup>rd</sup> order high stand system tract of sequence 4 (HST4), sequence 5, and 6 into one depositional sedimentary sequence, hereafter called the early Miocene HST.

During the early Miocene HST, the basin subsidence became less significant. This can be seen as the global sea level rose (Miller *et al.*, 2020), yet the recorded lithology and gamma ray logs show a progradation trends. This combination demonstrates that the sediment supply surpassed the accommodation space generation. In the middle Miocene, there was an intensification of monsoon-related precipitation that led to higher erosion rates and increased sediment discharge volumes over south and southeast Asia (Clift *et al.*, 2008; Clift and Jonell, 2021; Clift and Webb, 2019). This series of increased monsoon activity may also be recorded in the Ardjuna sub-basin and responsible for the increased sediment supply in the Burdigalian - early Langhian. The strong progradational seismic and the coarsening upward gamma ray stacking pattern in the Burdigalian – Early Langhian confirmed the increase in sediment supply.

By the end of early Miocene HST deposition, the entire embayment was covered by siliciclastic deposits of Upper Cibulakan. The isopach map of Burdigalian – early Langhian shows relatively uniform thickness with a slight thickening trend towards the South (figure 5.26). Although the remaining embayment is slightly noticeable, the thinning trend towards the footwall of the border fault is diminishing. This confirms that there was limited tectonic activity during this period and most of the faults were inactive, and subsidence was most probably caused by isostasy.

#### 5.4.3.3. Langhian – Tortonian (middle - late Miocene Transgressive System Tract)

An overall fining upward trend of gamma-ray logs starting from SB7 and lasting until MFS12, combined to a deepening stacking pattern of gamma-ray facies and a landward evolution of onlap seismic reflector point out to a transgressive trend during middle-late Miocene. We interpret those criteria as a 2<sup>nd</sup> order transgressive period, integrating the deposition of third order sequence 7 to 11 and the transgressive system tract of sequence 12 (TST12) into one depositional sequence, the middle to late Miocene TST.

During the Langhian-Tortonian, the thickening pattern towards the boundary faults reappeared, as confirmed by the Langhian-Tortonian isopach map (figure 5.26). The major faults in this area appear to have reactivated and contributed to the generation of accommodation space for the Langhian - Tortonian strata. This activity seems to be related to thermal subsidence due to lower plate ductile extension (Clerc *et al.*, 2018; Karner *et al.*, 2003; Phillips *et al.*, 2019), as evidenced by the thickness in the central area corresponding to early Miocene embayment. Alternatively, it could also be associated to a NW-SE extensional tectonic event dated around 17-15 Ma in southern Sundaland (Hall and Morley, 2004; Morley, 2002).

The formation of accommodation space in the Langhian - Tortonian period does not seem to be matched by the supply of sediments formed at that time. Global sea level appears to be gradually falling (Miller *et al.*, 2020) while lithological records and gamma ray logs show a retrogradation followed by aggradation trend. This reduction in sediment supply might also be associated with the declining monsoon intensity during the Langhian period where the mass flux in East Asia decreased significantly (Clift *et al.*, 2008; Clift and Jonell, 2021). This phenomenon facilitates carbonate formation, indicated by the increasing proportion of limestone in the Langhian - Tortonian. Several carbonate reef bodies can be easily observed on seismic cross sections.



## 5.5. Depositional Environments

Detailed seismic, wireline log, and lithology analysis reveal that the depositional environment of the UCF can be summarized into four stages based on the common tectonic events and sediment supply discussed in the previous section. For the middle - late Miocene transgression period, we subdivide into two depositional environments due to the drastic change of depositional environment from clastics to carbonate production.

In the Aquitanian – early Burdigalian, sediment sources from the emerged area in the north - northeast were transported into the basin in a transgressive delta/estuary environment (figure 5.27). Several delta progradation seismic facies (SF4, 5, and 6) can be observed in the northern and eastern areas, especially adjacent to the bordering fault. We mark the approximate boundary of the progradation seismic facies to sub parallel seismic facies (SF4) in all seismic sections as the apparent limit of the delta plain distribution. Gamma-ray facies in almost all wells shows delta front and prodelta facies consisting of mouth bar deposits (FA2), while delta plain facies were absent in the wells. Micropaleontological data indicates a marine environment (inner sublittoral) associated with this interval on SZN-1 and SD-1 (Noon *et al.*, 1993; Romein *et al.*, 1987). Based on seismic facies mapping, sediment deposition occurring during this period consisted of two main sources: the first source originating from the north forming a deltaic system that became the main filler of the embayment, and the second source originating from the northeast through the footwall area, where the shelf carbonate of BRF were developed, which formed a deltaic system that was relatively smaller than the one from the main source. Those deltaic systems can be recognized from seismic facies analysis. In addition, smaller delta fan facies can be found in the fault plane area forming its own delta system along the fault border area.

In the Burdigalian - early Langhian, delta environment continued, a large sediment supply led to the deltaic plain prograding further south (figure 5.27). Gamma-ray log indicating the delta plain facies were increasingly common in almost all wells, whereby deeper facies were found in association with the delta plain. Micropaleontological evidence in SZN-1 and SD-1 indicates a shallower environment characterized by a decrease in faunal diversity and abundance compared to the previous interval (Noon *et al.*, 1993; Romein *et al.*, 1987). SF4, SF5, and SF6 are becoming recognized more clearly on north-south oriented seismic sections, and the limit of the delta plain has been followed from the transition of SF4, to SF8. The

sedimentary source from the north increased and caused the pre-existing delta to progress southwards. By this time, the pre-existing embayment was almost completely covered allowing the distribution of the delta to be unrestricted by the previous topography. By mid-Burdigalian, carbonate growth in the East had ceased entirely, replaced by a new northeast-southwest trending delta progradation. This new clastic source might have caused the demise of BRF carbonate.

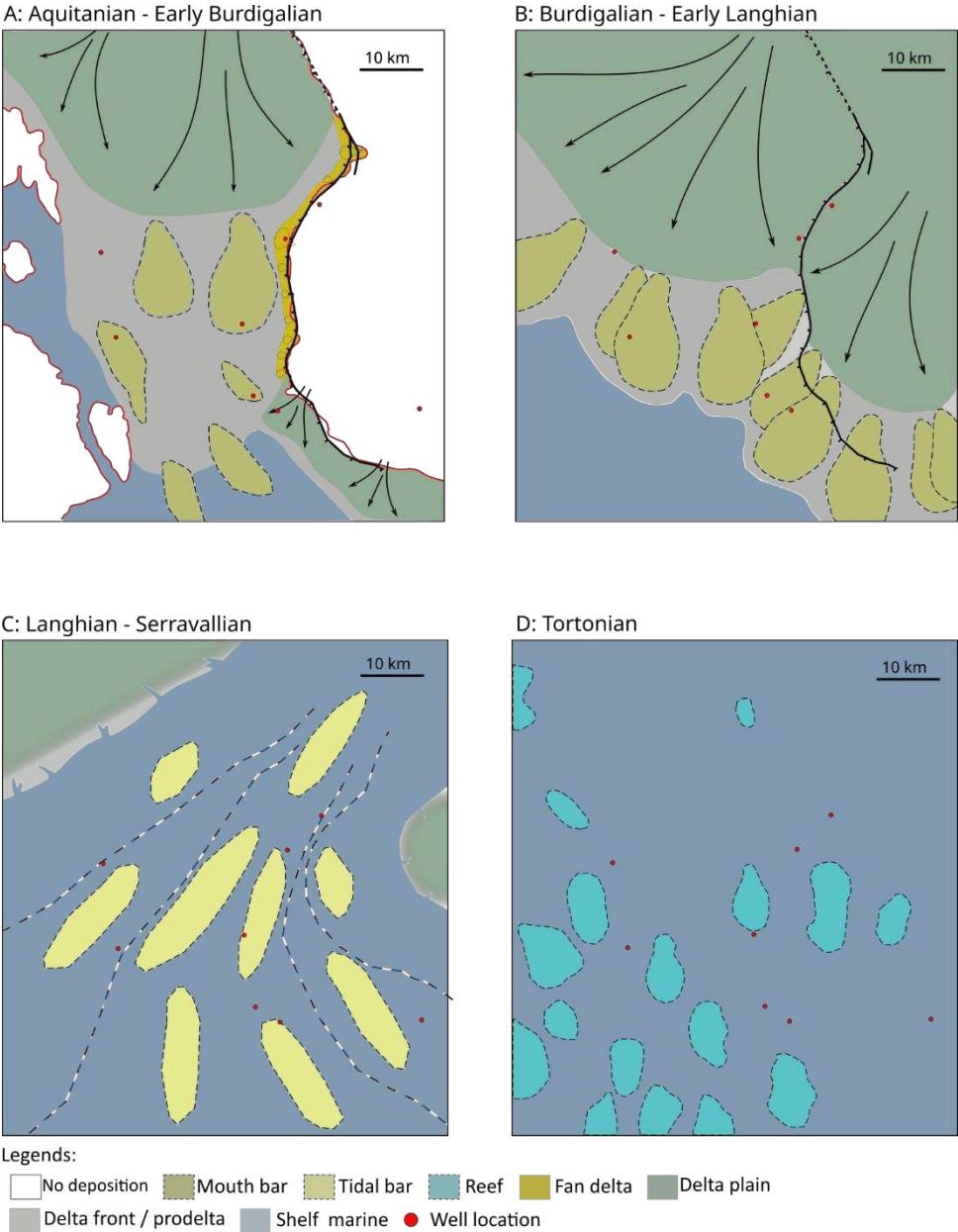


Figure 5.27 Schematic gross depositional environment of the Upper Cibulakan Formation in the Ardjuna sub-basin of the North West Java Basin.

The transgression event returned in the Langhian - Serravallian resulted in almost the entire study area being covered by marine environment. During this time, the decreased sediment supplies, presumably caused by the reduced monsoon activity (Clift *et al.*, 2008), caused the previously existing delta to be abandoned. At early Langhian interval, gamma-ray facies analysis shows deltaic facies retreating northwards, and being replaced by deeper facies, marked by marine tidal bar facies. The reactivation of Ardjuna faults during this time resulted in the re-establishment of the embayment which controlled the direction of tidal bar distribution (figure 5.27). Micropaleontological data indicate a marine environment in SZN-1 and SD-1 (Noon *et al.*, 1993; Romein *et al.*, 1987). We were unable to estimate the dimensions of the tidal bar due to the lack of supporting data, previous studies using 3D seismic data in a southern area suggest that the tidal bar distribution can reach 0.3 to 2 km wide, 20 km long, and up to 17 m thick (Posamentier, 2002). Seismic facies analysis shows that the Langhian - Serravallian intervals were dominated by SF8 with several SF9 occurrences in the north. This suggests that the northern area was closer to the shorelines.

During the Tortonian, the generation of accommodation space due to basin subsidence accompanied by diminishing sediment supply resulted in a favorable depositional environment for carbonate formation, whereby some isolated carbonate reefs have been identified in the studied interval. Gamma ray facies analysis reveals that the interval is dominated by storm dominated shallow shelf facies and exhibit thin layers of limestone within thick shale intervals. Seismic facies analysis shows that SF3 appears to be relatively elongated with a length of 10 - 15 km and a width of 5 - 10 km in a northwest - southeast trending orientation (figure 5.23). This direction is believed to be strongly influenced by pre-existing faults that provided an elevated topography suitable for the deposition of platform carbonate and reef facies. By this time, the coastline is interpreted to have moved further north and the entire study area was covered by marine environment. The seismic facies analysis also demonstrates that the southernmost reefs are older than the northern ones, suggesting transgressive event during development of the carbonate. These reefs could not keep up with the rate of sea level rise and drowned, migrated northward and completely died out before the MFS12.

## 5.6. Conclusions

This study combined seismic, wireline log, biostratigraphy, sedimentology, and sequence stratigraphy analysis to understand the depositional history of Miocene interval (BRF, UCF, and Parigi Formation) in the Ardjuna sub-basin of the North West Java Basin. The study identified thirteen third-order depositional sequences organized in three second-order sequences. The GR facies analysis shows that the sediment strata are made up of mixed siliciclastic-carbonate rocks deposited during a transgression period. Nine GR facies have been identified and interpreted based on the sedimentary facies and biostratigraphic data (GR1 – GR9). The GR facies interpretation is consistent with the sequence stratigraphic framework established in this study. The seismic facies analysis identified Nine facies in the study area, each with its unique lithological and depositional characteristics. The interpretation of these facies includes carbonate deposits in the inner and periplatform area, and clastics deposit in progradation and retrogradation periods. This information is essential in understanding the depositional environment and stratigraphic architecture of the study area.

This study provides new insights into the interactions between tectonic and sediment supply and their implications for sediment depositional patterns and distributions in the study area. Pre-Oligocene tectonic has generated local highs and lows that significantly controlled depositional patterns in the Aquitanian - Early Burdigalian. By this time, the presence of clastic sources from the north resulted in the formation of deltas in the embayment area. Tectonic activity in the Ardjuna sub-basin is interpreted as relatively quiescent until Early Langhian. Combined with an increasing supply of clastic sediments from the north, multiple deltas were established during this period. During the Langhian period, seismic and wellbore interpretations indicate there was significant tectonic activity which resulted in the transgression period reoccurring and the depositional environment gradually shifted to the shelf. This transgression period continued to the Tortonian, combined with the loss of sediment supply from the north resulting in carbonate growth.

Seismic interpretation demonstrated the plausibility of having two sediment sources from the emerged area from the north and northeast. The assessment of responsible petroleum potential and explorations risks will benefit from these data and the associated new subdivisions, which can be reproduced on similar cases providing further insights into sedimentary processes.





## **CHAPTER 6: STRATIGRAPHIC FORWARD MODELING**



## 6.1. Introduction

The Upper Cibulakan Formation in the Ardjuna sub-basin offers a valuable opportunity to evaluate the use of Stratigraphic Forward Modeling (SFM) and to improve the understanding of reservoir presence, distribution, quality, and architecture in an environment characterized by predominantly transgressive conditions. The depositional environment evolution initiates with the dominance of a river-dominated delta at the base (Massive unit (sequences 1-7)), evolving to a tidal shelf environment (Lower Main unit (sequences 8-10)), and finishing with the establishment of a mixed siliciclastic-carbonate system in a shallow marine environment (Upper Main unit (sequences 11 and 12)). Furthermore, this study provides a chance to examine the interactions between tectonic forces and sediment supply, as discussed in Chapter 5, and explore their implications for sediment depositional patterns and reservoir distributions in the study area.

To test conceptual geological models and understand controlling factors, numerical modeling techniques were employed to predict the impact of various factors (e.g., tectonic deformation, subsidence vs. uplift, eustatic sea level fluctuations, sediment flux) on sedimentation within the basin. A deterministic 4D multi-lithology forward stratigraphic model was used to simulate basin infill over geological time scales. This model replicates the net result of sediment supply, transport, and accommodation concerning uplift, subsidence, and sea level fluctuations in large-scale sedimentary systems.

The simulated area covers the Ardjuna sub-basin with a total area of 90 x 78 km ([figure 6.1](#)). To build the base model, several parameters must be determined first. These parameters include: 1) accommodation parameters; 2) transport parameters; and 3) sediment input parameters. The determination of these parameters is a combination of data from previous interpretations and literature studies.

Accommodation is primarily governed by eustasy (global sea level changes) and tectonics that deform the substratum. Both of these important parameters will determine the total volume of sediment that could deposit in the basin. In this model, the global sea level curve by [Miller \(2020\)](#) was utilized to accommodate the eustatic curve in the model. To obtain the initial bathymetry map, we used a combination of the thickness maps ([figure 4.27, 4.28, 4.29](#)), along with the results from seismic stratigraphy analysis, GDE mapping, and bathymetry from biostratigraphy analysis as a trend. Eight reference wells were used to constrain the bathymetry

maps. The schematic diagram illustrating the stages for obtaining paleobathymetric maps can be seen in [figure 6.2](#). In the initial stage, the youngest layer (upper Main unit) was reconstructed first. During this stage, water depth indications obtained from biostratigraphic data, and our interpretation of gamma-ray facies associations, were used as a first water level depth estimates for each well. Subsequently, the layer below, Lower Main unit, was reconstructed using the same process. This workflow was repeated until the first set of bathymetric maps were obtained. Within our model, special attention was given to the initial morphology of the substratum (initial bathymetry). The geological interpretation indicated reef and clastic carbonate facies in the Baturaja Formation, and the morphology at the end of its deposition was not flat. In particular, for the paleobathymetric map at the end of the Baturaja formation deposition, we assumed that the thickness map of the Baturaja formation reflects the paleomorphology at the end of its deposition. This assumption may not be valid in areas where the Baturaja formation thins out due to proximity to the coastline, where carbonate development was limited. However, such areas are concentrated in the western part of the Seribu platform and were not included in the model.

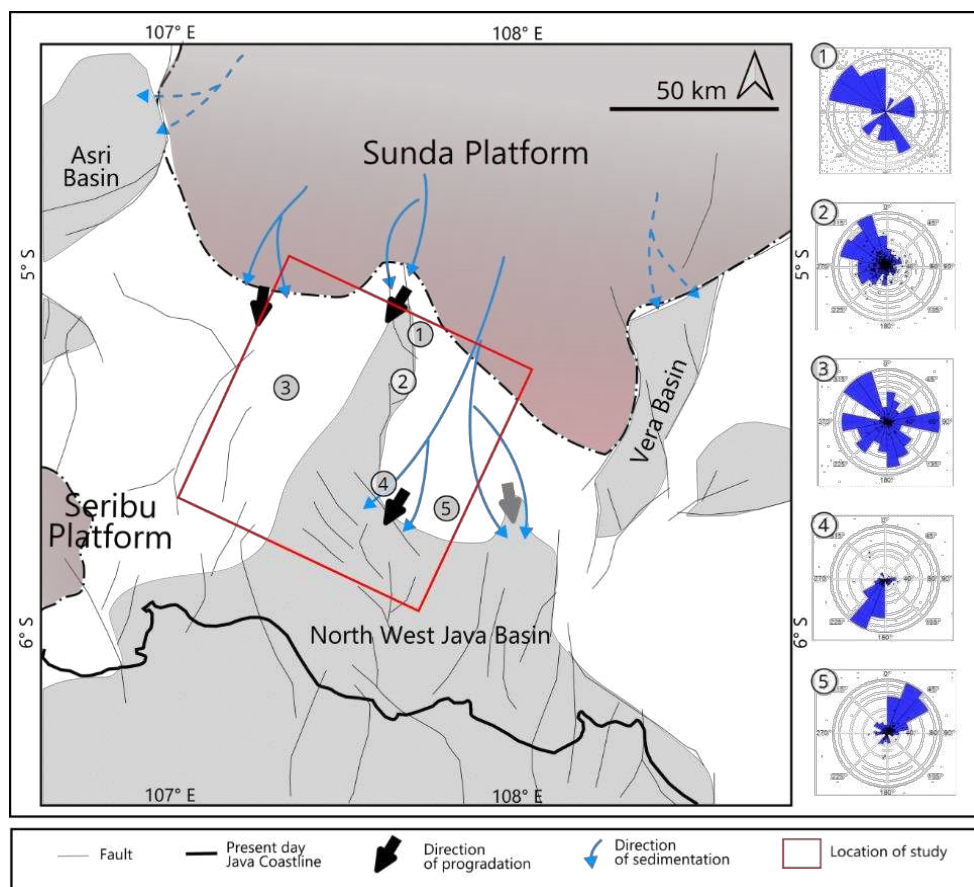


Figure 6.1 Proposed paleogeography of North West Java basin at Langhian (modified from Noble et al., 1997; Ponto et al., 1988)

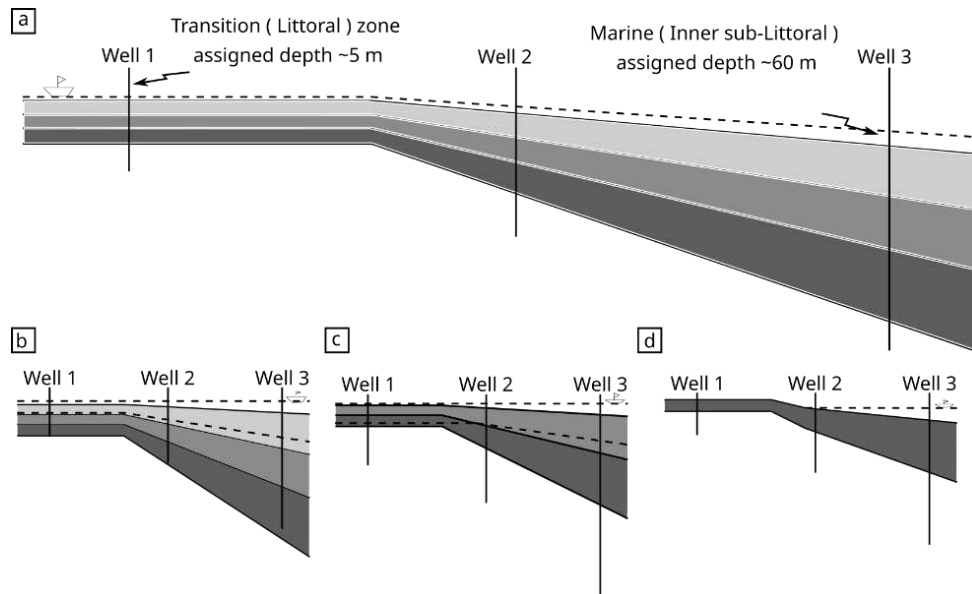


Figure 6.2 Schematic diagram illustrating the paleobathymetric reconstruction applied in this study

Tectonic influences are determined through a set of subsidence/uplift maps, describing substratum deformation at various key time markers. The subsidence map was obtained by using thickness maps from the interpretation of seismic horizons (chapter 4) that have been validated and tied to well data. In this case, total subsidence is the thickness of the interval plus the difference in bathymetry between the initial and final deposition. Subsidence for each grid node in every timestep is subsequently computed via linear interpolation of these maps across.

After obtaining the initial bathymetric and subsidence map, the next step involves conducting sensitivity analysis on the assumed depth values for each well (figure 6.3). In this stage, several scenarios were explored, and the thickness generated by the model was compared to the thickness map derived from seismic interpretation. If there was a significant discrepancy between the model and the data, corrections to the bathymetric map was applied (figure 6.4). This iteration process repeats until a satisfactory match was achieved. The results of the paleobathymetric maps used for 22.5 Ma can be seen in figure 6.5.

Diffusion coefficients serve as indicators of sediment behavior, with differences observed among various sediment types. For instance, silt and clay are more diffusive compared to sand. The ratio between water-driven and gravity-driven coefficients tends to rise with grain size, as coarse sediments are more responsive to flow regimes (Allen, 2017). The published sediment diffusivity range varies significantly, varying from  $<0.01 \text{ km}^2/\text{ky}$  (Gawthorpe *et al.*, 2003) to



$1.6 \times 10^7 \text{ km}^2/\text{ky}$  (Burgess *et al.*, 2006). We employed non-linear equations that account for both water and slope-driven processes (Granjeon, 2014) to model the transport of sediment within our model.

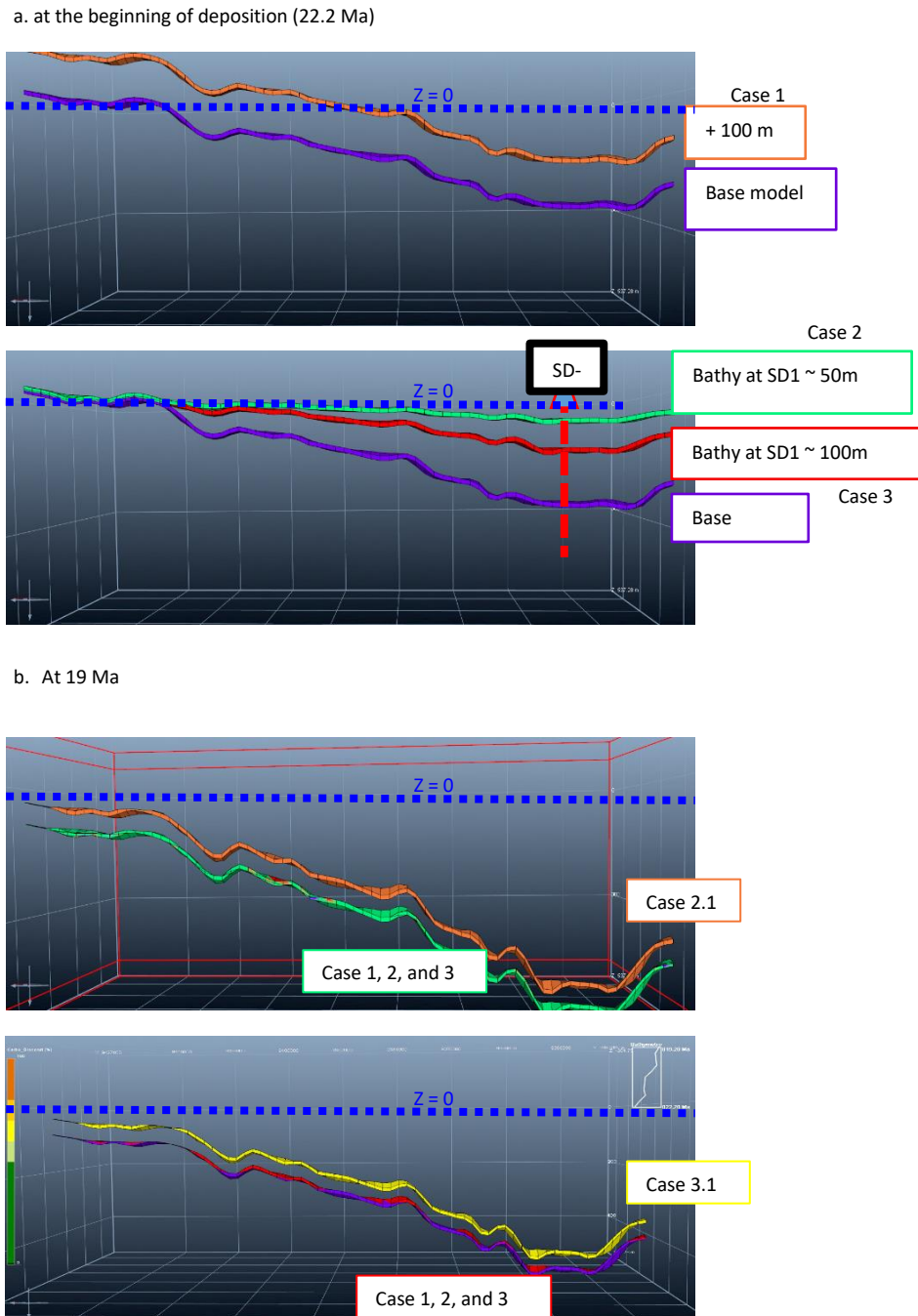


Figure 6.3 North-south cross section of base model depth (base of Upper Cibulakan Formation) scenario at the beginning of deposition (a). In case 1, 100 m of bulk shift up was applied to the base model; in case 2, and 3, different depth shifts (50 m and 100 m) were applied at SD1 well area only. The base model depth at 19 Ma illustrates the depth after subsidence (b). In cases 1,2, and 3, there is no modification to the subsidence; in the case 3.1, 50 m bulk shift was applied to the 19 Ma subsidence. The best fit model is the case 2.1 (see figure 6.4 for correction in case 2.1)

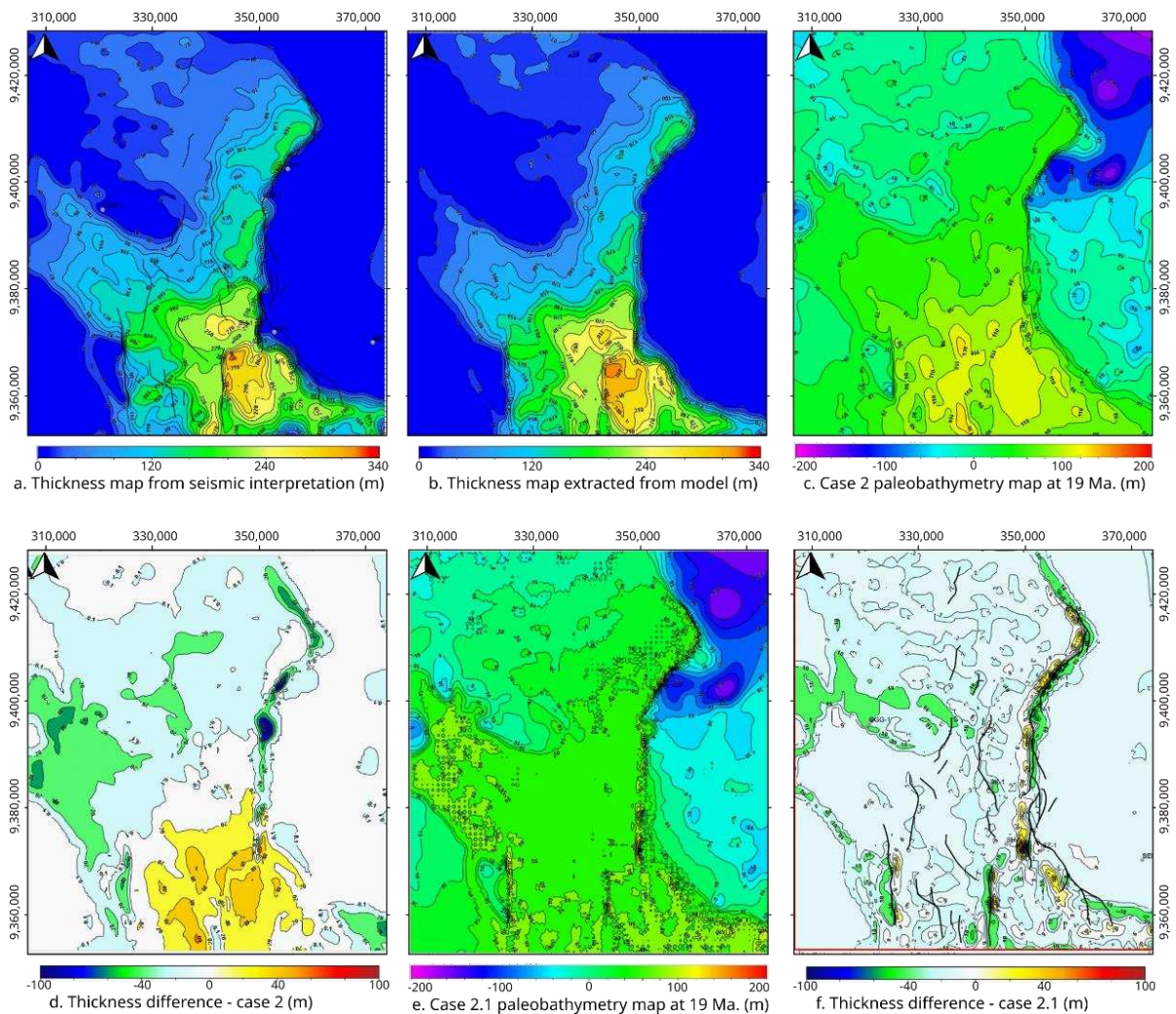


Figure 6.4 Example of the adjustment applied to subsidence at 19 Ma. The reference thickness is derived from our seismic interpretation (a); the resulting thickness (b) is extracted from the model using initial bathymetry in case 2 (c). Thickness difference in case 2 simulation (d) is calculated from simple subtraction of seismic thickness (a) with model thickness (b). The adjusted bathymetry (e) is from subtraction of case 2 bathymetry (c) with (d). The resulting model thickness is then compared again with (a), resulting in a minimum thickness difference (f).

In this study, four sediment classes were defined, each representing the transportation characteristics of fine (clay) and coarser (sand) particles; as well as carbonate clastic and carbonate reef. Subsequently, a systematic analysis was undertaken to analyze the optimal continuous sediment supply ( $Q_s$ ) and sand-to-shale ratio variations that replicate the observed thickness and lithological variations in the reference well. This process involved iterative testing of various sediment values until the most suitable combination for the model was identified. Iterations persisted until calibration values for thickness and lithology percentage surpassed 90%, with a 10% error threshold, when compared to the reference wells. This means

that differences less than the error threshold are considered well-validated. The error threshold is applied to accommodate the vertical scale differences between the generated model and validation data.

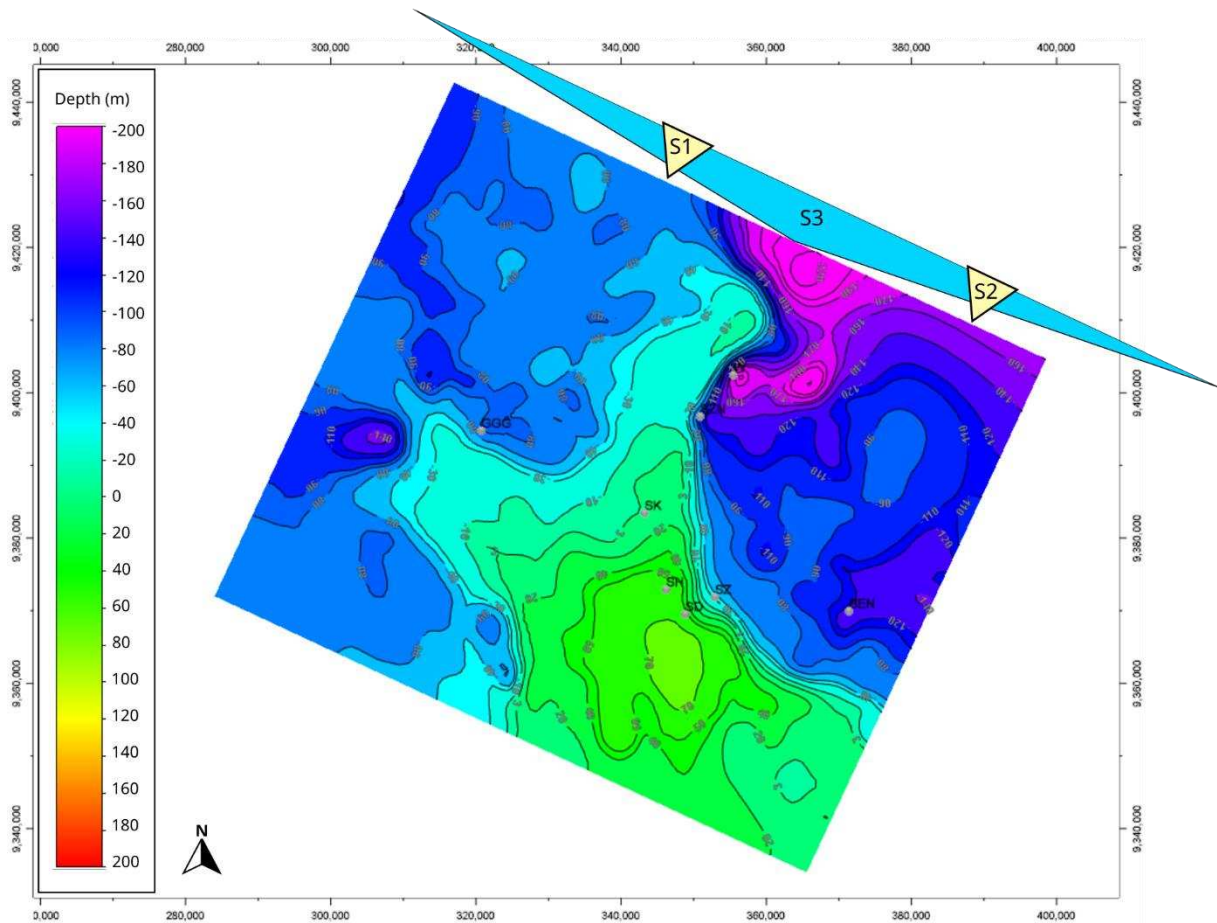


Figure 6.5 Paleobathymetry map at the base of the model (22.2 Ma) used in stratigraphic forward modeling (positive depth means below sea level). S1, S2, and S3 are sediment entry point used in the model

Wave energy parameters such as wave base, azimuth, and frequency per year, as well as diffusion coefficients due to wave action, are also can be modelled in SFM. However, the apparent absence of wave-influenced deposits in this area has been reported by several researchers (e.g., [Possamentier 2021](#)). Therefore, we did not conduct a more in-depth analysis of wave impact.

The direction of sediment deposition in this area has been extensively analyzed by previous researchers ([Abdurrokhim and Ito, 2013](#); [Arpandi and Patmosukismo, 1975](#); [Atkinson, 1993](#); [Clements and Hall, 2007](#); [Posamentier, 2002](#)), who have mentioned that sediment supply originates from the emerged areas to the north-northeast ([figure 6.1](#)). We combined the

observed progradation direction (Ponto *et al.*, 1988) with our seismic observation to estimate the location of river input in the area. The delineation of the Sunda Platform boundary shown in the (figure 6.1) represents an estimated boundary for the Langhian age, where coastal onlap can be observed in the northernmost seismic area. It should be noted that the Sunda Platform boundary and sedimentation direction beyond the study location are not supported by seismic data, and interpretations outside the study area remain speculative.

## **6.2. Base Model Simulation**

A bounding box of 90 X 78 km with cell size of 1 X 1 km was modeled for Upper Cibulakan Formation in Miocene (22.2 to 8.4 Ma), with simulation time steps of 100 ky. This boundary encompasses the Ardjuna sub-basin, the eastern section of the Seribu platform, and the Central platform (figure 6.1). A clockwise rotation of 25° to the block boundary has been applied to optimize the cell orientation to facilitate the sedimentation input direction during the UCF deposition.

### **6.2.1. Accommodation**

In Dionisos Flow, the regional sea level at the first timestep in the model always started from zero meters. Therefore, the eustatic curve was shifted by +10 meters so that the regional sea level surface was defined as 0 meters at 22.2 Ma. This curve then solely defined the magnitude of sea level rise and fall at each timestep, while the depth of the sea level at every coordinate was defined by the bathymetry map.

The initial bathymetry map used in this work suggests a maximum depth of 90 meters (295.3 ft) in the area adjacent to the Ardjuna fault, whereas the Seribu and Central platform were considered to be emerged figure 6.5. The configuration of the basin at this time reflects the later stages of the rifting phase, during which the faults configuration continued to play an important role in the formation of the basin. The north-south fault trend, which corresponds to the Eocene rift direction, remains clearly visible forming a N-S oriented embayment in the modeled area. Fault configuration provides high accommodation space at the downthrown area of the Ardjuna fault. In addition, the former reef topography of the BRF throughout the high relief area also contributes into providing accommodation space. The base of the model composition is predominantly characterized by reef carbonates in the platform areas and reworked carbonates in the deeper regions (see chapter 4). This composition is employed in our modeling to define the substratum composition of the model.



### 6.2.2. Transport Parameters

We have systematically conducted tests to capture all diffusivity values for both sand and shale, whether induced by gravity ( $K_g$ ) or driven by fluid ( $K_w$ ), in both continental and marine environments. For continental settings, we explored  $K_w$  values ranging from 2 to 1000  $\text{km}^2/\text{my}$  and 0.2 to 600  $\text{km}^2/\text{my}$  for  $K_g$  (figure 6.6). In marine environments, the tested  $K_w$  values were 0.2 to 200  $\text{km}^2/\text{my}$  and 0.001 to 0.2  $\text{km}^2/\text{my}$  for  $K_g$  (figure 6.7). The selected values are then analyzed and chosen based on their ability to distribute sediment throughout the entire basin area. In this context, these values must satisfy two conditions: they should provide good calibration for thickness in both wells and seismic data, and they should facilitate the transfer of coarse sediment (sand) into the basin, as calibrated by well facies. The diffusion coefficient is constant throughout all time intervals; therefore, its value must represent the sediment transport conditions across the entire model interval.

After conducting a comprehensive observation of each value, a specific set of  $K_g$  and  $K_w$  values is selected to best represent the geological conditions of the study area. The gravity diffusion coefficients employed for sand grains in our model are 1  $\text{km}^2/\text{ky}$  for continental and 0.05  $\text{km}^2/\text{ky}$  for marine settings, while the water transport coefficients are 50  $\text{km}^2/\text{ky}$  for continental and 5  $\text{km}^2/\text{ky}$  for marine conditions (table 6.1). The coefficients used in the model fall within the lower range of the published value. Careful observation was conducted for these diffusivity values and cross-examined with the thicknesses in the reference wells at each time marker, in conjunction with the geometry generated in the model. The values used in the model allowed a strong validation (e.g., <10% error) between the model and the geological data. The wave base that is used in the model is 5 meters, with an azimuth of  $-10^\circ$  and a frequency of once per year. The input wave energy values did not show a significant impact on the model and could be considered negligible. The values of transport parameters are summarized in the table 6.1.

Table 6.1. Sediment transport coefficient ( $\text{km}^2/\text{ky}$ ) used in model.

Parameter		Sand	Shale	Carbonate_clast
$K_{gravity}$	Continental	1	3	
	Marine	0.05	0.01	0.015
$K_{water}$	Continental	50	100	
	Marine	5	10	6
$K_{wave}$		1	5	3



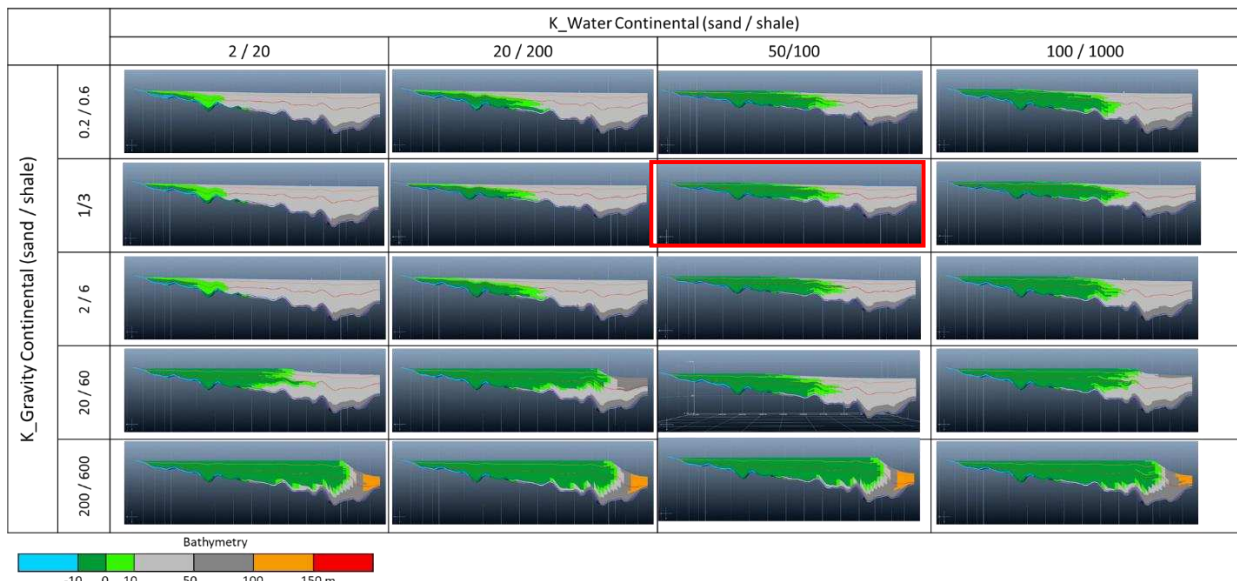


Figure 6.6 North-south cross section of the bathymetric model for 22.2 Ma to 19 Ma illustrating the bathymetry model is highly dependent of the different gravity and water driven diffusion coefficients ( $K_g$  and  $K_w$ ) value in the continental environment. The highlighted model (red box) was chosen for the base value employed in the model as it best fits with the data.

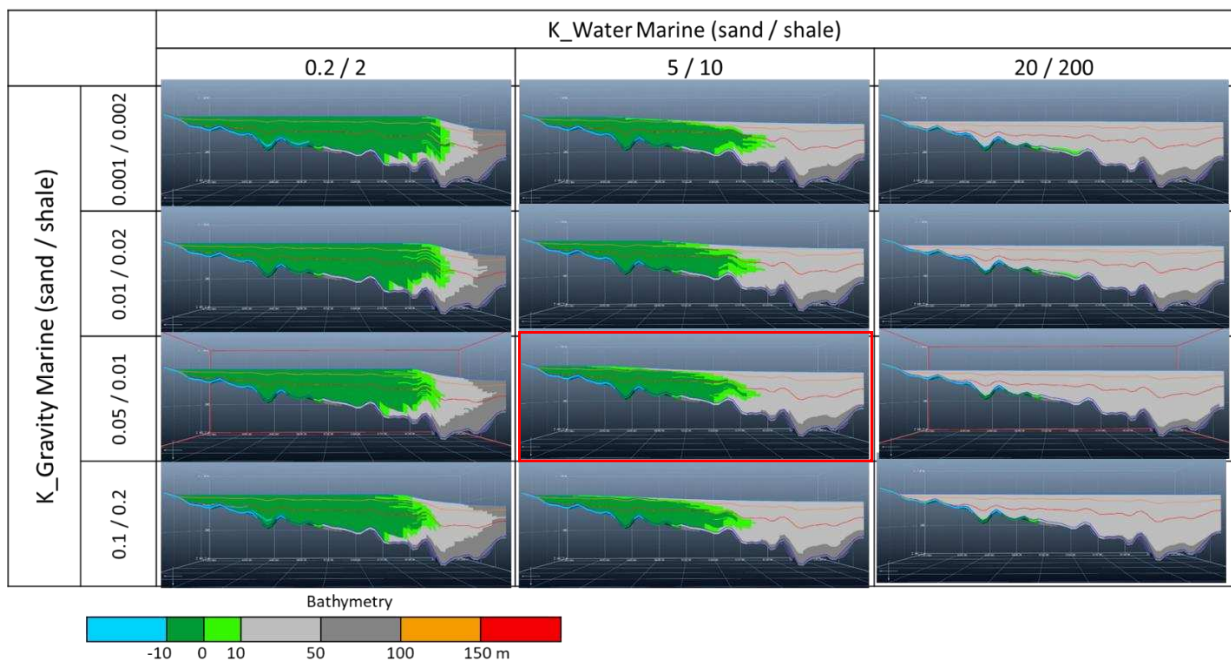


Figure 6.7 North-south cross section of the bathymetric model for the time interval from 22.2 Ma to 19 Ma illustrating the bathymetry model dependence toward the different  $K_g$  and  $K_w$  value in the marine environment. The highlighted model (red box) was chosen for the base value employed in the model as it best fits with the data.

### 6.2.3. Sediment Input

Two external sediment sources (S1 and S2 in figure 6.5) from the northeast direction, with a width of approximately 20 km, were used from the top BRF (22.2 Ma) to SB11 (11.1 Ma) interval to simulate sediment input points relatively close to the shoreline. Those two sediment sources account for reproducing sigmoid progradational seismic reflectors identified in Chapter 5 (SF4 and SF6). The continuous sediment supply used in the model can be seen in figure 6.8. To predict the sediment supply, fluvial discharge, and variations in lithology (sand, shale, and carbonate percentages), a trial-and-error analysis were conducted until a good calibration that matches the seismic thickness and shale volume in wells is obtained. In the initial stages, constant values for sediment supply, fluvial discharge, and sediment percentage were set for each sequence. Once a set of constant values was determined, detailed adjustments were applied, particularly to the sediment percentage at each timestep, to achieve better calibration with each well. The sediment supply, fluvial discharge, and sediment percentage curves can be seen in figure 6.8.

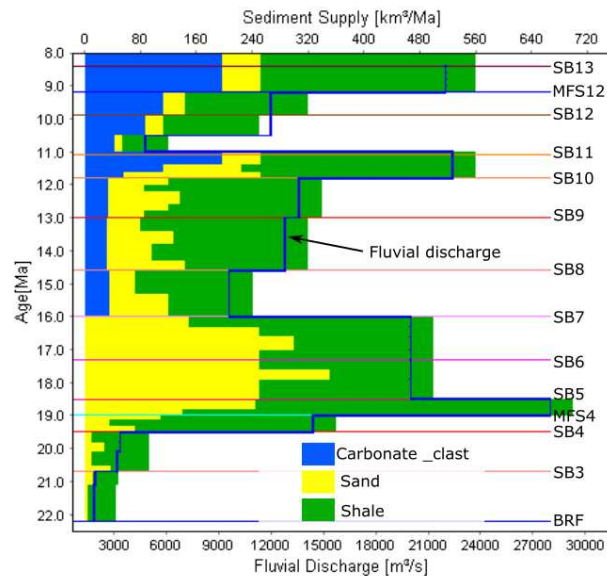


Figure 6.8 Sediment supply, fluvial discharge and lithological variation curve used in the model. Here are represented the sequence boundaries identified on the wells and seismic lines and main maximum flooding surfaces (MFS4 and MFS 12). The small scale variation in sediment percentage are used to achieve a good calibration with the lithology in the well data.

At the outset of the simulation (22.2 Ma), two sedimentary inputs (S1 and S2) were introduced from the northeast, utilizing a total sediment supply (S) of 48 km<sup>3</sup>/Ma and a fluvial discharge (FD) of 1,920 m<sup>3</sup>/Sec. Starting from 20.7 Ma (SB 3), there is an increase in the total

sediment supply to 92 km<sup>3</sup>/Ma and FD to 3,200 m<sup>3</sup>/Sec until 19.5 Ma. This then further rises to a combined supply of 360 km<sup>3</sup>/Ma and FD 14,500 m<sup>3</sup>/Sec until 19 Ma. Subsequently, from 19 Ma (MFS 4) to 18.5 Ma (SB 5), the simulation employs a short term total sediment peak of 700 km<sup>3</sup>/Ma and FD of 28,000 m<sup>3</sup>/Sec. This is then followed by a consistently high sediment supply of 500 km<sup>3</sup>/Ma and FD of 20,000 m<sup>3</sup>/Sec from 18.5 Ma (SB 5) to 16 Ma (SB 7) (figure 6.8).

Starting from 16 Ma (SB 7), the sediment supply from S1 was diminishing and the carbonate clastic sediment input is introduced to incorporate the lithological description data from well. There is a sudden drop in the total sediment supply, to 240 km<sup>3</sup>/Ma with FD of 20,000 m<sup>3</sup>/Sec. Commencing at 14.6 Ma (SB 8), the total supply gradually increased to 320 km<sup>3</sup>/Ma FD of 12,800 m<sup>3</sup>/Sec until 13 Ma (SB 9). Subsequently, it further rose to 340 km<sup>3</sup>/Ma – 13,600 m<sup>3</sup>/Sec until 11.8 Ma (SB 10), and finally reached 560 km<sup>3</sup>/Ma – 22,400 m<sup>3</sup>/Sec until 11.1 Ma (SB 11) (figure 6.8).

Commencing from 11.1 Ma (SB11), a significantly broader (100 km) entry point (S3 in figure 6.5) was modeled to simulate northeast-directed shoreline retrogradation, leading to sediment dispersion in the input point area. During this period, the simulation incorporated in-situ carbonate production at a rate of 160 m/Ma in shallow waters (up to 15 m). To ensure realistic modeling, two environmental constraints were implemented: a production vs. depth curve (figure 6.9) and a maximum turbidity of 20 m/Ma. This means that carbonate growth will be restricted if the clastic sediment content at a specific location exceeds 20 m/Ma.

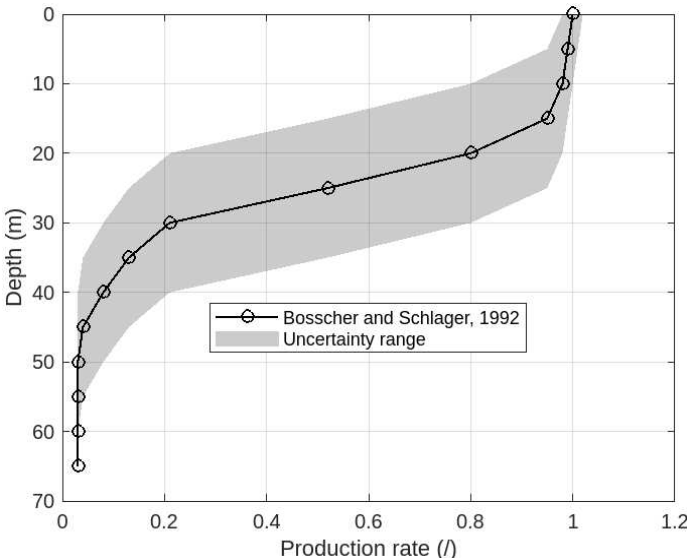


Figure 6.9 In-situ carbonate production rate vs depth curve (Bosscher and Schlager, 1992) used in the simulation. To assess the uncertainty of the parameter the curve is shifted 10 m (both direction) in depth.

To accurately depict the distribution of carbonate mounds obtained from seismic interpretation, specific locations for carbonate growth were defined in the model. This was achieved using a subsidence map for a single timestep (11.1 – 11.0 Ma). In areas identified for facies reefs based on seismic interpretation, the bathymetry was set to be 5 meters shallower compared to the surrounding areas. This 5-meter elevation difference triggered the initiation of carbonate reef growth at specific locations identified from the seismic interpretation.

The deposition from 11.0 Ma began with a minimal sediment supply of 120 km<sup>3</sup>/Ma with FD of 4,600 m<sup>3</sup>/sec. Subsequently, there was an increase in sediment supply to 320 km<sup>3</sup>/Ma with FD of 12,000 m<sup>3</sup>/sec until 9.2 Ma (MFS 12). Following this, the sediment supply further rose to 560 km<sup>3</sup>/Ma with FD of 22,000 m<sup>3</sup>/sec until 8.4 Ma (SB 13) (figure 6.8).

The sediment content parameter constitutes the final aspect analyzed in the model. Initially, constant percentage values for sediment content were set at each interval: carbonate clastic/sand/shale at 0/0.1/0.9 from 22.2 Ma to 19 Ma (BRF - MFS4). This was followed by a transition to 0/0.5/0.5 until 16 Ma (SB7), then 0.1/0.2/0.7 until 12 Ma (SB 10), and 0.2/0.2/0.6 until 11.1 Ma. From 11.1 Ma to 8.4 Ma (SB 13), the content was adjusted to 0.35/0.1/0.55 v/v. These sediment proportions are essentially derived from sediment percentage calculations in well log analyses. To enhance correlation with well data, the sediment content is fine-tuned at each timestep until a final sediment content curve is obtained, as illustrated in figure 6.8.

#### 6.2.4. Model Calibration

During the construction of the base model, all parameters are fine-tuned to achieve a robust alignment with both seismic thickness (figure 6.10) and sediment proportions in wells (figure 6.11). In the error percentage map (figure 6.10), variations in total thickness within the modeled intervals are observable, with a maximum difference of 4%. This suggests that the model thickness has been effectively calibrated to match the seismic thickness. Moreover, it indicates successful calibration of the subsidence map, total sediment supply, and transport coefficient.

To assess the influence of the total sediment supply on model thickness, we systematically adjusted the average total sediment supply, ranging from 250 km<sup>3</sup>/Ma to 380 km<sup>3</sup>/Ma (the base model average is 320 km<sup>3</sup>/Ma). Calibration rate calculations were carried out at each sediment supply value (figure 6.10). Subsequently, error thresholds (maximum tolerated difference) of

0%, 5%, and 10% were applied. For example, a 5% error threshold implies that if the difference in thickness within a zone is <5%, that zone is considered fully (100%) calibrated.

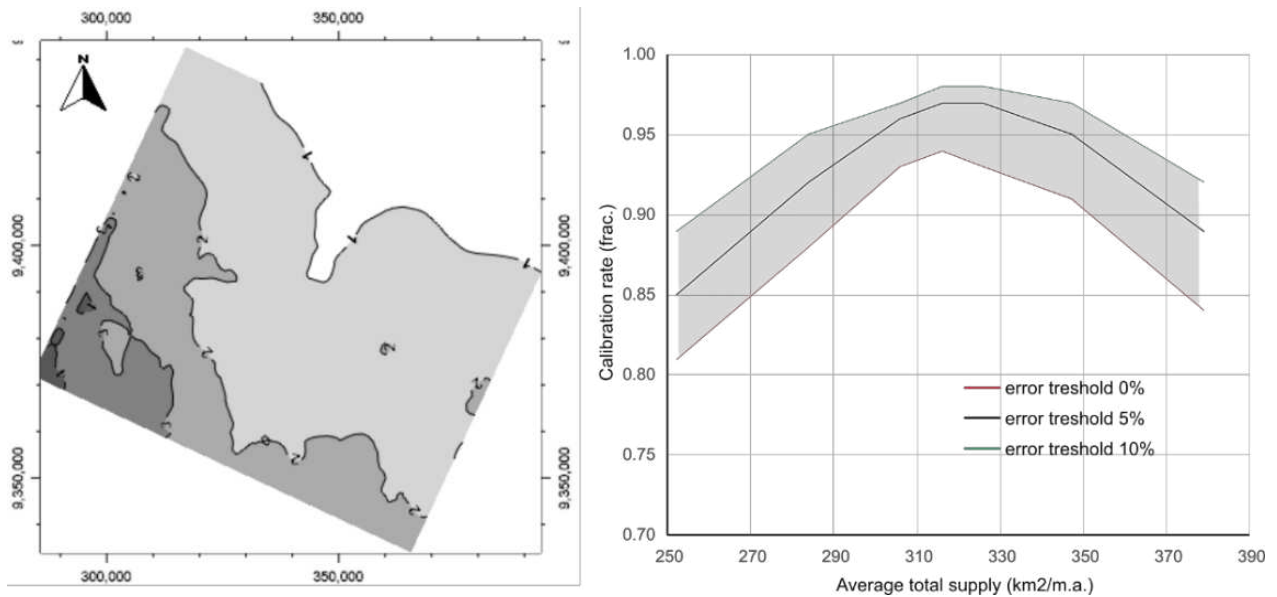


Figure 6.10 Left: thickness error percentage map showing an overall good thickness calibration along simulated grid with a very low different (<5% difference) between seismic and simulated thickness in the reference case scenario. Right: thickness calibration rate as a result of different total supply. Good calibration rates (>90%) are achieved between 280 to 380 km<sup>3</sup>/Ma sediment supply.

From the total supply vs calibration rate plot in figure 6.10, it can be observed that without employing an error threshold, an overall calibration rate of 94% has been achieved. Table 6.2 shows a thickness calibration across all simulated zone. The overall thickness calibration is satisfactory, except for the SB 11 - SB 12 interval, which includes carbonate reef facies. The lowest calibration is found in wells SZ-1 (34%) and BEN-1 (49%), particularly in the SB 11 - SB 12 interval. This is attributed to the challenging determination of boundaries between SB 11 and SB 12 in well correlations, mainly due to the maximum growth of the carbonate reef facies in this interval, as indicated by seismic stratigraphic interpretation (see Chapter 5).

In addition to thickness calibration, evaluations were also conducted on the calibration of sediment content obtained from well log analyses, particularly shale volume derived from the gamma-ray logs. Table 6.3 presents the shale volume calibration in each zone. To accommodate scale differences in well data compared to the model, a 10% threshold was applied to calculate calibration in each zone. It can be observed that overall validation rate of 98% has been achieved. This indicates that the sediment proportion values (shale, sand, carbonate clast, and reef) generated by the model have been validated against the available well data. In figure 6.11,



the proportion curves of each modeled sediment can be observed. In the lower intervals of the model (SB 2 - SB 7), the shale volume trend is noticeably well-validated against well data. However, in the upper intervals (SB 7 - SB 13), where the carbonate is introduced, the trend slightly deviates from the well data. Despite the model shale volume trend not capturing detailed variations from well logs due to vertical scale differences, the overall trend aligns with the shale volume trend observed in well logs.

Table 6.2 Thickness calibration (%) between well log and simulated model.

Stratigraphic Units	BEN-1	GGG-1	SD-1	SH-1	SK-1	SZ-1	W-1	All Wells	
All Sequences	97	97	100	100	95	97	94	94	
SB 12 – SB 13	89	72	97	91	99	88	82	88	
SB 11 – SB 12	49	61	82	87	93	34	58	76	
SB 10 – SB 11	95	95	95	98	97	95	95	95	
SB 9 – SB 10	93	100	98	99	99	100	90	97	
SB 8 – SB 9	100	90	97	97	99	97	94	96	
SB 7 – SB 8	81	71	87	87	86	78	69	84	
SB 6 – SB 7	90	96	98	98	99	100	93	96	
SB 5 – SB 6	100	92	97	96				96	
SB 4 – SB 5			97	97				97	
SB 3 – SB 4			94	97				95	
SB 2 – SB 3			98	100				99	
SB 1 – SB 2				Substratum					

Table 6.3 Shale volume calibration (%) between well log and simulated model. The value was calculated using 10% error threshold

Stratigraphic Units	BEN-1	GGG-1	SD-1	SH-1	SK-1	SZ-1	W-1	All Wells	
All Sequences	98	98	100	94	99	100	91	98	
SB 12 – SB 13	99	100	100	100	99	100	92	99	
SB 11 – SB 12	84	84	94	99	88	100	90	93	
SB 10 – SB 11	99	100	100	100	99	100	89	99	
SB 9 – SB 10	96	97	100	100	99	100	100	97	
SB 8 – SB 9	100	100	100	100	100	100	100	100	
SB 7 – SB 8	100	100	100	100	100	100	100	100	
SB 6 – SB 7	100	100	100	98	100	100	100	100	
SB 5 – SB 6	94	99	100	100				99	
SB 4 – SB 5			100	100				100	
SB 3 – SB 4			100					100	
SB 2 – SB 3			100	100				100	
SB 1 – SB 2				Substratum					

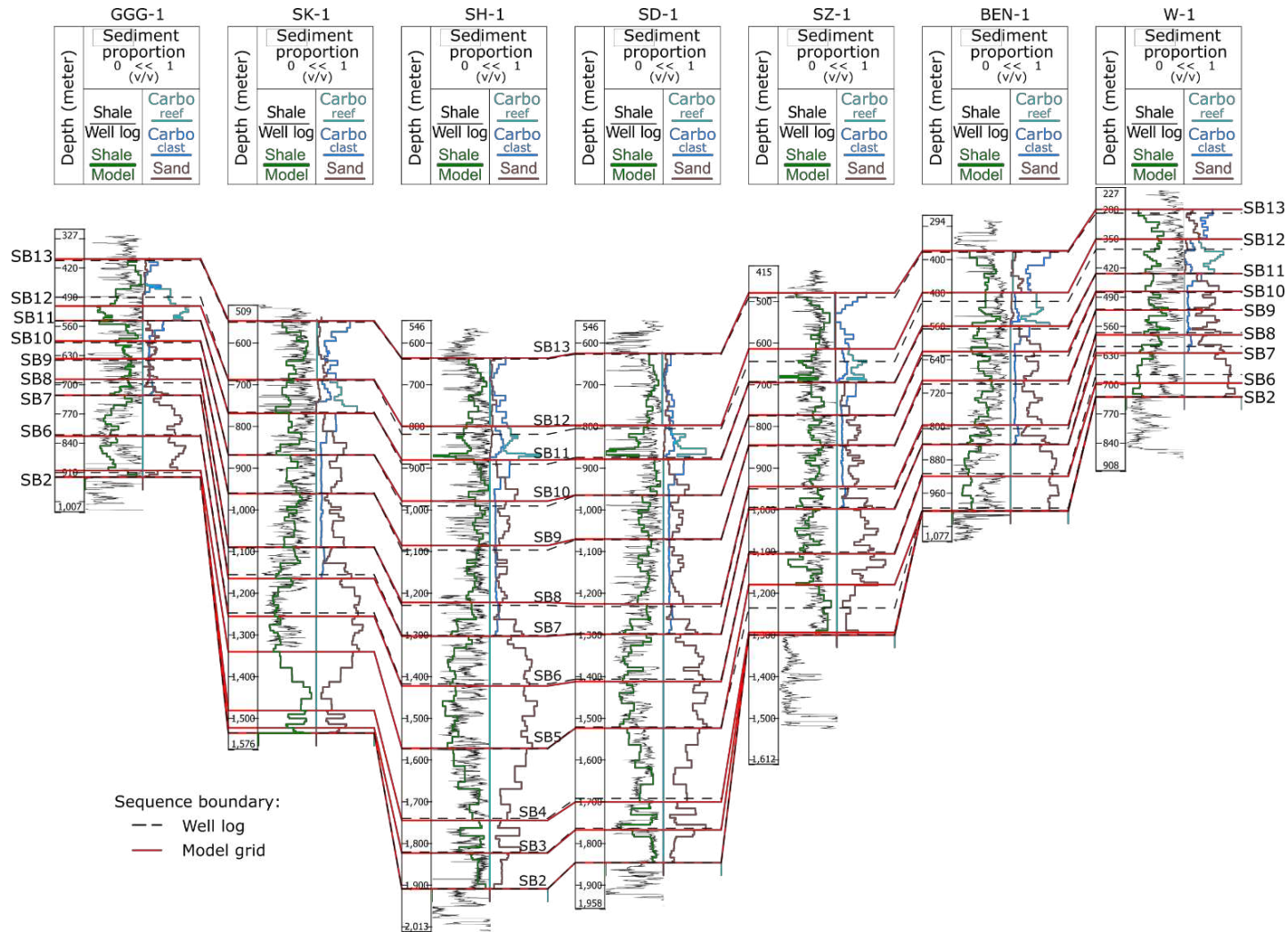


Figure 6.11 Well correlation plane showing the comparison of shale volume from simulated grid (green) with well log (black). An overall trend of the shale volume from well log has been captured in the model. The carbonate reef and carbonate clastic from the simulated grid ( light blue and blue) as well as sand proportion (brown) is presented to show the overall sediment content.

### 6.3. Model Result

The simulated models were then classified according to a depositional facies scheme based on bathymetry of deposition, sand percentage, carbonate percentage, and the volume of fluvial discharge (table 6.4). In this facies scheme, the distinction between a delta and submerged delta lobe is based on the bathymetry of deposition. The use of fluvial discharge is not intended to represent the actual channelization process but rather to signify high-discharge transport conditions where distributary channels might be expected to develop. Areas with lower discharge may experience more dispersed sediment.

In the simulation, the three sediment entry points, combined with paleobathymetry and sediment supply rates during deposition, result in the formation of a prograding delta during the initial deposition phase, followed by back stepping and aggradation geometry. Figure 6.12 illustrates the model results in a three-dimensional form at four times; the MFS 4 (19 Ma); SB 7 (16 Ma); SB 10 (11.8 Ma); and two timesteps above SB 11 (10.9 Ma) to shows the maximum extend of reef carbonate facies. While figure 6.13 shows the fence diagram of the 3D model.

Table 6.4. Properties cutoff used to define facies in the model

<i>Facies name</i>	<i>Bathymetry (m)</i>	<i>Sand (%)</i>	<i>Fluvial discharge (m<sup>3</sup>/sec)</i>	<i>Carbonate reef (%)</i>	<i>Thickness (m)</i>
<i>Distributary channel (FD 300 - 700)</i>		>20	300-700		
<i>Distributary channel (FD&gt;700)</i>		>20	>700		
<i>Upper delta plain</i>	<5				
<i>Lower delta plain</i>	>5	>20			
<i>Delta front</i>	>5	>10			
<i>Prodelta - marine</i>	>5				
<i>Marine - reef</i>				>75	>5
<i>Marine - intrareef</i>				>75	<5

At the beginning of the simulation (22.2 Ma) to 19 Ma, the combination of two sediment input points (figure 6.12 a1), along with paleobathymetry and sediment proportion, yielded the best fit model. It can be observed that the entire embayment in the Ardjuna sub-Basin has been covered by the sea, whereas the Central platform area still remains above the sea level (figure 6.12 a2). The sand sediments are distributed in accordance with areas characterized by relatively high fluvial discharge (figure 6.12 a3). During the 22.2 Ma – 20.7 Ma, the fluviodeltaic facies resulting from the sediment input in S1 extends up to a maximum of 40 km along the embayment from the north into the central part of the model block, followed by distal environments (lower delta plain to prodelta) with a maximum bathymetry up to 40 m.

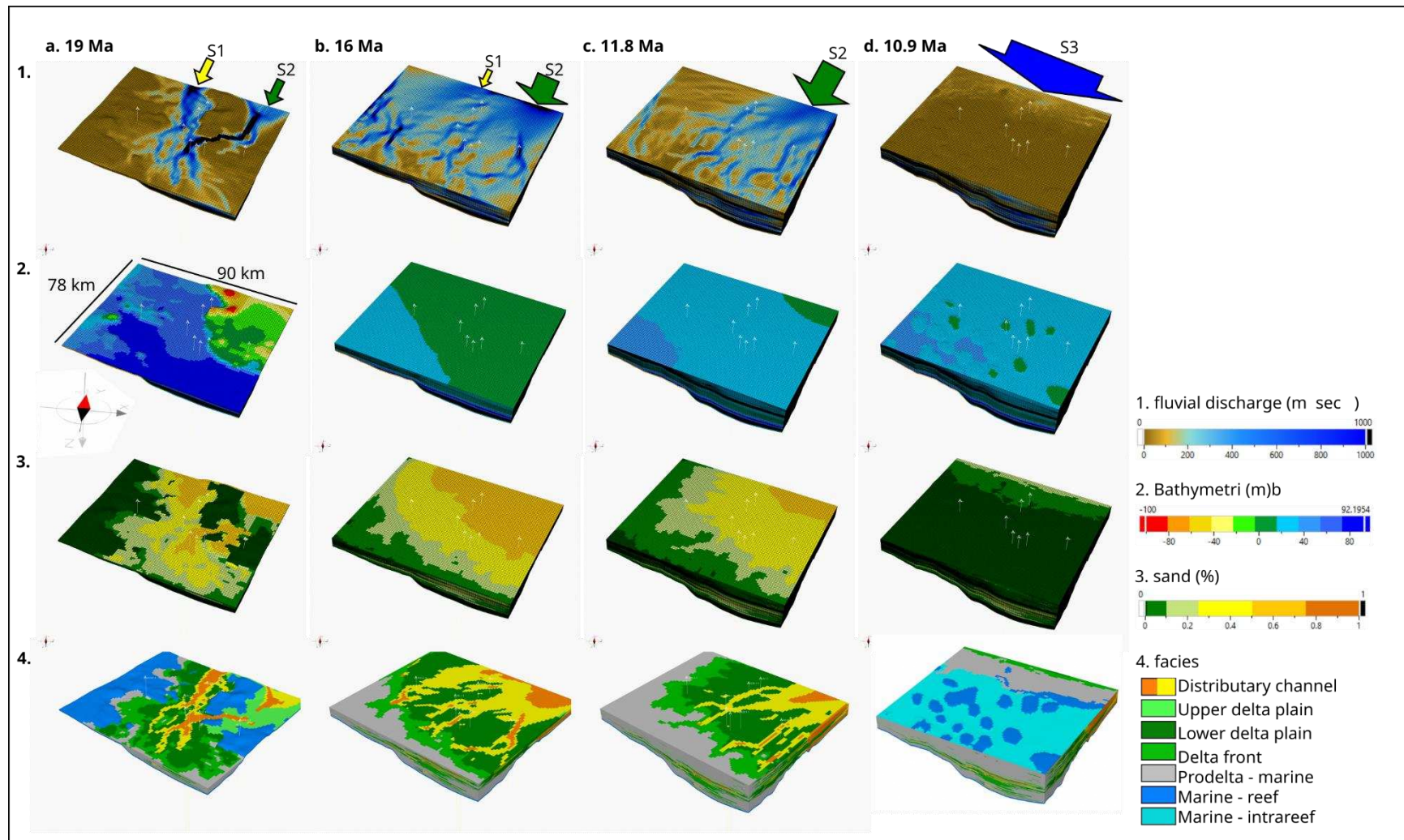


Figure 6.12 Stratigraphic forward modeling simulation result showing the bathymetry of deposition (a); sand percentage (b); the diversion of water pathways (c); and depositional facies (d) in four important time steps. Three sediment supply input (S1, S2, and S3) were used in the model, the size of the arrows reflect the relative quantity of sediment input. Vertical exaggeration is 20x.



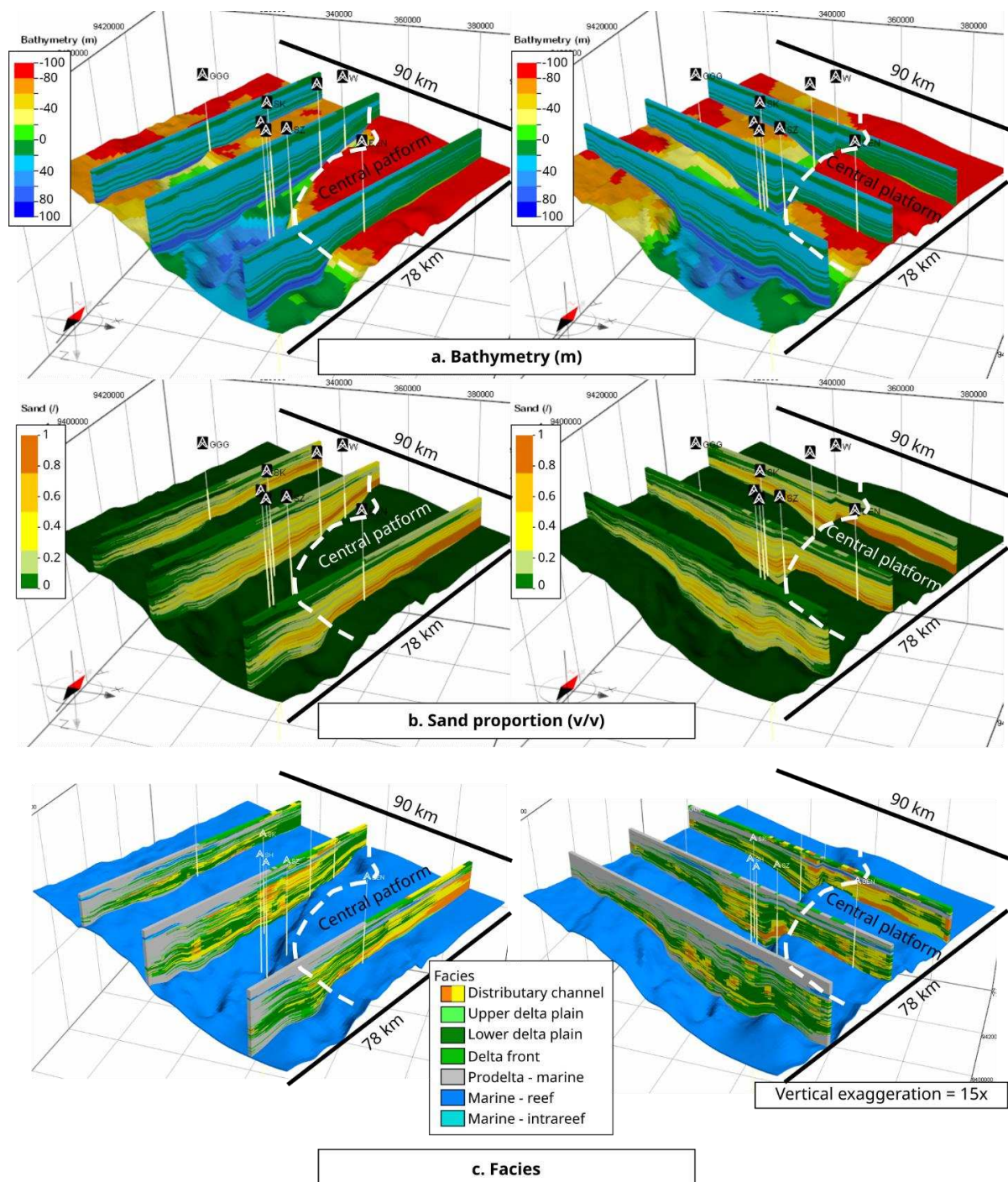


Figure 6.13 3D fence diagrams illustrating the evolution of bathymetry (top), sand proportion (middle) and facies (bottom) distribution during the deposition of Upper Cibulakan Formation. (left) The NE-SW direction representing the dip direction; and (right) the NW-SE direction representing the strike direction.

Similarly, the fluviodeltaic facies generated by input S2 shows the same geometry, extending up to 50 km, from the foot of Ardjuna fault to the basin (figure 6.13). The depositional system generated in the model shows that the distribution of depositional environments was



highly influenced by the paleogeography at the time, indicating a large accommodation space during the final stages of the rifting. These two distributary inputs produce a progradational pattern. The resulting progradational pattern of distributary channel from S1 and S2 can also be observed in the 2D seismic section, indicating deposition in the lower part of the upper Cibulakan Formation initiated by a major regression (figures 6.14 and 6.15). At 20.7 – 19 Ma, there was a significant sea-level transgression that submerged the entire upper delta plain facies from source S1. As a result, the entire embayment area saw the deposition of submarine lobes, with a maximum bathymetry of up to 90 m (figure 6.12 a2). However, the sea-level rise and subsidence during this period were not sufficient to submerge the high areas along the border fault, thus the deposition continued to be dominated by a fluviodeltaic system (figure 6.12 a4). The deposition pattern formed during this time involved back stepping followed by aggradation, which can still be observed in the 2D seismic section (figure 6.14 and 6.15).

During 19 – 16 Ma, there was a substantial increase in sediment supply from the northeast region (S2), overpowering the rise in sea level and subsidence, resulting in a very significant regression during this period, while the sediment input from S1 was decreasing and became less significant (figure 6.12 b1). Fluvial discharge is evenly distributed across the entire area (figure 6.12 b1), as all previous topography has been completely submerged. The bathymetry was dominated by <15 m depths, with NW-SE orientation (figure 6.12 b2). The fluviodeltaic facies once again dominated and transported large amount of sand materials into the depositional center (figure 6.12 b3). During this time, sediment deposition covered the entire study area in a delta environment (figure 6.12 b4), resulting in a relatively flat paleotopography with a gentle deposition slope (<1°) and an average bathymetry of 20 m at the beginning of deposition to as low as 5 m at the end (figure 6.13).

In the 16–11.8 Ma intervals, the sediment input from S1 was diminishing, while S2 became the dominant sediment source (figure 6.12 c1). The fluvial discharge model indicates a decrease in the distribution of the channel during this period (figure 6.12 c1). The resulting bathymetry indicated an overall deepening, transitioning from an average of 5 m to an average of 35 m 11.8 Ma (figure 6.12 c2). This transgressive phase combined with less sand fraction (figure 6.12 c3) formed a deposition environment that submerged most of the upper delta plain, with distal delta lobe facies (lower delta plain to prodelta) dominating the study area (figure 6.12 c4, 6.13). Aggradation deposition patterns are clearly observed in the simulation results, which are confirmed by the 2D seismic section (figure 6.14 and 6.15).

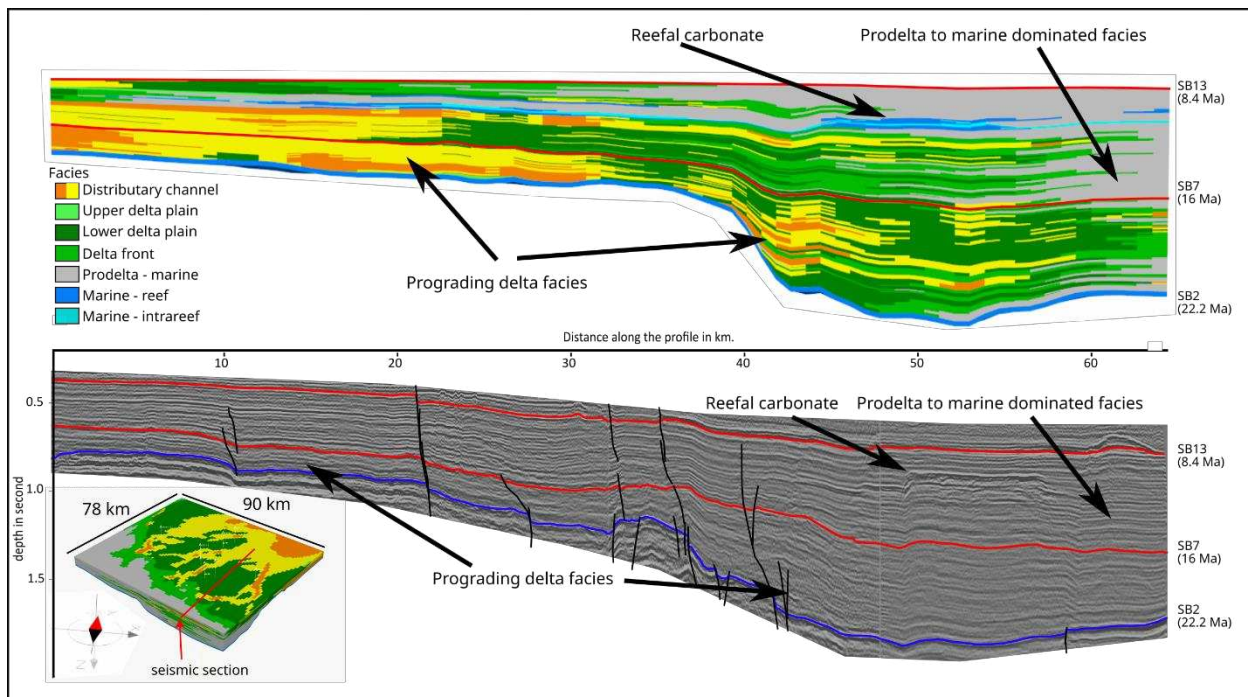


Figure 6.14 Simulated facies and seismic section in North – South direction showing a good geometry and facies matching between model and seismic data. The red horizon in 16 Ma is top Massive unit.

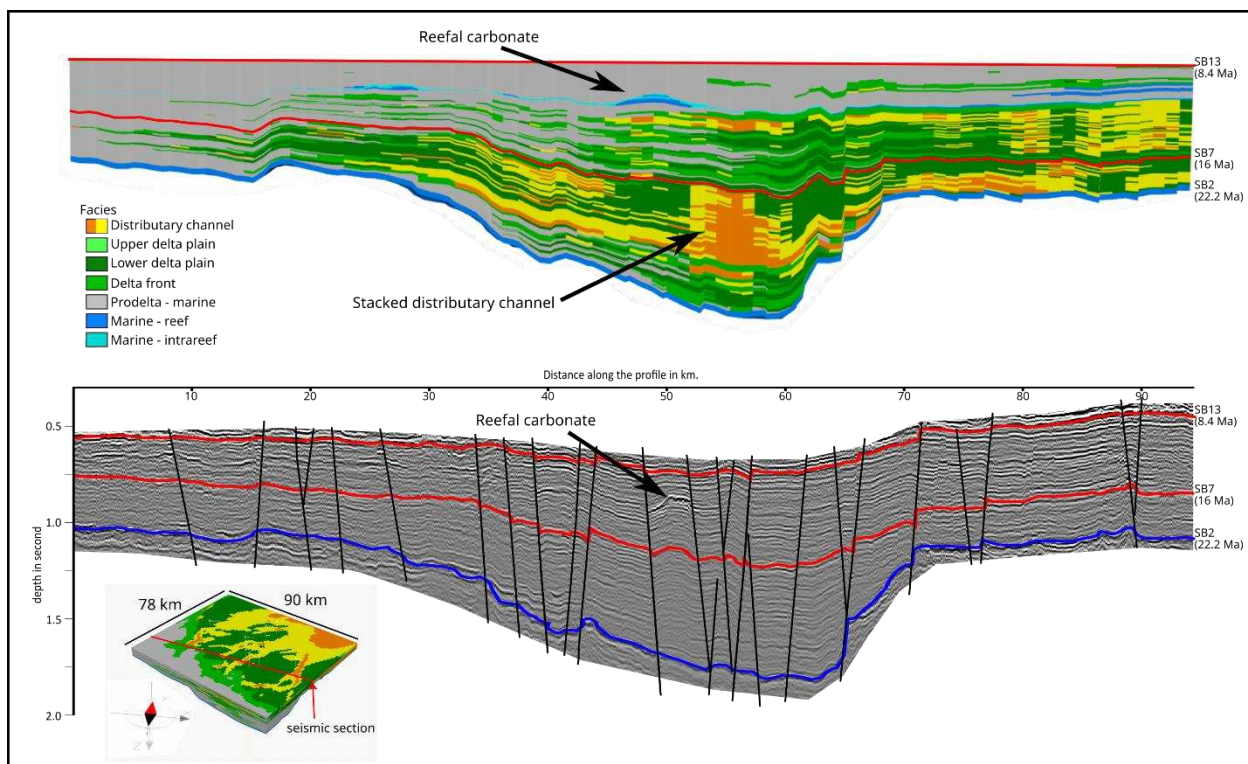


Figure 6.15 Simulated facies and seismic section in West – East direction showing a good geometry and facies matching between model and seismic data. The red horizon in 16 Ma is top Massive unit.

The drop in sediment supply and the resulting decrease in fluvial discharge input at 11.1 Ma were marked by relatively homogenous and low fluvial discharge values (figure 6.12 d1, d3). This was responded to by the formation of a relatively flat bathymetric model, with some locations exhibiting elevation differences that we determined in the model (figure 6.12 d2). Several carbonate reef facies with mound geometries grown in pre-determined locations (figure 6.12 d4). The location of each carbonate body has been adjusted based on seismic interpretation. The carbonate production parameters used in the model result in a good match in thickness and distribution of reefs that align with the observed reef geometry in the 2D seismic section (figure 6.14 and 6.15). During The 9.2 – 8.4 Ma, high sediment supply and the consequent high turbidity prevented carbonate growth. However, the distribution of carbonate clastic sediment increased. The bathymetry deepened again, reaching up to 25 meters at the end of the simulation. The deposition environment was dominated by marine facies.

#### **6.4. Multi simulation uncertainty and sensitivity**

A total of 120 simulations were conducted to understand the influence of input parameters within the model. These parameters encompassed all critical aspects necessary for constructing the base model, including those affecting accommodation space, sediment supply, and sediment transport coefficients. The parameters used in the uncertainty and sensitivity analysis are detailed in table 6.5. In the initial stage, the values of uncertainty for each parameter are determined deterministically to assess the impact of each parameter on the base model. This means that initially, one parameter is altered (e.g., initial bathymetry) with extreme low values, while base values are used for other parameters. Subsequently, calibration is performed against thickness and shale volume. The deterministic uncertainty approach is carried out continuously until suitable values are obtained to conduct automatic multirealization of uncertainty and sensitivity.

For the initial bathymetry map, a bulk shift adjustment of 20 m (bathymetry modifier) is made upwards and downwards to examine the influence of bathymetry variations on the model. In the subsidence map, a total subsidence of 100 m is added to the final model subsidence map (8.4 Ma), and this total subsidence is linearly distributed at each timestep in the model. In the table, this variation is represented by a 100 m change in well SD-1. Total sediment supply is adjusted by 10 km<sup>3</sup>/Ma (addition and subtraction) for all timesteps, and in Table 6.5, this variation is represented by the average total supply. For fluvial discharge, a modifier value of

50% is applied to assess its impact on the model if the fluvial discharge is reduced by half, and a modifier value of 150% is applied to assess its impact if the fluvial discharge is increased to 150%.

The maximum in-situ carbonate production ranges from 140 m/Ma to 180 m/Ma, with the maximum production occurring at depths from 0 meters to 20 meters. This maximum production depth is obtained by shifting the production vs. depth curve on the base model by 10 m upwards and downwards. The sediment diffusion coefficient in marine sands ranges from 2 to 8 km<sup>2</sup>/Ka, with a continental/marine ratio between 2 and 8, and a shale/sand ratio between 1.2 and 2.8, obtained from sensitivity analysis. For the non-linear water flow coefficient, the entire range of possible values is explored, ranging from 1 (linear) to 2. The distribution of each parameter designed using Latin Hypercube can be observed in [figure 6.16](#).

Table 6.5. Parameters and parameter values used in the model scenarios. The letter (d to k) are notation in figure 6.17

Input parameters		Minimum	Base model	Maximum
Accommodation	f Initial bathymetry modifier (m)	-20	0	20
	g Total subsidence on reference well (m)	1141	1241	1341
Sediment supply	h Average total supply (km <sup>3</sup> /Ma)	306	316	326
	d Fluvial discharge modifier (%)	50	100	150
	k Carbonate in-situ production	140	160	180
	k Carbonate vs depth curve (m) (max production depth )	0	10	20
Sediment transport	i Sand marine diffusion coefficient (km <sup>2</sup> /Ka)	2	5	8
	i Continental / marine diffusion coefficient ratio	2	10	18
	i Shale/sand diffusion coefficient ratio	1.2	2	2.8
	h Non linear water flow law coefficient	1	1.5	2

Total sediment supply has the most significant influence in terms of total sediment thickness. The standard deviation map generated at 22.2 to 11.1 Ma and 11.1 to 8.4 Ma indicates relatively uniform thickness differences (28 m) resulting from the range of total sediment supply used in the sensitivity analysis suggesting that parameters other than total sediment supply have very little to no effect on the total thickness. From the calibration rate to seismic thickness, a sediment supply range from 280 km<sup>3</sup>/Ma to 380 km<sup>3</sup>/Ma provides calibration levels exceeding 90% ([figure 6.9](#)), with the maximum calibration achieved at the base value used in the reference model (316 km<sup>3</sup>/Ma). However, an exception occurred from 22.2 Ma to 16 Ma, where the nonlinear water flow coefficient still had noticeable influences on thickness ([figure 6.17e](#)). These phenomena changed after 16 Ma when the paleo topography



had been completely covered by sediment, resulting in a relatively flat topography and causing the water driven coefficient to dominate the transport process (equation 1).

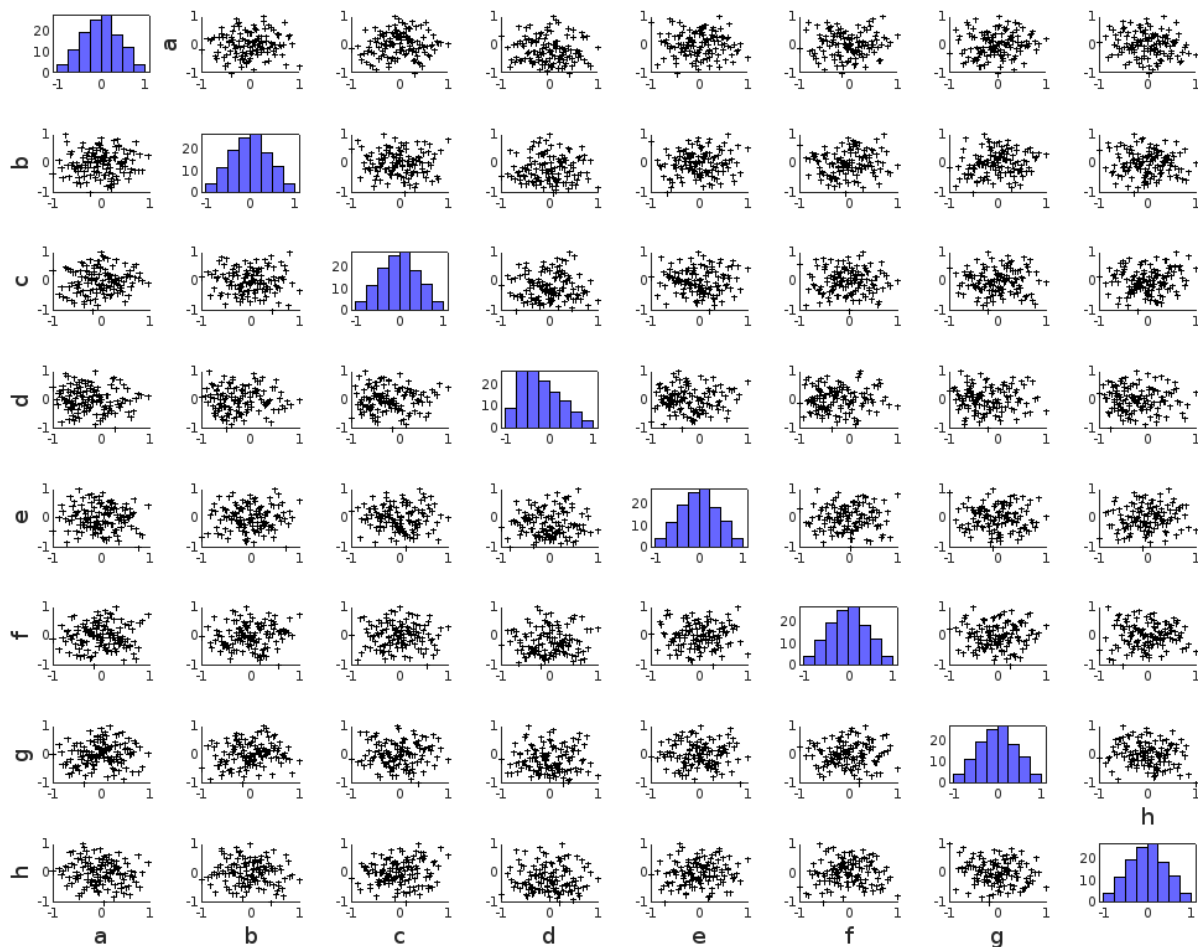


Figure 6.16. Matrix scatter plot of designed parameters in the multi simulation analysis. a) maximum carbonate in-situ production; b) carbonate vs depth curve; c) fluvial discharge; d) nonlinear water flow coefficient; e) initial bathymetry; f) total subsidence; g) total sediment supply; h) sediment transport (including sand marine diffusion coefficient, continental-marine ratio, shale/sand coefficient ratio). Note that the parameters value was normalized by using gaussian transformation.

Overall net to gross (ntg) map from all the simulation shows the ntg averages 0.3 – 0.7 along delta plain area and decreases rapidly to prodelta and marine facies to less than 0.15 (figure 6.17a). Standard deviation of net to gross prediction map showing a SD of <0.08 across the entire modeled area indicates the high predictability of ntg (figure 6.17b and 6.17k). In the interval from 22.2 Ma to 11.1 Ma, higher standard deviations (0.05 – 0.08) were observed in proximal areas where delta plain facies developed and in very distal areas where prodelta facies were present (figure 6.17k).



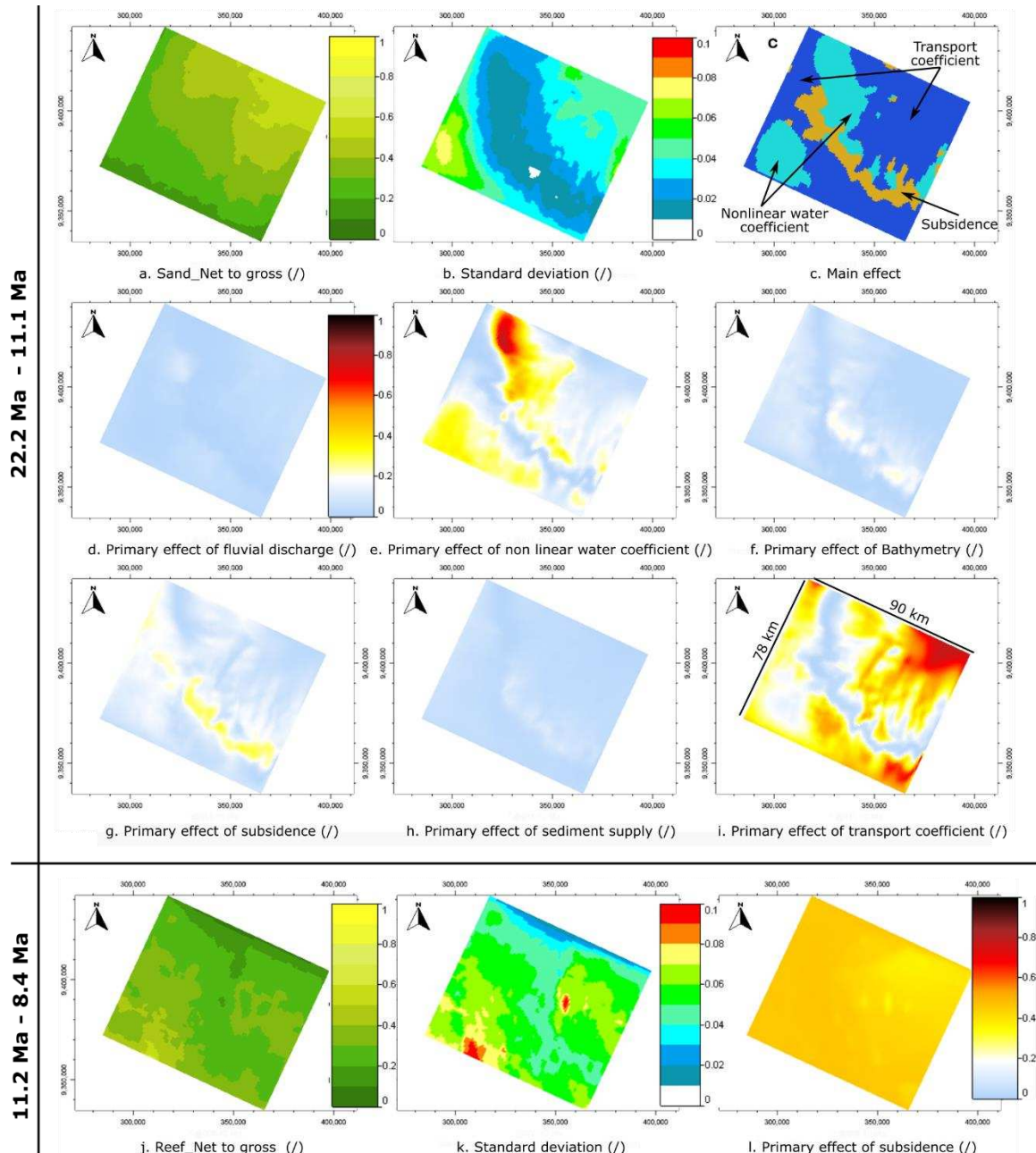


Figure 6.17. The multi parameters simulation sensitivity results indicate a high level of ntg (a) predictability, with a low standard deviation (SD < 0.1) in net-to-gross properties (b). During the period from 22.2 Ma to 11.1 Ma, the main effect map (c) shows that three parameters (transport coefficient, subsidence, and nonlinear water coefficient) were sensitive. The effect of each parameter are presented in (d) to (i), while from 11.2 Ma to 8.4 Ma, the good predictability of ntg (j) can be seen with low SD (k), all parameters had a relatively uniform effect, with subsidence being the most influential factor (i).

In the proximal area, the higher standard deviations were primarily caused by transport coefficients ( $K_{w,k}$  in equation 1), as shown in main effect map (figure 6.17c) and primary effect map of the transport coefficient (figure 6.17i). In contrast, in the more distal regions (delta front

and prodelta), variability of ntg distribution was predominantly caused by the nonlinear transport coefficient ( $n$  in equation 1) as evidenced by our multi parameters simulation (figure 6.117e). In the central part of the model, standard deviations were low ( $<0.03$ ) (figure 6.17b), indicating a high level of predictability of ntg distribution with a northwest-southeast direction, where lower delta plain and delta front facies developed. In this area, the most sensitive parameter was the subsidence rate (figure 6.17g). Note that the locations, where these transport coefficients and subsidence were dominant, were also the locations of the embayment that existed during the basin's formation. This suggests that the distribution of facies is still influenced by the remnants of these inactive faults during the deposition.

During the 11.1 Ma to 8.4 Ma, the net to gross (ntg) map generally indicates ntg values ranging from 0.3 to 0.6 in distal areas where sediment shedded from the northeast no longer reach the basin (clean of clastic sediments). These ntg values significantly dropped to 0.1 in the northeast region (figure 6.17j). The standard deviation map also displayed a relatively consistent distribution with the ntg distribution, suggesting that as the reef facies thickness increases, so is the standard deviation, reaching up to 0.1. The effects of each parameter appeared uniform, with the most sensitive parameter being the subsidence rate, influencing at a rate of 40% to 50% (figure 6.17l). This indicates that the sea level during the early deposition significantly affected the growth rate of carbonate reefs.

## **6.5. Reservoir prediction**

From an exploration perspective, a reservoir is a rock formation where fluids of whatever origin may accumulate. This implies that the rock should have good petrophysical parameters such as porosity and permeability. In this study, we did not attempt to model those parameters within the model. Therefore, the best reservoir distribution was determined based on the distribution of facies that are considered to have the potential for good porosity and permeability. In this context, we defined reservoir as layers that have a minimum fluvial discharge of 100 - 150 m<sup>3</sup>/Sec to ensure that the deposited sediment have enough energy to disperse clay size sediment (figure 6.18a), and have sand and reef composition greater than 25% - 30 % (figure 6.18b), with thickness greater than 150 – 200 m (figure 6.18c). Risk maps from these properties are then combined by simple multiplication off each map to provide the probability map (P10, P50, P90) (figure 6.18d).

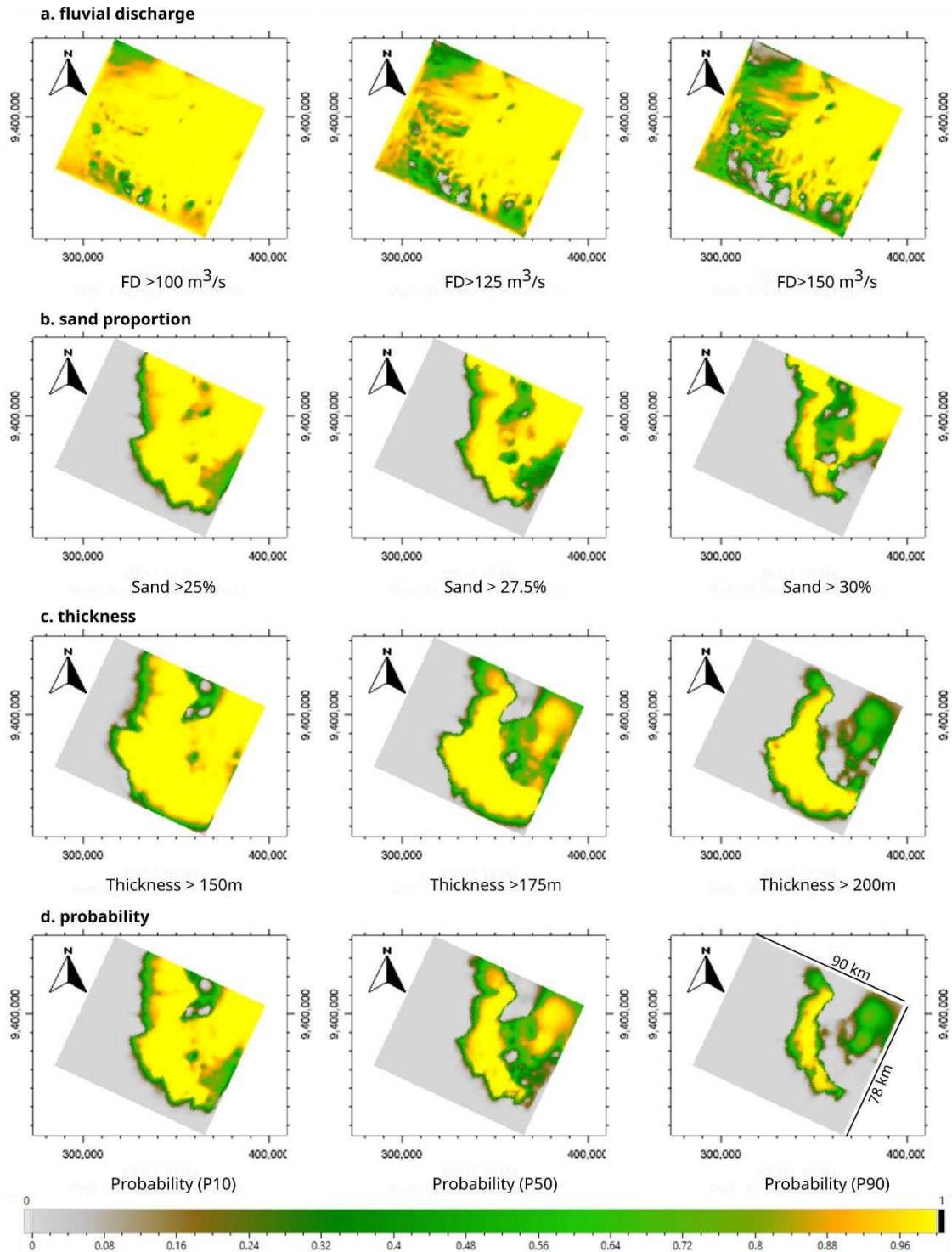


Figure 6.18. Reservoir distribution probability map based on three properties cutoff criteria: sand and reef composition greater than 25% - 30 %, thickness greater than 150 – 200 m, and minimum water discharge of 100 - 150 m<sup>3</sup>/Sec. The probability maps (P10, P50, P90) are based on combined water discharge, sand-reef %, and thickness cut off

Figure 6.18a shows the probability of areas with fluvial discharge values above the cutoff. It can be observed that fluvial discharge is not a limiting factor for the distribution of reservoirs.

At a cutoff value of  $FD > 100 \text{ m}^3/\text{s}$ , almost the entire study area is considered favorable in terms of fluvial discharge. If the cutoff value is increased to  $150 \text{ m}^3/\text{s}$ , the distribution of locations above the cutoff appears to spread across the Central platform to the Ardjuna sub-Basin. This distribution seems to be controlled by the modeled sediment input point locations.

The sand proportion map highlights areas with a high likelihood of developing sandstone lithofacies (figure 6.18b). This distribution is consistently observed, irrespective of the chosen cutoff value, primarily within the Ardjuna sub-Basin, aligning with the Ardjuna fault direction follows the direction of the paleo embayment preceding the UCF deposition. Additionally, it extends into the Central platform region with a southeast to southwest orientation. The total thickness of the sandstone facies is derived from the product of the overall thickness and its sand proportion (figure 6.18c). Here, the distribution of areas exhibiting substantial thickness closely aligns with the embayment direction, mirroring the pattern observed in the sand proportion distribution.

The probability of reservoir facies distribution is illustrated in the probability map of reservoir presence (figure 6.18d). This distribution is generally concentrated in the footwall area of the Ardjuna fault (P90), with potential presence also identified in the Central platform area (P50 and P10).

## 6.6. Discussion

### 6.6.1. Sediment supply, bathymetry and subsidence curve

The sediment supply trend used to achieve good calibration levels in the model exhibits three cycles of sediment supply fluctuations (figure 6.8, 6.19). From 22.2 Ma to 16 Ma, sediment supply increased from  $48 \text{ km}^3/\text{Ma}$  to as high as  $700 \text{ km}^3/\text{Ma}$  at 19 – 18.5 Ma and  $500 \text{ km}^3/\text{Ma}$  until 16 Ma, followed by a significant reduction to  $240 \text{ km}^3/\text{Ma}$ . Subsequently, sediment supply increased again to  $560 \text{ km}^3/\text{Ma}$  until 11.1 Ma (SB 11). This was followed by a decrease to  $120 \text{ km}^3/\text{Ma}$  and another increase to  $560 \text{ km}^3/\text{Ma}$ . Clift and Plumb (2008) based on the sediment budget calculation across 13 major basin across Asia and minerals analysis from diffuse reflectance spectroscopy (DRS) (chlorite vs. hematite and goethite) estimated an increase in mass flux in the Asian region triggered by the intensification of the monsoon, resulting in heavy rainfall and accelerated erosion during the Mid Miocene up to 11 Ma (figure 6.19). This phenomenon might as well be recorded in the study area: the recurring patterns of sediment supply increase might be the result of this monsoon activity.



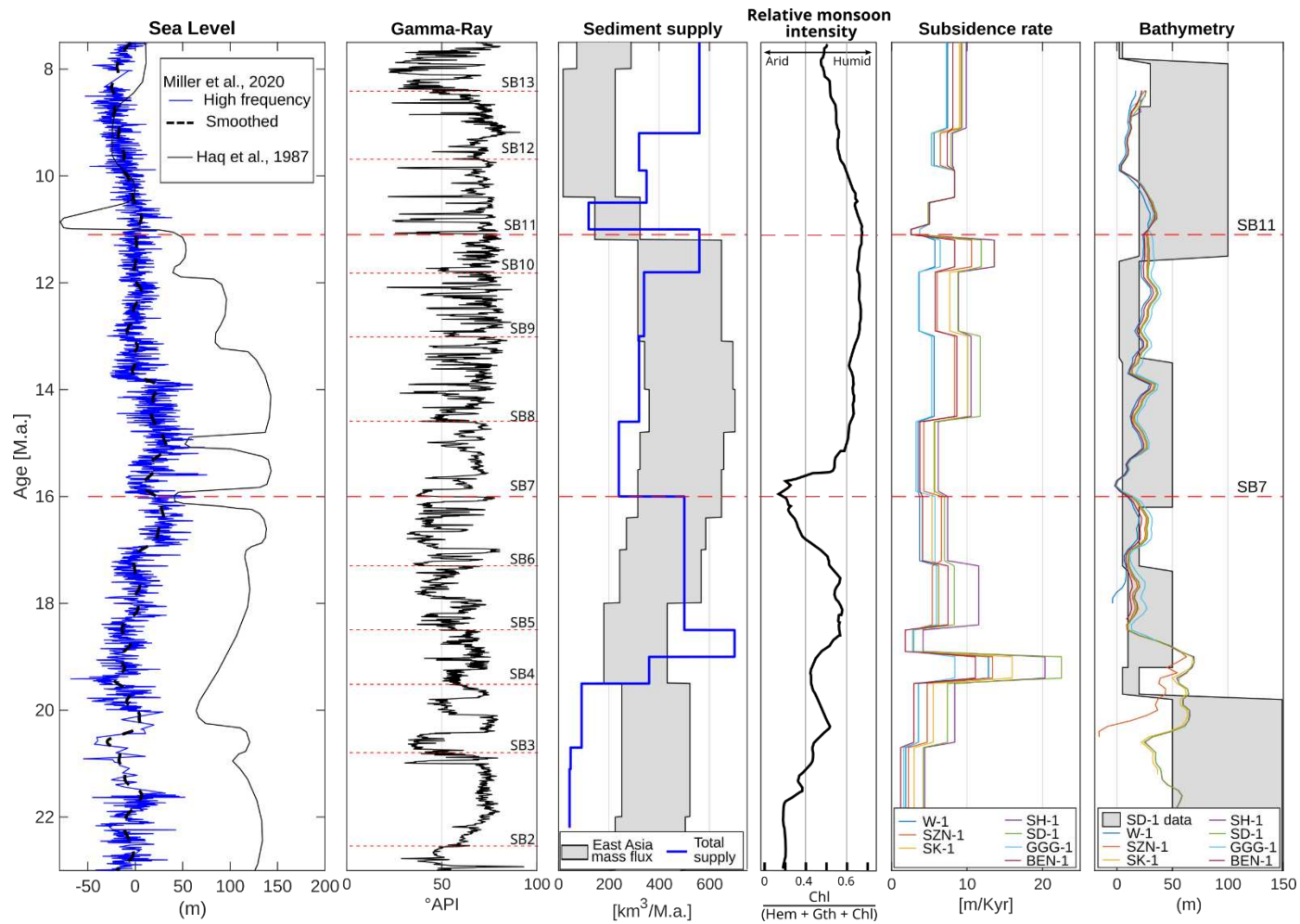


Figure 6.19 Final input curve that were used in the stratigraphic modeling. The gamma-ray curve is from SD-1; East Asia mass flux are modified from Clift and Plumb (2008). Relative monsoon intensity based on Chlorite content (Chl) vs hematite (Hem) and goethite (Gth) from Clift and Plumb (2008). SD-1 bathymetry data are from unpublished report (Noon et al., 1993). Please note that the bathymetry curve does not display bathymetry above sea level (as seen in the curves for W-1 and SZN-1, which do not start from the beginning of deposition).



Furthermore, we identified more detailed patterns, with two cycles of sediment supply increase in the early to mid-Miocene interval.

During the period from 22.2 to 16 million years ago, even though the sediment budget calculations conducted by [Clift and Plumb \(2008\)](#) could not capture the variations in sediment supply caused by the increased intensity around 20-Ma from the DRS data, our modeling results recorded the cycles of increased sediment supply. This discrepancy might arise from the differences in the geographical positions of the research locations. The sediment provenance region in the NWJB basin, interpreted to be from the Schwaner Mountains ([Martodjojo, 1984](#)), was located in the equator during the deposition age (Pubellier and Morley, 2014) (see [figure 2.1 for location of Schwaner Mountain](#)). This geographical position could lead to more intense changes in rainfall intensity, thereby potentially intensifying the impact of monsoon on the rate of sediment supply.

From 22.2 Ma to 16 Ma, the observed progradational stacking pattern in the gamma-ray log appears to be primarily controlled by sediment supply. When compared to the eustasy curve ([Miller \*et al.\*, 2020](#)), the Langhian major flooding (at 15.5 Ma), in addition to subsidence rate, could not provide accommodation space high enough to counterbalance the total sediment supply to the basin. The bathymetry curve extracted at the reference wells locations shows a deep bathymetry (>40 m) that appears from the beginning of deposition until 18.5 Ma, and changes to 5 – 10 m afterward. This change in bathymetry also appears to be triggered by the big sediment supply that occurred between 19 and 16Ma. Furthermore, the combination of accommodation and sediment supply parameters leads the sands to be deposited into the basin and form the prograding stacking pattern in the well log data.

The extracted subsidence rate curve at the locations of each reference well also indicates that subsidence is directly proportional to the magnitude of sediment supply ([figure 6.19](#)), suggesting that subsidence is controlled by sediment loading, which is common in post-rift basins. A spike in subsidence rate can be observed at around 19 Ma ([figure 6.19](#)). This spike is particularly interesting as we attempted to create a scenario in which the evolution of subsidence rate is smooth. However, we were unable to achieve a good calibration level with the seismic derived thickness, thus the spike at 19 Ma is retained. This spike may potentially be correlated with a brief tectonic event that reactivated rifting in the Early to Middle Miocene as stated by [Adnan \*et al.\*, \(1991\)](#) .

From 16 Ma to 11.1 Ma, a similar sediment supply and subsidence rate pattern occurred. However, regional eustasy indicated a decrease in sea level, and there were no significant changes in bathymetry. This suggests a good balance between sediment supply and accommodation space creation, allowing an aggradational pattern to be observed in the gamma-ray log of the well (figure 6.19). This is further supported by the aggradational pattern visible in the model cross-sections and 2D seismic profiles (figure 6.14).

At the beginning of sequence 11 (11.1 Ma), there was a decrease of sediment supply. Subsequently, the minimal clastic sediment input in the basin, in combination with favorable water depths with average bathymetry of <30 m, led to the growth of carbonates in the area. This was followed by a significant increase in sediment supply (250 km<sup>3</sup>/Ma) and shallowing up sea level to 5 m at SB12 (9.9 Ma), leading to the demise of all carbonates at the beginning of sequence 12. The sediment supply increasing continued until the end of the simulation. We primarily focused on analyzing the location and geometry of carbonate reef growth in the model. However, a more detailed analysis and modeling are needed to capture the fine facies details of carbonates in the study area.

#### 6.6.2. Reservoir distribution

Sedimentology and stratigraphy studies, based on core analysis, seismic data, and well data, indicate that the study area and its surroundings were deposited in a series of deltaic to nearshore sub-environments, including mouth-bar, channel, and sand ridge facies (Atkinson, 1993; Posamentier, 2002; Purantoro *et al.*, 1994). The bathymetry trend and facies geometry produced by stratigraphic forward modeling support the interpretation of a depositional environment transitioning from fluviodeltaic to marine, with sediment sources originating from the northeast of the study area. The depositional facies that developed include distributary channel facies, upper and lower delta plain, delta front, prodelta, and marine carbonate facies.

The probability maps generated based on three cutoff properties (figure 6.18) indicate a relatively extensive distribution of potential reservoirs in this area, with a north-south orientation following the rift direction. These trends seem to be driven by the interplay between accommodation by compaction and delta geometry. Loading and compaction occurring simultaneously with deposition appears to provide additional accommodation space in thicker areas (former embayment areas), influencing the sediment distribution to this direction. Moreover, given the very low depositional slope (<1°), additional accommodation space in

certain locations triggers sediment distribution. Regarding depositional facies, the favorable reservoir distribution appears to be within the distributary channel, upper and lower delta plain, and delta front facies. These four facies have sufficient fluvial discharge to transport sand sediments and have adequate thickness. In contrast, the prodelta and marine facies seem to contain very little sand material and thus do not fall into the provided classification.

## **6.7. Conclusion**

This comprehensive stratigraphic forward modeling simulation provides valuable insights into the complex geological factors influencing the sedimentary evolution of the Upper Cibulakan Formation in the Miocene (22.2 to 8.4 Ma) within the Ardjuna Sub-Basin. This research enhances our understanding of sedimentary dynamics, depositional environments, and the potential distribution of reservoir zones in this region.

Gravity diffusion coefficients for sand grains were set at 1 km<sup>2</sup>/ky for continental and 0.05 km<sup>2</sup>/ky for marine settings, while water transport coefficients were 50 km<sup>2</sup>/ky for continental and 5 km<sup>2</sup>/ky for marine conditions. The simulation initiated with two sediment entry point, totaling 48 km<sup>3</sup>/Ma. The sediment supply increased over time, reaching 560 km<sup>3</sup>/Ma by 11.1 Ma. At this point, a broader entry point (S3) modeled northeast-directed shoreline retrogradation, incorporating in-situ carbonate production with environmental constraints. From 11.0 Ma, carbonate growth locations were defined, triggering reef initiation in specific areas. Sediment supply fluctuated, peaking at 560 km<sup>3</sup>/Ma by 8.4 Ma. Sediment content parameters evolved from constant values to match well data, refining at each timestep. The model detailing sediment supply, fluvial discharge, and sediment percentage curves provide a comprehensive overview of sediment dynamics over the studied timeframe.

The influence of total sediment supply on model thickness was assessed by systematically adjusting the average supply, revealing an overall calibration rate of 94%. However, challenges arose in the SB 11 - SB 12 interval. Sediment content calibration, specifically shale volume from gamma-ray logs, achieved an overall validation rate of 98%, indicating successful validation of model-generated sediment proportion values against well data. The proportion curves of modeled sediments show strong validation in lower intervals (SB 2 - SB 7), but a slight deviation in upper intervals (SB 7 - SB 13) with the introduction of carbonate. Despite these deviations, the model accurately captures the general trends in shale volume, demonstrating robust calibration and validation processes.

Several key factors shape sedimentary evolution, notably sediment supply, initial bathymetry, and subsidence rates. Sediment supply fluctuations within three cycles significantly impact the sedimentary patterns and depositional environments. Increases in sediment supply are associated with shifts in depositional environments and facies distribution. Temporal changes in paleo bathymetry provide accommodation space variations in the basin. Alterations in bathymetry influence sediment transport directions and the dominant facies types. Furthermore, subsidence rates, primarily driven by sediment loading, play a crucial role in sediment accumulation. A subsidence rate spike around 19 Ma hints at a potential tectonic event that briefly reactivated rifting during the Early to Middle Miocene.

The analysis of potential reservoir distribution shows that the prospective reservoir zones tend to follow a north-south orientation, influenced by rift direction that led to different sediment compaction and delta geometry, which influence accommodation space.

## **CHAPTER 7: CONCLUSIONS AND OUTLOOKS**





## 7.1. Conclusion

The integration of biostratigraphic, well and seismic data enhances our understanding of the geological evolution and provides valuable insights into the stratigraphy and depositional history of the North West Java Basin. The findings of this contribution add valuable information for regional geological studies in the North West Java Basin. The biostratigraphic age reinterpretation and the identification of the age of key boundaries, such as the top of Talangakar, top of Baturaja Formation and the top of Upper Cibulakan Formation presented in this study, based on the comprehensive analysis of biostratigraphy report from five well, provides a new timescale frame for the Lower to Upper Miocene stratigraphic series of the NWJB into the Cenozoic geological history of the North West Java Basin.

The comprehensive sequence stratigraphic analysis of the Upper Cibulakan Formation in the Ardjuna sub-basin provides a thorough description into the depositional history and depositional sequences. Four facies association has been revealed, based on gamma-ray log values, stacking patterns, dip meter analysis, and core descriptions. These include distributary channel and point bar facies in delta plain settings (FA1), delta front to prodelta environment with tidal-influenced mouth bar or shelf ridge (FA2), reworked or clastic carbonate in a marine environment (FA3), and reefal carbonate (FA4). Twelve third-order sequences, embedded within three second-order sequences, were interpreted within the Upper Cibulakan Formation. The age assignments for those sequence boundaries were determined based on biostratigraphic markers, gamma-ray trends, and correlation with global sea-level curves. Notably, the study identified key events such as short-term sea-level falls during the Aquitanian, followed by significant transgressions until the early Burdigalian. In the Burdigalian to early Langhian period, the basin experienced regressive cycles followed by major transgressions until the Tortonian

Nine seismic facies (SF1-SF9) were identified, characterized by unique geometry and reflector configuration as well as stratal termination, and was supported by wellbore and biostratigraphic data. These facies include both carbonate reef and clastic deposit, as well as clastic deposits including delta progradation (proximal and distal facies), retrogradation /backstepping, and channel fill and levees in delta plain.

The study highlights the role of tectonic activity in controlling sediment distribution patterns. Pre-Oligocene tectonic events shaped the basement morphology that significantly

influenced depositional patterns during the Aquitanian to Early Burdigalian. The presence of clastic sources from the north led to the formation of deltas in the embayment area of the Ardjuna sub-basin during this period. Tectonic quiescence prevailed until the Early Langhian when tectonic activity was renewed, coupled with increased clastic sediment supply. This resulted in the establishment of multiple deltas. Subsequent transgression events during the Langhian to Tortonian shifted the depositional environment gradually to the shelf, accompanied by a reduction in sediment supply and the onset of carbonate growth.

The application of Stratigraphic Forward Modeling (SFM) in this study allowed testing the effect of various physical parameters on the sedimentary architecture and the geometry of the sedimentary sequences present in the basin. SFM also allowed to study and predict the reservoir facies and distribution in the area. The simulation, involving a timeframe from 22.2 to 8.4 Ma, was constructed. Results of the SFM showed the sediment thickness for 22.2 – 11.1 Ma is governed mainly by sediment supply, while for 11.1 – 8.4 Ma is mainly influenced by subsidence. The sediment transport parameters, including diffusion coefficients, were carefully selected through systematic analysis and sensitivity testing, ensuring accuracy of the models in replicating observed thickness and lithological variations. The calibrated base model achieves a strong match with seismic thickness and well data, providing a reliable platform for further analysis and interpretation of the reservoir distribution. The simulation results, validated against seismic profiles and well data, demonstrate the evolution of the depositional environment from fluviodeltaic dominance to submarine lobe and eventually to a transgressive phase with carbonate reef facies.

The study encompassed 120 simulations, carefully examining input parameters crucial for assessing the uncertainty to the reference model. The net-to-gross (ntg) map, standard deviation map, and sensitivity analysis clarify the distribution of reservoir facies. The reservoir prediction methodology focused on identifying layers with sand and reef composition greater than 25% - 30%, thickness exceeding 150 – 200 m, and minimum water discharge of 100 - 150 m<sup>3</sup>/Sec. The resulting probability maps (P10, P50, P90) offered a comprehensive view of potential reservoir zones.

## 7.2. Outlook

In summary, this research significantly advances our understanding of the geological factors shaping the sedimentary evolution in the Ardjuna Sub-Basin. The findings provide a robust foundation for future studies and potential exploration activities in the region. Based on the comprehensive analysis conducted in this study, several approach for future research can be explored to enhance our understanding of the geological and reservoir potential in the Ardjuna Sub-Basin. The following outlines potential future research:

1. Incorporate additional data sources, specifically at a lower scale, including petrophysical properties for comparison with the model. This should involve integrating core analysis, 3D seismic data, and well data to refine sedimentology and stratigraphy studies.
2. Investigate the underlying causes of the cycles of sediment supply fluctuations observed in the study: explore whether regional climatic events, such as incorporating the monsoons effect and/or orbital cycle (cyclostratigraphy), had a significant impact on sedimentation dynamics.
3. Conduct a more detailed and comprehensive analysis of carbonate reef growth, considering the impact of sea-level fluctuations and sediment supply on different stages of reef development in influencing the growth rate and distribution of carbonate reefs.

By addressing these research directions, future studies can build upon the foundation laid by the current research, providing more complete insights into the geological complexities of the Ardjuna Sub-Basin and contributing to the advancement of sedimentary and reservoir science in the region.





## References

- Abdurrokhim, 2014. A prograding slope-shelf succession of the Middle-Late Miocene Jatiluhur formation : sedimentology and genetic stratigraphy of mixed siliciclastic and carbonate deposits in the Bogor Trough, west Java. Graduate School of Science CHIBA UNIVERSITY.
- Abdurrokhim, Ito, M., 2013. The role of slump scars in slope channel initiation: A case study from the Miocene Jatiluhur Formation in the Bogor Trough, West Java. *Journal of Asian Earth Sciences* 73, 68–86. <https://doi.org/10.1016/j.jseaes.2013.04.005>
- Adnan, A., Sukowitono, Supriyanto, 1991. Jatibarang Sub Basin - A Half Graben Model in the Onshore of Northwest Java. <https://doi.org/10.29118/ipa.2549.279.297>
- Advokaat, E.L., Marshall, N.T., Li, S., Spakman, W., Krijgsman, W., van Hinsbergen, D.J.J., 2018. Cenozoic Rotation History of Borneo and Sundaland, SE Asia Revealed by Paleomagnetism, Seismic Tomography, and Kinematic Reconstruction. *Tectonics* 37, 2486–2512. <https://doi.org/10.1029/2018TC005010>
- Ainsworth, R.B., Bosscher, H., Newall, M.J., 2000. Forward stratigraphic modelling of forced regressions: evidence for the genesis of attached and detached lowstand systems, in: Hunt, D., Gawthorpe, R.L. (Eds.), *Sedimentary Responses to Forced Regressions*. Geological Society of London, p. 0. <https://doi.org/10.1144/GSL.SP.2000.172.01.08>
- Allen, G.P., Posamentier, H.W., 1993. Sequence stratigraphy and facies model of an incised valley fill; the Gironde Estuary, France. *Journal of Sedimentary Research* 63, 378–391.
- Allen, P., Allen, R., 2013. *Basin Analysis: Principles and Application to Petroleum Play Assessment*.
- Allen, P.A., 2017. *Sediment Routing Systems: The Fate of Sediment from Source to Sink*. Cambridge University Press, Cambridge. <https://doi.org/10.1017/9781316135754>
- Allen, P.A., 2008. From landscapes into geological history. *Nature* 451, 274–276. <https://doi.org/10.1038/nature06586>
- Alves, T.M., Kurtev, K., Moore, G.F., Strasser, M., 2014. Assessing the internal character, reservoir potential, and seal competence of mass-transport deposits using seismic texture: A geophysical and petrophysical approach. *AAPG Bulletin* 98, 793–824. <https://doi.org/10.1306/09121313117>
- Aribowo, S., Husson, L., Natawidjaja, D.H., Authemayou, C., Daryono, M.R., Puji, A.R., Valla, P.G., Pamumpuni, A., Wardhana, D.D., de Gelder, G., Djarwadi, D., Lorcery, M., 2022. Active Back-Arc Thrust in North West Java, Indonesia. *Tectonics* 41, e2021TC007120. <https://doi.org/10.1029/2021TC007120>
- Arpandi, D., Patmosukismo, S., 1975. The cibulakan formation as one of the most prospective stratigraphic units in the north-west Java basinal area, in: *Proc. Indonesian Petrol. Assoc. 4th Ann. Conv. Presented at the Fourth Annual Convention, Indonesian Petroleum Association (IPA)*.
- Asquith, G., Krygowski, D., Henderson, S., Hurley, N., 2004. *Basic well log analysis*. American Association of Petroleum Geologists. <https://doi.org/10.1306/Mth16823>
- Atkinson, C.D., 1993. Sedimentological and reservoir characteristics of the Upper Cibulakan sandstones (main interval) in cores from the B-field, Offshore Northwest Java, in: *Proc. Indon. Petrol. Assoc., Clastic Rocks and Reservoirs of Indonesia: A Core Workshop, 1993. Presented at the Clastic Rocks and Reservoirs of Indonesia: A Core Workshop, Indonesian Petroleum Association (IPA)*. <https://doi.org/10.29118/IPA.528.59.90>
- Aveliانشyah, Ponco, P., Triono, W., Saefullah, U.A., 2016. Pre-Talang Akar Formation: New Hopes for Hydrocarbon Exploration in the Offshore North West Java Basin, in: *Proc. Indonesian Petrol.*

- Assoc., 40th Ann. Conv. Presented at the Fortieth Annual Convention, Indonesian Petroleum Association (IPA). <https://doi.org/10.29118/IPA.0.16.146.G>
- Ayranci, K., 2022. Applications of Forward Stratigraphic Modelling in Modern Siliciclastic Settings: A Case Study from the Fraser River Delta, Canada. *Applied Sciences* 12, 2399. <https://doi.org/10.3390/app12052399>
- Barber, A.J., Crow, M.J., 2009. Structure of Sumatra and its implications for the tectonic assembly of Southeast Asia and the destruction of Paleotethys. *Island Arc* 18, 3–20.
- Barber, A.J., Crow, M.J., Milsom, J., 2005. Sumatra: geology, resources and tectonic evolution. Geological Society of London.
- Bishop, M.G., 2000. Petroleum systems of the northwest Java province, Java and offshore southeast Sumatra, Indonesia (Open-File Report), Open-File Report. U. S. Geological Survey.
- Bond, C.E., Lunn, R.J., Shipton, Z.K., Lunn, A.D., 2012. What makes an expert effective at interpreting seismic images? *Geology* 40, 75–78. <https://doi.org/10.1130/G32375.1>
- Bosscher, H., Schlager, W., 1992. Computer simulation of reef growth. *Sedimentology* 39, 503–512. <https://doi.org/10.1111/j.1365-3091.1992.tb02130.x>
- Burbury, J.E., 1977. Seismic Expression of Carbonate Build-Ups, Northwest Java Basin, in: PROCEEDINGS INDONESIAN PETROLEUM ASSOCIATION. Indonesian Petroleum Association (IPA), p. 30.
- Burgess, P.M., Lammers, H., van Oosterhout, C., Granjeon, D., 2006. Multivariate sequence stratigraphy: Tackling complexity and uncertainty with stratigraphic forward modeling, multiple scenarios, and conditional frequency maps. *AAPG Bulletin* 90, 1883–1901. <https://doi.org/10.1306/06260605081>
- Carter, D., Hutabarat, M., 1994. The geometry and seismic character of Mid-Late Miocene carbonate sequences, SS area, Offshore Northwest Java, in: Proc. Indon Petrol. Assoc., 23rd Ann. Conv. Presented at the Twenty Third Annual Convention, Indonesian Petroleum Association (IPA). <https://doi.org/10.29118/IPA.1103.323.338>
- Cattaneo, A., Steel, R.J., 2003. Transgressive deposits: a review of their variability. *Earth-Science Reviews* 62, 187–228. [https://doi.org/10.1016/S0012-8252\(02\)00134-4](https://doi.org/10.1016/S0012-8252(02)00134-4)
- Catuneanu, O., 2019. Model-independent sequence stratigraphy. *Earth-Science Reviews* 188, 312–388. <https://doi.org/10.1016/j.earscirev.2018.09.017>
- Catuneanu, O., 2017. Chapter One - Sequence Stratigraphy: Guidelines for a Standard Methodology, in: Montenari, M. (Ed.), *Stratigraphy & Timescales, Advances in Sequence Stratigraphy*. Academic Press, pp. 1–57. <https://doi.org/10.1016/bs.sats.2017.07.003>
- Catuneanu, O., Abreu, V., Bhattacharya, J.P., Blum, M.D., Dalrymple, R.W., Eriksson, P.G., Fielding, C.R., Fisher, W.L., Galloway, W.E., Gibling, M.R., Giles, K.A., Holbrook, J.M., Jordan, R., Kendall, C.G.St.C., Macurda, B., Martinsen, O.J., Miall, A.D., Neal, J.E., Nummedal, D., Pomar, L., Posamentier, H.W., Pratt, B.R., Sarg, J.F., Shanley, K.W., Steel, R.J., Strasser, A., Tucker, M.E., Winker, C., 2009. Towards the standardization of sequence stratigraphy. *Earth-Science Reviews* 92, 1–33. <https://doi.org/10.1016/j.earscirev.2008.10.003>
- Catuneanu, O., Galloway, W.E., Kendall, C.G.S. t. C., Miall, A.D., Posamentier, H.W., Strasser, A., Tucker, M.E., 2011. Sequence Stratigraphy: Methodology and Nomenclature. nos 44, 173–245. <https://doi.org/10.1127/0078-0421/2011/0011>

- Chaki, S., Routray, A., Mohanty, W., 2018. Well-Log and Seismic Data Integration for Reservoir Characterization: A Signal Processing and Machine-Learning Perspective. *IEEE Signal Processing Magazine* 35, 72–81. <https://doi.org/10.1109/MSP.2017.2776602>
- Clements, B., Hall, R., 2011. A record of continental collision and regional sediment flux for the Cretaceous and Palaeogene core of SE Asia: implications for early Cenozoic palaeogeography. *Journal of the Geological Society* 168, 1187–1200. <https://doi.org/10.1144/0016-76492011-004>
- Clements, B., Hall, R., 2007. Cretaceous to Late Miocene stratigraphic and tectonic evolution of West Java, in: *Proc. Indon Petrol. Assoc., 31st Ann. Conv. Presented at the Thirty-First Annual Convention, Indonesian Petroleum Association (IPA)*. <https://doi.org/10.29118/IPA.1520.07.G.037>
- Clements, B., Hall, R., Smyth, H.R., Cottam, M.A., 2009. Thrusting of a volcanic arc: a new structural model for Java. *Petroleum Geoscience* 15, 159–174. <https://doi.org/10.1144/1354-079309-831>
- Clerc, C., Ringenbach, J.-C., Jolivet, L., Ballard, J.-F., 2018. Rifted margins: Ductile deformation, boudinage, continentward-dipping normal faults and the role of the weak lower crust. *Gondwana Research, Rifting to Passive Margins* 53, 20–40. <https://doi.org/10.1016/j.gr.2017.04.030>
- Clift, P., Plumb, R., 2008. The Asian Monsoon: Causes, History and Effects. <https://doi.org/10.1017/CBO9780511535833>
- Clift, P.D., Hodges, K.V., Heslop, D., Hannigan, R., Van Long, H., Calves, G., 2008. Correlation of Himalayan exhumation rates and Asian monsoon intensity. *Nature Geosci* 1, 875–880. <https://doi.org/10.1038/ngeo351>
- Clift, P.D., Jonell, T.N., 2021. Monsoon controls on sediment generation and transport: Mass budget and provenance constraints from the Indus River catchment, delta and submarine fan over tectonic and multimillennial timescales. *Earth-Science Reviews* 220, 103682. <https://doi.org/10.1016/j.earscirev.2021.103682>
- Clift, P.D., Webb, A.A.G., 2019. A history of the Asian monsoon and its interactions with solid Earth tectonics in Cenozoic South Asia. *SP* 483, 631–652. <https://doi.org/10.1144/SP483.1>
- Cobbing, E.J., Mallick, D.I.J., Pitfield, P.E.J., Teoh, L.H., 1986. The granites of the Southeast Asian Tin Belt. *Journal of the Geological Society* 143, 537–550. <https://doi.org/10.1144/gsjgs.143.3.0537>
- Crombez, V., Rohais, S., Baudin, F., Chauveau, B., Euzen, T., Granjeon, D., 2017. Controlling factors on source rock development: implications from 3D stratigraphic modeling of Triassic deposits in the Western Canada Sedimentary Basin. *Bull. Soc. géol. Fr.* 188, 30. <https://doi.org/10.1051/bsgf/2017188>
- Crow, M., 2005. Chapter 8 Tertiary volcanicity. *Geological Society, London, Memoirs* 31, 98–119.
- Curtis, A., 2012. The science of subjectivity. *Geology* 40, 95–96. <https://doi.org/10.1130/focus012012.1>
- Davies, R.J., 2007. *Seismic geomorphology: applications to hydrocarbon exploration and production, Geological Society special publication*. Geological Society, London.
- Deutsch, C., Journel, A., 1995. *GSLIB: Geostatistical Software Library and User's Guide*, in: *Technometrics*. p. 126. <https://doi.org/10.2307/1269177>
- Deutsch, J.L., Deutsch, C.V., 2012. Latin hypercube sampling with multidimensional uniformity. *Journal of Statistical Planning and Inference* 142, 763–772. <https://doi.org/10.1016/j.jspi.2011.09.016>

- Donselaar, M.E., Schmidt, J.M., 2005. Integration of outcrop and borehole image logs for high-resolution facies interpretation: example from a fluvial fan in the Ebro Basin, Spain. *Sedimentology* 52, 1021–1042. <https://doi.org/10.1111/j.1365-3091.2005.00737.x>
- Embry, A.F., 1995. Sequence boundaries and sequence hierarchies: problems and proposals, in: Steel, R.J., Felt, V.L., Johannessen, E.P., Mathieu, C. (Eds.), *Norwegian Petroleum Society Special Publications, Sequence Stratigraphy on the Northwest European Margin*. Elsevier, pp. 1–11. [https://doi.org/10.1016/S0928-8937\(06\)80059-7](https://doi.org/10.1016/S0928-8937(06)80059-7)
- Falade, A.O., Amigun, J.O., Makeen, Y.M., Kafisanwo, O.O., 2022. Characterization and geostatistical modeling of reservoirs in ‘Falad’ field, Niger Delta, Nigeria. *J Petrol Explor Prod Technol* 12, 1353–1369. <https://doi.org/10.1007/s13202-021-01397-7>
- Falivene, O., Prather, B.E., Martin, J., 2020. Quantifying sand delivery to deep water during changing sea-level: Numerical models from the Quaternary Brazos Icehouse continental margin. *Basin Research* 32, 1711–1733. <https://doi.org/10.1111/bre.12449>
- Galloway, W.E., 1989. Genetic stratigraphic sequences in basin analysis I: architecture and genesis of flooding-surface bounded depositional units. *AAPG bulletin* 73, 125–142.
- Gawthorpe, R.L., Fraser, A.J., Collier, R.E.Li., 1994. Sequence stratigraphy in active extensional basins: implications for the interpretation of ancient basin-fills. *Marine and Petroleum Geology* 11, 642–658. [https://doi.org/10.1016/0264-8172\(94\)90021-3](https://doi.org/10.1016/0264-8172(94)90021-3)
- Gawthorpe, R.L., Hardy, S., Ritchie, B., 2003. Numerical modelling of depositional sequences in half-graben rift basins. *Sedimentology* 50, 169–185. <https://doi.org/10.1046/j.1365-3091.2003.00543.x>
- Geoservices [LTD], 1999. Biostratigraphical and Paleoenvironmental Analysis of Well NI-4 (4200 - 7006 ftD), Drilled in the Java Sea, Offshore Indonesia. P.T. Geoservices [LTD], Report No.99/1002/LAB. Prepared for Atlantic Richfield Indonesia INC, [ARII]. (Unpublished No. 99/1002/LAB). P.T. Geoservices [LTD], Jakarta.
- Gervais, V., Ducros, M., Granjeon, D., 2018. Probability maps of reservoir presence and sensitivity analysis in stratigraphic forward modeling. *Bulletin* 102, 613–628. <https://doi.org/10.1306/0913171611517242>
- Gradstein, F.M., Ogg, J.G., Schmitz, M.D., Ogg, G.M. (Eds.), 2020. *The geologic time scale 2020*. Elsevier, Amsterdam.
- Granjeon, D., 2019. Use of high-performance stratigraphic forward modelling to improve siliciclastic and carbonate reservoir depositional architecture description. *J. JAPANESE. ASSOC. PETROL. TECHNOL.* 84, 59–70. <https://doi.org/10.3720/japt.84.59>
- Granjeon, D., 2014. 3D forward modelling of the impact of sediment transport and base level cycles on continental margins and incised valleys, in: Martinius, A.W., Ravnås, R., Howell, J.A., Steel, R.J., Wonham, J.P. (Eds.), *From Depositional Systems to Sedimentary Successions on the Norwegian Continental Margin*. John Wiley & Sons, Ltd, Chichester, UK, pp. 453–472. <https://doi.org/10.1002/9781118920435.ch16>
- Gresko, M., Suria, C., Sinclair, S., 1995. Basin Evolution of the Ardjuna Rift System and Its Implications for Hydrocarbon Exploration, Offshore Northwest Java, Indonesia, in: *Proc. Indon Petrol. Assoc., 24th Ann. Conv. Indonesian Petroleum Association (IPA)*.
- Hall, R., 2012. Late Jurassic–Cenozoic reconstructions of the Indonesian region and the Indian Ocean. *Tectonophysics* 570–571, 1–41. <https://doi.org/10.1016/j.tecto.2012.04.021>

- Hall, R., 2011. Australia–SE Asia collision: plate tectonics and crustal flow. Geological Society, London, Special Publications 355, 75–109. <https://doi.org/10.1144/SP355.5>
- Hall, R., 2002. Cenozoic geological and plate tectonic evolution of SE Asia and the SW Pacific: computer-based reconstructions, model and animations. *Journal of Asian Earth Sciences* 20, 79.
- Hall, R., Morley, C.K., 2004. Sundaland basins, in: Clift, P., Kuhnt, W., Wang, P., Hayes, D. (Eds.), *Geophysical Monograph Series*. American Geophysical Union, Washington, D. C., pp. 55–85. <https://doi.org/10.1029/149GM04>
- Hamilton, W., 1991. Tectonics of the Indonesian Region. U.S. Geological Survey Professional Paper 1078 356.
- Hawie, N., Marfisi, E., Saint-Ange, F., MacDonald, A.W.A., 2019. Statistical analysis of forward stratigraphic models in complex salt provinces: The central Scotian Basin case study. *AAPG Bulletin* 103, 433–467. <https://doi.org/10.1306/07031817054>
- Helland-Hansen, W., Hampson, G.J., 2009. Trajectory analysis: concepts and applications. *Basin Research* 21, 454–483. <https://doi.org/10.1111/j.1365-2117.2009.00425.x>
- Helton, J.C., Davis, F.J., 2003. Latin hypercube sampling and the propagation of uncertainty in analyses of complex systems. *Reliability Engineering & System Safety* 81, 23–69. [https://doi.org/10.1016/S0951-8320\(03\)00058-9](https://doi.org/10.1016/S0951-8320(03)00058-9)
- Höcker, C., Eastwood, K.M., Herweijer, J.C., Adams, J.T., 1990. Use of Dipmeter Data in Clastic Sedimentological Studies1. *AAPG Bulletin* 74, 105–118. <https://doi.org/10.1306/0C9B2263-1710-11D7-8645000102C1865D>
- Hunt, D., Tucker, M.E., 1992. Stranded parasequences and the forced regressive wedge systems tract: deposition during base-level fall. *Sedimentary Geology* 81, 1–9. [https://doi.org/10.1016/0037-0738\(92\)90052-S](https://doi.org/10.1016/0037-0738(92)90052-S)
- Hutchinson, C.S., 1989. Geological Evolution of South-East Asia. *Oxford Monographs on Geology and Geophysics*. Geological Magazine 127, 185–185. <https://doi.org/10.1017/S0016756800013947>
- Isworo, H., Saefullah, U.A., Prasetyo, T., 1999. Depositional model of the MB Field Mid-Main carbonate reservoir Offshore Northwest Java Indonesia, in: Proc. Indon. Petrol. Assoc., 27th Ann. Conv. Presented at the Twenty Seventh Annual Convention & Exhibition, Indonesian Petroleum Association (IPA). <https://doi.org/10.29118/IPA.870.G.186>
- Jahn, F., Cook, M., Graham, M., 2008. *Hydrocarbon Exploration and Production*. Elsevier.
- Karner, G.D., Driscoll, N.W., Barker, D.H.N., 2003. Syn-rift regional subsidence across the West African continental margin: the role of lower plate ductile extension. Geological Society, London, Special Publications 207, 105–129. <https://doi.org/10.1144/GSL.SP.2003.207.6>
- Koesoemadinata, R.P., Pulungono, A., 1974. Offshore Tertiary Sedimentary Basins in Indonesia. *Journal of Mathematical and Fundamental Sciences* 8, 91–108.
- Malod, J.A., Karta, K., Beslier, M.O., Zen, M.T., 1995. From normal to oblique subduction: Tectonic relationships between Java and Sumatra. *Journal of Southeast Asian Earth Sciences* 12, 85–93. [https://doi.org/10.1016/0743-9547\(95\)00023-2](https://doi.org/10.1016/0743-9547(95)00023-2)
- Martins-Neto, M.A., Catuneanu, O., 2010. Rift sequence stratigraphy. *Marine and Petroleum Geology* 27, 247–253. <https://doi.org/10.1016/j.marpetgeo.2009.08.001>
- Martodjojo, S., 1984. *Evolusi Cekungan Bogor Jawa Barat*. Disertasi Doktor, ITB, Bandung (Tidak diterbitkan).



- Matthews, S.J., Bransden, P.J.E., 1995. Late Cretaceous and Cenozoic tectono-stratigraphic development of the East Java Sea Basin, Indonesia. *Marine and Petroleum Geology* 12, 499–510. [https://doi.org/10.1016/0264-8172\(95\)91505-J](https://doi.org/10.1016/0264-8172(95)91505-J)
- McBride, E.F., 1984. Compaction in Sandstones--Influence on Reservoir Quality: ABSTRACT. *AAPG Bulletin* 68, 505–505.
- Mckay, M.D., Beckman, R.J., Conover, W.J., 1979. A Comparison of Three Methods for Selecting Values of Input Variables in the Analysis of Output From a Computer Code. *Technometrics*.
- Metcalfe, I., 2013. Gondwana dispersion and Asian accretion: Tectonic and palaeogeographic evolution of eastern Tethys. *Journal of Asian Earth Sciences* 66, 1–33.
- Metcalfe, I., 1996. Pre-Cretaceous evolution of SE Asian terranes. Geological Society, London, Special Publications 106, 97–122. <https://doi.org/10.1144/GSL.SP.1996.106.01.09>
- Miller, K.G., Browning, J.V., Schmelz, W.J., Kopp, R.E., Mountain, G.S., Wright, J.D., 2020. Cenozoic sea-level and cryospheric evolution from deep-sea geochemical and continental margin records. *Science Advances* 6, eaaz1346. <https://doi.org/10.1126/sciadv.aaz1346>
- Miller, K.G., Lombardi, C.J., Browning, J.V., Schmelz, W.J., Gallegos, G., Mountain, G.S., Baldwin, K.E., 2018. Back To Basics of Sequence Stratigraphy: Early Miocene and Mid-cretaceous Examples from the New Jersey Paleoshelf. *Journal of Sedimentary Research* 88, 148–176. <https://doi.org/10.2110/jsr.2017.73>
- Mitchum, R.M., Vail, P.R., Iii, S.T., 1977. Seismic Stratigraphy and Global Changes of Sea Level: Part 2. The Depositional Sequence as a Basic Unit for Stratigraphic Analysis: Section 2. Application of Seismic Reflection Configuration to Stratigraphic Interpretation 165, 53–62.
- Mitchum, R.M., Van Wagoner, J.C., 1991. High-frequency sequences and their stacking patterns: sequence-stratigraphic evidence of high-frequency eustatic cycles. *Sedimentary Geology, The Record of Sea-Level Fluctuations* 70, 131–160. [https://doi.org/10.1016/0037-0738\(91\)90139-5](https://doi.org/10.1016/0037-0738(91)90139-5)
- Mode, A.W., Anyiam, O.A., John, S.I., 2017. Depositional environment and reservoir quality assessment of the “Bruks Field,” Niger Delta. *J Petrol Explor Prod Technol* 7, 991–1002. <https://doi.org/10.1007/s13202-017-0346-y>
- Montaggioni, L.F., Borgomano, J., Fournier, F., Granjeon, D., 2015. Quaternary atoll development: New insights from the two-dimensional stratigraphic forward modelling of Mururoa Island (Central Pacific Ocean). *Sedimentology* 62, 466–500. <https://doi.org/10.1111/sed.12175>
- Moore, C.H., Wade, W.J., 2013. Chapter 2 - The Application of the Concepts of Sequence Stratigraphy to Carbonate Rock Sequences, in: Moore, C.H., Wade, W.J. (Eds.), *Developments in Sedimentology, Carbonate Reservoirs*. Elsevier, pp. 23–38. <https://doi.org/10.1016/B978-0-444-53831-4.00002-1>
- Morley, C.K., 2002. A tectonic model for the Tertiary evolution of strike–slip faults and rift basins in SE Asia. *Tectonophysics* 347, 189–215. [https://doi.org/10.1016/S0040-1951\(02\)00061-6](https://doi.org/10.1016/S0040-1951(02)00061-6)
- Noble, R.A., Pratomo, K.H., Nugrahanto, K., Ibrahim, A.M.T., Prasetya, I., Mujahidin, N., Wu, C.H., Howes, J.V.C., 1997. Petroleum systems of Northwest Java, Indonesia, in: *Proceedings of an International Conference on Petroleum Systems of SE Asia and Australasia*. Presented at the International Conference on Petroleum Systems of SE Asia and Australasia, Indonesian Petroleum Association (IPA). <https://doi.org/10.29118/IPA.1470.585.600>
- Noble, R.A., Wu, C.H., Atkinson, C.D., 1991. Petroleum generation and migration from Talang Akar coals and shales offshore N.W. Java, Indonesia. *Organic Geochemistry* 17, 363–374. [https://doi.org/10.1016/0146-6380\(91\)90100-X](https://doi.org/10.1016/0146-6380(91)90100-X)

- Noon, S.W., Frame, P., Quidayan, V., Sukarno, 1993. Biostratigraphy of the SD-1 Well (420'-10175'TD) Drilled Offshore N.W. Java Indonesia. Prepared for Atlantic Richfield Indonesia Inc. (Unpublished No. GSI-92055).
- Ortiz C., J., Deutsch, C.V., 2002. Calculation of Uncertainty in the Variogram. *Mathematical Geology* 34, 169–183. <https://doi.org/10.1023/A:1014412218427>
- Otoo, D., Hodgetts, D., 2021. Porosity and permeability prediction through forward stratigraphic simulations using GPMTM and PetrelTM: application in shallow marine depositional settings. *Geoscientific Model Development* 14, 2075–2095. <https://doi.org/10.5194/gmd-14-2075-2021>
- Park, R.K., Crevello, P., Hantoro, W., 2010. Equatorial Carbonate Depositional Systems of Indonesia. *SEPM (Soc. Sed. Geol.), Spec. Publ* 95, 41–77. <https://doi.org/10.2110/sepm.095.041>
- Patmosukismo, S., Yahya, I., 1974. The Basement Configuration of the North West Java Area, in: *Proc. Indon Petrol. Assoc., 3rd Ann. Conv. Presented at the Third Annual Convention, Indonesian Petroleum Association (IPA)*. <https://doi.org/10.29118/IPA.2164.129.152>
- Permana, A., Pratama, R., Husein, S., 2019. New Play of Pre-Talang Akar Carbonate Limestone in South Sumatra Basin for Future Deep Target Exploration. Presented at the 2nd EAGE Conference on Reservoir Geoscience, European Association of Geoscientists & Engineers, pp. 1–3. <https://doi.org/10.3997/2214-4609.201977059>
- Phillips, T.B., Fazlikhani, H., Gawthorpe, R.L., Fossen, H., Jackson, C.A.-L., Bell, R.E., Faleide, J.I., Rotevatn, A., 2019. The Influence of Structural Inheritance and Multiphase Extension on Rift Development, the Northern North Sea. *Tectonics* 38, 4099–4126. <https://doi.org/10.1029/2019TC005756>
- Plint, A.G., 1988. Sharp-Based Shoreface Sequences and 'Offshore Bars' in the Cardium Formation of Alberta: Their Relationship to Relative Changes in Sea Level, in: Wilgus, C.K., Hastings, B.S., Posamentier, H., Wagoner, J.V., Ross, C.A., Kendall, C.G.St.C. (Eds.), *Sea-Level Changes: An Integrated Approach*. *SEPM Society for Sedimentary Geology*, p. 0. <https://doi.org/10.2110/pec.88.01.0357>
- Plint, A.G., Nummedal, D., 2000. The falling stage systems tract: recognition and importance in sequence stratigraphic analysis. *Geological Society, London, Special Publications* 172, 1–17.
- Polson, D., Curtis, A., 2010. Dynamics of uncertainty in geological interpretation. *Journal of the Geological Society* 167, 5–10. <https://doi.org/10.1144/0016-76492009-055>
- Ponto, C.V., Wu, C.H., Pranoto, A., Stinson, W.H., 1988. Improved Interpretation of the Talang Akar Depositional Environment as an Aid to Hydrocarbon Exploration in the ARII Offshore Northwest Java Contract Area 397–422.
- Posamentier, H.W., 2002. Ancient shelf ridges-A potentially significant component of the transgressive systems tract: Case study from offshore northwest Java. *Bulletin* 86. <https://doi.org/10.1306/61EEDA44-173E-11D7-8645000102C1865D>
- Posamentier, H.W., Allen, G.P., James, D.P., Tesson, M., 1992. Forced regressions in a sequence stratigraphic framework: concepts, examples, and exploration significance. *AAPG bulletin* 76, 1687–1709.
- Posamentier, H.W., Davies, R.J., Cartwright, J.A., Wood, L., 2007. Seismic geomorphology – an overview, in: Davies, R.J., Posamentier, H.W., Wood, L.J., Cartwright, J.A. (Eds.), *Seismic Geomorphology: Applications to Hydrocarbon Exploration and Production*. *Geological Society of London*, p. 0. <https://doi.org/10.1144/GSL.SP.2007.277.01.01>

- Posamentier, H.W., Jervey, M.T., Vail, P.R., 1988. Eustatic Controls on Clastic Deposition I—conceptual Framework.
- Posamentier, H.W., Morris, W.R., 2000. Aspects of the stratal architecture of forced regressive deposits. Geological Society, London, Special Publications 172, 19–46.
- Posamentier, H.W., Vail, P.R., 1988. Eustatic Controls on Clastic Deposition II—Sequence and Systems Tract Models, in: Wilgus, C.K., Hastings, B.S., Posamentier, H., Wagoner, J.V., Ross, C.A., Kendall, C.G.St.C. (Eds.), *Sea-Level Changes: An Integrated Approach*. SEPM Society for Sedimentary Geology, p. 0. <https://doi.org/10.2110/pec.88.01.0125>
- Pubellier, M., Meresse, F., 2013. Phanerozoic growth of Asia: Geodynamic processes and evolution. *Journal of Asian Earth Sciences* 72, 118–128. <https://doi.org/10.1016/j.jseaes.2012.06.013>
- Pubellier, M., Morley, C.K., 2014. The basins of Sundaland (SE Asia): Evolution and boundary conditions. *Marine and Petroleum Geology* 58, 555–578. <https://doi.org/10.1016/j.marpetgeo.2013.11.019>
- Purantoro, R., Butterworth, P.J., Kaldi, J.G., Atkinson, C.D., 1994. A Sequence Stratigraphic Model of the Upper Cibulakan Sandstones (Main Interval), Offshore Northwest Java Basin: Insights from U-11 Well, in: *Proc. Indon Petrol. Assoc., 23rd Ann. Conv. Indonesian Petroleum Association (IPA)*, p. 18.
- Ratkolo, T., 1994. Reservoir characteristics and petroleum potential of the mid main carbonate, Upper Cibulakan Group, Northwest Java Basin, Indonesia. University of Wollongong Thesis Collection 1954-2016.
- Reksalegora, S.W., Kusumanegara, Y., Lowry, P., 1996. A Depositional Model for the “Main” Interval, Upper Cibulakan Formation: Its Implications for Reservoir Distribution and Prediction, ARII ONWJ, in: *Proc. Indon Petrol. Assoc., 25th Ann. Conv. Presented at the Twenty-Fifth Silver Anniversary Convention, Indonesian Petroleum Association (IPA)*. <https://doi.org/10.29118/IPA.1970.163.173>
- Reuter, M., Auer, G., Brandano, M., Harzhauser, M., Corda, L., Piller, W.E., 2017. Post-rift sequence architecture and stratigraphy in the Oligo–Miocene Sardinia Rift (Western Mediterranean Sea). *Marine and Petroleum Geology* 79, 44–63. <https://doi.org/10.1016/j.marpetgeo.2016.10.025>
- Rider, M.H., Kennedy, M., 2011. *The Geological Interpretation of Well Logs*. Rider-French.
- Rose, P.R., 1987. Dealing with Risk and Uncertainty in Exploration: How Can We Improve? *AAPG Bulletin* 71, 1–16.
- Royden, L., Keen, C.E., 1980. Rifting process and thermal evolution of the continental margin of Eastern Canada determined from subsidence curves. *Earth and Planetary Science Letters* 51, 343–361. [https://doi.org/10.1016/0012-821X\(80\)90216-2](https://doi.org/10.1016/0012-821X(80)90216-2)
- Sacchi, Q., Salina Borello, E., Weltje, G.J., Dalman, R., 2016. Increasing the predictive power of geostatistical reservoir models by integration of geological constraints from stratigraphic forward modeling. *Marine and Petroleum Geology* 69, 112–126. <https://doi.org/10.1016/j.marpetgeo.2015.10.018>
- Satyana, A.H., 2005. Oligo-Miocene carbonates of Java, Indonesia: tectonic-volcanic setting and petroleum implications, in: *Proc. Indon Petrol. Assoc., 30th Ann. Conv. Presented at the Thirtieth Annual Convention, Indonesian Petroleum Association (IPA)*. <https://doi.org/10.29118/IPA.1592.05.G.031>

- Satyana, A.H., Armandita, C., Raharjo, B., Syafri, I., 2002. New Observations on the Evolution of the Bogor Basin, West Java: Opportunities for Turbidite Hydrocarbon Play. BULETIN GEOLOGI INSTITUT TEKNOLOGI BANDUNG Special Publication.
- Serra, O., Serra, L., 2004. Well logging: data acquisition and applications. Serralog, Méry Corbon, France.
- Sevastjanova, I., Clements, B., Hall, R., Belousova, E.A., Griffin, W.L., Pearson, N., 2011. Granitic magmatism, basement ages, and provenance indicators in the Malay Peninsula: Insights from detrital zircon U–Pb and Hf-isotope data. *Gondwana Research* 19, 1024–1039. <https://doi.org/10.1016/j.gr.2010.10.010>
- SKKMIGAS, 2021. Annual Report 2020: Towards 1 Million Bopd & 12 Bscfd In 2030 Through Massive, Aggressive, And Efficient Activities. Satuan Kerja Khusus Pelaksana Kegiatan Usaha Hulu Minyak dan Gas Bumi Indonesia.
- Sloss, L., 1949. Integrated facies analysis, in: *Sedimentary Facies in Geologic History: Conference at Meeting of the Geological Society of America Held in New York, New York, November 11, 1948*. p. 91.
- Smalley, P.C., Begg, S.H., Naylor, M., Johnsen, S., Godi, A., 2008. Handling risk and uncertainty in petroleum exploration and asset management: An overview. *AAPG Bulletin* 92, 1251–1261. <https://doi.org/10.1306/06040808063>
- Smyth, H.R., Hamilton, P.J., Hall, R., Kinny, P.D., 2007. The deep crust beneath island arcs: Inherited zircons reveal a Gondwana continental fragment beneath East Java, Indonesia. *Earth and Planetary Science Letters* 258, 269–282. <https://doi.org/10.1016/j.epsl.2007.03.044>
- Smyth, H.R., Morton, A., Richardson, N., Scott, R.A., 2014. Sediment provenance studies in hydrocarbon exploration and production: an introduction. *Geological Society, London, Special Publications* 386, 1–6. <https://doi.org/10.1144/SP386.21>
- Stright, L., Bernhardt, A., Boucher, A., Mukerji, T., Derksen, R., 2009. Revisiting the use of seismic attributes as soft data for subseismic facies prediction: Proportions versus probabilities. *The Leading Edge* 28, 1460–1468. <https://doi.org/10.1190/1.3272701>
- Sudarmono, Suherman, T., Eza, B., 1997. Paleogene Basin Development in Sundaland and Its Role to the Petroleum Systems in Western Indonesia 545–560.
- Suyono, Sahudi, K., Prasetya, I., 2005. Exploration in West Java: play concepts in the past, present and future, efforts to maintain reserves growth, in: *Proc. Indon Petrol. Assoc., 30th Ann. Conv. Presented at the Thirtieth Annual Convention, Indonesian Petroleum Association (IPA)*. <https://doi.org/10.29118/IPA.748.05.G.085>
- Tetzlaff, D., Tveiten, J., Salomonsen, P., Christ, A.-B., Athmer, W., Borgos, H., Sonneland, L., Martinez, C., Raggio, F., 2014. GEOLOGIC PROCESS MODELING.
- Tinker, S.W., 1996. Building the 3-D Jigsaw Puzzle: Applications of Sequence Stratigraphy to 3-D Reservoir Characterization, Permian Basin. *AAPG Bulletin* 80, 460–484. <https://doi.org/10.1306/64ED8818-1724-11D7-8645000102C1865D>
- Tobin, R.C., Schwarzer, D., 2014. Effects of sandstone provenance on reservoir quality preservation in the deep subsurface: experimental modelling of deep-water sand in the Gulf of Mexico. *Geological Society, London, Special Publications* 386, 27–47. <https://doi.org/10.1144/SP386.17>
- Todini, E., 2001. Influence of parameter estimation uncertainty in Kriging: Part 1 - Theoretical Development. *Hydrol. Earth Syst. Sci.* 5, 215–223. <https://doi.org/10.5194/hess-5-215-2001>

- Wagoner, J.C.V., Mitchum, R.M., Campion, K.M., Rahmanian, V.D., 1990. Siliciclastic Sequence Stratigraphy in Well Logs, Cores, and Outcrops: Concepts for High-Resolution Correlation of Time and Facies. <https://doi.org/10.1306/Mth7510>
- Wagoner, J.C.V., Posamentier, H.W., R. M. Mitchum, Vail, P.R., Sarg, J.F., Loutit, T.S., Hardenbol, J., 1988. An Overview of the Fundamentals of Sequence Stratigraphy and Key Definitions.
- Waltham, D., Hall, R., Smyth, H.R., Ebinger, C.J., 2008. Basin formation by volcanic arc loading, in: Draut, A.E., Clift, Peter.D., Scholl, D.W. (Eds.), *Formation and Applications of the Sedimentary Record in Arc Collision Zones*. Geological Society of America, p. 0. [https://doi.org/10.1130/2008.2436\(02\)](https://doi.org/10.1130/2008.2436(02))
- Wan, L., Bianchi, V., Hurter, S., Salles, T., Zhang, Z., Yuan, X., 2022. Morphological controls on delta-canyon-fan systems: Insights from stratigraphic forward models. *Sedimentology* 69, 864–890. <https://doi.org/10.1111/sed.12930>
- Wescott, W.A., Krebs, W.N., Dolson, J.C., Karamat, S.A., Nummedal, D., 1996. Rift Basin Sequence Stratigraphy: Some Examples from the Gulf Of Suez. *GeoArabia* 1, 343–358. <https://doi.org/10.2113/geoarabia0102343>
- Wibowo, I.D., Sobani, Fransiska, L., Luciwaty, M., 2018. Successful Story of Proving-Up a New Play, An Eocene Carbonate as a Naturally Fractured Reservoir in Offshore North West Java.
- Widodo, R.W., 2018. Evolution of the Early Miocene Carbonate: Baturaja Formation in Northwest Java Basin, Indonesia (Thesis).
- Williams, P.R., Johnston, C.R., Almond, R.A., Simamora, W.H., 1988. Late cretaceous to early tertiary structural elements of west Kalimantan. *Tectonophysics* 148, 279–297. [https://doi.org/10.1016/0040-1951\(88\)90135-7](https://doi.org/10.1016/0040-1951(88)90135-7)
- Wu, C.C., 1991. Depositional environments and source rock investigations of the Oligocene to Middle Miocene deposits in the Ardjuna Basin, offshore Northwest Java, Indonesia. Dallas, TX (United States); Univ. of Texas.
- Xu, G., Pang, X., 2021. Sequence-stratigraphic dynamics: Variations of genetic stratigraphic units driven by basin subsidence. *Global and Planetary Change* 201, 103482. <https://doi.org/10.1016/j.gloplacha.2021.103482>
- Yong, H., Yongning, M., Bincheng, G., Zhaopu, G., Wenxiang, H., 2019. Application of stratigraphic-sedimentological forward modeling of sedimentary processes to predict high-quality reservoirs within tight sandstone. *Marine and Petroleum Geology* 101, 540–555. <https://doi.org/10.1016/j.marpetgeo.2018.11.027>
- Young, R., Atkinson, C.D., 1993. A Review of Talang Akar Formation (Oligo-Miocene) Reservoirs in the Offshore Areas of Southeast Sumatra and Northwest Java. Indonesian Petroleum Association Clastic Rocks and Reservoirs of Indonesia: A Core Workshop, 1993, 177–210.
- Yu, N.-T., Teng, L.S., Chen, W.-S., Yue, L.-F., Chen, M.-M., 2013. Early post-rift sequence stratigraphy of a Mid-Tertiary rift basin in Taiwan: Insights into a siliciclastic fill-up wedge. *Sedimentary Geology* 286–287, 39–57. <https://doi.org/10.1016/j.sedgeo.2012.12.009>
- Zecchin, M., Catuneanu, O., Caffau, M., 2019. Wave-ravinement surfaces: Classification and key characteristics. *Earth-Science Reviews* 188, 210–239.